SAKARYA UNIVERSITY JOURNAL OF SCIENCE

SAKARYA
ÜNİVERSİTESİ

Osman Sönmez
Department of Civil Engineering
Sakarya University
Sakarya - Türkiye
osonmez@sakarya.edu.tr

Serap Coşansu
Department of Food Engineering
Sakarya University
Sakarya - Türkiye
scosansu@sakarya.edu.tr

Tahsin Turgay
Department of Architecture
Sakarya University
Sakarya - Türkiye
turgay@sakarya.edu.tr

Ufuk Durmaz
Department of Mechanical Engineering
Sakarya University
Sakarya - Türkiye
udurmaz@sakarya.edu.tr

Section Editor (Civil Engineering)

Issa Al-Harthy
Department of Civil and Architectural Engineering
Sultan Qaboos University
Oman
aissa@squ.edu.om

Jamal Khatib
Department of Civil Engineering
University of Wolverhampton
United Kingdom
jmkhatib@wlv.ac.uk

Khalifa Al-Jabri
Department of Civil and Architectural Engineering
Sultan Qaboos University
Oman
aljabri@squ.edu.om

Hakan Alp
Department of Geophysical Engineering
İstanbul University-Cerrahpaşa
İstanbul - Türkiye
hakanalp@iuc.edu.tr

Tuba Tatar
Department of Civil Engineering
Sakarya University
Sakarya - Türkiye
ttatar@sakarya.edu.tr

Gökhan Dok
Department of Civil Engineering
Sakarya University of Applied Sciences
Sakarya - Türkiye
gokhandok@subu.edu.tr

Section Editor (Chemistry)

Can Serkan Keskin
Department of Chemistry
Sakarya University
Sakarya - Türkiye
ckeskin@sakarya.edu.tr

Murat Tuna
Department of Chemistry
Sakarya University
Sakarya - Türkiye
tuna@sakarya.edu.tr

Nahit Gencer
Department of Biochemistry
Balıkesir University
Sakarya - Türkiye
ngencer@balikesir.edu.tr

Section Editor (Biology)

Sezen Toksoy Köseoğlu
Department of Biology
Sakarya University
Sakarya - Türkiye
sezentoksoy@sakarya.edu.tr

Nihan Akıncı Kenanoglu
Department of Biology
Çanakkale Onsekiz Mart University
Çanakkale - Türkiye
nakinci@comu.edu.tr

Oğuz Kurt
Department of Biology
Manisa Celal Bayar University
Manise - Türkiye
oguz.kurt@cbu.edu.tr

Sezgi Somuncu
Department of Biology
Sakarya University
Sakarya - Türkiye
sezgisomuncu@sakarya.edu.tr

Section Editor (Mathematics)

Murat Sarduvan
Department of Mathematics
Sakarya University
Sakarya - Türkiye
msarduvan@sakarya.edu.tr

Selma Özçağ
Department of Mathematics
Hacettepe University
Ankara - Türkiye
sozcag@hacettepe.edu.tr

Necati Olgun
Department of Mathematics
Gaziantep University
Gaziantep - Türkiye
olgun@gantep.edu.tr

Ali Demir
Department of Mathematics
Kocaeli University
Kocaeli - Türkiye
ademir@kocaeli.edu.tr

Section Editor (Computer Science and Engineering)

Fahrettin Horasan
Computer Science and Engineering
Kırıkkale University
Kırıkkale - Türkiye
fhorasan@kku.edu.tr

Kevser Ovaz Akpınar
Computer Science and Engineering
Rochester Dubai Institute of Technology
Dubai
kxocad1@rit.edu

Muhammed Maruf Öztürk
Computer Science and Engineering
Süleyman Demirel University
Isparta - Türkiye
muhammedozturk@sdu.edu.tr

Mustafa Akpinar
Computer Science and Engineering
High Tech Collages
United Arab Emirates
mustafakpinar@gmail.com

Section Editor (Physics)

Ceren Tayran
Department Physics
Gazi University
Ankara - Türkiye
c.tayran@gazi.edu.tr

Section Editor (Industrial Engineering)

Feyza Gürbüz
Department Industrial Engineering
Erciyes University
Kayseri - Türkiye
feyza@erciyes.edu.tr

Mehmet Emin Aydın
Department Industrial Engineering
University of The West of England Bristol
England
mehmet.aydin@uwe.ac.uk,

Barış Yüce
Department Industrial Engineering
University of Exeter
United Kingdom
b.yuce@exeter.ac.uk

Benjamin Durakovic
Department Industrial Engineering
International University of Sarajevo
Bosnia and Herzegovina
bdurakovic@ius.edu.ba

Section Editor (Mechanical Engineering)

Elif Eker Kahveci
Department of Mechanical Engineering
Sakarya University
Sakarya - Türkiye
eeker@sakarya.edu.tr

Erman Aslan
Department of Mechanical Engineering
Kocaeli University
Kocaeli - Türkiye
erman.aslan@kocaeli.edu.tr

Abderrahmane Benbrik
Department of Mechanical Engineering
M'hamed Bougara University
Egypt
abderrahmane.benbrik@univ-boumerdes.dz

Ali Cemal Benim
Department of Mechanical Engineering
Düsseldorf University of Applied Sciences
Germany
alicemal@prof-benim.com

Shi-Chune Yao
Department of Mechanical Engineering
Carnegie Mellon University
USA
sy0d@andrew.cmu.edu

Section Editor
(Environmental Sciences and Engineering)

Senay Çetin Doğruparmak
Department of Environmental Engineering
Kocaeli University
Kocaeli - Türkiye
senayc@kocaeli.edu.tr

Section Editor (Food Science)

Aslı Uçar
Department of Food Sciences
Ankara University
Ankara - Türkiye
aucar@ankara.edu.tr

Section Editor
(Electrical and Electronics Engineering)

Francesco De Paulis
Department of Electrical and Electronics Engineering
L'Aquila University
Italy
francesco.depaulis@univaq.it

Rıfkı Terzioğlu
Department of Electrical and Electronics Engineering
Bolu Abant Izzet Baysal University
Bolu - Türkiye
rifkiterzioğlu@ibu.edu.tr

Section Editor (Architecture)

İsmail Hakkı Demir
Department of Architecture
Sakarya University
Sarkaya - Türkiye
idemir@sakarya.edu.tr

Section Editor (Materials Science)

Miraç Alaf
Department Metallurgical and Materials Engineering
Bilecik Şeyh Edebali University
Bilecik - Türkiye
mirac.alaf@bilecik.edu.tr

English Language Editor

Seçkin Arı
Department of Computer Engineering
Sakarya University, Sakarya-Türkiye
ari@sakarya.edu.tr

Editorial Assistant

Evrim Yüksel
Department of Environmental Enginering
Instıtute of Sciences, Sakarya University
Sakarya-Türkiye
eyuksel@sakarya.edu.tr

Statistical Editor

Önder Gökmen Yıldız
Department of Mathematics
Bilecik Şeyh Edebali University, Bilecik-Türkiye
ogokmen.yildiz@bilecik.edu.tr

Indexing

Scopus®

DOAJ

ULAKBİM
TR DİZİN

ERIHPLUS
EUROPEAN REFERENCE INDEX FOR THE
HUMANITIES AND SOCIAL SCIENCES

Academic
Search
Premier

Business
Source® Premier

Business
Source® Elite

Contents

Research Article

Eco-friendly Bacterial Cellulose/Castor Oil Hydrogels: Physicochemical Behavior and Biocompatibility

Elif Işıkçı Koca[1,2] (iD), Orkun Pinar[3,4] (iD), Özlem Yalçın Çapan[5] (iD), Gökhan Çaylı[6] (iD), Dilek Kazan[1,4] (iD), Pınar Çakır Hatır[7,8*] (iD)

[1] Marmara University, Faculty of Engineering, Department of Bioengineering, Istanbul, Türkiye, elif.isikci@gmail.com, kzndlk@gmail.com, ror.org/02kswqa67

[2] Işık University, Faculty of Engineering and Natural Sciences, Department of Electrical and Electronics Engineering, Istanbul, Türkiye, elif.isikci@gmail.com, ror.org/02j8k6t75

[3] Lappeenranta-Lahti University of Technology LUT, LUT School of Engineering Science, Department of Separation Science, Mikkeli, Finland, orkunpinar@gmail.com, ror.org/0208vgz68

[4] BacPolyZyme Bioengineering Ltd. Şti., Istanbul, Türkiye, orkunpinar@gmail.com, kzndlk@gmail.com

[5] Tekirdag Namik Kemal University, Faculty of Medicine, Department of Medical Biology, Tekirdag, Türkiye, ozlemyalcincapan@gmail.com, ror.org/01a0mk874

[6] Istanbul University - Cerrahpaşa, Faculty of Engineering, Department of Engineering Sciences, Istanbul, Türkiye, gokhan.cayli@istanbul.edu.tr, ror.org/01dzn5f42

[7] Istinye University, Faculty of Engineering and Natural Sciences, Department of Biomedical Engineering, Istanbul, Türkiye, pinar.hatir@istinye.edu.tr, ror.org/03081nz23

[8] Istanbul Arel University, Faculty of Engineering and Architecture, Department of Biomedical Engineering, Istanbul, Türkiye, pinarcakir@gmail.com, ror.org/03natay60

* Corresponding Author

ARTICLE INFO

ABSTRACT

In the present work, novel thermoresponsive hydrogels were developed from renewable resources, and the influence of bacterial cellulose molar ratio on their chemical structure, thermal properties, swelling behavior, morphology, and biocompatibility was systematically investigated. The hydrogels were fabricated using castor oil, 4,4'-diphenylmethane diisocyanate, bacterial cellulose, N-isopropylacrylamide, and N,N'-Methylenebisacrylamide. Structural and physicochemical characterizations were performed by Fourier-transform infrared spectroscopy, scanning electron microscopy, differential scanning calorimetry, and thermogravimetric analysis. The highest equilibrated swelling degree was achieved as 592.6% at the maximum bacterial cellulose content. SEM images revealed that the formation of spongy architecture is caused by the increase in the bacterial cellulose content. In vitro biocompatibility studies revealed that the hydrogel with the highest bacterial cellulose content exhibited the greatest cytocompatibility, with an IC50 value of 11.16 mg/ml. Overall, the findings demonstrate the successful fabrication of a novel bio-based thermoresponsive hydrogel through an eco-friendly approach, highlighting its potential for diverse biomedical applications.

1. Introduction

Hydrogels are crosslinked networks of hydrophilic polymers capable of absorbing large amounts of water. Owing to their structural and functional resemblance to living tissues, they are widely applied in the medical field. A particular class of these materials, known as stimuli-responsive hydrogels, can undergo changes in response to environmental triggers such as temperature, enzymatic activity, electrical signals, pH, light, or ionic strength [1]. These hydrogels exhibit swelling or shrinking behavior in response to external stimuli. Among them, thermoresponsive hydrogels, which respond to temperature changes, are particularly preferred

for the design of controlled drug release systems (CDRS) [1, 2]. It is crucial to have enhanced CDRS to maximize the efficacy of drug molecules. CDRS may be engineered as self-activated hydrogels by diffusion, decomposition, dissolution, and other methods under the right conditions [3, 4].

The changes of thermoresponsive hydrogels in response to temperature, combined with their crosslinked hydrophilic networks, make them highly valuable for controlled drug release systems and tissue engineering applications. Thermoresponsive hydrogels are generally classified into two types: those that undergo changes in aqueous environments as the temperature increases, known as lower critical solution temperature (LCST) hydrogels, and those that respond to decreasing temperature, referred to as upper critical solution temperature (UCST) hydrogels [5].

Hydrogels made of N-isopropyl acrylamide (NIPAM) exhibit LCST-type behavior, in which they are solvated and swollen below LCST and become insoluble and shrink above LCST. Since the LCST of NIPAM-based hydrogels is close to physiological temperature, they are considered excellent candidates for CDRS applications. Controlling solubility and LCST enables accurate control over drug release behavior. Hydrogel systems can be tailored by adjusting the types and ratios of monomers and crosslinkers. Incorporating hydrophobic monomers lowers the LCST, whereas hydrophilic monomers raise it [6, 7].

Various studies regarding thermoresponsive hydrogels have been reported in the literature. For instance, Cao and coworkers investigated mixed thermoreversible gels [8]. They designed a thermosensitive sol-gel system based on poly(N-isopropyl acrylamide) (PNIPAM) for the controlled and targeted delivery of a short antibacterial peptide. Another study includes PNIPAM-based polymeric nanocomposites [9]. Fundueanu et al. [10] synthesized poly(N-isopropyl acrylamide-co-N-vinylpyrrolidone) as a thermosensitive material and assessed how the comonomer molar ratio influenced the LCST. Park et al. [11] designed poly(NIPAM-co-butyl acrylate) hydrogels using NIPAM and butyl acrylate as comonomers, with N,N'-methylenebisacrylamide as the crosslinker. They demonstrated that the crosslinked poly(NIPAM-co-butyl acrylate) hydrogels have a high potential for application as smart materials. Another study involving controlled release profiles of the hydrogels was conducted by Onaciu et al. [12]. They examined the 3D polymeric network structures of hydrogels, focusing on their compatibility with living tissue and ability to degrade properties, along with their controlled release profiles. Studies have also explored the use of N-vinyl caprolactam in the synthesis of thermoresponsive hydrogels [13, 14]. In these studies, NIPAM was utilized to impart thermoresponsive properties to the hydrogels. NIPAM is widely recognized as one of the most used monomers for producing thermoresponsive hydrogels. Accordingly, NIPAM-based hydrogels swell below their LCST and shrink above it.

Nowadays, scientific efforts are increasingly directed toward developing materials from renewable resources due to their biodegradability, biocompatibility, cost effectiveness, and environmental sustainability [15]. Castor oil (CO) is a kind of vegetable oil and one of the most widely sourced plant-based raw materials. Because of their low toxicity, functional versatility, affordability, and broad availability, plant oil-based compounds are often employed in polymerization reactions instead of petroleum-derived compounds [16]. In addition to plant-based raw materials, functional polymers can also be produced from microorganism-derived sources. Bacterial cellulose (BC) is one of the microbial raw materials. BC exhibits a fibrous network architecture composed of highly organized three-dimensional nanofibers.

This characteristic of cellulose gives the material a porous morphology and significant surface area per unit total space [17]. Other notable characteristics of cellulose include its high purity, extensive polymerization and crystallinity, as well as remarkable biocompatibility [18]. In addition to its flexibility, BC's elasticity, biodegradability, high water absorption, and potential for chemical

modification make it an excellent material for medical research [19-21].

The literature includes several examples of BC and CO-based polymers designed for biomedical applications. Among these works, Alosmanov et al. [22] effectively manufactured grafted PNIPAM brushes from wet BC cellulose sheets. PNIPAM structures included wet BC affected the swelling characters and drying features of PNIPAM brushes. Wang and coworkers [23] designed a novel material for biological applications, including artificial muscles, and investigated how the molar ratio between MDI and the glucose units in BC affects the material's structure. Arikibe et al. [24] explored how pH affects drug release in BC/chitosan-based hydrogels behaviors and swelling profiles.

Similarly, swelling properties were analyzed on scaffolds included BC based hydrogels filled with calcium phosphate by Basu et al. [25]. Moreover, an investigation into the combination of CO and citric acid was reported by Parada Hernandez et al. [26]. Arévalo-Alquichire et al. [27] also designed a polyurethane-based material from CO for biomedical applications. In our previous study, we synthesized thermo-responsive hydrogels from BC and CO and investigated the effect of CO on the hydrogels' physicochemical properties [28]. The hydrogel derived from CO demonstrated improved sensitivity to temperature fluctuations in contrast to the hydrogel without CO. Building on this background, the present study aims to develop thermoresponsive hydrogels from sustainable sources and to examine how changes in the molar ratio of bacterial cellulose (BC) influence their chemical composition, thermal properties, swelling behavior, morphology, and biocompatibility.

2. General Methods

2.1. Materials and microorganisms

N-Isopropylacrylamide (NIPAM), dimethoxy-2-phenyl acetophenone (DMPA), N,N'-Methylenebisacrylamide (MBAM), and quercetin were sourced from Sigma Aldrich. Acetone and triethylamine were obtained from Merck. 3-(4,5-dimethyl-2-thiazolyl)-2,5-diphenyl-2H-tetrazoline bromide (MTT) and Dulbecco's Modified Eagle Medium (DMEM) were obtained from Sigma Aldrich. 4,4'-diphenylmethane diisocyanate (MDI) was provided by Kimpur Kimteks Polyurethane Corporation. L-glutamine (Gibco) was obtained from Thermo Fisher Scientific, and Castor oil (CO) was obtained from Zag Kimya. All solvents were supplied from Merck. Fetal bovine serum (FBS) was supplied from Lonza. Pure water was obtained by Direct Q-3UV device. UV absorbance readings were acquired using a Photolab 6600 UV-VIS spectrophotometer. UVGL-58 230V 50Hz lamp was used for light-induced polymerization reactions that were realized at 365 nm. 10000 MWt dialysis membranes were used for release experiments. The MMM Vacucell vacuum oven was used to dry the hydrogels. *Komagataeibacter hansenii* DSMZ 5602 was obtained from the German Collection of Microorganisms and Cell Cultures (DSMZ).

2.2. Synthesis of BC from *Komagataeibacter hansenii*

Hutchens et al. [29] and Uzyol et al. [30] detailed the production process of BC. *Komagataeibacter hansenii* and yeast extract-peptone-mannitol medium (YPM) (5 g/L of yeast extract, 3 g/L of peptone, and 25 g/L of mannitol) were used to synthesize BC. BC production occurred at 28°C and pH 6.8. YPM medium served as the preculture medium for all fermentations. After sterilization, a single colony of *Komagataeibacter hansenii* cells was isolated on a petri dish. Subsequently, it was placed to a test tube containing 5 ml of pre-culture medium for further processing.

The incubation occurred at 28°C for two days without agitation. Subsequently, 50 ml of sterile medium was introduced with 10% (v/v) in a 500 ml flask. After 14 days incubation time, the BC was treated with 0.1 N NaOH for 20 min at 80°C to remove bacterial cells and residual medium. Finally, it was extensively washed multiple times with distilled water and stored at 4°C for subsequent procedures.

2.3. Synthesis of Poly(CO-BC-NIPAM) thermoresponsive hydrogels

Two sets of hydrogels were prepared with varying BC molar ratios. Wang et al. [23] described the procedure that was used to create hydrogels from polyurethane. Details of the synthesis method are given in our previous study where the effect of CO on the physical, thermal and morphological characterization of hydrogels was investigated [28]. Furthermore, in our previous study the MDI:BC:CO ratio was kept constant at 1:1:1 and two different hydrogels with and without CO were successfully synthesized. Given the observed positive effects of CO on the hydrogel, it was considered appropriate for all hydrogels in this study to include CO. The present study aimed to explore how variations in the BC ratio influence the thermal, physical, and morphological properties of the hydrogels. The molar ratio of MDI, the glucose units of BC, and CO were set as 1:0.5:1 (poly(CO-BC)-I), and 1:2:1 (poly(CO-BC)-II) (Table 1).

Table 1. Molar equivalency of reactants

Hydrogels	CO[a]	BC[a]	MDI[b]
poly(CO-BC-NIPAM)-I	1	0.5	1
poly(CO-BC-NIPAM)-II	1	2	1

[a]Molar ratio of glucose units; [b]molar ratio of MDI.

First, BC was cut up into the smallest possible fragments. Next, BC fragments were mixed with CO and MDI. TEA and dehydrated acetone were introduced into the mixtures. All the mixtures were kept at 40°C for two days. Then, poly(CO-BC) hydrogels were washed three times with acetone. Next, acrylamide-based monomers were incorporated into hydrogels in the second phase of polymerization to provide them thermoresponsive properties. For this purpose, NIPAM (50.0 and 200.0 mg) and MBAM (0.5 and 2.0 mg) were dissolved in distilled water for poly(CO-BC-NIPAM)-I, poly(CO-BC-NIPAM)-II, respectively.

Poly(CO-BC) hydrogels were transferred into acrylamide solutions (NIPAM and MBAM), and the mixtures were kept at room temperature (RT, 25˚C) for 12h. Afterward, radical polymerization was initiated by adding DMPA (1.0% mol of NIPAM). 1h of UV irradiation (365 nm) was applied for photopolymerization. Then, distilled water was used for washing the polymers three times, followed by the drying process under reduced pressure at 40°C for two days. Finally, poly (CO-BC-NIPAM) hydrogels were obtained as opaque crystal structures.

2.4. Characterization of hydrogels

Fourier-transform infrared spectroscopy (FTIR) spectroscopy was used to investigate the functional groups of hydrogels. FTIR analyses were realized by a Tetra JASCO 6600 spectrophotometer. Thermal analysis was performed by Tetra DSC7000X Differential Scanning Calorimeter (DSC) and HITACHI STA7200 Simultaneous Thermogravimetric Analyzer (TGA). FEI QUANTA 450 FEG ESEM Scanning Electron Microscope (SEM) was used for morphological analyses of hydrogels.

2.5. Swelling measurements

Hydrogels were transferred into distilled water at RT to determine the degree of swelling (%). The gravimetric method was conducted. The hydrogels were occasionally taken out of the water, and their weights were reported. Degree of swelling (%) of hydrogels (Equation 1) was calculated as below:

Degree of swelling (%) $= ((W_w - W_d) / W_d) \times 100$ (1)

where Ww is the weight of the hydrogel after swelling at RT, while Wd represents the weight of the hydrogel after drying at RT. The deswelling behavior of the hydrogels was studied at 40°C, which exceeds the LCST. Hydrogels were weighed after being removed from water periodically. Water retention (%) (WR(%)) (Equation 2) is calculated as described below:

WR (%) $= [(W_r - W_d)/(W_s - W_d)] \times 100$ (2)

where Wr denotes the weight of the hydrogel at a specific time at 40°C and Ws represents the weight of the hydrogel after equilibrating its swelling at RT.

2.6. In vitro cytotoxicity assays

In vitro cytotoxicity of poly(CO-BC-NIPAM) hydrogels were analyzed by MTT (3-(4,5-dimethylthiazol-2-yl)-2,5-diphenyltetrazolium bromide) assay in COS-7 cells (African green monkey kidney fibroblast-like cell line) [31]. COS-7 cells (14×10^4 cells/well) were seeded into 24-well cell culture plates with complete medium consisting of DMEM high glucose with 10% L-glutamine (Gibco), supplemented with 10% FBS, and then cultivated at 37°C in a 5% CO_2 atmosphere.

After the 24-hour growth phase, cells were treated with hydrogels at concentrations ranging from 1 to 20 mg/mL. All experiments were conducted in duplicate. The control group comprised cells that were not treated with hydrogels. After another 24h of incubation, cytotoxicity was determined. 100 μL of sterilized MTT reagent (5 mg/ml) was added to each well, followed by a 4h incubation period. After incubation, the medium was aspirated, and 500 μL of DMSO was added to dissolve the formazan crystals. Following a 15-min incubation in the dark using an orbital shaker, 100 μL of the dissolved formazan solution was transferred to a 96-well plate for absorbance measurement at 570 nm using an AMR-100 Eliza Plate Reader.

The amount of formazan produced is directly proportional to the number of viable cells, and cell viability (%) (CV (%)) was calculated using the following formula:

CV (%) = (Absorbance of the sample/Absorbance of the control group) x 100   (3)

2.7. Statistical analysis

For assessing cell viability, each experiment was independently conducted twice in triplicate. The results are reported as mean ± standard deviation (SD). Statistical evaluation was performed using one-way analysis of variance (ANOVA) with Bonferroni correction for post hoc comparisons to assess comparative statistical analysis between groups, with $p < 0.05$ considered statistically significant.

3. Results and Discussion

3.1. FTIR analyses of hydrogels

FTIR spectra were examined to analyze the functional groups present in the hydrogels. FTIR spectra of poly(CO-BC-NIPAM)-I, and poly(CO-BC-NIPAM)-II were compared with FTIR spectra of starting materials (CO, BC, MDI, and NIPAM). We analyzed FTIR spectra of the BC, MDI, CO, and NIPAM in our previous study [28]. FTIR spectra of poly(CO-BC-NIPAM)-I, and poly(CO-BC-NIPAM)-II are shown in Figure 1. The bands caused by NIPAM are seen in all hydrogels. Amide-II and amide-I groups are observed at 1535 cm^{-1} and 1629 cm^{-1}. The peaks revealed at around 3075 cm^{-1} and 3282 cm-1 indicate NH stretching of NIPAM. There is also a broad peak around 3300 cm^{-1}, likely due to the OH stretching of free hydroxyl groups in BC. The band at 1739 cm^{-1} demonstrates the existence of ester carbonyl groups in CO. [28]. We believe that the absence of the CO band in poly(CO-BC-NIPAM)-I shows that this polymer contains less amount of CO than expected. In our previous study, it was demonstrated that amide II and amide I groups are seen in the 1535 cm-1 and 1629 cm-1 bands [28]. In addition, the bands resulting from the OH stretching of the free hydroxyl groups in BC are also seen in the FTIR analysis of the hydrogels synthesized in our previous study.

Consistent with our findings, Alosmanov et al. [22] noted that the peaks at approximately 3340 cm^{-1} correlated with the existence of amide groups in PNIPAM chains. It was also noted that these bands overlap with those produced by OH stretching vibrations. Moreover, the broad band could have formed as a result involving hydrogen bonds forming among the PNIPAM polymer chains and the BC surface.

3.2. Morphology of hydrogels

Figure 2 illustrates SEM images of poly(CO-BC-NIPAM)-I, and poly(CO-BC-NIPAM)-II. Poly(CO-BC-NIPAM)-I has a layered structure with discrete irregular particles on it, whereas poly(CO-BC-NIPAM)-II has sponge-like structures with spherical particles.
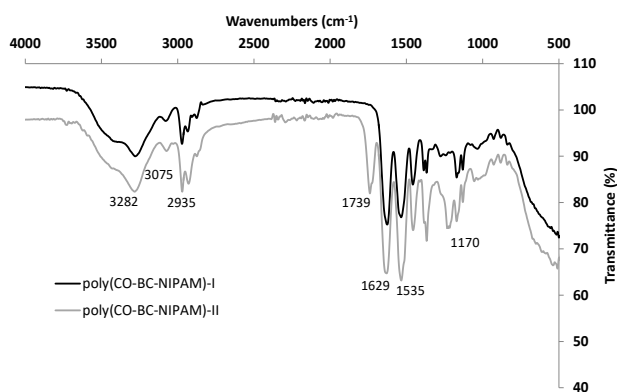
Figure 1. FTIR spectra of the hydrogels

Wang et al. [23] demonstrated that pure BC has a perfect vertical layer structure, whereas BC/PNIPAM composites show porous morphology. In the present study, the sponge-like morphology was observed in the hydrogels with a higher molar ratio of BC. Similarly, Luo et al. [32] showed that there are undulations on the surface of cellulose-based composites and the structure has many folds, resulting in more surface area, and capillary action.

The results from Moura Neto et al. [33] and Alaa et al. [34] are consistent with the hydrogel images obtained in the current study. Moura Neto et al. [33] also reported that CO provided a layered structure in BC/NIPAM composite, which is consistent with our results. As the molar ratio of CO/BC increased, a more layered structure was examined.
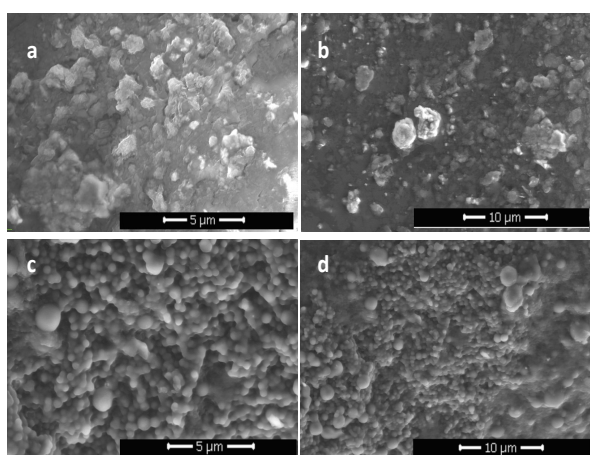
Figure 2. SEM images of produced hydrogels. (a, b) poly(CO-BC-NIPAM)-I, (c, d) poly(CO-BC-NIPAM)-II

Moreover, the quantity of pores in the structures rose as the BC ratio increased because of the porous structure of BC. Layered structures are added to these hydrogels by the addition of CO. As expected from the results of the study, the porosity increases as the BC ratio increases, confirming the results of our previous study [28]. It was also observed that porous and spongy structures were formed with the addition of BC in the hydrogels synthesized in our previous study where the BC ratio was lower compared to poly(CO-BC-NIPAM)-II. The data from this study demonstrates that porosity increases with increasing BC ratio.

3.3. Thermal characterizations

DSC technique gives valuable information about the thermal transition in the polymers such as glass transition and melting. DSC thermograms of the polymers synthesized are shown in Figure 3. Poly(CO-BC-NIPAM)-I showed a glass transition at -45°C. Other polymers do not show any Tg. All polymers showed melting behaviors between certain temperature ranges. Melting temperature of the samples are obtained at 107.2°C, and 114.7°C for poly(CO-BC-NIPAM)-I, poly(CO-BC-NIPAM)-II respectively. The heat of fusion of poly(CO-BC-NIPAM)-I, and poly(CO-BC-NIPAM)-II was determined as 43.1 mJ/mg, and 70.4 mJ/mg, respectively. These melting behaviors might be the results of the degenerative chain transfer reactions of the allylic positions of CO which can cause premature polymerization. Another explanation of these melting peaks would be an action of the long carbon chain domains of fatty acid moieties of CO. These findings are congruent with the literature [28].

TGA (DTA) thermograms give valuable information about the thermal decomposition of the materials. TGA thermograms are illustrated in Figure 4. All samples were heated to 600°C with a 10°C/min heating rate under 200 ml/min nitrogen atmosphere. Thermal stabilities of the materials synthesized can be expressed by 15% and 50% weight loss temperatures. The 15% weight loss temperatures were measured as 272, and 277°C for poly (CO-BC-NIPAM)-I, poly (CO-BC-NIPAM)-II, respectively. The 50% weight loss temperatures of the samples were assessed as 403, and 401°C for poly (CO-BC-NIPAM)-I, poly (CO-BC-NIPAM)-II, respectively.
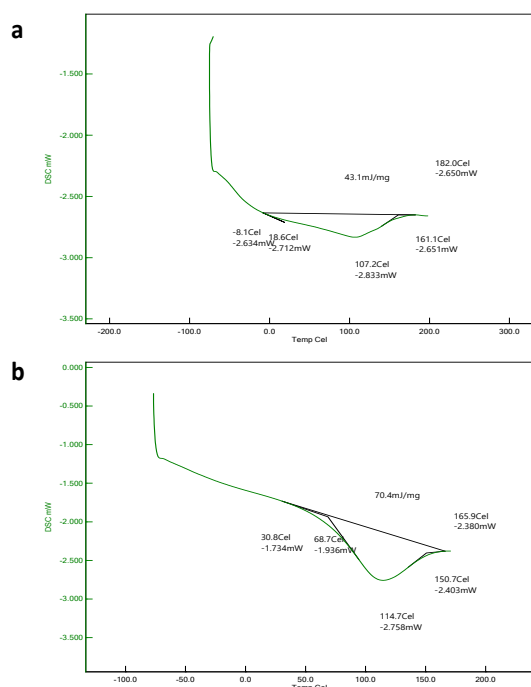
Figure 3. DSC thermograms. **(a)** poly(CO-BC-NIPAM)-I, **(b)** poly(CO-BC-NIPAM)-II

Figure 4. TGA curves. **(a)** poly(CO-BC-NIPAM)-I, **(b)** poly(CO-BC-NIPAM)-II

By using derivative TGA, one can evaluate the thermal degradation rate. In this sense, when the thermal degradation rate increases the intensity of the DTGA increases as well. The lowest one belonged to poly(CO-BC-NIPAM)-II as 22.5 DTG%/min at 401°C.

3.4. Swelling and shrinking dynamics of hydrogels

The hydrogels' swelling properties were investigated. Hydrogels can be visually distinguished from one another when they are dry or wet. Swelling and water retention profiles of the hydrogels over time are demonstrated in Figure 5a and 5b. Equilibrated swelling degree (ESD) of the hydrogels was accomplished in 120 min at room temperature (Figure 5a). ESD of poly(CO-BC-NIPAM)-I, and poly(CO-BC-NIPAM)-II, was calculated as 228.6%, and 592.6%, respectively. Due to BC's greater potential for retaining water than CO, ESD of the hydrogels is dramatically rising as BC's molar ratio is increasing.

A similar correlation between the BC molar ratio and swelling capacity was reported by Lin et al. [35] The exceptional water retention capability of BC can be attributed to robust molecular interactions between the water molecules and OH groups of BC.

In a separate investigation, poly(glycidyl methacrylate)/BC nanocomposites were synthesized through in-situ polymerization of glycidyl methacrylate via free radicals within the BC network. They reported that the increasing poly(glycidyl methacrylate) matrix in composites resulted in a decrease in water uptake ratios. At RT, water uptake capabilities were assessed during a 48h period. For the poly(glycidyl methacrylate)/BC composites, the performances were measured at 32.8%, whereas for BC's hydrophilic nature, they were 138% [36]. In contrast to Faria et al. [36], we found a higher swelling ratio than 138% in the current study. This could be because NIPAM's presence may make the hydrogel network more hydrophilic.

Since the CO ratio was kept constant in the hydrogels of this study, any impact on their swelling and shrinking behavior will be attributed to variations in the BC ratio. The effect of CO on the swelling and shrinking behavior of hydrogels was investigated by our group in our previous study [28]. It was reported that CO has a negative effect on swelling behavior due to its hydrophobic properties. In addition, when the results of this study are examined in the literature, it is shown that increasing the BC ratio has a positive effect on the swelling behavior of hydrogels.
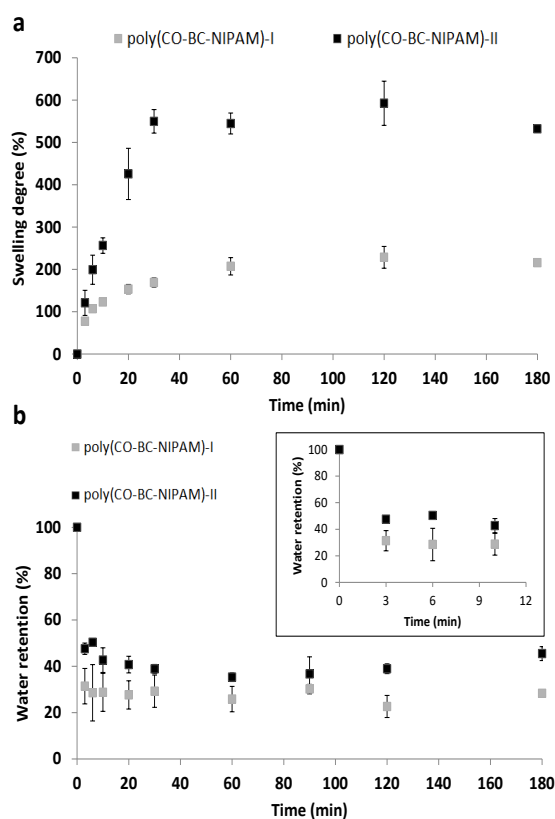
Figure 5. Swelling and water retention behaviors of hydrogels. **(a)** swelling behaviors at RT of the hydrogels; **(b)** water retention profiles of all hydrogels at 40°C for 180 min and 10 min

As the temperature increased above the LCST in this study, the hydrogels' capacity to absorb water rapidly decreased. Figure 5b shows deswelling profiles of the hydrogels. All hydrogels immediately shrink and release water when heated. In comparison to poly(CO-BC-NIPAM)-I, which lost 68.6% of its water in 3 min, and poly(CO-BC-NIPAM)-II suffered losses of 52.4%, respectively. After 180 min, the total water loss for poly(CO-BC-NIPAM)-I, poly(CO-BC-NIPAM)-II, was obtained to be 71.7%, and 54.5%, respectively.

3.5. Cytotoxicity of hydrogels

In the present study, cytotoxicity was evaluated on COS-7 cells for 1 mg/ml, 2 mg/ml, 5 mg/ml, 10 mg/ml, and 20 mg/ml hydrogels which were prepared with different cellulose ratios poly(CO-BC-NIPAM)-I, and poly(CO-BC-NIPAM)-II, as shown in Figure 6. The results revealed that cells exhibited at least 69% viability when exposed to 1 mg/ml of hydrogels and exposing the cells to higher concentrations of hydrogels or cellulose did not change the cell viability significantly

indicating that the cytotoxic effect of polymers was independent of the BC concentrations.

IC_{50} values, representing the concentration that inhibits 50% of cell growth, were determined to assess polymer cytotoxicity by plotting cell survival (%) against hydrogel concentration (mg/mL). The IC_{50} concentrations for poly(CO-BC-NIPAM)-I, and poly(CO-BC-NIPAM)-II are 5.33 mg/ml, and 11.16 mg/ml, respectively. These values also support the biocompatibility of the hydrogels as lower IC_{50} values mean more toxicity to the cells.
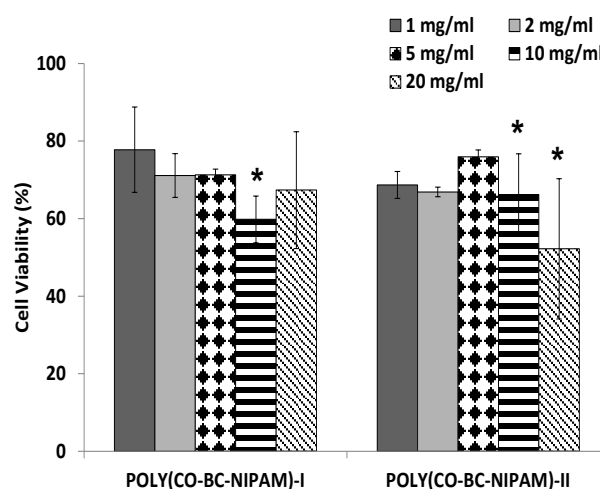
Figure 6. Cell viability values of the hydrogels

Recently, renewable biomaterial-based BC hydrogels are gaining significant attention due to their abundant natural presence and applications in wound care, tissue repair, and pharmaceutical applications. Therefore, researchers emphasize biocompatibility of these novel hydrogels by assessing the cytotoxicity in numerous in vitro and in vivo studies [37-39]. Evaluations regarding the cytotoxicity of composites based on BC in different cellular models and animal studies revealed that these hydrogels are biocompatible, however, the combination of BC with other ingredients such as polymers and natural materials may improve not only the structure and mechanical properties but also their biocompatibility, cell binding ability, and low antigenicity.

For instance, a BC/collagen hydrogel was reported to show a higher adhesive property and was used as wound dressing material in vivo studies [40]. Han et al. [41] on the other hand prepared a BC/polyvinyl alcohol hydrogel

scaffold for corneal reconstruction and the hydrogel showed higher biocompatible property supported by low cytotoxic effect in cell lines and almost no immune response in rabbits. In this study, we evaluated the BC hydrogels prepared with a plant-based castor oil monomer and observed high biocompatibility.

In the following studies, cell binding ability should be evaluated to determine its suitability as a scaffold for wound dressing and tissue engineering applications.

4. Conclusion

In the present study, CO and BC based thermoresponsive hydrogels poly(CO-BC-NIPAM)-I, and poly(CO-BC-NIPAM)-II were successfully synthesized. The influence of the BC ratio on the physical and structural properties of the BC/PNIPAM hydrogels was investigated. FTIR analysis was performed to evaluate structural differences between poly(CO-BC-NIPAM)-I and poly(CO-BC-NIPAM)-II, while SEM studies were employed to examine their morphological variations. The thermal properties of the hydrogels were characterized using TGA and DSC. Additionally, their swelling and deswelling behaviors were examined, and biocompatibility was assessed via the MTT assay.

The BC ratio in the hydrogels influences their swelling and deswelling profiles. The increased BC content of poly(CO-BC-NIPAM)-II resulted in the highest swelling degree. Poly(CO-BC-NIPAM)-II reached the highest equilibrium swelling degree of 592.6% within 120 min at room temperature. These findings may be attributed to the strong affinity of cellulose for water. Furthermore, the swelling and deswelling profiles demonstrated that all the hydrogels exhibited thermosensitive characteristics. SEM images revealed that the formation of spongy structure in hydrogels is caused by the increase in BC ratio and the presence of CO.

When the results of the thermal analysis were examined, the highest 15% weight lost temperature for poly(CO-BC-NIPAM)-II was found to be 299°C and the maximum absorbed heat was determined as 183 mJ/mg. IC50 values

are 5.33 mg/ml, and 11.16 mg/ml for poly(CO-BC-NIPAM)-I, and poly(CO-BC-NIPAM)-II, respectively. The cell viability increased with the molar ratio of BC.

Overall, the findings highlight the potential of renewable resources in hydrogel development. This study introduces a hydrogel derived from renewable raw materials using an eco-friendly process. The resulting thermoresponsive hydrogels exhibit high swelling capacity and biocompatibility, with those containing bacterial cellulose showing enhanced properties. These novel hydrogels hold promise for a wide range of biomedical applications.

Article Information Form

Authors' Contribution
Conceptualization, E.I.K., Ö.Y.Ç., D.K. and P.Ç.H..; methodology, E.I.K., Ö.Y.Ç., G.Ç., D.K. and P.Ç.H.; validation, E.I.K., O.P., Ö.Y.Ç., G.Ç., D.K. and P.Ç.H.; formal analysis, E.I.K., O.P., Ö.Y.Ç., G.Ç., D.K. and P.Ç.H.; resources, E.I.K., O.P., G.Ç., D.K. and P.Ç.H.; data curation, E.I.K., and P.Ç.H.; writing—original draft preparation, E.I.K., O.P., G.Ç., D.K. and P.Ç.H.; writing—review and editing, E.I.K., O.P., Ö.Y.Ç., D.K. and P.Ç.H. All authors have read and agreed to the published version of the manuscript.

The Declaration of Conflict of Interest/ Common Interest
No conflict of interest or common interest has been declared by the authors.

Artificial Intelligence Statement

During the preparation of this work, the authors used ChatGPT for grammar checking and editing. After using this tool, the authors reviewed and edited the content as needed and take full responsibility for the content of the publication.

Copyright Statement

References

[1] S. Bucatariu, G. Fundueanu, I. Prisacaru, M. Balan, I. Stoica, "Synthesis and characterization of thermosensitive poly (N-isopropylacrylamide-co-hydroxyethylacrylamide) microgels as potential carriers for drug delivery," Journal of Polymer Research, vol. 21, pp. 580, 2014.

[2] N. Sood, A. Bhardwaj, S. Mehta, A. Mehta, "Stimuli-responsive hydrogels in drug delivery and tissue engineering," Drug Delivery, vol. 23, no. 3, pp. 748–777, 2016.

[3] D. Althans, P. Schrader, S. Enders, "Solubilisation of quercetin: Comparison of hyperbranched polymer and hydrogel," Journal of Molecular Liquids, vol. 196, pp. 86–93, 2014.

[4] Q. Wang, Z. Dong, Y. Du, J. F. Kennedy, "Controlled release of ciprofloxacin hydrochloride from chitosan/polyethylene glycol blend films," Carbohydrate Polymers, vol. 69, no. 2, pp. 336–343, 2007.

[5] F. Käfer, F. Liu, U. Stahlschmidt, V. Jérôme, R. Freitag, "LCST and UCST in one: Double thermoresponsive behavior of block copolymers of poly (ethylene glycol) and poly (acrylamide-co-acrylonitrile)," Langmuir, vol. 31, no. 32, pp. 8940–8946, 2015.

[6] L. Klouda, "Thermoresponsive hydrogels in biomedical applications: A seven-year update," European Journal of Pharmaceutics and Biopharmaceutics, vol. 97, pp. 338–349, 2015.

[7] B. Özkahraman, I. Acar, G. Güçlü, "Synthesis and characterization of poly (VCL-HEA-IA) terpolymer for drug release applications," Journal of Polymer Materials, vol. 33, no. 2, pp. 351–363, 2016.

[8] M. Cao, Y. Wang, X. Hu, H. Gong, R. Li, "Reversible thermoresponsive peptide–PNIPAM hydrogels for controlled drug delivery," Biomacromolecules, vol. 20, no. 9, pp. 3601–3610, 2019.

[9] E. M. Frazar, R. A. Shah, T. D. Dziubla, J. Z. Hilt, "Multifunctional temperature-responsive polymers as advanced biomaterials and beyond," Journal of Applied Polymer Science, vol. 137, no. 25, pp. 48770, 2020.

[10] G. Fundueanu, M. Constantin, S. Bucatariu, P. Ascenzi, "Poly (N-isopropylacrylamide-co-N-vinylpyrrolidone) thermoresponsive microspheres: The low drug loading ensures the pulsatile release mechanism," Express Polymer Letters, vol. 14, no. 1, pp. 63–76, 2020.

[11] J. H. Park, J. W. Jang, J. H. Sim, I. J. Kim, D. J. Lee, "Preparation and properties of thermoresponsive P (N-Isopropylacrylamide-co-butylacrylate) hydrogel materials for smart windows," International Journal of Polymer Science, 3824207, 2019.

[12] A. Onaciu, R. A. Munteanu, A. I. Moldovan, C. S. Moldovan, I. Berindan-Neagoe, "Hydrogels based drug delivery synthesis, characterization and administration," Pharmaceutics, vol. 11, no. 9, pp. 432, 2019.

[13] L. Etchenausia, E. Villar-Alvarez, J. Forcada, M. Save, P. Taboada, "Evaluation of cationic core-shell thermoresponsive poly (N-vinylcaprolactam)-based microgels as potential drug delivery nanocarriers," Materials Science and Engineering C, vol. 104, 109871, 2019.

[14] S. Durkut, Y. M. Elçin, "Synthesis and Characterization of thermosensitive poly (n-vinyl caprolactam)-grafted-aminated alginate hydrogels," Macromolecular Chemistry and Physics, vol. 221, no. 2, 1900412, 2020.

[15] S. Das, P. Pandey, S. Mohanty, S. K. Nayak, "Insight on castor oil based polyurethane and nanocomposites: Recent trends and development," Polymer-Plastics Technology and Materials, vol. 56, no. 14, pp. 1556–1585, 2017.

[16] S. Ibrahim, A. Ahmad, N. S. Mohamed, "Synthesis and characterization of castor oil-based polyurethane for potential application as host in polymer electrolytes," Bulletin of Materials Science, vol. 38, pp. 1155–1161, 2015.

[17] F. Esa, S. M. Tasirin, N. A. Rahman, "Overview of bacterial cellulose production and application," Agriculture and Agricultural Science Procedia, vol. 2, pp. 113–119, 2014.

[18] D. Lin, P. Lopez-Sanchez, R. Li, Z. Li, "Production of bacterial cellulose by *Gluconacetobacter hansenii* CGMCC 3917 using only waste beer yeast as nutrient source," Bioresource Technology, vol. 151, pp. 113–119, 2014.

[19] W. K. Czaja, D. J. Young, M. Kawecki, R. M. Brown, "The future prospects of microbial cellulose in biomedical applications," Biomacromolecules, vol. 8, no. 1, pp. 1–12, 2007.

[20] A. Akoğlu, A. G. Karahan, M. L. Çakmakçı, İ. Çakır, "Bakteriyel selülozun özellikleri ve gıda sanayisinde kullanımı," Gıda, vol. 35, no. 2, pp. 127–134, 2010.

[21] J. Kucińska-Lipka, I. Gubanska, H. Janik, "Bacterial cellulose in the field of wound healing and regenerative medicine of skin: Recent trends and future prospectives," Polymer Bulletin, vol. 72, pp. 2399–2419, 2015.

[22] R. Alosmanov, K. Wolski, S. Zapotoczny, "Grafting of thermosensitive poly (N-isopropylacrylamide) from wet bacterial cellulose sheets to improve its swelling-drying ability," Cellulose, vol. 24, pp. 285–293, 2017.

[23] Q. Wang, T. A. Asoh, H. Uyama, "Rapid uniaxial actuation of layered bacterial cellulose/poly (N-isopropylacrylamide) composite hydrogel with high mechanical strength," RSC Advances, vol. 8, no. 23, pp. 12608–12613, 2018.

[24] J. E. Arikibe, R. Lata, K. Kuboyama, T. Ougizawa, D. Rohindra, "pH-responsive studies of bacterial cellulose/chitosan hydrogels crosslinked with Genipin: Swelling and drug release behaviour," ChemistrySelect, vol. 4, no. 34, pp. 9915–9926, 2019.

[25] P. Basu, N. Saha, P. Saha, "Swelling and rheological study of calcium phosphate filled bacterial cellulose-based hydrogel scaffold," Journal of Applied Polymer Science, vol. 137, no. 14, 48522, 2019.

[26] N. L. Parada Hernandez, J. O. Bahú, M. I. R. Schiavon, A. J. Bonon, C. I. Benites, "(Epoxidized castor oil–citric acid) copolyester as a candidate polymer for biomedical applications," Journal of Polymer Research, vol. 26, pp. 149, 2019.

[27] S. Arévalo-Alquichire, C. Ramírez, L. Andrade, Y. Uscategui, L. E. Diaz, "Polyurethanes from modified castor oil and chitosan: Synthesis, characterization, in vitro degradation, and cytotoxicity," Journal of Elastomers and Plastics, vol. 50, no. 5, pp. 419–434, 2018.

[28] E. Isikci Koca, G. Bozdag, G. Cayli, D. Kazan, P. Cakir Hatir, "Thermoresponsive hydrogels based on renewable resources," Journal of Applied Polymer Science, vol. 137, no. 28, 48861, 2020.

[29] S. A. Hutchens, R. V. Leon, H. M. O'Neill, B. R. Evans, "Statistical analysis of optimal culture conditions for *Gluconacetobacter hansenii* cellulose production," Letters in Applied Microbiology, vol. 44, no. 2, pp. 175–180, 2007.

[30] H. K. Uzyol, M. T. Saçan, "Bacterial cellulose production by *Komagataeibacter hansenii* using algae-based glucose," Environmental Science and Pollution Research, vol. 24, pp. 11154–11162, 2017.

[31] T. Mosmann, "Rapid colorimetric assay for cellular growth and survival: Application to proliferation and cytotoxicity assays," Journal of Immunological Methods, vol. 65, no. 1–2, pp. 55–63, 1983.

[32] M. T. Luo, H. L. Li, C. Huang, H. R. Zhang, L. Xiong, "Cellulose-based absorbent production from bacterial cellulose and acrylic acid: Synthesis and performance," Polymers, vol. 10, no. 7, pp. 702, 2018.

[33] F. D. S. Moura Neto, A. C. V. Fialho, W. L. Moura, A. G. F. Rosa, J. M. Matos, "Castor polyurethane used as osteosynthesis plates: Microstructural and thermal analysis," Polímeros, vol. 29, no. 2, e2019029, 2019.

[34] M. A. Alaa, K. Yusoh, S. F. Hasany, "Pure polyurethane and castor oil-based polyurethane: Synthesis and characterization," Journal of Mechanical Engineering Sciences, vol. 8, pp. 1507–1515, 2015.

[35] Q. Lin, Y. Zheng, L. Ren, J. Wu, H. Wang, "Preparation and characteristic of a sodium alginate/carboxymethylated bacterial cellulose composite with a crosslinking semi-interpenetrating network," Journal of Applied Polymer Science, vol. 131, no. 3, 39848, 2014.

[36] M. Faria, C. Vilela, F. Mohammadkazemi, A. J. Silvestre, C. S. Freire, "Poly (glycidyl methacrylate)/bacterial cellulose nanocomposites: Preparation, characterization and post-modification," International Journal of Biological Macromolecules, vol. 127, pp. 618–627, 2019.

[37] W. Liu, H. Du, T. Zheng, C. Si, "Biomedical applications of bacterial cellulose-based composite hydrogels," Current Medicinal Chemistry, vol. 28, no. 40, pp. 8319–8332, 2021.

[38] B. He, X. Liu, S. Qi, R. Zheng, M. Chang, "A review of water-resistant cellulose-based materials in pharmaceutical and biomedical application," Current Medicinal Chemistry, vol. 28, no. 40, pp. 8296–8318, 2021.

[39] F. G. Torres, S. Commeaux, O. P. Troncoso, "Biocompatibility of bacterial cellulose-based biomaterials," Journal of Functional Biomaterials, vol. 3, no. 4, pp. 864–878, 2012.

[40] P. R. F. D. S. Moraes, S. Saska, H. Barud, L. R. D. S. Lima, V. D. C. A. Martins, "Bacterial cellulose/collagen hydrogel for wound healing," Materials Research, vol. 19, pp. 106–116, 2016.

[41] Y. Han, C. Li, Q. Cai, X. Bao, L. Tang, "Studies on bacterial cellulose/poly (vinyl alcohol) hydrogel composites as tissue-engineered corneal stroma," Biomedical Materials, vol. 15, no. 3, 035022, 2020.

Research Article

Investigation of Thermal and Mechanical Behaviors of Plaster Mixed with Granite Cutting Waste

Onur Yontar[1] (iD), Arife Kübra Yontar[2*] (iD), Emre Şirin[3] (iD)

[1] Department of Mechanical Engineering, Ondokuz Mayıs University, Samsun, Türkiye, onur.yontar@omu.edu.tr, ror.org/028k5qw24
[2] Department of Mechanical and Metal Technologies, Ondokuz Mayıs University, Samsun, Türkiye, kubra.demirbas@omu.edu.tr, ror.org/028k5qw24
[3] Samsun Anakent Turizm Ticaret A.Ş, Samsun, Türkiye, emre_s_irin@outlook.com
[*]Corresponding Author

ARTICLE INFO	ABSTRACT
	This study investigated the usability of granite cutting waste in plaster. In the samples produced in the study, granite dust was observed with a scanning electron microscope, and it was homogeneously distributed in the microstructures. The presence of calcite, quartz, portlandite, hematite, and magnesium oxide phases in the samples was detected with an X-ray diffractometer. It was calculated that the highest compressive strength was obtained by adding 30% granite dust. In the samples whose thermal conductivities were examined by imaging with a thermal camera, it was determined that the lowest conductivity belonged to the sample containing 30% granite dust. This study revealed that plaster with high mechanical strength and low thermal conductivity could be produced by adding 30% granite dust.

1. Introduction

Plasters are frequently utilized in building construction because of their simple production method, widespread availability, cost-effectiveness, and better fire resistance. Gypsum-based plasters are commonly used as the principal interior finish for building wall and ceiling surfaces. Furthermore, with the proper method, it may be recycled numerous times [1–3].

Plaster (β-$CaSO_4$ $0.5H_2O$) is prepared at a particular calcination temperature for large-scale applications using phosphor as the basic material. Plaster offers numerous benefits, including being lightweight, having excellent temperature resistance, and being low cost. The packing density of a board made from plaster is approximately 1 g/cm^3. Gypsum-based materials can resist temperatures up to 200 °C without significant damage and retain 50% of their

genuine toughness at 400 °C. However, due to its disadvantages such as inherent brittleness, short setting time, poor water resistance, low resistance to cracking and inability to withstand humid conditions, gypsum plaster becomes an undesirable product for exterior plaster applications [4, 5]. Studies have been conducted with many natural and synthetic filling materials in recent years to increase plasters' thermal and mechanical resistance [6–8]. The most prominent of these filling materials are the cutting wastes of natural stones.

An igneous rock called granite is formed when some lava remains below the earth's surface and gradually cools to form crystalline rock. The primary chemical components of granite are magnesium oxide (MgO), calcium oxide (CaO), silicon dioxide (SiO_2), ferric oxide (Fe_2O_3), and aluminum oxide (Al_2O_3). SiO_2 makes up around 65–70% of the total, which is plentiful based on the chemical compositions above [9, 10]. Granite

cutting waste, a byproduct of the mining industry, can replace aggregate materials in concrete mass production to some extent (or entirely). Granite waste is made up of both solid and sludge. Granite colloidal waste accounts for around 58% of total plant output and is typically disposed of in dumping zones.

Unfortunately, the rising buildup of non-biodegradable wastes over landfill sites poses major environmental concerns and contamination in the adjacent regions [11, 12]. Although granite mud is thought to be inert and non-toxic, its inconsiderate manufacturing and improper disposal cause difficulty and costs for businesses in addition to a host of adverse environmental effects, including altered soil drainage conditions, air and visual pollution, alteration and destruction of the natural landscape, and harm to human health because the mud dries and turns into a powder that may result in silicosis if inhaled [13]. As a result, granite waste has been classified as an airborne and hazardous substance that generates air pollution and lung and sinus ailments, decreases soil porosity, contaminates subterranean water, and interrupts the normal flow of aquifers [14, 15].

Many forms of non-biodegradable waste are discharged into the environment due to stone mining and processing. Over several years, gathering these wastes from the stone business has caused environmental damage in various ways. Waste recycling has been strongly encouraged across the industrial chain in recent years. It is a particularly efficient method to mitigate the consequences of large-scale raw material utilization and waste generation.

Construction is one of the industries with the most significant environmental impact, accounting for 75% of all natural resources removed from the earth. As a result, it has become critical to discover safe disposal techniques or recycling in the business for some high-value goods [16, 17]. Over the last decade, the granite mining sector has increased by roughly 6% of global output each year, and granite waste from processing is estimated to represent about half of the finished granite quantity. Because using granite stone as a construction and architectural material creates

significant waste during mining and processing, discovering new applications might decrease potential environmental contamination and raw material requirements [17].

The literature has limited knowledge and experimental data on the usage and effects of granite cutting remains in plaster. In light of the aforementioned information, the use of granite cutting waste in plaster and its impact on plaster's thermal and mechanical properties were investigated in this study. It has been a valuable step in reducing manufacturing waste and developing new-generation building materials.

2. Materials and Methods

2.1. Preparation of samples

Commercial plaster was used to prepare the samples. Samsun Anakent Turizm Ticaret A.Ş., a Samsun Metropolitan Municipality state-owned enterprise, supplied granite cutting wastes. The granite cutting waste used are shown in Figure 1 (a). The samples were prepared in 50 x 50 x 50 mm cubic plastic molds. The sample (P) without granite cutting waste was prepared as a control sample. Granite cutting waste were added to the plaster at 15, 30 and 45 wt%. After mixing, the granite cutting waste and water were poured into the mold, as shown in Figure 1 (b). The samples dried in the mold for a day and then dried at room temperature for 6 days. The ratios used to prepare the samples are given in Table 1.

2.2. Characterizations and tests

A scanning electron microscope (SEM) model (JEOL 7001F) equipped with an EDS analysis adapter and an 80 mm^2 X-MAX detector was used to evaluate the chemical composition and microstructure of the samples. After the compression test, an SEM examination was performed to determine the structure and distribution of the broken pieces from all samples. The resolution was measured under 5 and 10 kV acceleration voltage. The pieces taken for imaging in the SEM were coated with gold and palladium. EDS spectra and map analysis were used to determine the chemical contents of the granite particles and how they were distributed throughout the samples. XRD

analysis was performed using a Rigaku Smart Lab CuK radiation monochromatic filter device in the range of 10°–70° at room temperature, 2°/min speed, and 1.2 Å wavelength to determine the phases in and granite found in the samples. XRD data were collected using 2D HyPix-3000 area detectors. The Debye-Scherrer Equation (1) was used to calculate the crystallite size and microstrain of the samples. The Debye-Scherer equation;

$$D = K\lambda/\beta\cos\theta \tag{1}$$

Table 1. Sample names and quantities of ingredients used

Samples	Water (mL)	Plaster (g)	Granite (g)
P	200	300	-
PG15	200	255	45
PG30	200	210	90
PG45	200	165	135

where D is the crystallite size (nm), K is the so-called shape or geometry factor, which usually takes a value of about 0.9 (Scherer constant), λ the X-ray wavelength (k = 0.1541 nm), β the full width at half maximum (FWHM) of the diffraction peak, and "θ" the diffraction angle. Williamson-Hall (W–H) Equation (2) used for microstrain calculations. The microstrain values of crystallites have been calculated by using the W–H relation using the XRD peaks, and the equation is as follows;

$$B\cos\theta = \left(\frac{k\lambda}{D}\right) + 4\varepsilon\sin\theta \tag{2}$$
$$Microstrain(\varepsilon) = \beta/4\tan\theta$$

Compressive strengths of all samples were measured with a 6800 series INSTRON Universal testing machine. Three samples were prepared for each group. A total of 12 samples were subjected to compression testing, and the test speed was 3 mm/min. TESTO 881 thermal imager was used to examine the thermal conductivity properties of the samples. The upper surface of each sample was monitored by taking images with a thermal camera on a heated plate at 10-minute intervals for 1 hour. At the end of 1 hour, the temperature on the upper surface was recorded. The emissivity value was taken as 0.85 when making temperature measurements.
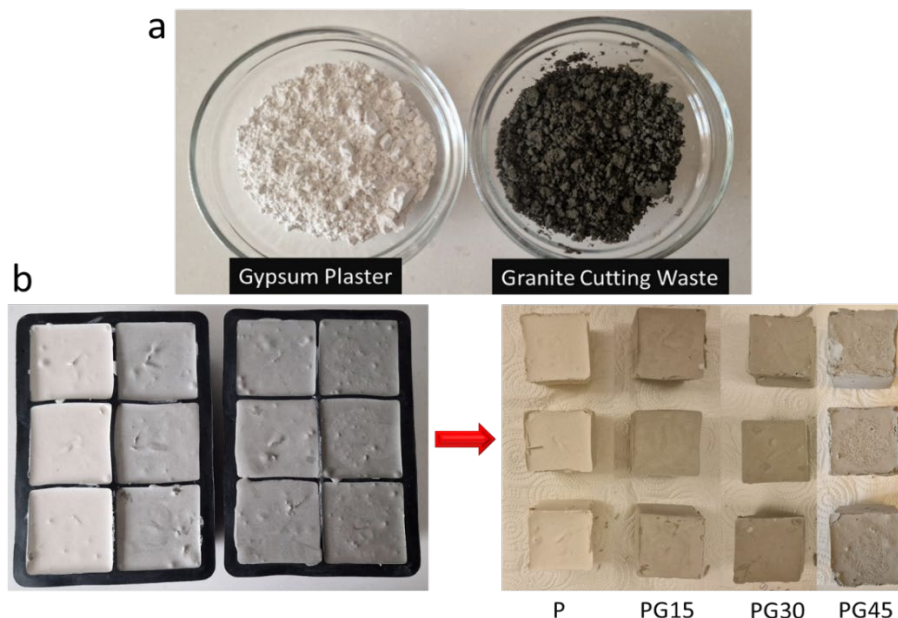
Figure 1. (a) Gypsum plaster and granite cutting wastes, (b) Samples in mold and dried samples

3. Results and Discussion

3.1. Scanning Electron Microscope (SEM)

After the compression test, SEM analysis was performed on the broken pieces to examine how the particles of plaster and granite were distributed within the structure. Since this distribution affects the samples' compression strength and thermal properties, it is crucial to examine the SEM images. The structure of the sample without granite in Figure 2 (a) shows that the waste particles are in rectangular and square-shaped crystal-like structures. As seen in Figure

2 (b) of the PG15 sample microstructure, granite particles with lighter colors and smaller sizes are scattered among the particles. Similarly, in the SEM images of Figure 2 (c) and (d), it was observed that the granite particles were dispersed among the particles but were more concentrated.

It was determined that the granite particles were homogeneously distributed throughout the structure of the PG45 sample, which had the highest amount of granite. It was also determined that the particles were dispersed quite a lot from each other due to the high granite ratio. In general, it has been determined that granite particles exhibit a homogeneous distribution in the structure, and their sizes are much smaller than those of particles, on average 1-2 μm.
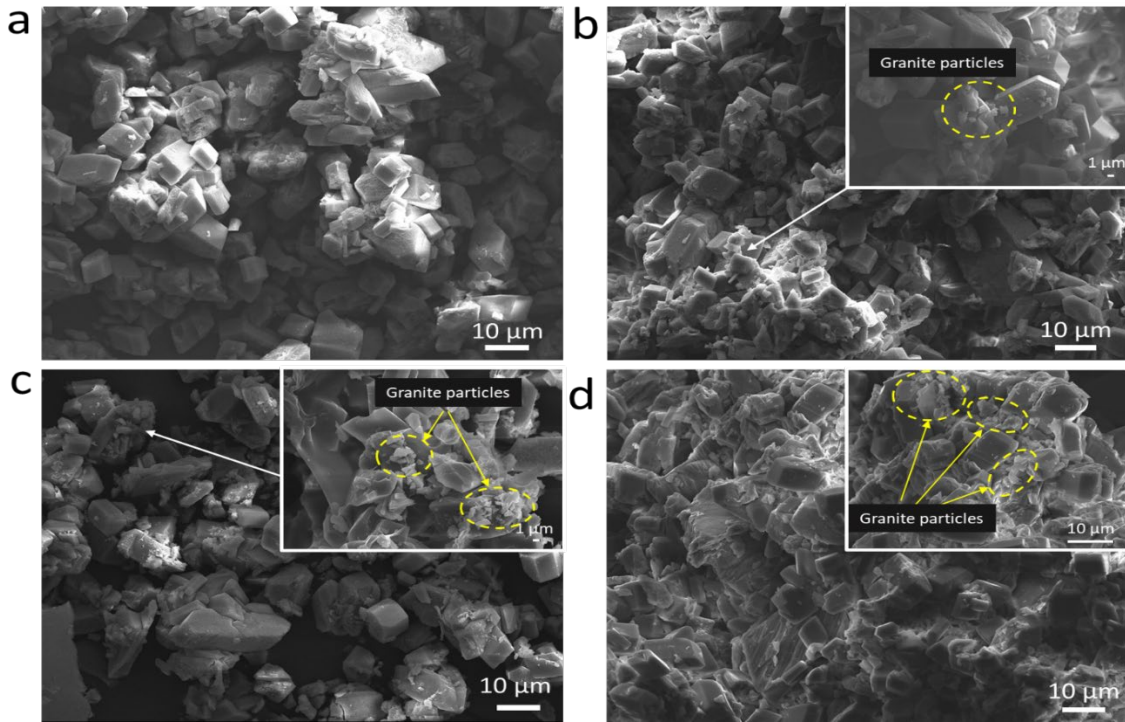
Figure 2. SEM images of (a) P, (b) PG15, (c) PG30 and (d) PG45 samples

3.2. Energy Dispersive Spectrometry (EDS)

The results of the EDS analysis performed to determine the elemental composition of blocks produced from granite are shown with the mapping method in Figure 3. The distributions of the elements found in the entire sample are given together with their percentages. Figure 3(a) shows the EDS mapping results of sample P that does not contain granite waste. Plaster is mainly made of calcium sulfate hemihydrate ($CaSO_4$ $2H_2O$) [18, 19]. The elements C, Ca, O and S seen in the map spectrum reveal that the material used in this sample is plaster. Granite's primary chemical ingredients are calcium oxide (CaO), silicon dioxide (SiO_2), aluminum oxide (Al_2O_3), ferric oxide (Fe_2O_3), and magnesium oxide (MgO). According to the formulas for substances above, SiO_2 is plentiful, accounting for 65 to 70% of the total [20, 21]. Figures 3 (b), (c), and (d) show the presence of Si, Al, Mg, Fe, K, and Na elements coming from granite, in addition to C, Ca, O, and S elements belonging to, in samples containing granite cutting waste.

Table 2. Chemical composition of granite cutting waste

Element	Wt%
P	56.37
O	0.58
Na	3.52
Mg	3.84
Al	8.52
Si	8.35
S	2.05
K	10.34
Ca	0.64
Ti	0.46
Cr	5.33
Fe	56.37

According to the EDS spectrum analysis results, the chemical composition of the granite cutting wastes used in the study is shown in Table 2. The results of EDS spectrum analyses performed to detect granite particles in samples containing granite cutting waste are given in Figure 4. The large dark particles seen in SEM images are mainly composed of C, Ca, O and S, while other small light-colored particles are particles containing high amounts of Fe, Si, Mg, Na, Al, Ti and K, and these elements belong to granite cutting waste. It is estimated that elements such as Ti and Cr are present due to contamination from cutting tools during cutting. Pd comes from the coating material used for SEM.
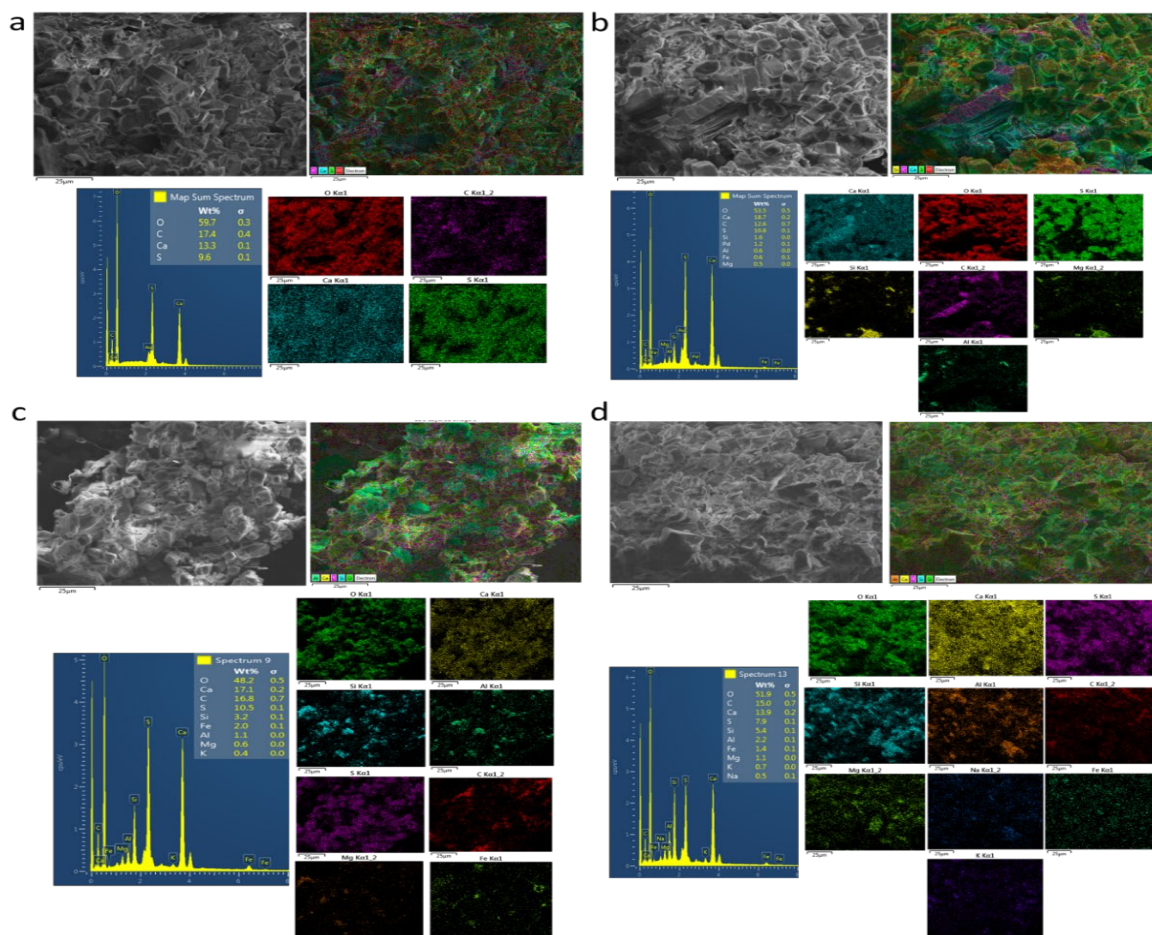
Figure 3. EDS mapping results (a) P, (b) PG15, (c) PG30 and (d) PG45 samples
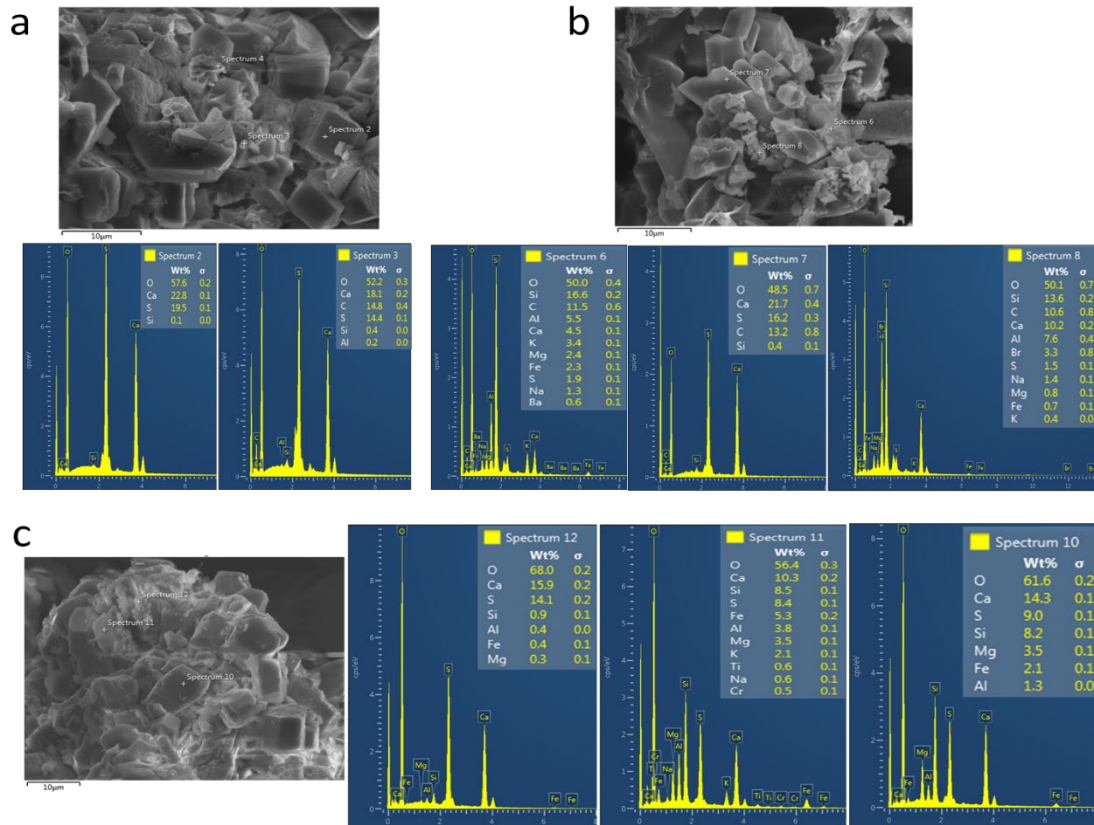
Figure 4. EDS spectrum results (a) PG15, (b) PG30, and (c) PG45 samples

3.3. X-Ray Diffraction analysis (XRD)

Figure 5 shows the XRD spectra of the samples. Since granite and plaster have similar chemical compositions, the peaks overlapped; therefore, no significant difference occurred. XRD peaks at 11.8°, 23.6°, 33.5°, 36.1°, 39.6°, 43.5°, 48°, and 56.9° belong to calcite; peaks at 11.8°, 31.1°, 32.2°, 43.5°, 50.5°, and 51.7° belong to dihydrate, peaks at 20.9°, 23.6°, 29.2°, 39.6°, 50.5°, 51.7°, and 55.3° belong to quartz, peaks at 23.5° and 48.6° belong to iron silicate, peak at 29.2° belongs to albite, peak at 33.5° belongs to portlandite, peaks at 33.5°, 39.6°, and 56.9° belong to silicon dioxide, peak at 40.9° belongs to hematite, and peak at 48.6° belongs to magnesium oxide phases [22–25].

All samples contain the phases and components of granite. As the amount of granite increases, the intensity of the quartz peaks decreases.
FWHM and the shape of the diffraction peak (size of the peak) reflect crystallinity. Perfect and blocky diffraction peaks occur in the presence of crystals as narrow vertical lines [26]. Figure 5 shows that XRD peaks have similar peak widths and power in all samples. In other words, the crystal structure ratio is high in all samples. It is

seen that the crystallite sizes given in Table 3 are PG30<PG15<P<PG45, respectively.

The decrease in crystallite size causes an increase in microstrain in the structure. Because smaller sizes cause higher surface area and higher bond ratio and energy. Microstrain refers to the stresses that occur in crystals due to the stress within the material caused by non-homogeneous plastic deformation [27]. When the microstrain values of the samples were compared for all samples, it was determined that PG45<P<PG15<PG30 Crystallite sizes and microstrain results showed that while microstrain decreased in the PG45 sample compared to the P sample, microstrain increased in the PG15 and PG30 samples. During the compression test, the microstrain rises with increasing pressure in stronger samples. This suggests that granite cutting waste was better embedded in the plaster lattice in PG15 and PG30 samples, and therefore, their compressive strengths may have been higher [28]. Microstrain values were consistent with the compression test results.

Table 3. Sample names and quantities of ingredients used

Samples	Crystallite Sizes D (nm)	Microstrain (ε)
P	51.4	3.02×10^{-3}
PG15	51.2	3.04×10^{-3}
PG30	48.2	3.21×10^{-3}
PG45	51.9	2.9×10^{-3}
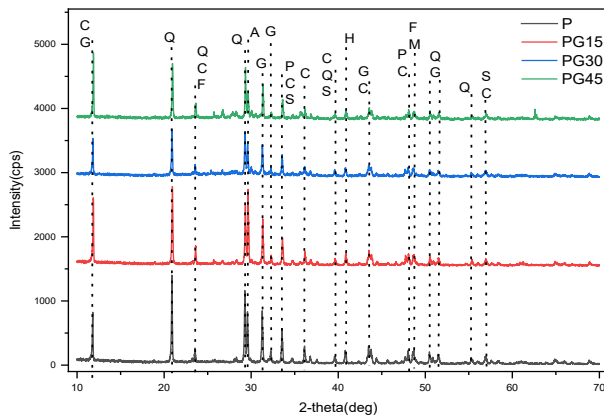
Figure 5. XRD results of all samples. (C: Calcite, Q: Quartz, G: dihydrate, F: Iron silicate, A: Albite, P: Portlandite, S: Silicon dioxide, H: Hematite, and M: Magnesium oxide)

3.4. Compressive strength

The results of all samples subjected to compression tests are given in the graphs in Figure 6, along with images of the samples after the test. The average compressive strength of the P sample was calculated as 0.53 MPa, the PG15 sample was 0.7 MPa, the PG30 sample was 0.74 MPa, and the PG45 sample was 0.39. It was determined that the amount of granite dust increased the compressive strength of the block by up to 30% while decreasing it by 45%.

This result showed that by adding 30% granite cutting waste into the plaster, a 39% increase in compressive strength could be achieved compared to the plaster sample without additives. The increase in strength of the PG30 sample is thought to be due to the finer inert particles of granite acting as nucleation points, causing the precipitation of hydrated products and activating the hydration [17]. The more prominent packing of the granite and plaster particles made the mixture more homogeneous and compact, thus exhibiting more excellent resistance. The strength of the PG45 sample decreased as the percentage of granite cutting waste was raised to 45%. Because plaster has strong binding qualities, lowering its concentration in the sample also decreased the quantity of bond that was produced between the plaster and the granite cutting waste. It has been reported in similar studies that the decrease in the amount of binder or its non-homogeneous distribution reduces the compressive strength [29, 30].
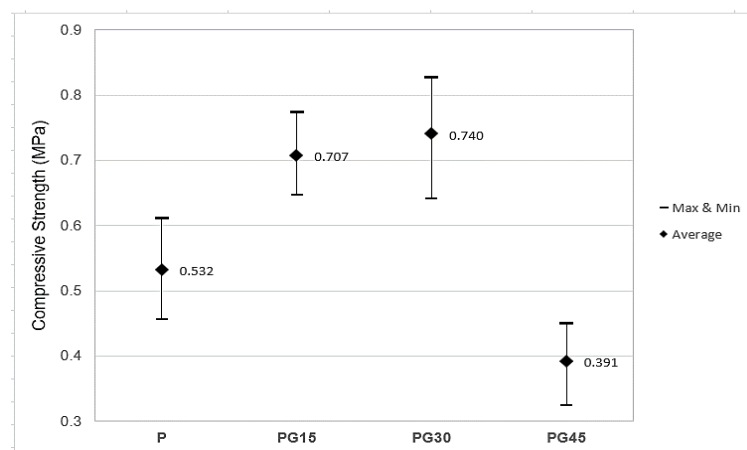
Figure 6. Compressive test result graphs of all samples

3.5. Thermal conductivity

To compare the thermal conductivities of the samples, each sample was placed on a heater heated to 100 °C and then kept for 1 hour. Measurements were taken with a thermal camera every 10 minutes, and the temperature changes between the bottom and top surfaces of the samples were recorded for one hour, as shown in the thermal camera images in Figure 7. For each sample, temperature changes were measured from 3 different points from the bottom to the top surface. The measurement points were determined as point A, 1 cm above the bottom;

point B, 3 cm above the bottom; and point C, 5 cm above the bottom on the top surface of the sample.

Figure 7 shows that the temperature difference between the bottom and top surfaces of all samples at the 10th and 60th minutes was highest at 37.9 ˚C for the P sample and lowest at 25 ˚C for the PG30 sample. The temperature values measured for each point in the samples are given comparatively in the graphs in Figure 8. It was noticed that the temperatures of point A in PG15 and PG45 samples decreased after 40 minutes. It is predicted that this may be due to the temperature balance between points A and B being achieved after 40 minutes.

The lowest temperature increases at point B after 60 minutes were observed in the PG30 and PG45 samples. In other words, the temperature differences occurring in the inner parts of the square prism samples are lower than the pure P sample, indicating that the thermal conductivities of these samples are lower. In the temperature changes of the uppermost surface, point C, it was determined that the lowest temperature belonged to the PG30 sample. In the PG15 and PG45 samples, the temperature values measured at point C were higher than the P sample. The temperature differences measured at point A of the samples at the end of the 10th and 60th minutes were calculated as 9.5 ˚C for the P sample, 9.2 ˚C for PG15, 8.2 ˚C for PG30, and 12.4 ˚C for PG45. The total temperature differences occurring at points A were calculated as 19.5 ˚C for P, 11.8 ˚C for PG15, 8.1 ˚C for PG30, and 12.4 ˚C for PG45.
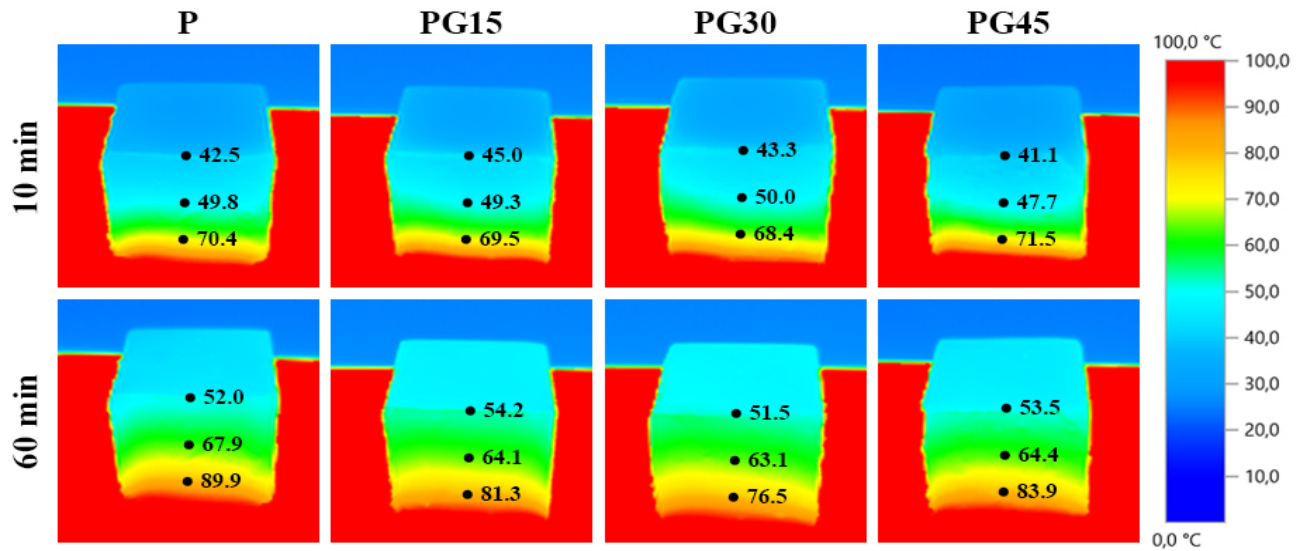
Figure 7. Thermal camera images of temperature changes of samples after 10 and 60 minutes

As a result, when all these temperature differences were compared, the thermal conductivity order between the samples was as follows: P>PG45>PG15>PG30. It was observed that a decrease in thermal conductivity occurred with the addition of granite cutting waste to the plaster. It was determined that the lowest thermal conductivity belonged to the PG30 sample. This decrease in thermal conductivity can be explained by the crystallite sizes and microstrain given in Table 2. The lowest crystallite size and the highest microstrain belong to the PG30 sample.

It is hypothesized that smaller-sized crystallites were created by mixing granite cutting waste with plaster and that increased porosity occurred in the structure with these combinations and agglomerations [31, 32]. Moreover, these agglomerations also led to higher microstrains in the structure. Therefore, it is thought that the thermal conductivity may have decreased with the increase in porosity and voids.

4. Conclusion

This study investigated the use of granite cutting waste in plaster for recycling. The characterizations, mechanical strengths, and thermal properties of the samples added to plaster

at 15%, 30%, and 45% were examined. SEM analysis showed that granite dusts were homogeneously distributed in plaster. EDS mapping and spectrum analysis revealed the

presence of granite dust and Si, Al, Mg, Fe, K, Na, C, Ca, O, and S elements from both granite and plaster.
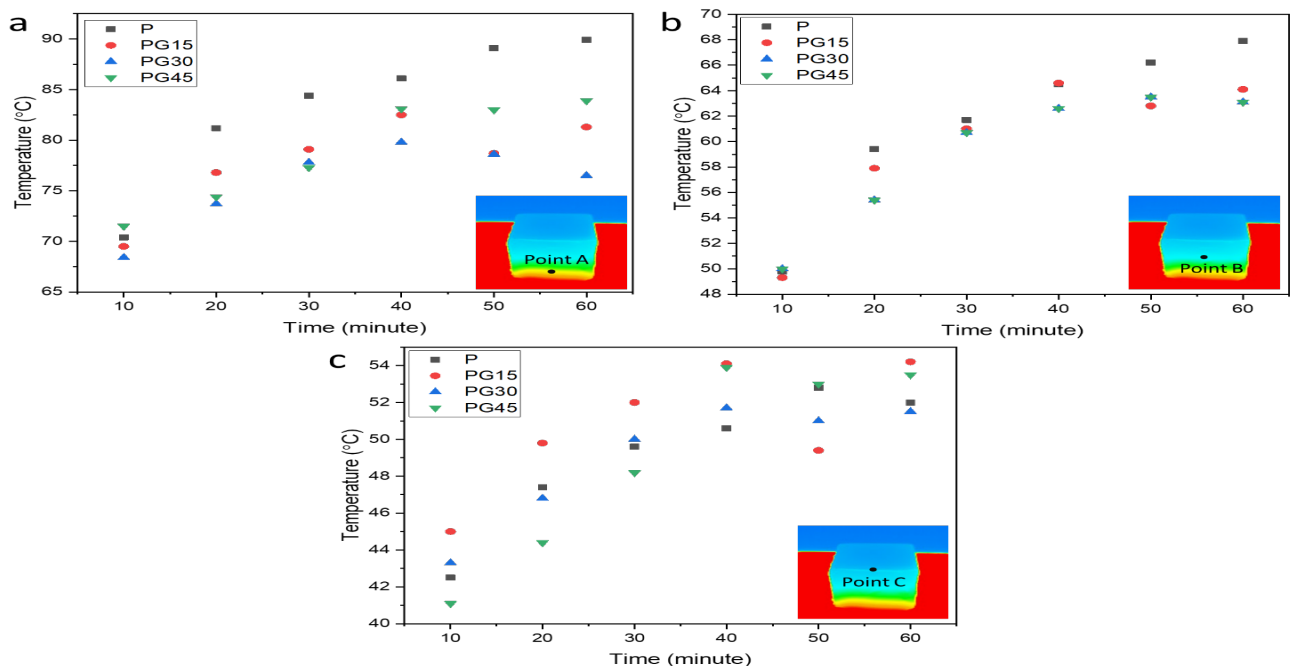
Figure 8. Graphs of temperature changes on surfaces (a) Point A, (b) Point B, and (c) Point C

In addition, XRD proved that the dust used in the study belonged to granite, with calcite, hematite, dihydrate, iron silicate, silicon dioxide, albite, portlandite, and magnesium oxide peaks. It was determined that the compressive strengths of the samples produced in the form of 50 x 50 mm cube blocks increased with granite dust. In particular, it was calculated that the PG30 sample containing 30% granite dust had the highest compressive strength with 0.74 MPa. It was determined that adding more granite dust than this rate reduced the compressive strength of the plaster.

When thermal properties were examined, it was found that thermal conductivities decreased with the addition of granite cutting waste. The lowest thermal conductivity belonged to the PG30 sample. Thus, it was concluded that the compressive strength of the plaster was increased, and its thermal conductivity was reduced with the addition of 30% granite cutting waste.

This study paves the way for evaluating granite cutting waste using it in plaster. With the findings obtained in the study, it was possible to produce

materials with superior properties while reducing waste formation.

Article Information Form

Authors' Contribution
Onur Yontar: Methodology, Research, Data editing, Manuscript writing and editing, Arife Kübra Yontar: Methodology, Research, Data editing, Manuscript writing and editing, Experimental Study, Emre Şirin: Methodology and Granite powder supply.

The Declaration of Conflict of Interest/ Common Interest
No conflict of interest or common interest has been declared by authors.

Artificial Intelligence Statement
No artificial intelligence tools were used while writing this article.

References

[1] H. E. Benchouia, H. Boussehel, B. Guerira, L. Sedira, C. Tedeschi, H. E. Becha, M. Cucchi, "An experimental evaluation of a hybrid bio-composite based on date palm petiole fibers, expanded polystyrene waste, and gypsum plaster as a sustainable insulating building material," Construction and Building Materials, vol. 422, p. 135735, 2024.

[2] K. Elert, P. Bel-Anzué, M. Burgos-Ruiz, "Influence of calcination temperature on hydration behavior, strength, and weathering resistance of traditional gypsum plaster," Construction and Building Materials, vol. 367, pp. 130361, 2023.

[3] M. Hagiri, K. Honda, "Preparation and evaluation of gypsum plaster composited with copper smelter slag," Cleaner Engineering and Technology, vol. 2, pp. 100084, 2021.

[4] L. Wang, M. Cao, X. Li, W. Du, X. Wang, "A novel approach for improving the water resistance of gypsum plaster by internal mixing hypromellose and external coating waterproofing agent," Construction and Building Materials, vol. 401, pp. 132940, 2023.

[5] S. Bouzit, F. Merli, M. Sonebi, C. Buratti, M. Taha, "Gypsum-plasters mixed with polystyrene balls for building insulation: Experimental characterization and energy performance," Construction and Building Materials, vol. 283, pp. 122625, 2021.

[6] J. Zehfuß, L. Sander, "Gypsum plasterboards under natural fire—Experimental investigations of thermal properties," Civil Engineering Design, vol. 3, no. 3, pp. 62-72, 2021.

[7] N. C. Amulah, A. M. El-Jummah, A. A. Hammajam, U. Ibrahim, "Experimental Investigation on the Thermal Properties of Gypsum Plaster-Rice Husk Ash Composite," Open Journal of Composite Materials, vol. 12, no. 04, pp. 131-138, 2022.

[8] Y. Agrawal, S. Siddique, R. K. Sharma, T. Gupta, "Valorization of granite production dust in development of rich and lean cement mortar," Journal of Material Cycles and Waste Management, vol. 23, no. 2, pp. 686-698, 2021.

[9] K. Shwetha, C. Mahesh Kumar, V. N. Dalawai, S. Anadinni, G. Sowjanya, "Comparative study on strengthening of concrete using granite waste," Materials Today: Proceedings, vol. 62, pp. 5317-5322, 2022.

[10] A. A. Mhamal, P. P. Savoikar, "Use of marble and granite dust waste as partial replacement of fine aggregates in concrete," IOP Conference Series: Earth and Environmental Science, vol. 1130, no. 1, pp. 12013, 2023.

[11] S. Tangaramvong, P. Nuaklong, M. T. Khine, P. Jongvivatsakul, "The influences of granite industry waste on concrete properties with different strength grades," Case Studies in Construction Materials, vol. 15, pp. 00669, 2021.

[12] M. A. Pedreño-Rojas, C. Rodríguez-Liñán, I. Flores-Colen, J. de Brito, "Use of Polycarbonate Waste as Aggregate in Recycled Gypsum Plasters," Materials (Basel, Switzerland), vol. 13, no. 14, 2020.

[13] F. Oliveira, R. Sousa, P. Silva, P. Lopes, G. Moreira, R. Leite, R. Arruda, "Analysis of the benefits of the addition of granite residues in the production of ecological brick," International Journal of Advanced Engineering Research and Science, vol. 8, no. 3, pp. 149-158, 2021.

[14] K. Weimann, C. Adam, M. Buchert, J. Sutter, "Environmental Evaluation of Gypsum Plasterboard Recycling," Minerals, vol. 11, no. 2, pp. 101, 2021.

[15] B. Ngayakamo, A. Bello, A. P. Onwualu, "Valorization of granite waste powder as a secondary flux material for sustainable production of ceramic tiles," Cleaner Materials, vol. 4, pp. 100055, 2022.

[16] A. S. Nascimento, C. P. dos Santos, F. M. C. de Melo, V. G. A. Oliveira, R. M. P. Betânio Oliveira, Z. S. Macedo, H. A. de Oliveira, "Production of plaster mortar with incorporation of granite cutting wastes," Journal of Cleaner Production, vol. 265, pp. 121808, 2020.

[17] M. R. Gehlot, S. Shrivastava, "Utilization of stone waste in the development of sustainable mortar: A state of the art review," Materials Today: Proceedings, 2023.

[18] N. Kondratieva, M. Barre, F. Goutenoire, M. Sanytsky, "Study of modified gypsum binder," Construction and Building Materials, vol. 149, pp. 535-542, 2017.

[19] A. Erbs, A. Nagalli, K. Querne de Carvalho, V. Mymrin, F. H. Passig, W. Mazer, "Properties of recycled gypsum from gypsum plasterboards and commercial gypsum throughout recycling cycles," Journal of Cleaner Production, vol. 183, pp. 1314-1322, 2018.

[20] G. Amulya, A. A. B. Moghal, A. Almajed, "A State-of-the-Art Review on Suitability of Granite Dust as a Sustainable Additive for Geotechnical Applications," Crystals, vol. 11, no. 12, pp. 1526, 2021.

[21] A. A. Mahmoud, A. A. El-Sayed, A. M. Aboraya, I. N. Fathy, M. A. Abouelnour, I. M. Nabil, "Influence of sustainable waste granite, marble and nano-alumina additives on ordinary concretes: a physical, structural, and radiological study," Scientific reports, vol. 14, no. 1, pp. 22011, 2024.

[22] M. E. Tawfik, S. B. Eskander, N. M. Ahmed, "Potential applications of granite waste powder as an add-value polymer composite product," Polymers and Polymer Composites, vol. 30, 2022.

[23] R. Saxena, T. Gupta, R. K. Sharma, S. Siddique, "Mechanical, durability and microstructural assessment of geopolymer concrete incorporating fine granite waste powder," Journal of Material Cycles and Waste Management, vol. 24, no. 5, pp. 1842-1858, 2022.

[24] C. Y. Rahimzadeh, A. S. Mohammed, A. A. Barzinjy, "Microstructure characterizations, thermal analysis, and compression stress–strain behavior of lime-based plaster," Construction and Building Materials, vol. 350, pp. 128921, 2022.

[25] A. Jain, S. Chaudhary, R. Gupta, "Mechanical, microstructural characterization of fly ash blended self-compacting concrete containing granite waste," Construction and Building Materials, vol. 314, pp. 125480, 2022.

[26] Y. Zhang, Q. Sun, J. Geng, "Microstructural characterization of limestone exposed to heat with XRD, SEM and TG-DSC," Materials Characterization, vol. 134, pp. 285-295, 2017.

[27] Y.-J. Shen, Y.-L. Zhang, F. Gao, G.-S. Yang, X.-P. Lai, "Influence of Temperature on the Microstructure Deterioration of Sandstone," Energies, vol. 11, no. 7, pp. 1753, 2018.

[28] C. Pesce, G. L. Pesce, M. Molinari, A. Richardson, "Effects of organic additives on calcium hydroxide crystallisation during lime slaking," Cement and Concrete Research, vol. 139, pp. 106254, 2021.

[29] Z. Z. Woźniak, A. Chajec, Ł. Sadowski, "Effect of the Partial Replacement of Cement with Waste Granite Powder on the Properties of Fresh and Hardened Mortars

for Masonry Applications," Materials (Basel, Switzerland), vol. 15, no. 24, 2022.

[30] M. Sufian, S. Ullah, K. A. Ostrowski, A. Ahmad, A. Zia, K. Śliwa-Wieczorek, M. Siddiq, A. A. Awan, "An Experimental and Empirical Study on the Use of Waste Marble Powder in Construction Material," Materials (Basel, Switzerland), vol. 14, no. 14, 2021.

[31] M. I. Romero-Gómez, R. V. Silva, M. F. Costa-Pereira, I. Flores-Colen, "Thermal and mechanical performance of gypsum composites with waste cellulose acetate fibres," Construction and Building Materials, vol. 356, pp. 129308, 2022.

[32] K. Stejskalová, D. Bujdoš, L. Procházka, B. Smetana, S. Zlá, J. Teslík, "Mechanical, Thermal, and Fire Properties of Composite Materials Based on Gypsum and PCM," Materials (Basel, Switzerland), vol. 15, no. 3, 2022.

Holistic Transcriptomic Analysis Identifies Prospective Reprogramming Factors for Induced Pluripotent Stem Cell Manufacturing

Zihni Onur Çalışkaner ᴵᴰ

Biruni University, Faculty of Engineering and Natural Sciences, Department of Molecular Biology and Genetics, İstanbul, Türkiye, zcaliskaner@biruni.edu.tr, ror.org/01nkhmn89
*Corresponding Author

ARTICLE INFO	ABSTRACT
	Induced pluripotent stem cells (iPSCs) offer a groundbreaking technology, which has transformed translational research and clinical applications in a wide range of fields, such as regenerative medicine, tissue engineering, cell therapy, disease modeling, developmental biology, etc. iPSCs are derived from terminally differentiated somatic cells by reprogramming the genetic and epigenetic program back to the pluripotent stem cell characteristics. iPSCs are very identical to embryonic stem cells in regards to differentiation into many cell types; however, iPSCs are exempt from the legal or ethical issues. These advantages enable iPSCs to advance the cell therapy and transplantation strategies. Nonetheless, low reprogramming efficiency and the risk for tumorigenicity are still limitations in the application of iPSCs in practice because the usage of the same pluripotency factors in all somatic cell types remains incapable of an efficient reprogramming. Here, we accomplished a holistic meta-analysis of the transcriptome datasets in a bidirectional perspective to achieve significant pluripotency-related genes that can commonly be applicable in all origin cells. The current study suggested prospective reprogramming factors, such as *POLR3G*, *TERF1*, and *PHC1*. Meanwhile, integrated drug repurposing also revealed certain small chemical molecules, which can promote transgene-free reprogramming and safer iPSC generation protocols.

1. Introduction

Induced Pluripotent Stem Cells (iPSCs) were first created utilizing retroviral transduction of certain genes into adult somatic cells by Takahashi and Yamanaka [1]. The basic principle is to switch terminally differentiated cells back into the embryonic stem cell characteristics by delivering certain nuclear reprogramming factors that sustain capacity for potency and self-renewal. *Octamer-binding transcription factor 4* (*OCT4*), *Sex-determining region Y-box 2* (*SOX2*), *Kruppel Like Factor 4* (*KLF4*), and the oncogene *c-MYC*, collectively known as OSKM or Yamanaka factors, were able to induce the transdifferentiation (reprogramming) of somatic cells to the embryonic-like pluripotent cells. These genes emerged as the crucial ones in the initial stages

of embryonic stem cell (ESC) formation as the output of a comprehensive screening assay [2, 3].

Since then, multiple studies revealed that ectopic expression of Yamanaka factors in the somatic cells is not sufficient alone to re-alter the complex epigenetic program required for the iPSC generation [4]. Hereby, only a small fraction of somatic cells (up to 1%) can successfully be reprogrammed into iPCSs from the terminally differentiated cells [5]. Another disadvantage is that overexpression of oncogenic genes such as *KLF4* and *c-MYC* is associated with a high carcinogenic risk in reprogrammed cells through various mechanisms, including p53 inactivation, development of drug resistance, inhibition of cell cycle suppressors, and epithelial-mesenchymal transition (EMT) [6, 7].

Over the last 15 years, a wide range of protocols, which are especially capable of overcoming epigenetic barriers, have been developed to generate clinical-grade iPSCs and/or to enhance reprogramming efficiency [2, 8]. To date, a) identification of alternative or additional transcription factors to OSKM, b) addition of small chemical molecules that induce transdifferentiation (chemical induction) into the growth medium, c) use of non-integrative viral and non-viral gene transfer methods (e.g., episomal plasmids, SeVdp, PiggyBac, etc.), d) origination from the alternate cell sources that are more talented for somatic reprogramming, and e) transfection of non-coding RNAs as epigenetic regulators have all been reported to increase the efficiency and in vivo safety of iPSC production [2, 4, 9].

Researchers have mainly focused on the gene delivery methods for improved reprogramming efficacy and biological safety [10-12]. However, exploration of alternate reprogramming factors, which re-establish the pluripotent nature within the somatic cells, has been overshadowed so far. This is because each somatic cell type requires a divergent reprogramming factor cocktail due to having a unique epigenetic profile, transcriptional regulatory networks, and molecular roadblocks [13-15].

Indeed, there are numerous studies that explored the transcriptomic signature and regulation during the differentiation processes (from somatic cell to iPSC and from iPSC to somatic cell) [16-19]. Nevertheless, this research only discussed the transcriptomic changes for a specific somatic cell. In the present study, we aimed to investigate common pluripotency-associated genes that can be used jointly as reprogramming factors independent of the origin somatic cell by evaluating the outcomes of multiple transcriptome analyses together.

Otherwise, chemical reprogramming is another approach for overcoming the challenges in efficient and safer iPSC manufacturing. Chemical reprogramming is based on the administration of small chemical compounds to somatic cells, which enable reprogramming of somatic cells by robustly tuning ESC-related signaling pathways [20]. For instance, Li et al.

defined a small-molecule cocktail, namely VC6T, consisting of valproic acid (an HDAC inhibitor), CHIR99021 (a GSK3 inhibitor), 616 452 (a TGF-β inhibitor), and tranylcypromine (an LSD1 inhibitor) that could substitute for *SOX2*, *KLF4*, and *c-MYC* in somatic cell reprogramming [21]. Thus, it offers a transgene-free, cost-effective, and customizable method to generate clinical-grade iPSCs [22]. Even so, the discovery of versatile chemical compounds simultaneously governing a wide range of pathways is still a necessity. Herein, our data also proposed several transcriptional targets to eliminate epigenetic barriers when downregulated and novel agents for the generation of chemically induced iPSCs (ciPSCs). In this regard, we sought differentially expressed genes (DEGs) in the microarray data published on the Gene Expression Omnibus (GEO) database. Here, we settled on a bidirectional approach through the meta-analysis of sorts of datasets: 1) detection of upregulated genes in the course of reprogramming various somatic cells to iPSCs, and 2) extraction of DEGs between the iPSC-derived somatic cells and the parental iPSCs.

2. General Methods

2.1. Transcriptome dataset acquisition

All transcriptomic datasets were acquired from the Gene Expression Omnibus (GEO) database (http://www.ncbi.nlm.nih.gov/geo). GSE55109 [23], GSE62066 [24], and GSE67915 [19] were the GEO datasets comparing the gene expression levels in iPSCs and their somatic cell origins in the course of somatic cell reprogramming (SomC to iPSC). Concurrently, the microarray datasets GSE175179 [25], GSE43143 [26], GSE55536 [27], GSE65423, GSE117086 [28], and GSE147498 [29] were used to evaluate DEGs between iPSCs and iPSC-derived somatic cells during the conversion of iPSCs into terminally differentiated cells (iPSC to SomC).

2.2. Evaluation of differentially expressed genes (DEGs)

Differentially expressed genes (DEGs) were identified using the GEO2R tool (https://www.ncbi.nlm.nih.gov/geo/geo2r/)

provided by the GEO database. Benjamini & Hochberg adjustment was applied to the p-values [30]. The Log2FoldChange (Log2FC) threshold was set as 1 (|log2foldchange| > 1.0) to consider the DEGs with at least a 2-fold change. Other options were kept as default. Common DEGs were displayed, and Venn diagrams were rendered in Jvenn, an open-source interactive tool [31]. After DEGs in each microarray dataset were individually dissected and descendingly ranked according to enrichment scores as Log2FC, mutual DEGs were revealed by using intersection-based Venn diagrams. Therefore, only concordant genes from independent platforms and biological contexts could be considered to identify the most probable candidates without needing batch correction.

Figure 1. Upregulated genes while somatic cells were reprogrammed into iPSCs (A) and enriched GO terms (B). Downregulated genes during iPSCs were terminally differentiated into somatic cell types (C) and related GO terms (D)

2.3. Gene enrichment analysis

Metascape, a web-based analysis resource, was utilized for gene annotation and interpretation of enriched Gene Onthology (GO) terms, including biological processes, molecular functions, and cellular components, KEGG pathways, etc [32].

For enrichment analysis, minimum overlap, p-value cutoff, and minimum enrichment were selected as 3, 0.01, and 1.5, respectively. Afterwards, charts including the three enriched terms (BP/CC/MF) were plotted using SRplot [33].

2.4. Identification of small chemical compounds

Upregulated common DEGs (37 genes) and downregulated core DEGs (9 genes) in iPSCs were submitted to L1000 Characteristic Direction Signature Search Engine (L1000CDS²) developed by the Ma'ayan Laboratory at the Icahn School of Medicine at Mount Sinai to extract repurposing small chemical ligands. There configuration was selected as "mimic" to search for the small molecules that may provide the input common gene expression profile.
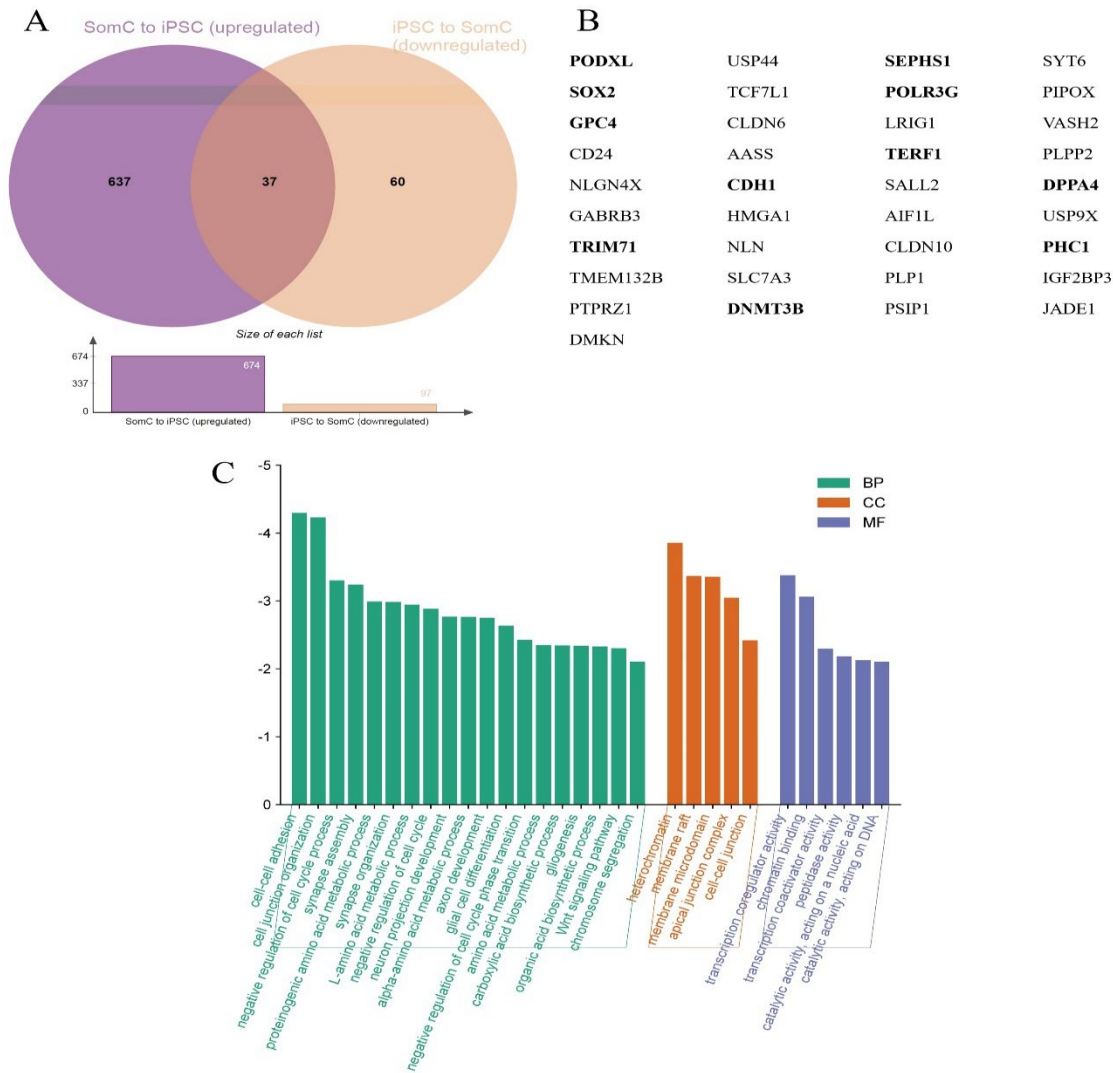
Figure 1. Common genes potentially linked to pluripotency in iPSCs (A, B) and related GO terms (C)

3. Results

3.1. Evaluation of the DEGs related to pluripotent state

Ongoing research has shown that each somatic cell type has a unique epigenetic profile that distinguishes transcriptional circuits [34, 35] and constitutes an epigenetic memory [36]. Thus, different somatic origins exhibit unusual iPSC production efficiency and quality during OSKM-induced reprogramming. In other words, utilization of the OSKM cocktail in all somatic cell types might give rise to nonequivalent impacts on the epigenetic memory-associated barriers [37-39]. Given that discrimination, we decided to collectively reevaluate the microarray data to unravel alternate or supporting pluripotency factors, comparing the transcriptomic profiles during reprogramming of different kinds of somatic cell origins to iPSCs.

First, we aimed to identify the common upregulated genes, whose overexpression in resultant iPSC lines was probably independent from the origin cell. After the increased DEGs in

iPSCs by at least 2-fold were listed for each dataset (GSE55109, GSE62066, and GSE67915), mutual DEGs were represented by creating a Venn scheme. It was found that 674 genes were upregulated in all iPSC lines (Figure 1A) reprogrammed from the human adult dermal fibroblasts and CD34+ cord blood cells from three different studies [19, 23, 24]. GO enrichment analysis showed that these upregulated genes are related to reasonable GO biological process, cellular component, and molecular function terms, including cell-cell interaction, cytoskeleton, adhesion, stem cell factor receptor activation, histone modifying activity, tube morphogenesis, and neuronal development (Figure 1B).

Meanwhile, we sought the common downregulated genes while iPSCs differentiate into somatic cells, suggesting these could also be related to the maintenance of pluripotency and should be silenced for a proper cell fate commitment. Here, we detected 97 genes downregulated (Figure 1C) in iPSC-derived human cardiomyocytes, neurons, macrophages, cerebellar-like neuronal cells, hepatocytes, and primordial germ cell-like cells (hPGCLCs) from 6 different gene expression datasets (GSE175179, GSE43143, GSE55536, GSE65423, GSE117086, and GSE147498). Likewise, downregulated genes were associated with the comparable GO biological process, cellular component, and molecular function terms, such as cell junction organization, synaptic signaling, membrane localization, and so on (Figure 1D).

Actually, genes associated with the pluripotent state are supposed to be upregulated while somatic cells are converted to iPSCs. Besides, similar genes related to pluripotency are likely to be suppressed while iPSCs differentiate into any somatic cell type. Of course, DEGs can differ between iPSCs and terminally differentiated somatic cell states according to the cell types. However, the most critical genes for the iPSC identity are not expected to diverge from cell type to cell type (in both directions; iPSC to somatic cell or somatic cell to iPSC).

Given this, upregulated genes in iPSCs (reprogrammed from somatic cells) and downregulated genes in iPSC-derived somatic cells were compared to unveil the common DEGs, which potentially retain indispensability for the pluripotent state independent from the cell type. Surprisingly, only 37 DEGs were shared between the two conditions explained above (Figure 2A). The genes already associated with stem cell biology, including *SOX2*, *DPPA4*, *DNMT3B*, *USP44*, *HMGA1*, etc., were intriguing among these common DEGs (Figure 2B), demonstrating outcomes of both analyses were consistent with each other. These genes were noticed to be involved in important biological processes and molecular functions, such as cell adhesion, cell junction, heterochromatin, cell cycle regulation, amino acid metabolism, the Wnt pathway, and transcription cofactor activity (Figure 2C). Taken together, these genes in Figure 2B stand out as alternative reprogramming factor candidates that can induce pluripotency alone or improve the efficacy of OSKM-mediated reprogramming protocols.

3.2. Dissecting the DEGs that potentially suppress the pluripotency

From another perspective, downregulated genes during iPSC formation can gain insights into hub proteins whose expression may be redundant in the pluripotent stage. Alternatively, these silenced genes may also hint at candidate targets for new compounds for chemical reprogramming protocols.

While reprogramming the human adult dermal fibroblasts and CD34+ cord blood cells into iPSCs, 215 common genes were downregulated in iPSCs compared to their origin somatic cells in all transcriptomic datasets (Figure 3A). Gene enrichment analysis showed that common DEGs were mainly involved in cellular responses to certain stimuli, cytokine production, immune regulation, secretion, and enzymatic activity (Figure 3B). With a reverse approach, we also assessed upregulated genes in terminally differentiated cells against iPSCs that they were derived from, suggesting that the expression of the pluripotency suppressor genes might be increased along with the lineage-specific genes. Herein, 149 genes were in the intersection of all GEO datasets (Figure 3C) with conceivable GO terms (biological process, molecular function,

and cellular component), such as the development of various tissues, morphogenesis, growth, extracellular matrix structure, transcriptional regulation, and cell adhesion were

certain (Figure 3D). Unexpectedly, enriched terms showed a discrepancy between two datasets (Figure 3B and Figure 3D).
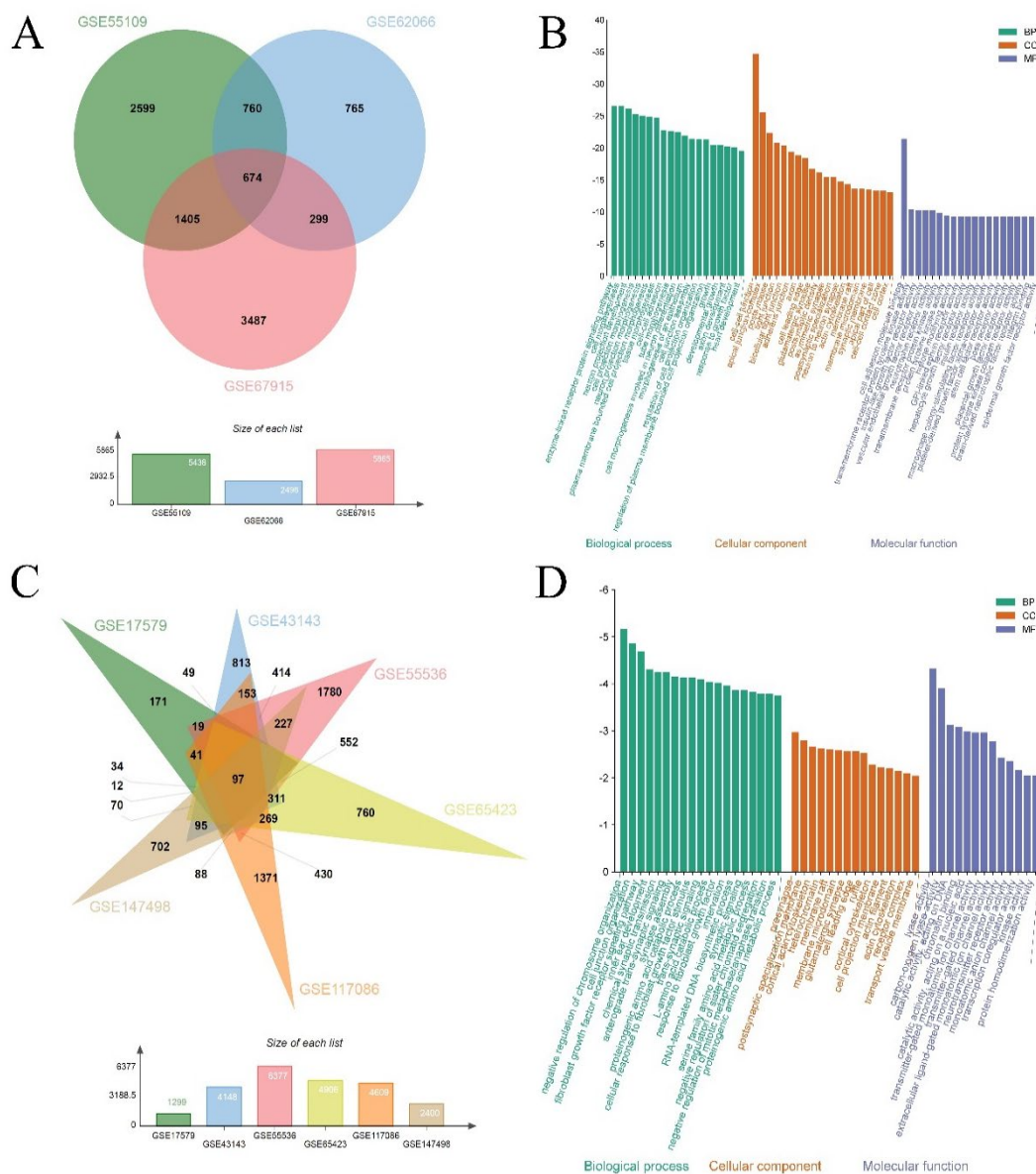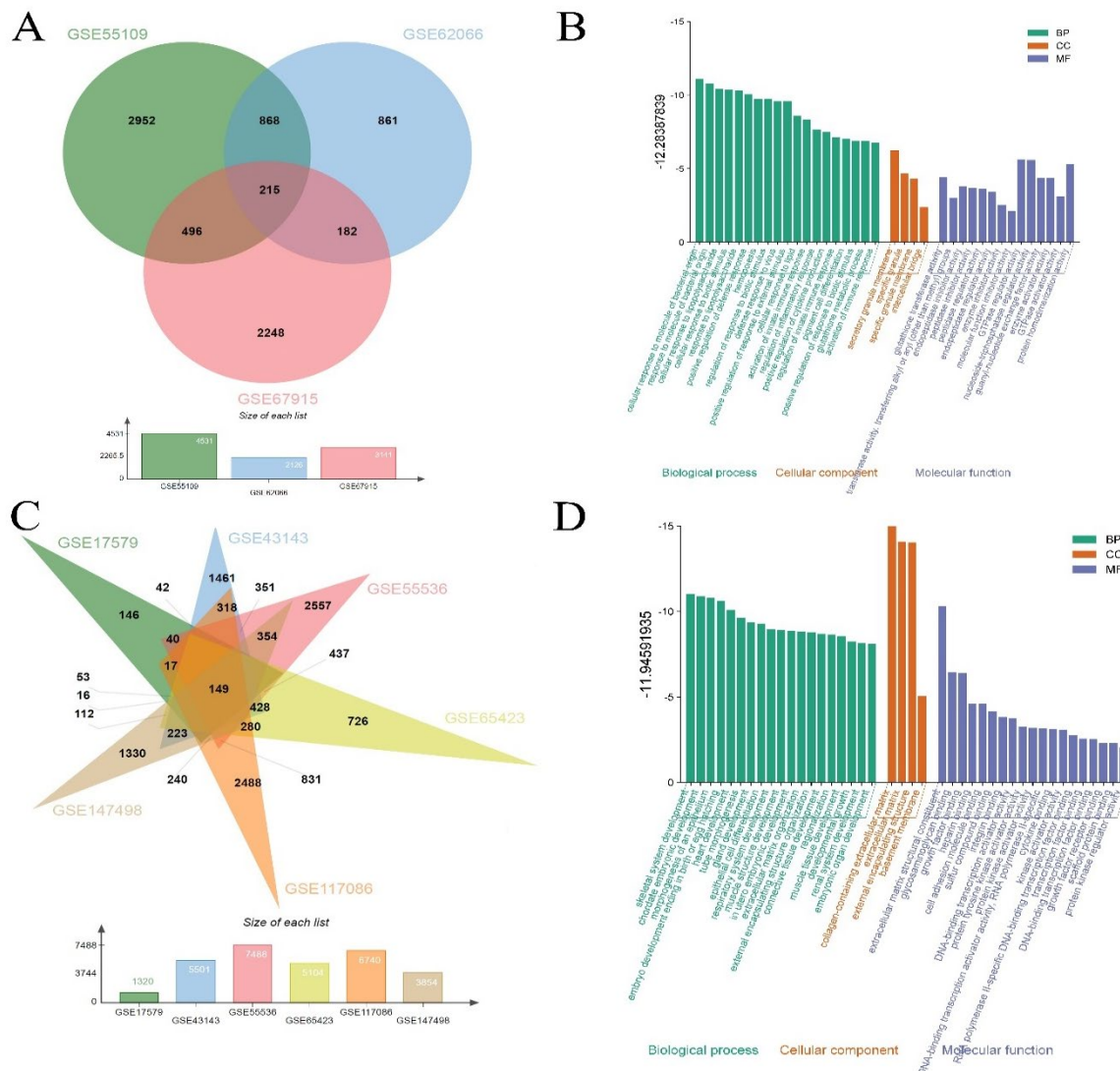

Figure 2. Downregulated genes while somatic cells were reprogrammed into iPSCs (A) and enriched GO terms (B). Upnregulated genes during iPSCs were terminally differentiated into somatic cell types (C) and related GO terms (D)

However, the number of common genes between two datasets was fewer than expected. Only 9 core genes (*RGCC*, *SUSD6*, *YAF2*, *RNF19A*, *ARID5B*, *RIN2*, *GSTM3*, *MTSS1*, *ARMCX3*) were unveiled as the mutual differentially expressed hub genes (Figure 4). Unfortunately, associated GO terms could not be enriched due to the inadequate number of hub genes.

3.3. Exploration of the small chemicals to mimic DEG profile in iPSCs

As figured out, 37 core upregulated genes and 9 core downregulated genes in iPSCs were found in all GEO datasets. This suggests that the

differential expression of these genes is probably independent from the type of somatic cell. Nominately, we hypothesized that mimicking the expressional pattern by using small chemical compounds could promote chemical reprogramming of human somatic cells. Repurposed molecules and their potential effects on the core genes were depicted in Figure 5. Treatment of the somatic cells with these promising compounds (alone or in combination) (Table 1) can holistically ensure the DEG signature deduced in our transcriptomic meta-analysis, enhancing OSKM-mediated or transgene-free reprogramming yield.

Figure 3. Common genes potentially inhibit pluripotency and promote differentiation in iPSCs (A, B)

Figure 4. The top ranked repurposed compounds mimicking expressional signature yielded in the transcriptomic meta-analysis. Red and blue squares in the matrix indicate up and down regulation, respectively

4. Discussion

Induced pluripotent stem cells (iPSCs) are marvellous cellular tools offering opportunities in a wide-range of application fields, such as regenerative medicine, developmental biology, disease modeling, tissue and organoid engineering, drug discovery, and cellular therapies. iPSCs are originated from the any terminally differentiated somatic cell by reprogramming them back into an embryonic-like pluripotent state [40]. Even though iPSCs almost represent all embryonic stem cell (ESC) characteristics, their applications are exempt from the legal obstacles and ethical issues in contrast to ESCs since living embryos are not destroyed during ESC isolation. Somatic cell

reprogramming have still been accomplished by the delivery of the pluripotency-related transcription factors, such as *OCT4*, *KLF4*, *c-MYC*, *SOX2*, and *LIN28* since these genes were first disscovered by Yamanaka and colleagues [1, 3]. It is challenging to compose a generalizable reprogramming protocol that utilizes the same transgens for each somatic cell type because terminally differentiated cells maintain unique genetic and epigenetic programs [13]. Therefore, utilization of alternative genes related to pluripotent state may enable a more efficient reprogramming for the most of somatic cell types.

Hereby, we sought out the probable genes for the pluripotent state, which jointly showed

significant expression levels in iPSCs during both bidirectional differentiation courses (somatic cell to iPSC and iPSC to somatic cell) by the integrated meta-analysis of transcriptome datasets in the GEO platform. Independent from the somatic cell type, 37 upregulated genes were noticed in iPSCs compared to the microarray data of terminally differentiated cells (Figure 2). Certain genes were quite intriguing among the upregulated transcripts (Figure 2B).

Podocalyxin-like protein (PODXL), a cell-adhesion glycoprotein, has previously been reported to present pluripotency markers, including ALP, SSEA3, SSEA4, SSEA5, TRA-1-60, and TRA-1-81 on the surface of human ESCs [41]. Additionally, *PODXL* gene was activated by KLF4 in human iPSCs at the early stage of reprogramming. Another current study has demonstrated *PODXL* is a crucial factor for primed pluripotency by promoting self-renewal, colony formation, c-Myc expression, and hTERT expression [42]. PODXL also regulated the cholesterol biosynthesis pathway to contribute to pluripotency. Notably, *PODXL* knockdown resulted in the loss of pluripotency, while *PODXL* overexpression augmented the human–mouse chimera formation in the mouse host embryos by regulating cell–cell and cell–extracellular matrix (ECM) interactions.

SOX2 (*SRY-box transcription factor 2*) is expected to appear because it is already an authenticated strong reprogramming factor [43], addressing the reliability of the current meta-analysis. Along with *SOX2*, *OCT4* (*POU5F1* or related isoforms), *LIN28*, *c-MYC*, and *NANOG* were detected in the upregulated transcriptome lists in only one or a few datasets (data not shown) not in the intersection, suggesting expression of other reprogramming factors can differ cell type to cell type.

Glypican 4 (GPC4), a cell surface heparan sulfate proteoglycan, was also reported as required for self-renewal in the mouse ESCs, and its downregulation in human iPSCs led to improvement in neuronal differentiation [44].

Chang et al. showed that expression of the *TRIM71* (*Tripartite motif containing 71*) gene that encodes an E3 ubiquitin-protein ligase was specific to undifferentiated mouse ESCs [45]. As reported, *TRIM71* is associated with the miR-290 and miR-302 families, the best-known ESC-specific miRNA clusters, and the Ago-2 protein to suppress *Cyclin-dependent kinase inhibitor 1A* (*CDKN1A*) expression. Thus, TRIM71 is a significant factor that induces rapid self-renewal of ESCs. Moreover, TRIM71, accompanied by let-7, contributed to human iPSC reprogramming by targeting differentiation genes, particularly the prodifferentiation transcription factor EGR1 [46].

CDH1 (*Cadherin 1* or *E-cadherin*) is another common upregulated gene in iPSCs in our analysis. *CDH1* was demonstrated to be involved in self-renewal and mesenchymal to epithelial transition (MET) in pluripotent stem cells [47-49]. Notably, An and coworkers exhibited that elevated *CDH1* expression enhanced the reprogramming of human spermatogonial stem cells (SSCs) and male germline stem cells (GSCs) into iPSCs [50], promoting a putative role in the maintenance of pluripotent status.

Otherwise, Qiao and colleagues unraveled that *SEPHS1* (*Selenophosphate synthetase 1*) was dispensable for pluripotency maintenance but critical for three germ layer differentiation of mouse ESCs [51]. Contradictorily, *SEPHS1* upregulation in all iPSCs datasets compared to somatic cells led us to conclude that it may be required at the initial stages of pluripotency and can not induce reprogramming alone.

RNA polymerase III subunit G (*POLR3G*) is another sensible gene yielded in our transcriptomic analysis. *POLR3G* was previously indicated that its level was higher in undifferentiated human ESCs and iPSCs, maintaining the pluripotent state of human ESCs [52]. Then, Lund et al. elaborated that POLR3G was essential to regulate the transcription or splicing of a specific subset of small RNAs (miRNAs, snoRNAs, lincRNAs, etc.) and the pluripotency-linked protein-coding genes, including *DNMT1*, *APC*, *SMARCA4*, *NIPBL*, *RIF1*, *RTF1*, *TET1*, and *LIN28A* [53].

Furthermore, POLR3G could recruit key transcription factors, NANOG, SOX2, and KLF4 on the promoters of POLR3G-regulated

transcripts. Taken together, *POLR3G* stands out as an alternative or supportive pluripotency factor candidate to be utilized in the reprogramming of various somatic cells.

TERF1 (Telomeric repeat binding factor 1) encodes a component of the shelterin complex, which is involved in the protection of chromosome ends. Schneider and coworkers pointed out TERF1 as a stem cell marker, which was crucial for both maintenance and induction of pluripotency in the mouse ESCs and iPSCs, respectively [54]. Endogenous *TERF1* expression in mouse iPSCs was enriched because it was a direct target of *OCT4* and *NANOG*. Further evidence about the contribution of *TERT1* to the maintenance of the naive state of mouse ESCs was also manifested by several researchers.

Interestingly, Marión et al. designated that *TERF1* depletion in mouse pluripotent stem cells led to downregulation of a series of genes, including *MYC*, *SOX2*, *NANOG*, *KLF4,* and *BMP*, indicating it might control key pluripotency transcription factors [55]. Liu and colleagues also elucidated the miR-590/Acvr2a/Terf1 axis was substantial for telomere elongation to modulate the pluripotency in the pluripotent cells [56]. Although these findings together reflect the critical involvement of TERT1 in the pluripotency control in ESCs or already reprogrammed iPSCs, there is no evidence about the consequences of ectopic overexpression of *TERT1* in the differentiated cells to induce reprogramming. Given its significance, *TERT1* also emerges as a candidate with high potential for use as a reprogramming factor.

DPPA4 (developmental pluripotency associated 4), a marker of pluripotent stem cells, shows overexpression in ESCs and certain cancers. DPPA4 acts as a transcriptional regulator of endogenous targets in pluripotent cells and tumor cells, promoting cell proliferation [57]. However, *DPPA4* knockout only affected cell fate commitment at later developmental stages but not pluripotency in mice [58]. Nevertheless, its ectopic overexpression in somatic cells came out with oncogenic impacts [57-59]. Therefore, we concluded that *DPPA4* gene is not promising to facilitate clinical-grade iPSC production.

PHC1 (polyhomeotic homolog 1) is a subunit of canonical polycomb repressive complex 1 (PRC1), a crucial regulator of pluripotency and early embryonic development [60]. A recent study revealed that *Phc1* had the highest-ranking score in the mouse integrated stemness signatures (ISSs) composed of a gene regulatory network for self-renewal and differentiation [61]. On the other hand, Chen and colleagues also reported *PHC1* maintained the pluripotency of human ESCs by regulating genome-wide chromatin architecture and particularly activating *NANOG* transcription [62].

Conversely, analysis of transcriptomic datasets revealed a restricted number of genes that were commonly downregulated in iPSCs compared to the related somatic cells (Figure 4). This limitation could have arisen from the biological variability among different somatic cell types and differentiation protocols, as well as technical constraints of the given transcriptomic datasets. For instance, YAF2, a polycomb group (PcG) protein, was shown as a transcriptional repressor and an important regulator for self-renewal of mouse ESCs [63]. Surprisingly, YAF1 also has a function in the differentiation programs in mESCs and the formation of the embryoid body, highlighting that targeting YAF1 by small molecules can indeed gain an advantage in reprogramming protocols. Likewise, there are several studies exhibiting that ARMCX3 (Armadillo repeat containing X-linked 3) and RGCC (regulator of cell cycle) balance self-renewal and neural differentiation of certain progenitors and stem cells [64-67].

Although identified chemical compounds are speculative, they may indirectly support pluripotency *in vitro*. For instance, BRD-K44432556, introduced as a potent HIF1α (hypoxia inducible factor 1α) activator before [68], was quite intriguing. Several studies have reported that HIF1 could contribute to pluripotency during somatic cell reprogramming by promoting the metabolic shift in this process [69]. In this regard, small molecules that can modulate key metabolic players, such as HIFs, are thought to be encouraging in iPSC production [70]. Besides, the studies lasting in recent years have highlighted the importance of managing the ubiquitin–proteasome system (UPS) either in the

induction or maintenance of pluripotency [71, 72]. Thereby, NSC 632839 hydrochloride seems to be plausible, hypothetically controlling UPS because Aleo and coworkers characterized it as the nonselective isopeptidase inhibitor [73]. Additionally, it has been indicated that ERK downregulates *NANOG*, *OCT4*, *KLF2*, and KLF4, and its pharmacological inhibition via VX-11e stimulates self-renewal [74].

Thereby, ERK inhibitor 11e (VX-11e) in Table 1 would already be anticipated. Kim and colleagues demonstrated that suppression of the mTOR signaling pathway by shRNA constructs

augmented pluripotency and ESC-like properties both in humans and mice [75]. Hence, selective mTOR kinase inhibitor AZD8055 was compatible with this data. Numerous studies have already evidenced CHIR-99021's outstanding roles in maintaining self-renewal and pluripotency of the mouse and human pluripotent stem cells [76-78]. This was considered as a corroborative indicator for the relevance of the outputs in Table 1. These findings altogether indicate that repurposed small chemical molecules may be applicable in the maintenance of the pluripotent state since some of them are in conformity with the published research.

Table 1. Top 20 candidate small molecules (alone and in combination) to facilitate somatic cell reprogramming

	Solo Administration		Administration in Combination
No	*Compound*	*Actual Target or Cellular Function*	*Compounds*
1	Carbazol-9-yl-p-tolyl-methanone	N/A	1. Carbazol-9-yl-p-tolyl-methanone 6. ERK inhibitor 11e
2	BRD-K44432556	Hypoxia inducible factor activator	2. BRD-K44432556 6. ERK inhibitor 11e
3	NSC 632839 hydrochloride	Ubiquitin isopeptidase inhibitor	1. Carbazol-9-yl-p-tolyl-methanone 11. BIBR1532
4	RHAMNETIN	Plant o-methylated flavonoid (antioxidant)	1. Carbazol-9-yl-p-tolyl-methanone 14. HY-11068
5	METHOXSALEN	Treatment of psoriasis, eczema, vitiligo, and some cutaneous lymphomas	1. Carbazol-9-yl-p-tolyl-methanone 16. ALW-II-38-3
6	ERK inhibitor 11e	Extracellular signal-related kinase 2 (ERK2) inhibitor	1. Carbazol-9-yl-p-tolyl-methanone 18. CHIR-99021
7	AZD8055	ATP-competitive inhibitor of mTOR kinase	1. Carbazol-9-yl-p-tolyl-methanone 2. BRD-K44432556
8	Dorsomorphin dihydrochloride	ATP-competitive AMPK inhibitor	1. Carbazol-9-yl-p-tolyl-methanone 3. NSC 632839 hydrochloride
9	CYT997	Microtubule polymerization inhibitor	1. Carbazol-9-yl-p-tolyl-methanone 4. RHAMNETIN
10	BRD-K25737009	Retinoic Acid Receptor Gamma (predicted)	4. RHAMNETIN 6. ERK inhibitor 11e
11	BIBR1532	Non-competitive human telomerase inhibitor	1. Carbazol-9-yl-p-tolyl-methanone 7. AZD8055
12	IMD 0354	IKKβ inhibitor	6. ERK inhibitor 11e 7. AZD8055
13	SB 239063	p38 MAPK inhibitor	1. Carbazol-9-yl-p-tolyl-methanone 9. Dorsomorphin dihydrochloride
14	ALW-II-38-3	A potent ephrin-A receptor (EphA3) kinase inhibitor	1. Carbazol-9-yl-p-tolyl-methanone 10. BRD-K25737009
15	WZ-3105	Potential targets SRC, ROCK2, NTRK2, FLT3, IRAK1	2. BRD-K44432556 11. BIBR1532
16	CHIR-99021	Selective inhibitor of glycogen synthase kinase 3 (GSK-3)	5. METHOXSALEN 11. BIBR1532
17	AT-7519	Selective inhibitor of certain Cyclin Dependent Kinases (CDKs)	6. ERK inhibitor 11e 11. BIBR1532
18	Taxol	Antimitotic chemotherapy agent	8. Dorsomorphin dihydrochloride 11. BIBR1532
19	GR 127935 hydrochloride	Selective 5-HT1B/1D receptor antagonist.	9. CYT997 11. BIBR1532
20	L-cis-DILTIAZEM	cGMP-activated K+ channel blocker	2. BRD-K44432556 12. IMD 0354

Albeit the current study provides a basis to uncover alternative reprogramming factor candidates, experimental validation for the transcriptomic analyses regarding these factors and small chemical compounds is crucial to substantiate their *in vitro* efficacy in somatic cell reprogramming. For instance, the impacts of the proposed genes (e.g., *POLR3G*, *TERF1*, *PHC1*) on the characteristics of different somatic cell types or the substitution potential of these candidate genes for the Yamanaka factors should be investigated through gain- and loss-of-function strategies. Furthermore, integration of single-cell transcriptomics and epigenomics may also yield deeper insights into cell-type-specific reprogramming dynamics. Meanwhile, bioavailability, cytotoxicity, and potential off-target effects of the small chemical molecules from the in silico repurposing remained unexplored here. Functional assays may also gain original knowledge about how these small molecule candidates could alter cellular identities.

5. Conclusion

Consequently, the current study holistically evaluated transcriptomic data in a bidirectional manner (differentiation from somatic cell to iPSC state, or vice versa) to reveal upregulated genes potentially associated with pluripotency. Otherwise, downregulated genes during iPSC differentiation led us to screen potent chemical molecules to facilitate somatic cell reprogramming. Overall, transcriptomic analysis has released novel findings that are worth taking into account to design more generalizable procedures for iPSC manufacturing.

Article Information Form

The Declaration of Conflict of Interest/ Common Interest
No conflict of interest or common interest has been declared by the author.

Artificial Intelligence Statement
No artificial intelligence tools were used while writing this article.

References

[1] K. Takahashi, S. Yamanaka, "Induction of pluripotent stem cells from mouse embryonic and adult fibroblast cultures by defined factors," Cell, vol. 126, no. 4, pp. 663–676, 2006.

[2] P. Karagiannis, K. Takahashi, M. Saito, Y. Yoshida, K. Okita, A. Watanabe, H. Inoue, J. K. Yamashita, M. Todani, M. Nakagawa, M. Osawa, Y. Yashiro, S. Yamanaka, K. Osafune, "Induced pluripotent stem cells and their use in human models of disease and development," Physiological Reviews, vol. 99, no. 1, pp. 79–114, 2019.

[3] K. Takahashi, K. Tanabe, M. Ohnuki, M. Narita, T. Ichisaka, K. Tomoda, S. Yamanaka, "Induction of pluripotent stem cells from adult human fibroblasts by defined factors," Cell, vol. 131, no. 5, pp. 861–872, 2007.

[4] K. Lin, A. Z. Xiao, "Quality control towards the application of induced pluripotent stem cells," Current Opinion in Genetics & Development, vol. 46, pp. 164–169, 2017.

[5] A. Al Abbar, S. C. Ngai, N. Nograles, S. Y. Alhaji, S. Abdullah, "Induced pluripotent stem cells: Reprogramming platforms and applications in cell replacement therapy," Bioresearch Open Access, vol. 9, no. 1, p. 121, 2020.

[6] Y. Qiao, O. S. Agboola, X. Hu, Y. Wu, L. Lei, "Tumorigenic and immunogenic properties of induced pluripotent stem cells: A promising cancer vaccine," Stem Cell Reviews and Reports, vol. 16, no. 6, pp. 1049–1061, 2020.

[7] C. Zhong, M. Liu, X. Pan, H. Zhu, "Tumorigenicity risk of iPSCs in vivo: Nip it in the bud," Precision Clinical Medicine, vol. 5, no. 1, 2022.

[8] Y. C. Lin, C. C. Ku, K. Wuputra, C. J. Liu, D. C. Wu, M. Satou, Y. Mitsui, S. Saito, K. K. Yokoyama, "Possible Strategies to Reduce the Tumorigenic Risk of Reprogrammed Normal and Cancer Cells," International Journal of Molecular Sciences, vol. 25, no. 10, p. 5177, 2024.

[9] C. Hu, L. Li, "Current reprogramming systems in regenerative medicine: From somatic cells to induced pluripotent stem cells," Regenerative Medicine, vol. 11, no. 1, pp. 91–105, 2016.

[10] T. Pozner, C. Grandizio, M. W. Mitchell, N. Turan, L. Scheinfeldt, "Human iPSC reprogramming success: The impact of approaches and source materials," Stem Cells International, vol. 2025, no. 1, p. 2223645, 2025.

[11] K. Nishimura, M. Ohtaka, H. Takada, A. Kurisaki, N. V. K. Tran, Y. T. H. Tran, K. Hisatake, M. Sano, M. Nakanishi, "Simple and effective generation of transgene-free induced pluripotent stem cells using an auto-erasable Sendai virus vector responding to microRNA-302," Stem Cell Research, vol. 23, pp. 13–19, 2017.

[12] K. Nishino, Y. Arai, K. Takasawa, M. Toyoda, M. Yamazaki-Inoue, T. Sugawara, H. Akutsu, K. Nishimura, M. Ohtaka, M. Nakanishi, A. Umezawa, "Epigenetic-scale comparison of human iPSCs generated by retrovirus, Sendai virus or episomal vectors," Regenerative Therapy, vol. 9, pp. 71–78, 2018.

[13] M. S. Poetsch, A. Strano, K. Guan, "Human induced pluripotent stem cells: From cell origin, genomic stability, and epigenetic memory to translational medicine," Stem Cells, vol. 40, no. 6, pp. 546–555, 2022.

[14] P. H. L. Krijger, B. Di Stefano, E. de Wit, F. Limone, C. van Oevelen, W. de Laat, T. Graf, "Cell-of-origin-specific 3D genome structure acquired during somatic cell reprogramming," Cell Stem Cell, vol. 18, no. 5, pp. 597–610, 2016.

[15] T. Vierbuchen, M. Wernig, "Molecular roadblocks for cellular reprogramming," Molecules and Cells, vol. 47, no. 6, pp. 827–838, 2012.

[16] J. Krauskopf, K. Eggermont, R. F. Madeiro Da Costa, S. Bohler, D. Hauser, F. Caiment, T. M. de Kok, C. Verfaillie, J.C. Kleinjans, "Transcriptomics analysis of human iPSC-derived dopaminergic neurons reveals a novel model for sporadic Parkinson's disease," Mol Psychiatry, vol. 27, no. 10, pp. 4355–4367, 2022.

[17] E. E. Burke, J. G. Chenoweth, J. H. Shin, L. Collado-Torres, S. K. Kim, N. Micali, Y. Wang, C. Colantuoni, R. E. Straub, D. J. Hoeppner, H. Y. Chen, A. Sellers, K. Shibbani, G. R. Hamersky, M. Diaz Bustamante, B. N. Phan, W. S. Ulrich, C. Valencia, A. Jaishankar, A. J. Price, A. Rajpurohit, S. A. Semick, R. W. Bürli, J. C. Barrow, D. J. Hiler, S. C. Page, K. Martinowich, T. M. Hyde, J. E. Kleinman, K. F. Berman, J. A. Apud, A. J. Cross, N. J. Brandon, D. R. Weinberger, B. J. Maher, R. D. G. McKay, A. E. Jaffe, "Dissecting transcriptomic signatures of neuronal differentiation and maturation using iPSCs," Nature Communications, vol. 11, no. 1, pp. 1–14, 2020.

[18] Y. Xu, M. Zhang, W. Li, X. Zhu, X. Bao, B. Qin, A. P. Hutchins, M. A. Esteban, "Transcriptional control of somatic cell reprogramming," Trends in Cell Biology, vol. 26, no. 4, pp. 272–288, 2016.

[19] Y. Tanaka, E. Hysolli, J. Su, Y. Xiang, K. Y. Kim, M. Zhong, Y. Li, K. Heydari, G. Euskirchen, M. P. Snyder, X. Pan, S. M. Weissman, I. H. Park, "Transcriptome signature and regulation in human somatic cell reprogramming," Stem Cell Reports, vol. 4, no. 6, pp. 1125–1139, 2015.

[20] S. Masuda, J. Wu, T. Hishida, G. N. Pandian, H. Sugiyama, J. C. Izpisua Belmonte, "Chemically induced pluripotent stem cells (CiPSCs): A transgene-free approach," Journal of Molecular Cell Biology, vol. 5, no. 5, pp. 354–355, 2013.

[21] Y. Li, Q. Zhang, X. Yin, W. Yang, Y. Du, P. Hou, J. Ge, C. Liu, W. Zhang, X. Zhang, Y. Wu, H. Li, K. Liu, C. Wu, Z. Song, Y. Zhao, Y. Shi, H. Deng, "Generation of iPSCs from mouse fibroblasts with a single gene, Oct4, and small molecules," Cell Research, vol. 21, no. 1, pp. 196–204, 2010.

[22] J. Guan, G. Wang, J. Wang, Z. Zhang, Y. Fu, L. Cheng, G. Meng, Y. Lyu, J. Zhu, Y. Li, Y. Wang, S. Liuyang, B. Liu, Z. Yang, H. He, X. Zhong, Q. Chen, X. Zhang, S. Sun, W. Lai, Y. Shi, L. Liu, L. Wang, C. Li, S. Lu, H. Deng, "Chemical reprogramming of human somatic cells to pluripotent stem cells," Nature, vol. 605, no. 7909, pp. 325–331, 2022.

[23] I. Dorn, K. Klich, M. J. Arauzo-Bravo, M. Radstaak, S. Santourlidis, F. Ghanjati, T. F. Radke, O. E. Psathaki, G. Hargus, J. Kramer, M. Einhaus, J. B. Kim, G. Kögler, P. Wernet, H. R. Schöler, P. Schlenke, H. Zaehres, "Erythroid differentiation of human induced pluripotent stem cells is independent of donor cell type of origin," Haematologica, vol. 100, no. 1, pp. 32–41, 2015.

[24] J. H. Lee, J. B. Lee, Z. Shapovalova, A. Fiebig-Comyn, R. R. Mitchell, S. Laronde, E. Szabo, Y. D. Benoit, M. Bhatia, "Somatic transcriptome priming gates lineage-specific differentiation potential of human-induced pluripotent stem cell states," Nature Communications, vol. 5, no. 1, pp. 1–13, 2014.

[25] The ENCODE Project Consortium, "An integrated encyclopedia of DNA elements in the human genome," Nature, vol. 489, no. 7414, pp. 57–74, 2012.

[26] J. Chen, M. Lin, J. J. Foxe, E. Pedrosa, A. Hrabovsky, R. Carroll, D. Zheng, H. M. Lachman, "Transcriptome comparison of human neurons generated using induced pluripotent stem cells derived from dental pulp and skin fibroblasts," PLoS One, vol. 8, no. 10, p. e75682, 2013.

[27] H. Zhang, C. Xue, R. Shah, K. Bermingham, C. C. Hinkle, W. Li, A. Rodrigues, J. Tabita-Martinez, J. S. Millar, M. Cuchel, E. E. Pashos, Y. Liu, R. Yan, W. Yang, S. J. Gosai, D. VanDorn, S. T. Chou, B. D. Gregory, E. E. Morrisey, M. Li, D. J. Rader, M. P. Reilly, "Functional Analysis and Transcriptomic Profiling of iPSC-Derived Macrophages and Their Application in Modeling Mendelian Disease," Circulation Research, vol. 117, no. 1, pp. 17–28, 2015.

[28] L. E. Viiri, T. Rantapero, M. Kiamehr, A. Alexanova, M. Oittinen, K. Viiri, H. Niskanen, M. Nykter, M. U. Kaikkonen, K. Aalto-Setala, "Extensive reprogramming of the nascent transcriptome during iPSC to hepatocyte differentiation," Scientific Reports, vol. 9, no. 1, pp. 1–12, 2019.

[29] Y. Murase, Y. Yabuta, H. Ohta, C. Yamashiro, T. Nakamura, T. Yamamoto, M. Saitou, M, "Long-term expansion with germline potential of human primordial germ cell-like cells in vitro," EMBO Journal, vol. 39, no. 21, 2020.

[30] Y. Benjamini, Y. Hochberg, "Controlling the false discovery rate: A practical and powerful approach to multiple testing," Journal of the Royal Statistical Society: Series B (Methodological), vol. 57, no. 1, pp. 289–300, 1995.

[31] P. Bardou, J. Mariette, F. Escudié, C. Djemiel, C. Klopp, "Jvenn: An interactive Venn diagram viewer," BMC Bioinformatics, vol. 15, no. 1, pp. 1–7, 2014.

[32] Y. Zhou, B. Zhou, L. Pache, M. Chang, A. H. Khodabakhshi, O. Tanaseichuk, C. Benner, S. K. Chanda, "Metascape

provides a biologist-oriented resource for the analysis of systems-level datasets," Nature Communications, vol. 10, no. 1, pp. 1–10, 2019.

[33] D. Tang, M. Chen, X. Huang, G. Zhang, L. Zeng, G. Zhang, S. Wu, Y. Wang, "SRplot: A free online platform for data visualization and graphing," PLoS One, vol. 18, no. 11, p. e0294236, 2023.

[34] Y. T. Zhao, M. Fasolino, Z. Zhou, "Locus- and cell type-specific epigenetic switching during cellular differentiation in mammals," Frontiers in Biology, vol. 11, no. 4, pp. 311–322, 2016.

[35] H. Chen, J. Guo, S. K. Mishra, P. Robson, M. Niranjan, J. Zheng, "Single-cell transcriptional analysis to uncover regulatory circuits driving cell fate decisions in early mouse development," Bioinformatics, vol. 31, no. 7, pp. 1060–1066, 2015.

[36] S. Thiagalingam, "Epigenetic memory in development and disease: Unraveling the mechanism," Biochimica et Biophysica Acta (BBA) - Reviews on Cancer, vol. 1873, no. 2, p. 188349, 2020.

[37] E. Hörmanseder, "Epigenetic memory in reprogramming," Current Opinion in Genetics and Development, vol. 70, pp. 24–31, 2021.

[38] B. Nashun, P. W. Hill, P. Hajkova, "Reprogramming of cell fate: Epigenetic memory and the erasure of memories past," EMBO Journal, vol. 34, no. 10, pp. 1296–1308, 2015.

[39] Y. H. Lin, J. D. Lehle, J. R. McCarrey, "Source cell-type epigenetic memory persists in induced pluripotent cells but is lost in subsequently derived germline cells," Frontiers in Cell and Developmental Biology, vol. 12, p. 1306530, 2024.

[40] J. Cerneckis, H. Cai, Y. Shi, "Induced pluripotent stem cells (iPSCs): Molecular mechanisms of induction and

applications," Signal Transduction and Targeted Therapy, vol. 9, no. 1, pp. 1–26, 2024.

[41] L. Kang, C. Yao, A. Khodadadi-Jamayran, W. Xu, R. Zhang, N. S. Banerjee, C. W. Chang, L. T. Chow, T. Townes, K. Hu, "The universal 3D3 antibody of human PODXL is pluripotent cytotoxic, and identifies a residual population after extended differentiation of pluripotent stem cells," Stem Cells and Development, vol. 25, no. 7, pp. 556–568, 2016.

[42] W. J. Chen, W. K. Huang, S. R. Pather, W. F. Chang, L. Y. Sung, H. C. Wu, M. Y. Liao, C. C. Lee, H. H. Wu, C. Y. Wu, K. S. Liao, C. Y. Lin, S. C. Yang, H. Lin, P. L. Lai, C. H. Ng, C. M. Hu, I. C. Chen, C. H. Chuang, C. Y. Lai, P. Y. Lin, Y. C. Lee, S. C. Schuyler, A. Schambach, F. L. Lu, J. Lu, "Podocalyxin-like protein 1 regulates pluripotency through the cholesterol biosynthesis pathway," Advanced Science, vol. 10, no. 1, p. 2205451, 2023.

[43] T. Schaefer, C. Lengerke, "SOX2 protein biochemistry in stemness, reprogramming, and cancer: The PI3K/AKT/SOX2 axis and beyond," Oncogene, vol. 39, no. 2, pp. 278–292, 2019.

[44] S. Corti, R. Bonjean, T. Legier, D. Rattier, C. Melon, P. Salin, E. A. Toso, M. Kyba, L. Kerkerian-Le Goff, F. Maina, R. Dono, "Enhanced differentiation of human induced pluripotent stem cells toward the midbrain dopaminergic neuron lineage through GLYPICAN-4 downregulation," Stem Cells Translational Medicine, vol. 10, no. 5, pp. 725–742, 2021.

[45] H. M. Chang, N. J. Martinez, J. E. Thornton, J. P. Hagan, K. D. Nguyen, R. I. Gregory, "Trim71 cooperates with microRNAs to repress Cdkn1a expression and promote embryonic stem cell proliferation," Nature Communications, vol. 3, no. 1, pp. 1–10, 2012.

[46] K. A. Worringer, T. A. Rand, Y. Hayashi, S. Sami, K. Takahashi, K. Tanabe, M. Narita, D. Srivastava, S. Yamanaka, "The let-7/LIN-41 pathway regulates reprogramming to human induced pluripotent stem cells by controlling expression of prodifferentiation genes," Cell Stem Cell, vol. 14, no. 1, pp. 40–52, 2014.

[47] S. Bhattacharyya, R. D. Mote, J. W. Freimer, M. Tiwari, S. Bansi Singh, S. Arumugam, Y. V. Narayana, R. Rajan, D. Subramanyam, D. et al., "Cell–cell adhesions in embryonic stem cells regulate the stability and transcriptional activity of β-catenin," FEBS Letters, vol. 596, no. 13, pp. 1647–1660, 2022.

[48] T. Ye, J. Li, Z. Sun, D. Liu, B. Zeng, Q. Zhao, J. Wang, H. R. Xing, "Cdh1 functions as an oncogene by inducing self-renewal of lung cancer stem-like cells via oncogenic pathways," International Journal of Biological Sciences, vol. 16, no. 3, pp. 447–459, 2020.

[49] C. E. Aban, A. Lombardi, G. Neiman, M. C. Biani, A. La Greca, A. Waisman, L. N. Moro, G. Sevlever, S. Miriuka, C. Luzzani, "Downregulation of E-cadherin in pluripotent stem cells triggers partial EMT," Scientific Reports, vol. 11, no. 1, pp. 1–11, 2021.

[50] J. An, Y. Zheng, C. T. Dann, "Mesenchymal to epithelial transition mediated by CDH1 promotes spontaneous reprogramming of male germline stem cells to pluripotency," Stem Cell Reports, vol. 8, no. 2, pp. 446–459, 2017.

[51] L. Qiao, S. H. Dho, J. Y. Kim, L. K. Kim, "SEPHS1 is dispensable for pluripotency maintenance but indispensable for cardiac differentiation in mouse embryonic stem cells," Biochemical and Biophysical Research Communications, vol. 590, pp. 125–131, 2022.

[52] R. C. B. Wong, S. Pollan, H. Fong, A. Ibrahim, E. L. Smith, M. Ho, A. L. Laslett, P. J. Donovan, "A novel role for an RNA polymerase III Subunit POLR3G in regulating pluripotency in human embryonic stem cells," Stem Cells, vol. 29, no. 10, pp. 1517–1527, 2011.

[53] R. J. Lund, N. Rahkonen, M. Malonzo, L. Kauko, M. R. Emani, V. Kivinen, E. Närvä, E. Kemppainen, A. Laiho, H. Skottman, O. Hovatta, O. Rasool, M. Nykter, H. Lähdesmäki, R. Lahesmaa, "RNA Polymerase III Subunit POLR3G Regulates Specific Subsets of PolyA+ and SmallRNA transcriptomes and splicing in human pluripotent stem cells," Stem Cell Reports, vol. 8, no. 5, pp. 1442–1454, 2017.

[54] R. P. Schneider, I. Garrobo, M. Foronda, J. A. Palacios, R. M. Marión, I. Flores, S. Ortega, M. A. Blasco, "TRF1 is a stem cell marker and is essential for the generation of induced pluripotent stem cells," Nature Communications, vol. 4, no. 1, pp. 1–16, 2013.

[55] R. M. Marión, J. J. Montero, I. López de Silanes, O. Graña-Castro, P. Martínez, S. Schoeftner, J. A. Palacios-Fábrega, M. A. Blasco, "TERRA regulate the transcriptional landscape of pluripotent cells through TRF1-dependent recruitment of PRC2," Elife, vol. 8, e44656, 2019.

[56] Q. Liu, G. Wang, Y. Lyu, M. Bai, Z. Jiapaer, W. Jia, T. Han, R. Weng, Y. Yang, Y. Yu, J. Kang, "The miR-590/Acvr2a/Terf1 axis regulates telomere elongation and pluripotency of mouse iPSCs," Stem Cell Reports, vol. 11, no. 1, pp. 88–101, 2018.

[57] R. H. Klein, P. Y. Tung, P. Somanath, H. J. Fehling, P. S. Knoepfler, "Genomic functions of developmental pluripotency associated factor 4 (Dppa4) in pluripotent stem cells and cancer," Stem Cell Research, vol. 31, pp. 83–94, 2018.

[58] R. H. Klein, P. S. Knoepfler, "DPPA2, DPPA4, and other DPPA factor epigenomic functions in cell fate and cancer," Stem Cell Reports, vol. 16, no. 12, pp. 2844–2851, 2021.

[59] P. Y. Tung, N. V. Varlakhanova, P. S. Knoepfler, "Identification of DPPA4 and DPPA2 as a novel family of pluripotency-related oncogenes," Stem Cells, vol. 31, no. 11, pp. 2330–2342, 2013.

[60] L. Morey, G. Pascual, L. Cozzuto, G. Roma, A. Wutz, S. A. Benitah, L. Di Croce, "Nonoverlapping functions of the polycomb group Cbx family of proteins in embryonic stem cells," Cell Stem Cell, vol. 10, no. 1, pp. 47–62, 2012.

[61] T. Barata, I. Duarte, M. E. Futschik, "Integration of stemness gene signatures reveals core functional modules of stem cells and potential novel stemness genes," Genes (Basel), vol. 14, no. 3, p. 745, 2023.

[62] L. Chen, Q. Tong, X. Chen, P. Jiang, H. Yu, Q. Zhao, L. Sun, C. Liu, B. Gu, Y. Zheng, L. Fei, X. Jiang, W. Li, G. Volpe, M. M. Abdul, G. Guo, J. Zhang, P. Qian, Q. Sun, D. Neculai, M. A. Esteban, C. Li, F. Wen, J. Ji, "PHC1 maintains pluripotency by organizing genome-wide chromatin interactions of the Nanog locus," Nature Communications, vol. 12, no. 1, pp. 1–13, 2021.

[63] W. Zhao, M. Liu, H. Ji, Y. Zhu, C. Wang, Y. Huang, X. Ma, G. Xing, Y. Xia, Q. Jiang, J. Qin, "The polycomb group protein Yaf2 regulates the pluripotency of embryonic stem cells in a phosphorylation-dependent manner," The Journal of Biological Chemistry, vol. 293, no. 33, p. 12793, 2018.

[64] Q. Zhou, Y. Lei, "ARMCX3 regulates ROS signaling, affects neural differentiation and inflammatory microenvironment in dental pulp stem cells," Heliyon, vol. 10, no. 17, 2024.

[65] S. Mirra, F. Ulloa, I. Gutierrez-Vallejo, E. Martì, E. Soriano, "Function of Armcx3 and Armc10/SVH genes in the regulation of progenitor proliferation and neural differentiation in the chicken spinal cord," Frontiers in Cellular Neuroscience, vol. 10, no. MAR2016, p. 168336, 2016.

[66] Z. Guo, M. Chen, Y. Chao, C. Cai, L. Liu, L. Zhao, L. Li, Q. R. Bai, Y. Xu, W. Niu, L. Shi, Y. Bi, D. Ren, F. Yuan, S. Shi, Q. Zeng, K. Han, Y. Shi, S. Bian, G. He, "RGCC balances self-renewal and neuronal differentiation of neural stem cells in the developing mammalian neocortex," EMBO Reports, vol. 22, no. 9, 2021.

[67] K. Mulfaul, J. C. Giacalone, A. P. Voigt, M. J. Riker, D. Ochoa, I. C. Han, E. M. Stone, R. F. Mullins, B. A. Tucker, "Stepwise differentiation and functional characterization of human induced pluripotent stem cell-derived choroidal endothelial cells," Stem Cell Research and Therapy, vol. 11, no. 1, pp. 1–10, 2020.

[68] Y. A. Wang, R. Neff, W. M. Song, X. Zhou, S. Vatansever, M. J. Walsh, S. H. Chen, B. Zhang, "Multi-omics-based analysis of high grade serous ovarian cancer subtypes reveals distinct molecular processes linked to patient prognosis," FEBS Open Bio, vol. 13, no. 4, pp. 617–637, 2023.

[69] T. Ishida, S. Nakao, T. Ueyama, Y. Harada, T. Kawamura, T, "Metabolic remodeling during somatic cell reprogramming to induced pluripotent stem cells: involvement of hypoxia-inducible factor 1," Inflammation and Regeneration, vol. 40, no. 8, 2020.

[70] J. B. Su, D. Q. Pei, B. M. Qin, "Roles of small molecules in somatic cell reprogramming," Acta Pharmacologica Sinica, vol. 34, no. 6, pp. 719–724, 2013.

[71] F. Schröter, J. Adjaye, "The proteasome complex and the maintenance of pluripotency: Sustain the fate by mopping up?" Stem Cell Research and Therapy, vol. 5, no. 1, p. 24, 2014.

[72] M. Bax, J. McKenna, D. Do-Ha, C. H. Stevens, S. Higginbottom, R. Balez, M. E. C. Cabral-da-Silva, N. E. Farrawell, M. Engel, P. Poronnik, J. J. Yerbury, D. N. Saunders, L. Ooi, "The ubiquitin proteasome system is a key regulator of pluripotent stem cell survival and motor neuron differentiation," Cells, vol. 8, no. 6, p. 581, 2019.

[73] E. Aleo, C. J. Henderson, A. Fontanini, B. Solazzo, C. Brancolini, "Identification of new compounds that trigger apoptosome-independent caspase activation and apoptosis," Cancer Research, vol. 66, no. 18, pp. 9235–9244, 2006.

[74] T. D. Lebedev, E. R. Vagapova, V. S. Prassolov, "The different impact of ERK inhibition on neuroblastoma, astrocytoma, and rhabdomyosarcoma cell differentiation," Acta Naturae, vol. 13, no. 4, pp. 69–77, 2021.

[75] J. K. Kim, L. G. Villa-Diaz, T. L. Saunders, R. P. Saul, S. Timilsina, F. Liu, Y. Mishina, P. H. Krebsbach, "Selective inhibition of mTORC1 signaling supports the development and maintenance of pluripotency," Stem Cells, vol. 42, no. 1, pp. 13–28, 2024.

[76] H. Kobayashi, H. Nishimura, N. Kudo, H. Osada, M. Yoshida, "A novel GSK3 inhibitor that promotes self-renewal in mouse embryonic stem cells," Bioscience, Biotechnology, and Biochemistry, vol. 84, no. 10, pp. 2113–2120, 2020.

[77] Y. Wu, Z. Ai, K. Yao, L. Cao, J. Du, X. Shi, Z. Guo, Y. Zhang, "CHIR99021 promotes self-renewal of mouse embryonic stem cells by modulation of protein-encoding gene and long intergenic non-coding RNA expression," Experimental Cell Research, vol. 319, vol. 17, pp. 2684–2699, 2013.

[78] N. Sato, L. Meijer, L. Skaltsounis, P. Greengard, A. H. Brivanlou, "Maintenance of pluripotency in human and mouse embryonic stem cells through activation of Wnt signaling by a pharmacological GSK-3-specific inhibitor," Nature Medicine, vol 10, no. 1, pp. 55–63, 2004.

A New Series of Bis (Thiosemicarbazone) Derivatives: Synthesis, Spectroscopic Characterization, and Antioxidant Activities

Hasan Yakan[1*] (iD), Halit Muğlu[2] (iD)

[1] Ondokuz Mayis University, Faculty of Education, Department of Chemistry Education, Samsun, Türkiye, hasany@omu.edu.tr, ror.org/028k5qw24

[2] Kastamonu University, Faculty of Science and Art, Department of Chemistry, Kastamonu, Türkiye, hmuglu@kastamonu.edu.tr, ror.org/015scty35

*Corresponding Author

ARTICLE INFO

ABSTRACT

New bis (thiosemicarbazone) derivatives (**1-5**) were obtained from thiophene-2,5-dicarbaldehyde and numerous thiosemicarbazides. The thiosemicarbazides were prepared various isothiocyanates and hydrazine monohydrate. The structure elucidation of all obtained products were determined *via* routine spectroscopic techniques, including proton and carbon NMR (^1H, ^{13}C), Fourier-transform infrared spectroscopy (FT-IR), and elemental composition analysis. In this research, the antioxidant activities of the newly synthesized compounds were assessed by the 1,1-diphenyl-2-picrylhydrazyl (DPPH) radical scavenging assay. Based on the percentage of inhibition, the IC_{50} values indicated the following order of activity: Trolox>**1**>**3**>**4**>**2**>**5**. Additionally, the reducing capabilities of the compounds were determined using the potassium ferricyanide reduction method. The absorbance values obtained from this assay for all the compounds were lower than that of Trolox, suggesting comparatively weaker reducing power. The study also explored how changes in molecular structure influence antioxidant activity, focusing especially on how various functional groups affect radical scavenging efficiency.

1. Introduction

The class of thiosemicarbazones holds substantial importance in synthetic organic chemistry, recognized for their organosulfur structure characterized by the –NH–C(=S)NH–N= functional group. Owing to their structural diversity, they serve as valuable intermediates used in the formation of diverse biologically relevant molecules. These compounds have been extensively studied for their broad spectrum of pharmacological and biological activities, including antimicrobial [1], antibacterial [2], antioxidant [3, 4], antitubercular [5], anticancer [6], antiviral [7], urease inhibitor [8], and anticonvulsant [9]. In recent years, numerous studies have focused on Schiff base-derived thiosemicarbazones due to their significant potential in biological assays conducted *in vitro* and *in vivo*. Such compounds have been reported significant antimicrobial [10], antibacterial and antifungal [11], antioxidant [12], enzyme inhibitory properties [13], anti-HIV [14], anticancer [15], ameliorative effect [16], and anti-inflammatory [17].

Reactive oxygen species (ROS) and free radicals have been extensively implicated in the onset and progression of numerous pathological conditions, including metabolic disorders, ischemia-reperfusion injury, chronic inflammation, aging-related cellular degeneration, and various forms of cancer [18-20]. The accumulation of these reactive species in biological systems disrupts redox homeostasis, contributing significantly to disease development. Consequently, antioxidants have garnered considerable attention due to their protective role in counteracting oxidative stress

and potentially reducing the risk of severe health conditions [19]. Schiff base derivatives containing thiophene ring and carbothioamide group can show significant antioxidant activity owing to the presence of conjugated π-systems and electron donating/withdrawing groups. In the literature, it has been reported that thiosemicarbazone derivatives, especially those with 2-thiophenylmethylene bond, give significant results in 1,1-diphenyl-2-picrylhydrazyl (DPPH) and (2,2′-azino-bis(3-ethylbenzothiazoline-6-sulfonic acid)) (ABTS) radical scavenging tests. For example, various aromatic Schiff base derivatives synthesized and showed increased free radical scavenging capacity with the presence of thiophene ring [21-23].

Schiff base derivatives with thiosemicarbazone structure and conjugated with aromatic rings can show significant reductive antioxidant properties due to their capacity to reduce iron (III) ions. It is reported that sulfur and nitrogen atoms, especially in compounds containing thiophene ring, facilitate electron transfer by providing coordination with Fe^{3+} ions and increase the reducing capacity [24-26]. In a study, it was reported that some thiosemicarbazone derivatives carrying thiophene and phenyl groups exhibited high iron reducing power by the FRAP (Ferric Reducing Antioxidant Power) method [26, 27].

In this study, a series of bis (thiosemicarbazone) derivatives were obtained and thoroughly elucidated using spectroscopic methods (FT-IR, ^{1}H-NMR, ^{13}C-NMR), and elemental analysis. Antioxidants play a crucial role in neutralizing free radicals and mitigating their harmful effects in the human body. Therefore, the antioxidant properties of these compounds were assessed *in vitro* using the DPPH· free radical scavenging assay. The effectiveness of each compound was calculated by determining its IC$_{50}$ value. In addition, the potassium ferricyanide reduction technique was employed to determine the reducing potential of these compounds. Moreover, the investigation examined how variations in molecular structure affect antioxidant performance, with particular emphasis on the impact of different groups on the efficiency of radical scavenging.

2. General Methods

2.1. Materials

All chemicals were acquired from Merck, Sigma, or Aldrich Chemical Company and used as received without further purification. Elemental analyses were performed using a Eurovector EA3000-Single analyzer. Melting points were determined using a Stuart SMP30 melting point apparatus and are reported without correction.

A Bruker Alpha spectrometer was used to obtain the FT-IR spectra. The ^{1}H and ^{13}C NMR spectra in DMSO-d_6 were recorded on a Bruker Avance DPX-400 MHz spectrometer. UV–Vis absorption spectra were measured using a Shimadzu Pharmaspec 1700 spectrophotometer. NMR signal multiplicities are abbreviated as follows: s (singlet), d (doublet), dd (doublet of doublets), t (triplet), and m (multiplet).

2.2. Synthesis of bis (thiosemicarbazones)

A mixture of various isothiocyanates (7.50 mmol) and hydrazine monohydrate (7.50 mmol) was added dropwise to 20 mL of ethanol under vigorous stirring while maintaining the temperature in an ice bath. Refrigeration of the reaction mixture overnight resulted in the precipitation of the thiosemicarbazide product, which was isolated by filtration, dried, and purified using ethanol.

Subsequently, a few drops of HCl were added to a solution of the thiosemicarbazides (4.00 mmol) and thiophene-2,5-dicarbaldehyde (2.00 mmol) in 20 mL of aqueous ethanol, refluxed at 78 °C for 3 to 5 hours. After completion, the solid product was isolated by filtration, washed, and air-dried. The successful synthesis of the target compounds, obtained in good yields (62–89%), is illustrated in Scheme 1. The procedure followed was adapted from previously reported methods with slight modifications [28, 29].
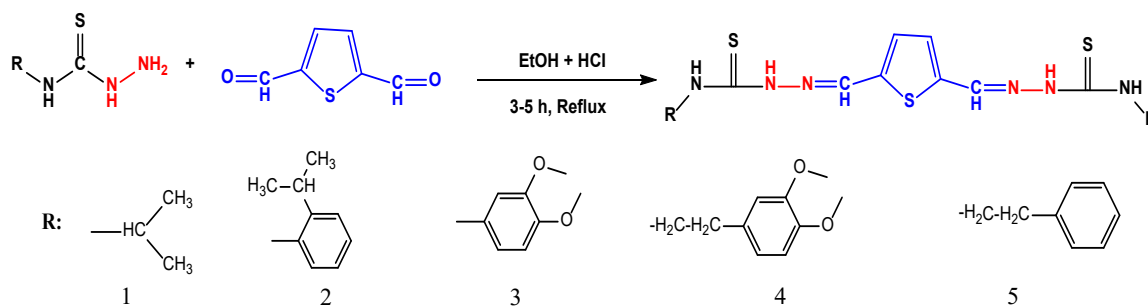
Scheme 1. Synthesis pathway of bis (thiosemicarbazone) derivatives (**1-5**)

2.3. Antioxidant activity by DPPH assay

A slightly modified version of a previously described method was employed to assess the antioxidant activity of the compounds [30-32]. A 1.0 mL aliquot of DPPH solution (0.1 mM) was mixed with 3.0 mL of the test compound solutions prepared in acetone at various concentrations (4.83–48.33 µM). The samples were kept in the dark at room temperature for 30 minutes, after which their absorbance was recorded at 517 nm using a UV-Vis spectrophotometer [33]. Butylated hydroxyanisole (BHA) was used as a standard antioxidant for comparison.

Lower absorbance values correspond to a higher DPPH· free radical scavenging capacity. The activity of the sample compounds was calculated as percentage inhibition and then compared to the standard (BHA). Percentage inhibition of DPPH radicals by the compounds was computed according to the equation below:

$$\text{Radical scavenging activity (\%)} = [(A_c - A) / A_c \times 100]$$

where A_c is the absorbance of the control (without sample) and A is the absorbance of the test compound or standard [34].

In addition to experimental measurements, the half-maximal inhibitory concentration (IC_{50}) values were determined using calibration curves for each compound. IC_{50} represents the concentration required to inhibit 50% of DPPH radicals under the tested conditions. This value serves as a common quantitative marker of antioxidant capacity, as lower IC_{50} values indicate that less compound is needed to achieve the same inhibitory effect. Thus, a decrease in IC_{50} directly demonstrates an improvement in the antioxidant potential of the tested sample [35].

2.4. Potassium ferricyanide reduction method

In an effort to determine the antioxidant capabilities of the compounds, the potassium ferricyanide reduction method was applied. This method is based on the reduction of $[Fe(CN)_6]^{3-}$ ions to $[Fe(CN)_6]^{4-}$ form and the subsequent formation of Prussian blue $(Fe[Fe(CN)_6]^-)$ complexes in the presence of Fe(III) ions in the medium. The absorbances of the formed complexes are usually measured at a wavelength of 700 nm and evaluated [25, 36].

In this study, firstly, 1 mL of 58×10^{-5} M DMSO solution of each compound was taken as a sample to determine the reducing capacity of the compounds. Then, 1.25 mL of 0.2 M pH 6.5 phosphate buffer and 1.25 mL of potassium ferricyanide (1 g/100 mL) solution were added, respectively. Following a 20 minutes incubation at 50 °C, 1.25 mL of 10% trichloroacetic acid was incorporated into the mixture, which was then centrifuged at 3000 rpm for 10 minutes at room temperature.

The supernatant obtained after centrifugation was first diluted with 2.5 mL of distilled water, then 0.25 mL of 1% ferric chloride solution was added. After this new mixture was incubated at 37 °C for 10 minutes, the iron (Fe^{3+}) reducing powers of the compounds were determined by measuring the absorbance values at 700 nm wavelength [37, 38].

3. Results and Discussion

3.1. Physicochemical data

Presented in Tables 1 and 2 are the experimental findings related to physicochemical properties, yields, melting points, and elemental analyses.

Table 1. The physicochemical data of the products

	M.P. (°C)	Yields (%)	Colour	Mol. Formula	M.W. (g/mol)
1	245-246	70	Dark Yellow	$C_{14}H_{22}N_6S_3$	370
2	213-214	89	Yellow	$C_{26}H_{30}N_6S_3$	522
3	186-187	86	Orange	$C_{24}H_{26}N_6O_4S_3$	558
4	212-213	88	Yellow	$C_{28}H_{34}N_6O_4S_3$	614
5	247-248	62	Dark Yellow	$C_{24}H_{26}N_6S_3$	494

Table 2. Elemental analysis results of the products

	Calculated			Experimental		
Comp.	C%	H%	N%	C%	H%	N%
1	45.38	5.98	22.68	45.42	6.00	22.71
2	59.74	5.78	16.08	59.81	5.79	16.06
3	51.59	4.69	15.04	51.57	4.68	15.02
4	54.70	5.57	13.67	54.78	5.57	13.63
5	58.27	5.30	16.99	58.22	5.29	17.03

3.2. IR spectral analysis

Analysis of the FT-IR spectra of the synthesized compounds revealed that the characteristic asymmetric and symmetric stretching vibrations of the amino group ($-NH_2$), typically observed as a doublet peak between 3500 and 3350 cm^{-1}, were absent. Additionally, the aldehyde stretching bands (–CHO) of thiophene-2,5-dicarbaldehyde, normally found between 2820 and 2700 cm^{-1}, were not detected. Instead, a new vibration corresponding to the imine group (CH=N) appeared prominently in the range of 1538–1506 cm^{-1}, confirming the successful formation of the target products (see Figures S1–S5 in the Supplementary Information).

Table 3. IR frequencies of the compounds (cm^{-1})
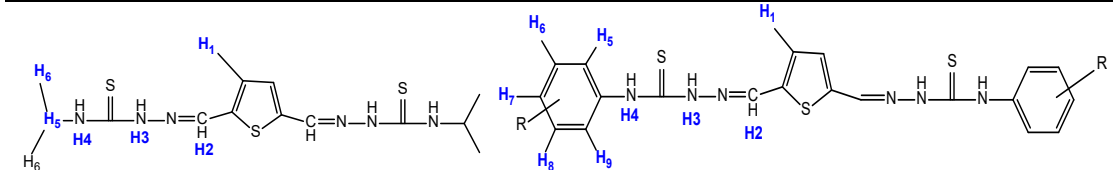
Comp.	υ_{NH}	$\upsilon_{C=N}$	$\upsilon_{C=S}$	υ_{C-N}	υ_{C-S}
1	3333, 3114	1536	1384	1211	774
2	3350, 3133	1532-1506	1381	1249	701
3	3339, 3116	1534-1509	1382	1219	718
4	3336, 3104	1529-1510	1355	1209	726
5	3346, 3136	1538-1512	1452	1213	804

For all compounds (**1–5**), the presence of a novel amine group (–NH) stretching vibration was observed between 3350 and 3104 cm^{-1}. Aromatic proton vibrations appeared in the 2999–2931 cm^{-1} range, while aliphatic proton vibrations were detected between 2924 and 2812 cm^{-1}. The characteristic –C=S stretching bands of the thiosemicarbazone moiety were found at 1452–1355 cm^{-1}, and the –C–N stretching vibrations appeared in the range of 1249–1209 cm^{-1}. Additionally, the –C–S vibrations were observed between 804 and 701 cm^{-1}. Notably, compounds **3** and **4** exhibited C–O stretching signals at 1022 and 1023 cm^{-1}, respectively. These spectral data are consistent with previously reported values for structurally related compounds [39-41]. Key FT-IR vibration frequencies for all compounds are summarized in Table 3.

3.3. ^{1}H NMR analysis

Chemical shifts from the ^{1}H NMR spectra of the compounds, recorded in DMSO-d_6 are summarized in Table 4.

Table 4. ^{1}H NMR data of the compounds, (δ/ppm)

Comp.	H1	H2	H3	H4	H5-H9
1	7.43 (s,1H)	8.22 (s, 1H)	11.55 (s, 1H)	7.79-7.77 (d, 1H)	4.55 – 4.45 (m, 1H, H5), 1.23-1.22 (d, J = 6.6 Hz, 6H, H6)
2	7.53 (s,1H)	8.29 (s, 1H)	11.96 (s, 1H)	9.57 (s, 1H)	7.37 – 7.16 (m, 4H)
3	7.51 (s,1H)	8.31 (s, 1H)	11.92 (s, 1H)	9.66 (s, 1H)	7.20 (s, 1H), 7.05-7.02 (d, J = 8.6 Hz, 1H), 6.93-6.90 (d, J = 8.7 Hz, 1H)
4	7.41 (s,1H)	8.21 (s, 1H)	11.67 (s, 1H)	8.09-8.07 (t, J = 5.5 Hz, 1H)	6.89 – 6.76 (m, 3H)
5	7.43 (s,1H)	8.22 (s, 1H)	11.69 (s, 1H)	8.24-8.22 (t, 1H)	7.35-7.20 (m, 5H)

For compounds **1-5**, aromatic proton signal (H1) of the thiophene ring was detected as a singlet at 7.53-7.41 ppm, the proton signal of imine (–CH=N, H2) was detected as a singlet in the ranges 8.31-8.21 ppm. When the amino signal (-NH, H3) of thiosemicarbazone moiety was observed as a singlet in the ranges 11.96-11.55 ppm, the amino signal (-NH, H4) was resonated as a doublet, singlet, and triplet at 9.66-7.77 ppm, respectively (see at Figures S6-S10 in Supplementary information).

For compound **1**, the –CH and –(CH$_3$)$_2$ protons of the isopropyl group were resonated as a multiplet/heptet and doublet in the ranges 4.55-4.45 and 1.23-1.22 ppm, respectively. The each –OCH$_3$ proton signals of compounds **3** and **4** were observed as a singlet at 3.75, 3.72, 3.73, and 3.69 ppm, respectively. For compounds **4** and **5**, the proton signal of the methylene group (N–CH$_2$) was observed as a quartet at 3.82–3.77 and 3.78-3.73 ppm (q, 2H); the –CH$_2$ proton signal was detected as a triplet at 2.87–2.83 and 2.93-2.89 ppm (t, 2H). For compounds **2-5**, aromatic proton signal (H5-H9) of the phenyl ring was detected at 7.37-6.76 ppm. The chemical shifts observed correspond closely to previously published data for related compounds [39-41]. DMSO-d_6 and water in DMSO (HOD, H$_2$O) signals were detected at approximately 2.50 ppm (quintet) and around 3.30 ppm, respectively, with the latter varying depending on solvent conditions and concentration [42].

3.4. ^{13}C NMR interpretations

Table 5 presents the ^{13}C NMR chemical shifts of the synthesized compounds recorded in in DMSO-d_6. For compounds **1**–**5**, the characteristic –C=S peaks (C4) of the thiosemicarbazone moiety were detected at 177.53–175.90 ppm. The characteristic –CH=N (imine, C3) peaks were observed in the ranges 141.09-140.70 ppm. The aromatic proton signals (C1 and C2) of the thiophene ring were detected at 131.77-131.52 and 137.74-137.40 ppm (figures S11-S15 in supplementary information).

For compound **1**, the –CH and –(CH$_3$)$_2$ carbon atoms of the isopropyl group were observed at 46.09 and 22.36 ppm, respectively.

For compounds **2-5**, aromatic carbon atoms (C5-C10) of the phenyl ring was detected at 149.19-110.85 ppm. The C5 carbon atom of the compounds **2-5** was detected at 139.61-131.94 ppm.

For compounds **3** and **4**, the C7 and C8 carbon atoms (149.19-147.02 ppm) were shifted down-field (high values of δ) relative to the signal of phenyl carbon (128.5 ppm) due to the presence of methoxy (–OCH$_3$) group. The each –OCH$_3$ carbon atom signals of compounds **3** and **4** were observed at 56.12, 56.02, 55.93, and 55.79 ppm, respectively.

For compounds **4** and **5**, the carbon atom signal of the methylene group (N–CH$_2$) was detected at 45.54 and 45.64 ppm; the –CH$_2$ proton signal was observed at 34.64 and 35.28 ppm. The values observed align with those found in earlier studies on similar compounds [39-41].

Table 5. ^{13}C NMR data of the compounds, (δ/ppm)

	C1	C2	C3	C4	C5-C10	R
1	131.5	137.4	140.7	175.9	46.09 22.36	-
2	131.6	137.6	141.1	177.5	136.9 145.7 129.4 126.1 127.7 126.0	28.2, 23.6
3	131.8	137.7	141.1	176.1	132.3 110.9 148.5 147.0 111.6 118.2	56.1, 56.0
4	131.7	137.5	140.8	177.0	131.9 112.5 149.2 147.8 112.8 120.9	55.9, 55.8, 45.5, 34.6
5	131.5	137.5	140.9	177.1	139.6 128.9 129.1 126.7 129.1 128.9	45.6, 35.3

3.5. Evaluation of antioxidant activity

The molecules synthesized in the study were studied against different concentrations using the DPPH radical quenching method. The antioxidant activities were compared with the help of the obtained (%) inhibition data in Figure 1. In the study where Trolox was used as the standard antioxidant, it was determined that the (%) inhibition values of the molecules increased regularly with the increase in concentration. As understood from the data in Figure 1, it can be said that especially compound **1** and **3** exhibited a significant increase in inhibition.

Additionally, IC$_{50}$ (mg/mL) values and linear regression equations used to compare the antioxidant activities of the synthesized compounds and Trolox are given in Table 6. When Table 6 is examined, we can say that some synthesized molecules show IC$_{50}$ values almost close to Trolox. In particular, it is seen that the values found for the DPPH radical reduction capacity of Trolox (16.62±0.15 μM) and for compound **1** (23.38±0.17) are close. IC$_{50}$ data show that compound **1** exhibits the highest antioxidant activity, while compound **5** exhibits the lowest antioxidant activity.
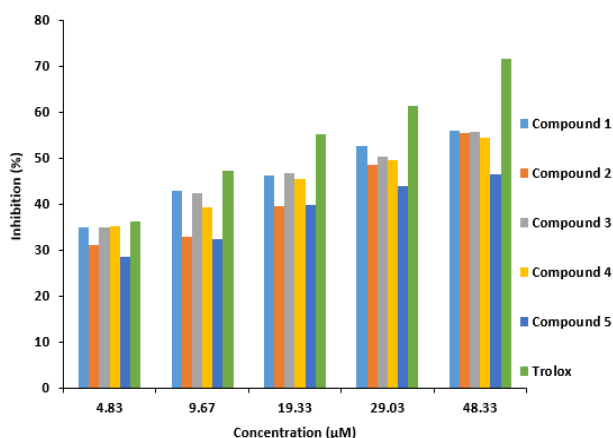
Figure 1. % Inhibition graph of all compounds (**1-5**)

Table 6. IC$_{50}$ values of Trolox and all compounds

Comp.	Linear Concentration equation (y=ax±b)	IC$_{50}$ (μM)	R^2
1	y=0.45x+39.39	23.38±0.17	0.879
2	y=0.59x+28.35	36.70±0.25	0.970
3	y=0.44x+36.31	31.44±0.21	0.902
4	y=0.43x+35.07	34.53±0.23	0.938
5	y=0.41x+28.97	50.76±0.37	0.874
Trolox	y=0.76x+37.41	16.62±0.15	0.934

In the compounds we synthesized in this study, the redox properties of the thiocarbamoyl group (–NH–C(=S)–NH–) are thought to play an important role in the antioxidant mechanism. In particular, the 2-ethylidene-*N*-isopropylhydrazine-1-carbothioamide group in the position attached to the thiophene structure is responsible for the effective antioxidant activity of compound **1**. This situation has been emphasized in previous studies and it has been stated that aliphatic chains such as the isopropyl group increase the lipophilicity of the molecule, facilitate its interaction with biological membrane surfaces and thus contribute to antioxidant activity [43-45].

3.6. Potassium ferricyanide total reduction method evaluation

In this study, the compounds synthesized were compared in terms of their reducing power using the potassium ferricyanide reduction method. The measured absorbance values are given in Figure 2 against concentration in comparison with Trolox. Absorbances for all compounds increased linearly with concentration.

Accordingly, all compounds showed low reducing power compared to Trolox. As in the IC$_{50}$ values we used for DPPH radical quenching activities for the compounds, it was seen that the reducing powers of the compounds gave similar results. Among these, compound **3** and **4**, which contain methoxy substituent groups, showed similar reducing power, while compound **5**, which does not contain any substituent attached to the aromatic ring, showed the lowest reducing power.
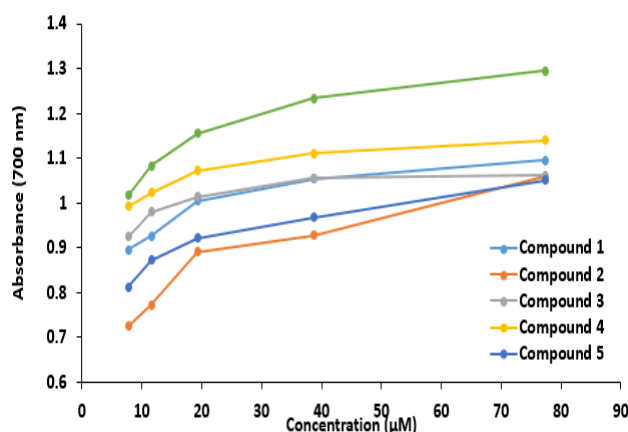
Figure 2. Total reducing power of the synthesized compounds and Trolox for potassium ferricyanide

In a study, alkyl side chains such as isopropyl increase the overall lipophilicity of the molecule, facilitate interaction with metal ions and support reducing behavior [27]. In such compounds, as in this study, C=N and C=S groups create electron donor sites with high redox potential, effectively reducing Fe^{3+} ions to the Fe^{2+} form.

4. Conclusion

A series of new bis (thiosemicarbazone) derivatives) were successfully synthesized and isolated in acceptable yields ranging from 62% to 89%. All synthesized compounds were structurally characterized by IR, ^{1}H NMR, ^{13}C NMR, and elemental analysis. Their antioxidant properties were tested *in vitro* using the DPPH assay, revealing IC_{50} values in the range of 23.38±0.17 to 50.76±0.37 μM. The comparative analysis of IC_{50} values, calculated from inhibition data, indicated that the antioxidant potential decreased in the order: Trolox > **1** > **3** > **4** > **2** > **5**. Among the tested derivatives, compound **1** exhibited the most potent antioxidant activity against the DPPH radical.

The molecules in this study exhibited free radical scavenging ability similar to Trolox, a standard industrial antioxidant, even at low concentrations. In conclusion, *N*-isopropyl-2-(thiophen-2-ylmethylene)hydrazine-1-carbothioamide-like structures are among the promising antioxidant agents due to both their structural and electronic properties. In addition, compound **1**-like structures seem to have remarkable potential in terms of antioxidant mechanisms based on metal reduction. Overall, these results provide valuable insight into the design of more effective antioxidant agents within the bis (thiosemicarbazone) structural framework and highlight the importance of electronic effects in modulating biological activity.

Article Information Form

Authors' Contribution
H.Y.; Formal analysis, investigation, writing – original draft, data curation, concept/design, data analysis, validation, writing – review & editing, visualization. H.M.; Investigation, methodology, data analysis, validation, writing – original draft, data curation. All authors reviewed the manuscript.

The Declaration of Conflict of Interest/ Common Interest
No conflict of interest or common interest has been declared by authors.

Artificial Intelligence Statement
No artificial intelligence tools were used while writing this article.

References

[1] M. G. Gündüz, B. Kaya, C. Özkul, O. Şahin, E. M. Rekha, D. Sriram, B. Ülküseven, "S-alkylated thiosemicarbazone derivatives: Synthesis, crystal structure determination, antimicrobial activity evaluation and molecular docking studies," Journal of Molecular Structure, vol. 1242, p. 130674, 2021.

[2] H. Govender, C. Mocktar, H. M. Kumalo, N. A. Koorbanally, "Synthesis, antibacterial activity and docking studies of substituted quinolone thiosemicarbazones," Phosphorus, Sulfur, and Silicon and the Related Elements, vol. 194, no. 11, pp. 1074-1081, 2019.

[3] W. Hernández, F. Carrasco, A. Vaisberg, E. Spodine, M. Icker, H. Krautscheid, L. Beyer, C. Tamariz-Angeles, P. Olivera-Gonzales, "Novel thiosemicarbazone derivatives from furan-2-carbaldehyde: synthesis, characterization, crystal structures, and antibacterial, antifungal, antioxidant, and antitumor activities,"

Journal of Chemistry, vol. 2023, pp. 1-20, 2023.

[4] M. S. Çavuş, "Synthesis of new 5-iodoisatin derivatives: Predicting antioxidant inhibition activity with DFT studies," Journal of Molecular Structure, vol. 1323, p. 140826, 2025.

[5] P. P. Netalkar, S. P. Netalkar, V. K. Revankar, "Nickel (II) complexes of thiosemicarbazones: Synthesis, characterization, X-ray crystallographic studies and in vitro antitubercular and antimicrobial studies," Transition Metal Chemistry, vol. 39, pp. 519-526, 2014.

[6] B. Shakya, P. N. Yadav, "Thiosemicarbazones as potent anticancer agents and their modes of action," Mini Reviews in Medicinal Chemistry, vol. 20, no. 8, pp. 638-661, 2020.

[7] Z. Ş. Sevinçli, G. N. Duran, M. Özbil, N. Karalı, "Synthesis, molecular modeling and antiviral activity of novel 5-fluoro-1H-indole-2, 3-dione 3-thiosemicarbazones," Bioorganic Chemistry, vol. 104, p. 104202, 2020.

[8] H. Pervez, N. Manzoor, M. Yaqub, A. Khan, K. M. Khan, F.-u.-H. Nasim, M. I. Choudhary, "Synthesis and urease inhibitory properties of some new N4-substituted 5-nitroisatin-3-thiosemicarbazones," Letters in Drug Design & Discovery, vol. 7, no. 2, pp. 102-108, 2010.

[9] A. Kshirsagar, M. P. Toraskar, V. M. Kulkarni, S. Dhanashire, V. Kadam, "Microwave assisted synthesis of potential anti infective and anticonvulsant thiosemicarbazones," International Journal of ChemTech Research, vol. 1, no. 3, pp. 696-701, 2009.

[10] A. A. Al-Amiery, Y. K. Al-Majedy, H. H. Ibrahim, A. A. Al-Tamimi, "Antioxidant, antimicrobial, and theoretical studies of the thiosemicarbazone derivative Schiff base 2-(2-imino-1-methylimidazolidin-4-ylidene) hydrazinecarbothioamide (IMHC)," Organic and Medicinal Chemistry Letters, vol. 2, no. 1, p. 4, 2012.

[11] H. Pervez, M. S. Iqbal, M. Y. Tahir, F. H. Nasim, M. I. Choudhary, K. M. Khan, "In vitro cytotoxic, antibacterial, antifungal and urease inhibitory activities of some N^4-substituted isatin-3-thiosemicarbazones," Journal of Enzyme Inhibition and Medicinal Chemistry, vol. 23, no. 6, pp. 848-854, 2008.

[12] H. Muğlu, "Synthesis, characterization, and antioxidant activity of some new N^4-arylsubstituted-5-methoxyisatin-β-thiosemicarbazone derivatives," Research on Chemical Intermediates, pp. 1-16, 2020.

[13] F. S. Tokalı, P. Taslimi, H. Usanmaz, M. Karaman, K. Şendil, "Synthesis, characterization, biological activity and molecular docking studies of novel schiff bases derived from thiosemicarbazide: Biochemical and computational approach," Journal of Molecular Structure, vol. 1231, p. 129666, 2021.

[14] T. R. Bal, B. Anand, P. Yogeeswari, D. Sriram, "Synthesis and evaluation of anti-HIV activity of isatin β-thiosemicarbazone derivatives," Bioorganic & Medicinal Chemistry Letters, vol. 15, no. 20, pp. 4451-4455, 2005.

[15] M. A. Arafath, "Thiosemicarbazone Schiff base ligands and their complexes with nickel, palladium and platinum show anticancer and antibacterial activities," Journal of Sulfur Chemistry, vol. 45, no. 1, pp. 138-171, 2024.

[16] F. G. Karakuş, S. Tunalı, T. Bal-Demirci, B. Ülküseven, R. Yanardağ, "Ameliorative effect of a vanadium-thiosemicarbazone complex on oxidative stress in stomach tissue of experimental diabetic rats," Sakarya University Journal of Science, vol. 28, no. 1, pp. 133-144, 2024.

[17] G. Subhashree, J. Haribabu, S. Saranya, P. Yuvaraj, D. A. Krishnan, R. Karvembu, D. Gayathri, "In vitro antioxidant, antiinflammatory and in silico molecular docking studies of thiosemicarbazones," Journal of Molecular Structure, vol. 1145, pp. 160-169, 2017.

[18] J. Robak, E. Marcinkiewicz, "Scavenging of reactive oxygen species as the mechanism of drug action," Polish Journal of Pharmacology, vol. 47, no. 2, pp. 89-98, 1995.

[19] K. Krumova, G. Cosa, "Overview of reactive oxygen species," Singlet Oxygen: Applications in Biosciences and Nanosciences, vol. 1, pp. 1-21, 2016.

[20] L. Wang, Z. Kuang, D. Zhang, Y. Gao, M. Ying, T. Wang, "Reactive oxygen species in immune cells: A new antitumor target," Biomedicine and Pharmacotherapy, vol. 133, p. 110978, 2021.

[21] Y. Ünver, K. Sancak, F. Çelik, E. Birinci, M. Küçük, S. Soylu, N. A. Burnaz, "New thiophene-1, 2, 4-triazole-5 (3)-ones: Highly bioactive thiosemicarbazides, structures of Schiff bases and triazole–thiols," European Journal of Medicinal Chemistry, vol. 84, pp. 639-650, 2014.

[22] A. Bhardwaj, A. Dubey, A. Tufail, N. Tufail, M. Kumar, S. Garg, "Unveiling the biomedical potential of thiophene-derived Schiff base complexes: A comprehensive study of synthesis, spectral characterization, antimicrobial efficacy, antioxidant activity, and computational insights," Applied Organometallic Chemistry, vol. 38, no. 5, p. e7398, 2024.

[23] K. Ozturk, M. S. Tanyildizi, H. Ciftci, O. G. Aytac, "Synthesis of thiophene-based imine and phosphoazometine compounds: in vitro antiproliferative, antimicrobial, antioxidant, carbonic anhydrase I and II enzyme inhibition evaluations and molecular docking study," Chemical Papers, pp. 1-17, 2025.

[24] R. Apak, K. Güçlü, B. Demirata, M. Özyürek, S. E. Çelik, B. Bektaşoğlu, K. I. Berker, D. Özyurt, "Comparative evaluation of various total antioxidant capacity assays applied to phenolic compounds with the CUPRAC assay," Molecules, vol. 12, no. 7, pp. 1496-1547, 2007.

[25] İ. Gülçin, "Fe^{3+} – Fe^{2+} transformation method: An important antioxidant assay," in Advanced Protocols in Oxidative Stress III: Springer, pp. 233-246, 2014.

[26] A. Mermer, S. Alyar, "Synthesis, characterization, DFT calculation, antioxidant activity, ADMET and molecular docking of thiosemicarbazide derivatives and their Cu (II) complexes," Chemico-Biological Interactions, vol. 351, p. 109742, 2022.

[27] M. M. F. Leal, M. F. D. Silva, D. S. C. Marques, R. F. V. Mendes, R. M. Ximenes, D. C. Machado, J. J. D. Silva, C. G. Rodrigues, I. J. D. C. Filho, M. D. C. A. D. Lima, "Preliminary evaluation of the toxicological, antioxidant and antitumor activities promoted by the compounds 2, 4-dihydroxy-benzylidene-thiosemicarbazones an in silico, in vitro and in vivo study," Anais da Academia Brasileira de Ciências, vol. 96, no. 2, p. e20231247, 2024.

[28] Y. M. Zhang, D. D. Wang, Q. Lin, T. B. Wei, "Synthesis and anion recognition properties of thiosemicarbazone based molecular tweezers," Phosphorus, Sulfur, and Silicon and the Related Elements, vol. 183, no. 1, pp. 44-55, 2007.

[29] H. Yakan, "Preparation, structure elucidation, and antioxidant activity of new bis (thiosemicarbazone) derivatives," Turkish Journal of Chemistry, vol. 44, no. 4, p. 1085, 2020.

[30] W. Brand-Williams, M. E. Cuvelier, C. Berset, "Use of a free radical method to evaluate antioxidant activity," LWT-Food Science and Technology, vol. 28, no. 1, pp. 25-30, 1995.

[31] F. Sönmez, E. Akgün, Z. Şahin, "Synthesis, DPPH and ABTS activity of novel furfuryl-chalcone derivatives," Sakarya University Journal of Science, vol. 26, no. 6, pp. 1224-1232, 2022.

[32] N. T. Karakullukçu, "The Impact of Hypericum perforatum L. as an Organic Free-Radical Scavenger in Biodiesel-Diesel Blends," Sakarya University Journal of Science, vol. 29, no. 1, pp. 100-112, 2025.

[33] V. Bondet, W. Brand-Williams, C. Berset, "Kinetics and mechanisms of antioxidant activity using the DPPH. free radical method," LWT-Food Science and Technology, vol. 30, no. 6, pp. 609-615, 1997.

[34] N. Naik, H. Vijay Kumar, P. B. Vidyashree, "Synthesis and evaluation of antioxidant potential of novel isatin analogues," Journal of Pharmacy Research, vol. 4, no. 8, pp. 2686-2689, 2011.

[35] E. N. Frankel, A. S. Meyer, "The problems of using one-dimensional methods to evaluate multifunctional food and biological antioxidants," Journal of the Science of Food and Agriculture, vol. 80, no. 13, pp. 1925-1941, 2000.

[36] F. Afroze, M. T. Hossain, "Proximate analysis, phytochemical screening and antioxidant activity of Psidium guajava leaves growing in coastal area of Bangladesh," World Journal of Pharmacy and Pharmaceutical Sciences, vol. 4, no. 5, pp. 140-51, 2015.

[37] M. Oyaizu, "Studies on products of browning reaction antioxidative activities of products of browning reaction prepared from glucosamine," The Japanese Journal of Nutrition and Dietetics, vol. 44, no. 6, pp. 307-315, 1986.

[38] T. K. Bakır, "New 5-methylisatin-thiosemicarbazones: preparation, spectroscopic study and antioxidant properties," Research on Chemical Intermediates, vol. 50, no. 11, pp. 5593-5615, 2024.

[39] A. A. Al-Amiery, Y. K. Al-Majedy, H. H. Ibrahim, A. A. Al-Tamimi, "Antioxidant, antimicrobial, and theoretical studies of the thiosemicarbazone derivative Schiff base 2-(2-imino-1-methylimidazolidin-4-ylidene) hydrazinecarbothioamide (IMHC)," Organic and Medicinal Chemistry Letters, vol. 2, no. 4, pp. 1-7, 2012.

[40] H. Yakan, M. Azam, S. Kansız, H. Muğlu, M. Ergül, P. Taslimi, Ü. M. Koçyiğit, M. Karaman, S. I. Al-Resayes, K. Min, "Isatin/thiosemicarbohydrazone hybrids: Facile synthesis, and their evaluation as anti-proliferatıve agents and metabolıc enzyme inhibitors," Bulletin of the Chemical Society of Ethiopia, vol. 37, no. 5, pp. 1221-1236, 2023.

[41] H. Yakan, H. Muğlu, C. Türkeş, Y. Demir, M. Erdoğan, M. S. Çavuş, Ş. Beydemir, "A novel series of thiosemicarbazone hybrid scaffolds: Design, synthesis, DFT studies, metabolic enzyme inhibition properties, and molecular docking calculations," Journal of Molecular Structure, vol. 1280, p. 135077, 2023.

[42] I. Fleming, D. Williams, Spectroscopic methods in organic chemistry, Seventh Edition ed. Switzerland: Springer Nature, 2020.

[43] S. F. Barbuceanu, D. C. Ilies, G. Saramet, V. Uivarosi, C. Draghici, V. Radulescu, "Synthesis and antioxidant activity evaluation of new compounds from hydrazinecarbothioamide and 1, 2, 4-triazole class containing diarylsulfone and 2, 4-difluorophenyl moieties," International Journal of Molecular Sciences, vol. 15, no. 6, pp. 10908-10925, 2014.

[44] S. Eğlence-Bakır, "Synthesis and antioxidant activities of new nickel (II) complexes derived from 4-

benzyloxysalicylidene-S-methyl/propyl thiosemicarbazones," Turkish Journal of Chemistry, vol. 45, no. 3, pp. 835-844, 2021.

[45] F. Qi, Q. Qi, J. Song, J. Huang, "Synthesis, Crystal Structure, Biological Evaluation and in Silico Studies on Novel (E)-1-(Substituted Benzylidene)-4-(3-isopropylphenyl) thiosemicarbazone Derivatives," Chemistry & Biodiversity, vol. 18, no. 2, p. e2000804, 2021.

Investigation of Hydrogen Adsorption Mechanism on Activated Carbon Surface Using Isotherm and Kinetic Models

Zeynep Bicil [iD]

Balıkesir University, Faculty of Science and Literature, Department of Chemistry, Balıkesir, Türkiye, zeynepbicil@balikesir.edu.tr, ror.org/02tv7db43
*Corresponding Author

ARTICLE INFO	ABSTRACT
	In this study, the hydrogen storage capacities and adsorption behaviors of activated carbons obtained from agricultural wastes such as tangerine peel and horse chestnut were investigated in detail. The carbons were synthesized by chemical activation using $ZnCl_2$ and characterized by BET surface area and pore analysis. The hydrogen storage capacities of activated carbons produced by chemical activation and carbonization processes were measured as a function of pressure at 77 K up to 80 bar. Horse chestnut-based activated carbon showed higher performance with a maximum hydrogen adsorption capacity of 4.47% at 80 bar, whereas tangerine peel-based activated carbon reached only 1.87% at 26 bar. Adsorption data were analyzed with Langmuir, Freundlich and Temkin isotherm models; the Langmuir model provided the highest fit ($R^2 > 0.99$) for both samples. In kinetic analyses, high correlation was obtained with pseudo-second-order and Weber–Morris models. The findings reveal the effectiveness of biomass-based activated carbons in the storage of hydrogen by physical adsorption and contribute to both theoretical and applied aspects of adsorption processes. In this respect, the study provides a scientific basis for the development of environmentally friendly and low-cost adsorbents that can be used in sustainable energy technologies.

1. Introduction

Energy is the driving force of industrialization as one of the fundamental dynamics of economic development and social welfare today. With population growth, industrialization and technological developments, energy demand is increasing rapidly; this situation necessitates a shift towards sustainable, environmentally friendly and economical energy sources [1]. Energy sources are generally divided into two main categories: renewable and non-renewable. The limited reserves of fossil fuels, environmental damage and market instabilities increase the interest in alternative solutions [2]. In this context, renewable energy sources such as solar, wind, geothermal, biomass and hydrogen are considered as strategic options in terms of environmental sustainability and energy security [3, 4].

The use of renewable resources plays an active role in combating climate change by reducing greenhouse gas emissions. In addition, it is important for the continuity of energy supply that resources such as solar and wind are not limited to direct electricity production but also used in the production of storable energy carriers [5]. In this context, hydrogen is a prominent energy carrier thanks to its high energy density of 120 MJ/kg, its clean combustion product that produces only water vapor, and its diverse production methods [6, 7].

However, making hydrogen usable in practice requires the development of efficient and safe storage technologies. Current hydrogen storage methods are divided into three main groups: compression under high pressure in the gas phase, condensation at low temperatures in the

liquid phase, and chemical or physical adsorption in the solid phase [8]. Each of these methods has its own advantages and limitations. For example, high-pressure gas storage systems require complex engineering infrastructure, while liquefied hydrogen systems have high energy costs due to the extremely low temperature requirement of -253 °C. Although chemical storage methods (e.g. metal hydrides) can reach high capacities, they are limited in terms of reversibility and reaction kinetics. Therefore, solid-phase physical adsorption has been considered as an alternative that has attracted great interest in recent years due to its low energy requirement, rapid recovery, safe transportation and environmentally friendly nature [9].

The main adsorbent materials in physical adsorption-based hydrogen storage systems are metal-organic frameworks (MOF), zeolites, boron hydrides, carbides and carbon derivatives [7, 10-14]. Among these groups, carbon-based adsorbents are prominent candidates with their high surface area, low cost, chemical stability and structureable pore properties [1, 15-16]. In addition, activated carbons obtained by carbonizing agricultural wastes offer additional advantages in terms of environmental sustainability and circular economy principles [17, 18].

In recent years, the hydrogen adsorption properties of activated carbons produced from biomass sources such as tangerine peel [16], olive leaf [7], coconut shell [19], almond shell [1] and horse chestnut shell [18] have been investigated. However, in these studies, only the storage capacity is usually reported, and adsorption isotherms and kinetic behaviors are not analyzed. Nevertheless, these parameters play a critical role in understanding the interaction of hydrogen with the surface and the adsorptive efficiency of the system [20]. Thus, the aim of this study is to fill this literature gap and to investigate in detail the hydrogen storage behaviors of activated carbons obtained from tangerine peel and horse chestnut in terms of both capacity and adsorption kinetics.

Adsorption processes were analyzed using Langmuir, Freundlich and Temkin isotherm models and several kinetic models (pseudo-first-order, pseudo-second-order, Boyd, Avrami and Weber–Morris). The results showed that horse chestnut–based activated carbon exhibited a higher hydrogen storage capacity (4.47 wt. % at 80 bar) compared to tangerine peel–based carbon, and the Langmuir and pseudo-second-order models best explained the adsorption behavior. These findings highlight that biomass-derived carbons can be effective and sustainable candidates for hydrogen storage applications.

2. General Methods

In this study, two different biomass sources, horse chestnut and tangerine peel, were used to produce activated carbon. Zinc chloride ($ZnCl_2$) used as the activation agent was supplied by Sigma-Aldrich.

2.1. Synthesis of activated carbons

Horse chestnut and tangerine peels were first washed with plenty of water to remove impurities and then dried at 110 ° C. Dried biomasses were ground in a Retsch PM100 brand ball mill and sieved in a Retsch AS200 device to a particle size range of 100–500 μm.

Horse chestnut shell was impregnated with $ZnCl_2$ at a ratio of 1:4 (1 g biomass with 4 g $ZnCl_2$ dissolved in 40 mL distilled water) by chemical activation method, then subjected to preheating at 220°C, then kept at room temperature for 24 hours to break down the lignocellulosic structure. After pretreatment, the sample was pyrolyzed at 600°C under nitrogen atmosphere for 2 hours. The activated carbon obtained after pyrolysis was washed with pure water until pH 7 was reached in order to remove excess $ZnCl_2$ and dried at 110°C [18].

The tangerine peel (25 g) was kept at room temperature for 24 hours with 5 M $ZnCl_2$ solution (50 ml) and then dried at 110°C. The dried sample was pyrolyzed at 700°C in an inert nitrogen atmosphere for 2 hours. The active carbon obtained after pyrolysis was washed with pure water and dried at 110°C [16]. The chemical activation method was preferred because it enables better pore development and higher surface area at lower activation temperatures compared to physical activation, making it more

suitable for hydrogen adsorption applications. $ZnCl_2$ was chosen as the activating agent since it decomposes cellulose and facilitates the formation of micropores, leading to higher surface area in the activated carbons [1].

2.2. Characterization

BET surface area measurements and pore size analyses of activated carbons were obtained using a Quantachrome Nova brand 2200e series device. Measurements of activated carbons, which were degassed at 105°C for 24 hours before analysis, were carried out using nitrogen gas at 77 K.

2.3. Hydrogen storage analysis

Hydrogen adsorption measurements of activated carbons were carried out in a Hiden IMI PSI brand hydrogen storage device at 77 K. Before analysis, the materials were degassed at 105°C for 4 hours.

3. Results and Discussion

3.1. Hydrogen storage

Table 1 shows the hydrogen storage capacities of activated carbons produced from horse chestnut and tangerine peel at cryogenic temperature. Hydrogen storage analyses of activated carbons were carried out at pressures between 0 and 80 bar and remarkable results were obtained in terms of storage capacity. Activated carbon produced from horse chestnut shells exhibited a very high storage capacity with a hydrogen storage capacity of 1.90% by weight at 1 bar, 4.24% at 20 bar and a maximum of 4.47% at 80 bar. Tangerine peel-based activated carbon, on the other hand, exhibited a lower performance

with a capacity of 0.89% by weight at 1 bar, 1.84% at 20 bar and a maximum of 1.87% at 26 bar. The basis of these differences lies in the surface properties of the materials and the separation in their pore structures. The N_2 adsorption-desorption isotherms presented in Figure 1 and the characterization data given in Table 1 provide information about the surface area and pore volumes of the mentioned activated carbons. The BET surface area of the horse chestnut-based activated carbon was determined as 2128 m²/g, while this value was at the level of 1230 m²/g for the tangerine peel-based activated carbon. This difference in surface area is due to the structural properties that develop depending on the pretreatment steps, activation parameters and biomass type.
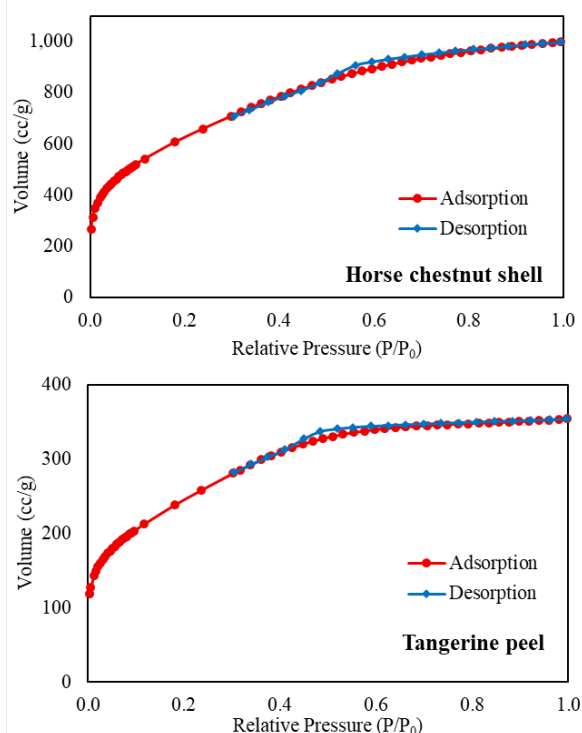
Figure 1. N_2 adsorption-desorption isotherms of activated carbons

Table 1. BET surface areas of activated carbons and hydrogen storage capacities at different pressures

Sample name	S_{BET} (m²/g)	V_t (cc/g)	V_{micro} (cc/g)	V_{DFT} (cc/g)	V_{meso} (cc/g)	H_2 % (w/w) (1 bar)	H_2 % (w/w) (20 bar)	Maximum value	
								H_2 % (w/w)	Pressure (bar)
Horse chestnut shell	2128	1.55	0.88	1.42	0.54	1.90	4.24	4.47	80
Tangerine peel	1230	0.55	0.36	0.49	0.13	0.89	1.84	1.87	26

Detailed information about the pore structure is supported by the cumulative pore volume-pore diameter distribution graph obtained using the Density Functional Theory (DFT) method, as

presented in Figure 2. The micropore volume of the horse chestnut-based activated carbon was calculated as 0.88 cm³/g and the mesopore volume as 0.54 cm³/g. The activated carbon

produced from tangerine peel has a micropore volume of 0.36 cm³/g and a mesopore volume of 0.13 cm³/g. These data show that the horse chestnut-based sample has not only a larger surface area but also a more developed pore volume and a more balanced micro/mesopore distribution. In particular, the ability of micropores to effectively adsorb hydrogen molecules ensures that high adsorption capacity is achieved in such structures.
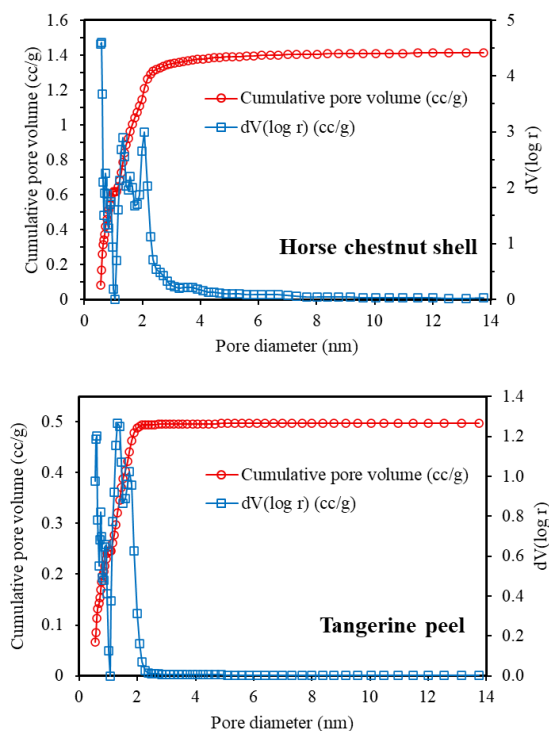
Figure 2. DFT pore size distribution graphs of activated carbons

Figure 3 shows the hydrogen adsorption isotherms of activated carbons at 77 K. When the figure is examined, it is observed that hydrogen adsorption increases with pressure for both activated carbons, but the rate of increase decreases after a certain point. This can be associated with the saturation of active points at high pressures. Activated carbon from horse chestnut was able to perform effective adsorption even at low pressures due to its high surface area and porosity. In addition, the material's micro and mesopore balance allowed the adsorption of hydrogen both on the surface and in the pores. On the other hand, activated carbon from tangerine peel reached a more limited hydrogen storage capacity due to its low surface area and low porosity. This clearly shows that the type of biomass and the applied activation methods are

the determining factors in adsorption performance. While the rapid adsorption observed in horse chestnut activated carbon indicates the high affinity and accessibility of the surface, the tangerine peel-based activated carbon sample reaches surface saturation early.

These results show that waste biomass can be converted into high-performance hydrogen storage materials with appropriate activation methods. In addition, such materials offer low-cost and environmentally friendly alternatives in energy storage systems. In the hydrogen storage processes that occur on the surfaces and pores of activated carbon at cryogenic temperatures, physical adsorption (physisorption) interactions mainly occur between the hydrogen molecules and the activated carbon surface [16]. These interactions are based on weak and reversible forces such as van der Waals forces. Low temperature reduces the kinetic energy of hydrogen molecules, allowing them to adhere more easily to the carbon surface and increasing the adsorption capacity [1]. Microporous structures in particular offer local areas with high surface energy to effectively adsorb hydrogen molecules. Therefore, activated carbons with high surface area and well-optimized pore size distribution can adsorb more hydrogen at cryogenic temperatures. However, since there is no chemical bonding in this process, adsorption and desorption processes are fast and easy.
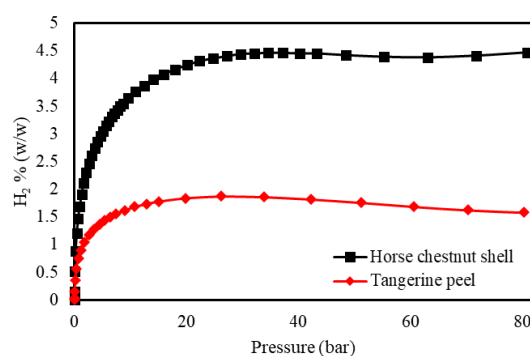
Figure 3. Hydrogen adsorption isotherms of activated carbons

The hydrogen adsorption data obtained in this study were also evaluated by comparing with various biomass-based carbon materials previously reported in the literature (Table 2). The hydrogen storage capacity of the samples in the table varies significantly depending on the

structural properties of the adsorbent such as surface area, pore size distribution, surface chemistry and activation method. According to the data in the table, pinecone has the highest hydrogen storage capacity with 5.25% (w/w), and this value was obtained as a result of experiments carried out under high pressure [21]. In this study, the activated carbon sample produced from horse chestnut shell has a storage capacity of 4.47% by weight, which is lower than pine cone-based activated carbon but higher than many samples such as coffee bean waste (4.00%) [22], almond shell (2.53%) [1] and olive pulp (2.59%) [23]. This result reveals that the surface properties and pore structure of horse chestnut activated carbon are extremely suitable for hydrogen adsorption.

Table 2. Hydrogen storage capacities of some biomass-based activated carbons at 77 K

| Materials	Max. value		Ref
	H₂ % wt.	P (bar)	
Almond shell	2.53	27	[1]
Pine cone	5.25	80	[21]
Coffee bean waste	4.00	40	[22]
Olive bagasse	2.59	25	[23]
Fruit bunch	2.14	20	[24]
Mandarin fruit	1.90	25	[25]
Horse chestnut shell	4.47	80	In this study
Tangerine peel	1.87	26	In this study

Examples with medium hydrogen storage capacity include fruit bunch (2.14%) [24] and tangerine fruit (1.90%) [25]. Although the tangerine peel-based activated carbon evaluated in this study was tested under low pressure conditions with a capacity of 1.87%, it gave similar results with some samples. Although they offer low capacity, these types of agricultural wastes are among the alternative raw materials that can be evaluated in sustainable energy applications due to their low cost and bioavailability. The differences observed between materials in terms of hydrogen storage capacity are related not only to the chemical structure but also to the effects of the applied carbonization and activation processes. The high capacity of pine cone and horse chestnut shell samples tested at high pressure confirms that adsorption pressure is a determining parameter. Under high pressure, effective filling of micropores in carbon structures is ensured and

hydrogen storage efficiency increases. As a result, activated carbon produced from horse chestnut shell within the scope of this study has only lower capacity than pine cone in terms of hydrogen storage capacity and higher storage capacity than all other samples in the table. In this context, horse chestnut shell can be considered as a sustainable, environmentally friendly and economical hydrogen storage material. On the other hand, materials with relatively low capacity such as tangerine peel can be made more efficient by surface modifications and porosity-enhancing processes.

3.2. Isotherm analysis

Understanding the adsorption behavior of hydrogen on solid surfaces is of great importance to evaluate the potential of these materials in energy storage applications. Hydrogen adsorption isotherms are used to explain the interaction of the amount of hydrogen held at different pressures at a certain temperature with the surface. With these isotherm models, quantitative assessments can be made about the adsorption capacity and the type and intensity of surface-adsorbate interaction. In addition, by comparing the agreement of different models with experimental data, inferences can be obtained about the mechanism of the adsorption process [26].

The Langmuir isotherm is a model based on the assumption of a monolayer and homogeneous surface developed to explain gas adsorption on solid surfaces. In this model, it is assumed that all active sites on the adsorption surface have equal energy and that each site can be occupied by only one molecule [27]. This model, which is developed assuming that there is no interaction between molecules, gives good results especially at low pressure conditions. The linearized mathematical expression of the isotherm is given below:

$$\frac{P}{n} = \frac{1}{n_m B} + \frac{P}{n_m} \qquad (1)$$

In the equation, P represents the partial equilibrium pressure, n_m represents the monolayer adsorption capacity, n represents the amount of adsorbate adsorbed by the unit mass of the layer, and B represents the Langmuir constant.

The Freundlich isotherm model is an empirical model that assumes that adsorption occurs in multiple layers on heterogeneous solid surfaces. According to this model, adsorption first occurs on regions with high binding energy; as adsorption increases, the binding strength of the active sites on the surface decreases. This model, which is generally valid in low and medium pressure ranges, is especially useful in systems with inhomogeneous surfaces [28]. The linearized Freundlich isotherm equation is given below:

$$\ln(n) = \ln(K_F) + \frac{1}{n_F} \ln(P) \qquad (2)$$

In the relevant equation, K_F is the Freundlich constant and n is the amount of adsorbate adsorbed. Temkin isotherm model takes into account the interactions between adsorbent and adsorbate during adsorption. The model assumes that the heat of adsorption does not remain constant as surface coverage increases but decreases linearly. In this respect, it differs from the Langmuir model and is particularly suitable for use at moderate surface saturations. Temkin constants can be calculated from graphs where the amount of adsorption is plotted logarithmically against pressure [28]. The isotherm equation is given below.

$$n = B \ln A_T + B \ln P \qquad (3)$$

In this equation, Temkin isotherm equilibrium binding constant is symbolized by A_T and the constant related to the heat of adsorption is symbolized by B.

The regression coefficients and isotherm parameters obtained by applying the experimental data to the Langmuir, Freundlich and Temkin isotherms are given in Table 3. In addition, the linearized Langmuir isotherm plots for both activated carbons are presented in

Figure 4. The Langmuir isotherm model was the model that best explained the hydrogen adsorption data by showing high regression coefficients for both biomass-based activated carbons (R^2 = 0.9920 and 0.9955). The Freundlich isotherm showed a lower level of fit (R^2 = 0.9626 and 0.8991), while the correlation coefficients of the Temkin model (R^2 = 0.9206 and 0.9662) showed a moderate fit. The Langmuir model is a model that assumes that adsorption occurs on single-layered surfaces with homogeneous energy and that there is no interaction between the adsorbed molecules [29]. These high correlation coefficients indicate that the surfaces establish regular and reversible interactions with hydrogen. When the model parameters are evaluated, the maximum adsorption capacity (n_m) of the horse chestnut shell-based activated carbon is calculated as 4.53 (%wt.).

This value is approximately 2.4 times higher than the capacity of 1.90 of the activated carbon produced from tangerine peel. This shows that the horse chestnut adsorbent has a larger surface area and a suitable pore structure. The Langmuir constant (B) is related to the surface-adsorbate interaction energy; this constant was higher in tangerine peel (0.79), which may indicate stronger local interactions. However, the low total surface area and capacity suggest that this advantage has limited contribution to storage performance. Such results have also been observed in previous studies on activated carbon and carbon-derived materials [30]. As a result, the Langmuir model is the model that best explains the regular and monolayer binding of hydrogen to both biomass-based adsorbents. Especially horse chestnut shell-based activated carbon stands out as a more suitable candidate for hydrogen storage applications with both its high adsorption capacity and high compliance with the Langmuir isotherm.

Table 3. Hydrogen adsorption isotherm data of activated carbons

Sample name	Langmuir			Freundlich			Temkin		
	n_m (%wt.)	B	R^2	n_F	K_F	R^2	A_T	B	R^2
Horse chestnut shell	4.53	0.53	0.9920	2.27	1.37	0.9626	0.57	2.18	0.9206
Tangerine peel	1.90	0.79	0.9955	2.27	0.64	0.8991	0.25	0.99	0.9662

This result is consistent with the findings in the literature that microporous carbon materials have a high hydrogen storage potential under low temperature and medium pressure conditions [1]. Thus, it has been confirmed once again that biomass-based carbon materials offer strong alternatives in terms of sustainable and environmentally friendly hydrogen storage solutions.
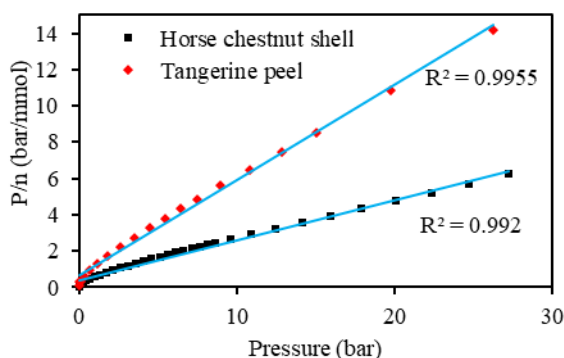
Figure 4. Langmuir isotherm plots for hydrogen adsorption on activated carbons

3.3. Adsorption kinetic

In gas phase adsorption processes, molecular interactions occurring during the contact period are the basic elements affecting the adsorption rate. Figure 5 shows the change in hydrogen adsorption capacities of horse chestnut and tangerine peel based activated carbon samples under different pressures. For both adsorbents, the adsorption process shows a rapid increase at the beginning of the contact period. At this stage, gas molecules are easily adsorbed to the active points on the surface and the adsorption amount increases over time. This rapid increase at the beginning is related to the surface being largely empty and accessible. As time progresses, the possibility of molecules reaching the surface decreases as the suitable areas on the surface decrease. This causes the adsorption rate to slow down. After a certain period of time, the system reaches equilibrium and no significant change is observed in the adsorption amount over time. At this stage, equilibrium is established between the adsorption and desorption processes.

Kinetic models are widely used to understand adsorption processes. In this study, the adsorption behavior of hydrogen gas onto activated carbon samples was analyzed by pseudo-first-order and pseudo-second-order kinetic models. Both models were derived from chemical reaction kinetics and applied to time-varying adsorption data, and the results are presented in Table 4. The pseudo-first-order kinetic model assumes that the adsorption rate is proportional to the difference between the adsorbed amount (q_e) at equilibrium and the adsorbed amount (q_t) at any instant. The linear form of the model is:

$$\ln(q_e - q_t) = \ln q_e - k_1 t \tag{4}$$
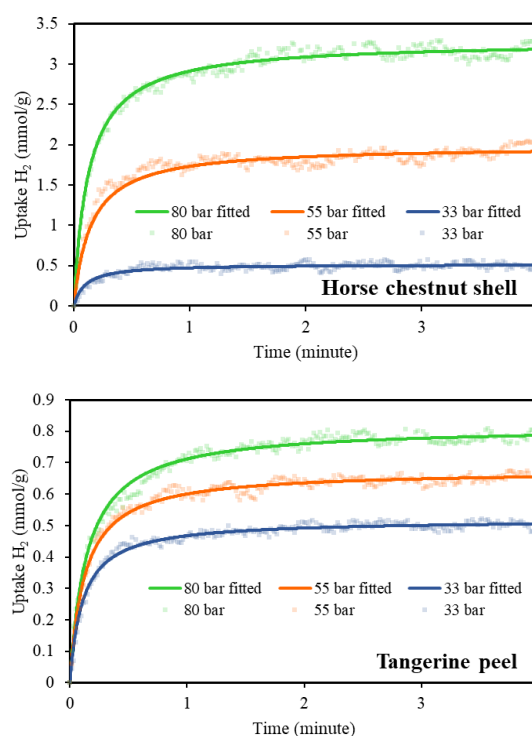
Figure 5. Change in hydrogen adsorption amounts of activated carbons with time at different pressures

In this equation, q_t is the amount adsorbed at time t (mmol/g); q_e is the amount adsorbed at equilibrium (mmol/g); k_1 is the pseudo-first-order rate constant (minute^{-1}), and t is the time (minute). This model generally gives more appropriate results when the amount of adsorbed substance is low compared to the adsorbent capacity. The correlation coefficients (R^2) obtained as a result of the application showed moderate agreement in some examples but generally remained at low values (Table 4).

The pseudo-second-order kinetic model assumes that the adsorption rate is proportional to the square of the amount of adsorbed material and is

generally suitable for systems with high surface capacity. The linear form of the equation is:

$$\frac{t}{q_t} = \frac{1}{k_2 q_e^2} + \frac{t}{q_e} \qquad (5)$$

In the relevant equation, k_2 is the pseudo-second order rate constant (g mmol^{-1} min^{-1}). According to the equation, the plot of t/q_t against t should give a straight line with a slope of $1/q_e$ and an extrapolation of $1/(k_2 q_e^2)$. Figure 6 shows the plots of t/q_t against t for horse chestnut and tangerine peel based activated carbons using the pseudo-second order kinetic model. In both graphs, the experimental data obtained for hydrogen adsorption under different pressure conditions show a linear distribution. The high correlation coefficients of the obtained linear graphs ($R^2 = 0.9769$–0.9982) and the closeness of the curves to the experimental points show that the pseudo-second order kinetic model successfully represents the systems.

Which step in the adsorption process is the rate-determining step is of critical importance both for understanding the mechanism and for industrial applications. Especially in gas phase applications, how quickly and by what mechanism the adsorbed substance is transported to the surface directly affects the design, storage and recovery processes. In this study, Boyd, Avrami and Weber–Morris models were used to evaluate the adsorption mechanism.
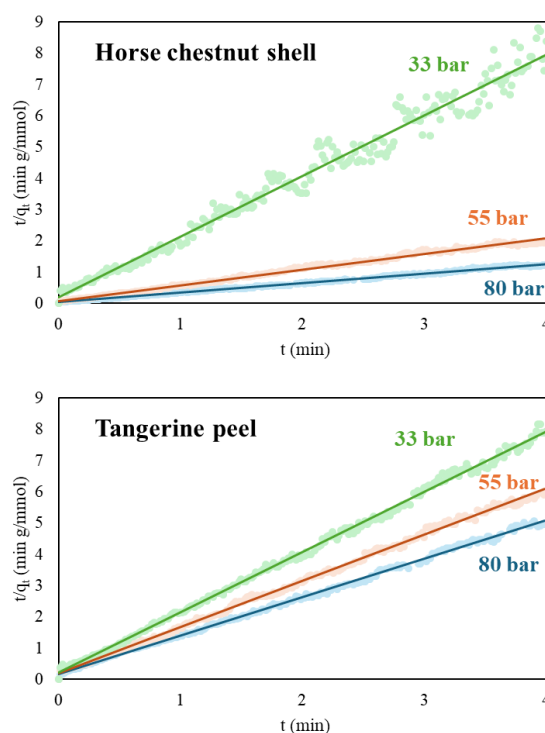
Figure 6. t/q_t–t curves plotted according to the pseudo-second-order kinetic model for activated carbons at different pressures

Table 4. Kinetic parameters for the adsorption of hydrogen on the surface of activated carbons

Sample name	Pressure (bar)	Pseudo-first order			Pseudo-second order			
		R^2	$q_{e(cal)}$ (mmol/g)	k_1	R^2	$q_{e(exp)}$ (mmol/g)	$q_{e(cal)}$ (mmol/g)	k_2
Horse chestnut shell	80	0.6451	4.083	1.13	0.9974	3.336	3.283	2.40
	55	0.6533	1.176	1.44	0.9932	2.081	1.984	3.43
	33	0.2652	0.356	1.12	0.9769	0.602	0.516	20.03
Tangerine peel	80	0.7120	0.082	1.17	0.9982	0.822	0.815	8.45
	55	0.7249	0.027	1.24	0.9981	0.683	0.675	11.91
	33	0.6500	0.019	1.18	0.9979	0.528	0.518	17.58

Boyd model is an approach to distinguish whether adsorption occurs on the outer surface (film diffusion) or in the inner regions (intrapore diffusion). The logarithmic form of the model is given below:

$$\ln(1 - \frac{q_t}{q_e}) = -Rt + A \qquad (6)$$

Here R represents the rate constant and A represents the Boyd constant. According to the equation, if the plot of $\ln(1 - q_t/q_e)$ versus t is linear, film diffusion is considered to be the rate-limiting step.

The Avrami model is a model used to evaluate the multi-step nature of the adsorption process. This model is defined by the following equation:

$$\ln[-\ln(1 - \theta)] = \ln k_{AV} + n \ln t \qquad (7)$$

Here $\theta = q_t/q_e$ represents the covering fraction, k_{AV} represents the rate constant and n represents the Avrami parameter. If n<1 and the resulting graph is linear, the process is considered to be diffusion

controlled. However, if the graph does not pass through the origin or the correlation coefficients are low, the validity of the model is considered limited.

The Weber–Morris model is an approach used to explain how gas diffuses through the internal pore structure of the adsorbent during the adsorption process. This model takes into account the movement of gas molecules within the porous structure of the adsorbent and the factors that affect the speed of this movement. The Weber–Morris equation is given as follows.

$$q_t = k_{dif} t^{1/2} + C \qquad (8)$$

In this equation, k_{dif} represents the diffusion rate constant and C represents the boundary layer effect. If intraparticle diffusion is the only rate-determining step in the adsorption process, the relationship between q_t and $t^{1/2}$ is linear according to the Weber–Morris model and this line passes through the origin. If it does not pass through the correct origin, this indicates that the adsorption cannot be explained by intraparticle diffusion alone and that other mechanisms such as film diffusion or surface interactions also contribute to the process. If the adsorption mechanism consists of more than one step, more than one intersecting linear regions are observed in the q_t-$t^{1/2}$ plot. In this case, each linear region corresponds to different mechanisms.

The validity of the models was evaluated based on the regression coefficients (R^2); it was determined which kinetic model best represented the adsorption mechanism (Table 5). When compared according to the regression coefficients, Avrami and Boyd models showed low correlation coefficients for both biomass samples. While the R^2 values of the Boyd model varied between 0.2855-0.4988, these values remained between 0.5995-0.8443 for the Avrami model. These results show that the models in question cannot adequately represent the adsorption process.

Figure 7 shows the q_t – $t^{1/2}$ curves drawn according to the Weber–Morris model for horse chestnut shell and tangerine peel based activated carbon samples. The linear curves in the figure show that the data points fit the model line well,

especially in the first region. This fit proves that surface adsorption is dominant in the first stage of the process. The fact that the linear curve does not pass through the origin at the beginning suggests that adsorption is not limited to intraparticle diffusion only; film diffusion or other surface-effect kinetics also contribute. In the second stage, the curve becomes more horizontal and the deviations increase. This indicates that adsorption becomes limited to intrapore diffusion in the later stages.

The R^2 values of the first stage of the Weber–Morris model are quite high (Table 5). In the horse chestnut peel sample, $R^2 = 0.9820$ at 80 bar pressure, and in the tangerine peel, $R^2 = 0.9775$ at the same pressure. These findings show that the first phase, namely the rapid surface diffusion step, is dominant in the adsorption process and that the adsorption rate is high in this phase. The low R^2 values of the second phase reveal that intraparticle diffusion occurs more slowly and in a dispersed manner. In this respect, the Weber–Morris model is a successful model in terms of representing the multi-stage structure of adsorption.
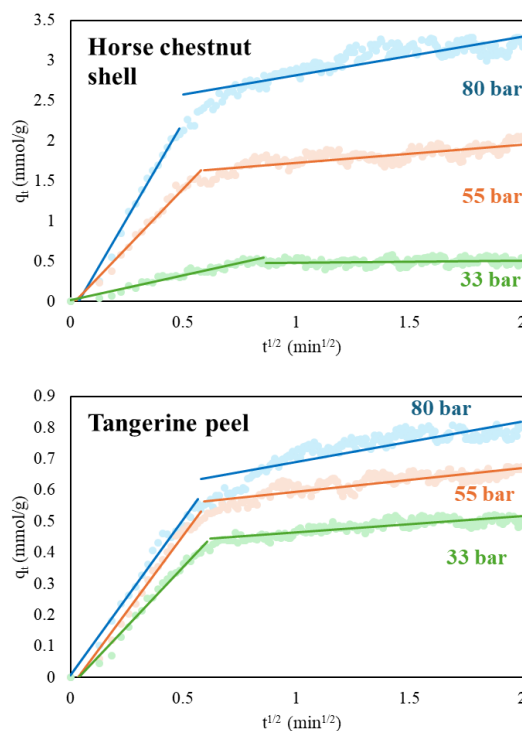

Figure 7. Weber-Morris curves for the adsorption of hydrogen on activated carbon surfaces

The kinetic parameters calculated according to the Weber–Morris equation also provide

important information about the nature of the process (Table 5). The k_1 value obtained at 80 bar pressure in the horse chestnut peel sample was 4.834 mmol g^{-1} $min^{-1/2}$, while this value was determined as 0.982 mmol g^{-1} $min^{-1/2}$ in the tangerine peel. This difference indicates that hydrogen molecules adsorb faster on the surface of the horse chestnut peel. In addition, a higher k_1 value is associated with more active surface area and better mass transfer. A lower k_1 value in the tangerine peel may indicate that the pores are less accessible or have a more complex structure.

At the same time, the high rate constant observed in the first stage of the adsorption process suggests that hydrogen interacts quickly and easily with the active centers of the adsorbent. This situation can be directly related to the microporous structure of the surface. In the second stage, the very low k_2 values and the significant decrease in R^2 values indicate that this step is a kinetically slow process controlled by diffusion. As a result, it was determined that the model that best explains the adsorption kinetics of hydrogen on activated carbons is the Weber–Morris model. The high regression coefficients and curve fit of this model, especially for the first phase, indicate that the process is surface diffusion controlled and progresses in multiple steps. The kinetic parameters reveal that the adsorbent structure and pore distribution directly affect the adsorption rate. However, the Boyd and Avrami models are limited in understanding the adsorption process.

Table 5. Calculated kinetic parameters for the adsorption of hydrogen on the activated carbon surface

Sample name	P (bar)	Boyd			Pseudo-second order				Avrami		
		R^2	R	A	R^2_1	k_1	R^2_2	k_2	R^2	n_{AV}	K_{AV}
Horse chestnut shell	80	0.4536	1.28	-2.65	0.9820	4.834	0.7231	0.479	0.8093	0.4745	1.823
	55	0.4292	1.48	-2.84	0.9809	2.935	0.6255	0.222	0.7816	0.3452	1.664
	33	0.2855	1.12	-1.39	0.9432	0.613	0.0570	0.029	0.5995	0.3795	1.405
Tangerine peel	80	0.4988	1.18	-2.60	0.9775	0.982	0.7119	0.130	0.8443	0.5033	1.770
	55	0.4220	1.24	-2.55	0.9818	0.978	0.7269	0.076	0.8344	0.4413	1.911
	33	0.3948	1.18	-2.48	0.9824	0.765	0.7121	0.051	0.8409	0.5022	2.007

4. Conclusion

In this study, activated carbons derived from horse chestnut shell and tangerine peel were investigated for hydrogen storage. The horse chestnut-based carbon exhibited a superior capacity of 4.47 wt. % at 80 bar compared to tangerine peel (1.87 wt. % at 26 bar) due to its higher surface area and well-developed micropore structure, whereas the tangerine peel-based carbon showed lower performance. Among the isotherm models used in the evaluation of adsorption data, the Langmuir model showed the highest fit ($R^2 > 0.99$) for both biomass-derived adsorbents, thus revealing the tendency of hydrogen to adsorb as a single layer on homogeneous surfaces. Within the scope of kinetic analyses, it was determined that the pseudo-second-order and Weber–Morris models overlapped with the data to a high degree. As a result, biomass-derived activated carbons can be considered an effective and sustainable alternative in hydrogen storage applications with appropriate synthesis conditions.

This study demonstrates the hydrogen storage potential of biomass-derived activated carbons, marking a significant step in the evaluation of alternative materials that can contribute to sustainable energy systems. However, further development is needed to extend the results to a wider range of applications. A comparative study of carbons synthesized by varying the activation parameters of different biomass types (e.g., nut waste, agricultural pulp) is recommended. Furthermore, examining the adsorption behavior of not only hydrogen but also other gases such as methane and carbon dioxide is crucial for assessing the materials' potential for versatile applications. In addition, supporting physisorption data with electrochemical hydrogen storage tests will enable a combined interpretation of different storage strategies.

Article Information Form

The Declaration of Conflict of Interest/ Common Interest
No conflict of interest or common interest has been declared by the author.

Artificial Intelligence Statement

No artificial intelligence tools were used while writing this article.

Copyright Statement

The author owns the copyright of their work published in the journal and their work is published under the CC BY-NC 4.0 license.

References

[1] Z. Bicil, M. Doğan, "Characterization of activated carbons prepared from almond shells and their hydrogen storage properties," Energy & Fuels, vol. 35, no. 12, pp. 10227–10240, 2021.

[2] B. K. Kızılduman, "Kaolinit kilinin hidrojen depolama amaçlı kullanımı için modifikasyonu ve karakterizasyonu," BAUN Fen Bilimleri Enstitüsü Dergisi, vol. 25, no. 1, pp. 186–202, 2023.

[3] I. Dincer, C. Acar, "Review and evaluation of hydrogen production methods for better sustainability," International Journal of Hydrogen Energy, vol. 40, no. 34, pp. 11094–11111, 2015.

[4] E. E. Doğan, "Hydrogen production and its storage from solar energy," Advances in Materials Science, vol. 20, no. 2, pp. 14–25, 2020.

[5] M. Sevilla, A. B. Fuertes, "Sustainable porous carbons with a superior performance for CO_2 capture," Energy & Environmental Science, vol. 4, no. 5, pp. 1765–1771, 2011.

[6] G. W. Crabtree, M. S. Dresselhaus, and M. V. Buchanan, "The hydrogen economy," Physics Today, vol. 57, no. 12, pp. 39–44, 2004.

[7] E. E. Doğan, P. Tokcan, B. K. Kızılduman, "Storage of hydrogen in activated carbons and carbon nanotubes," Advances in Materials Science, vol. 18, no. 4, pp. 5–16, 2018.

[8] L. Schlapbach, A. Züttel, "Hydrogen-storage materials for mobile applications," Nature, vol. 414, no. 6861, pp. 353–358, 2001.

[9] A. Züttel, "Materials for hydrogen storage," Materials Today, vol. 6, no. 9, pp. 24–33, 2003.

[10] M. Doğan, A. Selek, O. Turhan, B. K. Kızılduman, Z. Bicil, "Different functional groups functionalized hexagonal boron nitride (h-BN) nanoparticles and multi-walled carbon nanotubes (MWCNT) for hydrogen storage," Fuel, vol. 303, 121335, 2021.

[11] Ü. Çakır, M. Doğan, B. K. Kızılduman, Z. Bicil, "Functionalized and Schiff base-based multi-walled carbon nanotubes for hydrogen storage," Journal of Alloys and Compounds, vol. 1010, 177290, 2025.

[12] M. Doğan, M. Y. Kalafat, B. K. Kızılduman, Z. Bicil, Y. Turhan, E. Yanmaz, et al., "Hydrogen storage analysis of fullerene and defective fullerenes: The first experimental study," Fuel, vol. 390, 134705, 2025.

[13] H. Barthélémy, M. Weber, F. Barbier, "Hydrogen storage: Recent improvements and industrial perspectives," International Journal of Hydrogen Energy, vol. 42, no. 11, pp. 7254–7262, 2017.

[14] Z. S. Doğan, E. E. Doğan, Z. Bicil, B. K. Kızılduman, "The effect of Li-doping and doping methods to hydrogen storage capacities of some carbonaceous materials," Fuel, vol. 396, 135280, 2025.

[15] M. Sevilla, N. Díez, A. B. Fuertes, "More sustainable chemical activation strategies for the production of porous carbons," ChemSusChem, vol. 14, no. 1, pp. 94–117, 2021.

[16] M. Doğan, P. Sabaz, Z. Bicil, B. K. Kızılduman, Y. Turhan, "Activated carbon synthesis from tangerine peel and its use in hydrogen storage," Journal of the Energy

Institute, vol. 93, no. 6, pp. 2176–2185, 2020.

[17] O. Ioannidou, A. Zabaniotou, "Agricultural residues as precursors for activated carbon production—A review," Renewable and Sustainable Energy Reviews, vol. 11, no. 9, pp. 1966–2005, 2007.

[18] A. Turkyılmaz, K. Isinkaralar, M. Doğan, B. K. Kızılduman, Z. Bicil, "Production, characterization, and hydrogen storage properties of activated carbon from horse chestnut shell," Sustainable Chemistry and Pharmacy, vol. 40, 101634, 2024.

[19] H. Jin, Y. S. Lee, I. Hong, "Hydrogen adsorption characteristics of activated carbon," Catalysis Today, vol. 120, no. 3–4, pp. 399–406, 2007.

[20] Z. Bicil, "Adsorption kinetics and mechanism of hydrogen on pristine and functionalized multi-walled carbon nanotubes," Fuel, vol. 403, 136130, 2026.

[21] S. Stelitano, G. Conte, A. Policicchio, A. Aloise, G. Desiderio, R. G. Agostino, "Pinecone-derived activated carbons as an effective medium for hydrogen storage," Energies, vol. 13, no. 9, 2237, 2020.

[22] H. Akasaka, T. Takahata, I. Toda, H. Ono, S. Ohshio, S. Himeno, H. Saitoh, "Hydrogen storage ability of porous carbon material fabricated from coffee bean wastes," International Journal of Hydrogen Energy, vol. 36, no. 1, pp. 580–585, 2011.

[23] N. Bader, O. Abdelmottaleb, "CO_2 activation of olive bagasse for hydrogen storage," Environmental Progress & Sustainable Energy, vol. 36, no. 1, pp. 315–324, 2017.

[24] S. H. M. Arshad, N. Ngadi, S. Wong, N. S. Amin, F. A. Razmi, N. B. Mohamed, A. A. Aziz, "Optimization of phenol adsorption onto biochar from oil palm empty fruit bunch (EFB)," Malaysian Journal of Fundamental and Applied Sciences, vol. 15, no. 1, pp. 1–5, 2019.

[25] M. Jung, J. Park, K. Lee, N. F. Attia, H. Oh, "Effective synthesis route of renewable nanoporous carbon adsorbent for high energy gas storage and CO_2/N_2 selectivity," Renewable Energy, vol. 161, pp. 30–42, 2020.

[26] R. C. Bansal, M. Goyal, Activated Carbon Adsorption. Boca Raton, FL, USA: CRC Press, 2005.

[27] C. T. Chiou, Partition and Adsorption of Organic Contaminants in Environmental Systems. Hoboken, NJ, USA: Wiley, 2003.

[28] A. O. Dada, A. P. Olalekan, A. M. Olatunya, O. J. Dada, "Langmuir, Freundlich, Temkin and Dubinin–Radushkevich isotherms studies of equilibrium sorption of Zn^{2+} unto phosphoric acid modified rice husk," IOSR Journal of Applied Chemistry, vol. 3, no. 1, pp. 38–45, 2012.

[29] P. Benard, R. Chahine, "Determination of the adsorption isotherms of hydrogen on activated carbons above the critical temperature of the adsorbate over wide temperature and pressure ranges," Langmuir, vol. 17, no. 6, pp. 1950–1955, 2001.

[30] J. Serafin, B. Dziejarski, C. Solis, P. R. de la Piscina, N. Homs, "Medium-pressure hydrogen storage on activated carbon derived from biomass conversion," Fuel, vol. 363, 130975, 2024.

Investigation of a Bacterial and Arbuscular Mycoorhizal Fungus Spore Inoculation in Cultivation of Saffron

Muazzez Gürgan[1*] [iD], Sevinç Yeşilyurt[2] [iD], Seda Pamay[2] [iD]

[1] Tekirdağ Namık Kemal University, Faculty of Arts and Sciences, Department of Biology, Tekirdağ, Türkiye, mgurgan@nku.edu.tr, ror.org/01a0mk874

[2] Tekirdağ Namık Kemal University, Faculty of Agriculture, Department of Soil Science and Plant Nutrition, Tekirdağ, Türkiye, sevincyesilyurt1@gmail.com, sedapamay@gmail.com, ror.org/01a0mk874

*Corresponding Author

ARTICLE INFO

ABSTRACT

Saffron (*Crocus sativus* L.) is prized for its stigma, a valuable spice rich in bioactive compounds crucial for various industries and traditional medicine. Enriched with bioactive compounds crucial for numerous industries and traditional medicinal practices, saffron cultivation expansion hinges on assessing the vegetative process in soils with low organic content. Optimal fertilization, considering plant and soil conditions, is crucial. Leaves indicate vegetative status and serve as an agricultural byproduct. In this study, saffron was grown in clay loam soil (1.88% organic matter) with supplementation of the bacterium *Rhodobacter sphaeroides*, spores of an arbuscular mycorrhizal fungus *Glomus iranicum* var. *tenuihypharum*, and both. Sole bacterium application increased leaf fresh and dry weight by 25.5% and 36.8%, respectively, demonstrating growth promotion. *Rhodobacter sphaeroides* and AMF combination elevated leaf P, Mg, and Cu concentrations, while AMF alone increased Zn, Mn, and B accumulation. *Rhodobacter sphaeroides* reduced Fe, Zn, Mn, and B soil concentrations, with no corresponding increase in their accumulation in the plant, as observed with mycorrhiza and the combination of microorganisms, hinting at its applicability for saffron cultivation in environments contaminated with heavy metals. In summary, the findings underscore the importance of microorganism supplementation in saffron cultivation, offering insights into optimizing growth conditions.

1. Introduction

Saffron (*Crocus sativus* L.) is an angiosperm in Iridaceae family. It is distributed in Mediterranean-Europe and Western Asia. The dried stigma which is the upper part of the female reproductive system of the saffron flowers serves as a highly esteemed spice, recognized as the most expensive spice globally [1]. In traditional medicine it is widely used for treatment of constipation, depression, cough, inflammation, and menstruation difficulty [2]. The stigmas of the saffron flowers are rich in many bioactive chemicals: more than 300 volatile and non-volatile metabolites making the plant medicinally invaluable. That is why most researchers focused on the stigma and its valuable ingredients [1, 3–5].

After the harvest of flowers and the stigma, the daughter corms are left in the land for the leaves to dry and fall, then the corms are removed and kept in a dry place for 1-2 months and replanted. The size of corms influences the development of the plants, especially the number of flowers obtained, the stigma size and weight. The larger the circumference the higher the yield, and the suggested corm size was 7-10 cm circumference length [6]. The primary objectives of saffron cultivation encompass the production of its prized stigma and corms.

Meanwhile, the leaves are often regarded as an agricultural byproduct. The green leaves of *Crocus sativus* L. were found to be rich in bioactive compounds and research demonstrated the antibacterial activity of the leaves against *Listeria* species and anti-radical activity well comparable to alpha tocopherol [7]. Moreover, the leaves are the indicator of the situation of the plant in terms of plant nutrition, which can well be used to determine the nutrition status and the effectiveness of the fertilizer regime. It is also very important for the determination of plant status of flowering plants having a short flowering period, such as saffron which has a flowering period of only 3-4 weeks [8]. Flowers are one of the most important quality parameters of plant development, however, to understand the effects of fertilizers and nutrient elements on growth and development of plants, vegetative parts should be investigated.

Saffron has a significant market size in the world. Spain was the leading country in terms of saffron export volume in 2022 with 51.8 million USD followed by United Arab Emirates with 13.8 million USD [9]. The cultivation of this plant is restricted to one city in Türkiye right now, but proliferation of saffron cultivation is desired to expand the market size. This brings about the need for fertilizer use depending on the soil's properties. Microbial fertilization is of great interest to increase both the yield and the fertility of the soil, which has decreased dramatically due to unconscious agriculture applications such as immense use of chemical fertilizers. Such applications have damaged the microbial populations in the soil which decreased the fertility of soil [10].

To support soil fertility, organic fertilizers as well as microbial fertilizers have been suggested to use. Mycorrhizae are fungi that form symbiotic relationship with plant roots and enhance the plant growth, as well as protect the plants from diseases [11]. *Glomus iranicum* var. *tenuihypharum* is an arbuscular mycorrhizal fungus (AMF) which has been used in recent studies to enhance root system of plants and productivity [12–14]. Besides fungi, some bacteria have plant growth promoter abilities. Among them, nitrogen fixing bacteria can be used as fertilizers to enhance the plant growth

and soil [15–17]. Different bacteria and fungi species are of research focus for their potential to be used as microbial fertilizers for different agricultural crops. *Rhodobacter sphaeroides* is a purple non sulfur bacterium which is a plant growth promoter because it can fix nitrogen and contribute to the enrichment of soil besides the ability of producing plant hormones such as indole-3-acetic acid and 5-aminolevulinic acid [16, 18, 19].

In this context, this study aimed to determine the nutritional status of saffron leaves upon the use of three different microbial inoculation regimes: a nitrogen fixing bacterium, AMF spore, and the combination of these two.

2. Materials and Methods

Crocus sativus L. corms, which are the seeds of Saffron plant, were obtained from a local provider. Saffron multiplies by cormlets which form corms. Each corm contains 1-4 buds which form flowers and leaves [20] The corms with fibrous and thin roots were planted into the pots of 6L volume, which were filled with topsoil obtained from the experimental field of Tekirdağ Namık Kemal University Faculty of Agriculture, Tekirdağ, Türkiye. There were 5 corms in each pot. After the germination and formation of 3-4 leaves, applications of bacteria and mycorrhiza solutions were carried out to the root area. The experiment was carried out due to randomized block design with 3 pots of each treatment (control, bacteria, AMF, bacteria+AMF) The plants were watered with tap water when needed and plants were harvested after 2 months. The experiment was carried out in lab conditions with controlled temperature and humidity, 22 °C and 80%, respectively, during October and November (Figure 1).

Figure 1. Photos from the experiment. Left: pot experiment showing the leaves of saffron. Right: Saffron flowers

The bacterium applied to the bacteria and bacteria+AMF groups was *Rhodobacter sphaeroides* DSM O.U.001 which was obtained from Hydrogen Research Lab of Middle East Technical University, Ankara, Turkey. The bacteria were grown in Modified Peptone Yeast Extract (MPYE) medium which contains peptone, yeast extract, Ca and Mg sources [21]. When the bacterial concentration reached 1.5×10^8 cells/mL, the bacteria were collected, centrifuged, washed with sterile distilled water and resolved in distilled water. 10mL of bacterial suspension (1.5×10^9 bacterial cells in total) was applied around the root area in bacteria and bacteria+AMF groups at the time of planting the corms to the pots using pipettes. Equal amount of distilled water was applied to the other pots. Similarly, mycorrhiza solution containing 4.8×10^3 propagule of *Glomus iranicum* var. *tenuihypharum* (Symborg) was applied to the root area according to the mycorrhiza manufacturer's recommendations (after dissolving in water applying slowly to the root area) and according to a previous study [22].

2.1. Soil analysis

Soil samples were air-dried and sifted with 2 mm sieve. The pH and electrical conductivity values of the soil were established using 1:2.5 soil:water mixture [23, 24]. Lime ($CaCO_3$) content was measured using Scheibler calcimeter [24]. Bouyoucos Hydrometer method was adopted for the determination of the soil texture [25]. Organic matter content was measured using modified Walkey-Black method [26]. to determine the concentrations of available phosphorus, extractable potassium, magnesium, calcium, available iron, copper, zinc, manganese and extractable nickel, DTPA method with the buffer 0.005 M DTPA+0.01M $CaCl_2$+0.1 M TEA (pH 7.3) was used in ICP-OES [27]. The available boron content was determined according to Wolf (1971) [28]. The determined soil characteristics are given in Table 1.

2.2. Elemental analysis

The micro and macro nutrient element contents of the dried plant material (the aboveground parts without flowers) and the soil obtained in each treatment were determined with ICP-OES

(Agilent 700, Agilent) in the Central Lab of Namık Kemal University (NABILTEM). The nitrogen contents in soil and plant samples were determined with Kjeldhal method in the same lab [21, 22].

Table 1. Some physical and chemical characteristics of the trial soil

Parameters	Measurements	Evaluation
pH	7.10	Neutral
Lime (%)	15.70	High
Salt (µs/cm)	1630	Low
Texture	Clay %45, sand %35, silt %20	Clay loam
Organic matter (%)	1.88	Low
Available phosphorus (P) (mgkg^{-1})	17.04	Sufficient
Extractable boron (B) (mgkg^{-1})	0.17	Insufficient
Extractable potassium (K) (mgkg^{-1})	204.7	Sufficient
Extractable magnesium (Mg) (mgkg^{-1})	208.44	Sufficient
Extractable calcium (Ca) (mgkg^{-1})	4822.07	High
Available iron (Fe) (mgkg^{-1})	1.13	Sufficient
Available copper (Cu) (mgkg^{-1})	0.77	High
Available zinc (Zn) (mgkg^{-1})	0.71	Sufficient
Available manganese (Mn) (mgkg^{-1})	4.32	Sufficient
Extractable nickel (Ni) (mgkg^{-1})	5.02	Non-toxic

2.3. Statistical analysis

The biological parameters of the harvested plants, macro and micronutrient element concentrations of plant and soil samples were analysed for normality with Rjan Joiner test [23]. Followed by the comparison of groups either by ANOVA or Kruskal Wallis test depending on the normality test results with post hoc tests Duncan or Dunn's test, respectively, using SPSS version 22 [24, 25].

3. Results and Discussion

Saffron corm cultivation under controlled laboratory conditions was undertaken, accompanied by some morphological and

biological measurements conducted both throughout the experimental phase and post-harvest. The measurements are given in Table 2. The average leaf length of the control and treatments did not differ significantly, however, the root length of saffron upon mycorrhiza addition alone was almost twice that of control (Table 2). The root enhancement of mycorrhizae (root volume, root length, area etc.) were shown in previous studies carried out with different plant species [29, 30]. On the other hand, the root length of the plants treated with both mycorrhiza and bacteria was almost the same with the control, and lower than that of the bacterial treatment only. This result might suggest competition between fungi and bacteria. If the experiment was carried out for a longer time, a synergistic relationship might have probably been observed [31].

Table 2. Some morphological parameters of *Crocus sativus* L. grown by bacteria and AMF applications

	Leaf length (cm)	Fibrous root length (cm)	Leaf fresh weight (g)	Leaf dry weight (g)
Control	25.6±0.69	11.27±1.74	3.02±0.10	0.57±0.02
Bacteria	26.33±0.1	14.11±1.20	3.79±0.40	0.78±0.04
AMF	25.1±3.51	22.93±2.42	2.77±0.09	0.56±0.06
Bacteria + AMF	24.4±2.01	11.48±1.02	2.75±0.45	0.52±0.09
P value	0.712	0.000	0.01	0.003

The data are given as mean±standard deviation of triplicates.

The application of bacteria alone resulted in higher fresh and dry weight of leaves, 25.5% and 36.8% compared to the control condition (p=0.01 and p=0.003, respectively), while the other two treatments were not significantly different than the control condition. *R. sphaeroides*, but not AMF, exhibited some plant growth promoting effect on saffron. This experiment was carried out for one flowering period. If it proceeded for another flowering period, i.e., another year, the effect on the number of flowers could have been well observed. During the period of this experiment, the number of flowers formed was 8 for the control, 4 for bacteria, 3 for AMF and 5 for bacteria + AMF applications.

It is only safe to say that AMF application alone lowered the formation of flowers. Although the plant length (leaf length) was not significantly affected by the bacterial application, the fresh and dry weight of the leaves increased. Since this study aimed to investigate the development of above ground parts of the plant, it is safe to say *R. sphaeroides* positively affected the growth of saffron when applied alone. *R. sphaeroides* was tested for the growth of cucumber and sesame seedling. The results revealed that this bacterium enhanced the amino acid content and plant growth hormones such as IAA (indole acetic acid) and gibberellin and hence enhanced the growth of plants [32, 33]. Purple non sulfur bacteria were reported to produce 5-aminolevulinic acid (5-ALA) which helps the plants struggle with stress conditions and enhance the plant growth [34].

The effects of different microbial inoculations on some macro and micronutrient elements are tabulated in Table 3. The soil used in this study was low in organic content (1.88%). Therefore, the utilization of microbial inoculations holds promise for augmenting saffron cultivation, as these microorganisms facilitate the solubilization of essential elements making them more readily available to plants [35].

Macro and micro-nutrient elements' analyses of vegetative parts of the plants revealed how the plant benefit from the use of these microbial fertilizers. Among the macro nutrient elements, the nitrogen content of plants grown upon different applications was not significantly different from each other (Table 3). However, there were significant differences of all the other macro and micronutrient elements among the applications. The macro nutrient phosphorus (P) was observed to be the highest in saffron grown with the addition of bacteria and mycorrhiza combination, followed by the application of mycorrhiza alone (11.1% and 4.5% higher than the control) (p=0.008). *Rhodopseudomonas palustris*, a purple non sulfur bacteria were

documented to be a phosphate solubilizer as it increased the uptake of P of peanut from the soil [36].

In addition, two strains of *R. sphaeroides* were shown to increase the soil P by about 30% and these bacteria enhanced the plant height of pineapple by about 4% [37]. Phosphate solubilizer bacteria are therefore accepted as promising substitution for expensive chemical phosphate fertilizers [38]. This is achieved by the decrease of pH upon organic acid production by bacteria which results in solubilization of inorganic phosphate bound to the soil colloids [39].

Potassium solubilization in soil occurs via a similar mechanism with phosphate solubilization. The K content of saffron was found to be highest in the leaves of control condition and the lowest in mycorrhiza application alone. The solubilized K might have been used by the bacteria and fungi in the metabolism to replicate and increase population in this study. However, the combination of bacteria (2.36 mg kg^{-1}) and AMF resulted higher K content in leaves than the separate applications (2.30 and 2.01 mg kg^{-1} upon bacteria alone and AMF alone). In contrast to K, the highest Ca content was observed in saffron grown by the application of AMF only (p=0.000). It is known that mycorrhiza enhances the absorption of nutrients by plants [39]. On the other hand, the lowest was obtained by the application of only bacteria, and it was even lower than the control. This might suggest that bacteria can uptake Ca from the soil and compete with the plant roots, although the Ca in the soil was found to be high (Table 1).

Magnesium is another crucial macro nutrient element in plants as it has a central role in chlorophyll synthesis, besides being vital for protein synthesis [40]. The Mg content of saffron was found to be the highest in the plants grown upon the use of combination of bacteria and AMF, but the lowest in the application of bacteria alone. The Mg content of saffron upon application of AMF was 11.8% higher than the control and the combination of these microorganisms seemed to exert a synergistic interaction which served the plant to enrich in terms of Mg. Therefore, this combination can be suggested to be applied in saffron cultivation under the soil conditions used in this study.

Among the micronutrient elements, the application of AMF alone or in combination with *R. sphaeroides* led the plant to accumulate more Fe, Cu, Zn, Mn and B, where bacteria only treatment lowered the accumulation of Fe, Zn and Mn elements in saffron compared to the control condition (Table 3). The availability of Fe in the soil used in the trial was sufficient (Table 1). Bacteria can produce siderophores which are small organic molecules that act as iron chelator and keep most of the available Fe in rhizosphere [41]. In this study, the Fe concentration in soil was the highest in the pot where only bacteria were applied (Table 4). This might be the result of bacterial chelation of Fe in the soil. In terms of the micronutrients Fe, Zn, Mn and B application of the mycorrhiza can be suggested to enrich the soil.

Table 3. Macro and micronutrient element concentrations in leaves of *Crocus sativus* L.

	Control	Bacteria	AMF	Bacteria + AMF	P value
N (%)	4.19 ± 0.07	4.34 ± 0.05	4.21 ± 0.04	4.21 ± 0.04	0.178
P (%)	0.44 ± 0.01b	0.44 ± 0.02b	0.46 ± 0.00b	0.49 ± 0.01a	0.008
K (%)	2.88 ± 0.22a	2.30 ± 0.11b	2.01 ± 0.13b	2.36 ± 0.03b	0.002
Ca (%)	0.53 ± 0.01 c	0.48 ± 0.01 b	0.59 ± 0.01 a	0.57 ± 0.01 a	0.000
Mg (%)	0.17 ± 0.00 bc	0.16 ± 11.03 c	0.18 ± 0.00 ab	0.19 ± 0.00 a	0.001
Fe (mgkg^{-1})	81.71 ± 7.71b	61.67 ± 0.53b	170.34 ± 12.67a	98.08 ± 22.04a	0.004
Cu (mgkg^{-1})	6.61 ± 0.20b	7.58 ± 0.80ab	7.87 ± 0.62ab	8.77 ± 0.20a	0.010
Zn (mgkg^{-1})	25.79 ± 0.58b	22.27 ± 0.20ab	30.14 ± 0.67a	28.04 ± 0.67ab	0.000
Mn (mgkg^{-1})	15.6 ± 0.52 b	14.85 ± 0.59 b	18.13 ± 0.59 a	17.36 ± 0.22 a	0.000
B (mgkg^{-1})	21.27 ± 1.01c	27.89 ± 0.80b	54.1 ± 0.30a	26.38 ± 0.52b	0.003
Ni (mgkg^{-1})	0.51 ± 0.04b	1.29 ± 0.26a	1.06 ± 0.09a	0.86 ± 0.09a	0.001

The data are given as mean ±standard deviation of triplicates. Different letters indicate difference among groups according to Duncan's test following one way ANOVA or Dunn's test following Kruskal-Wallis test. No letters mean non-significant difference.

Table 4. Macro and micronutrient elements in soil with different applications

	Control	Bacteria	AMF	Bacteria + AMF	P value
N (%)	0.126 ± 0.002	0.124 ± 0.003	0.128 ± 0.003	0.125 ± 0.002	0.782
P (%)	0.002 ± 0.000	0.002 ± 0.000	0.002 ± 0.000	0.002 ± 0.000	0.786
K (%)	0.014 ±0.000	0.016 ± 0.001	0.015 ± 0.000	0.014 ± 0.000	0.562
Ca (%)	0.376 ± 0.004a	0.331 ± 0.002b	0.333 ± 0.003b	0.338 ± 0.004b	0.000
Mg (%)	0.027 ± 0.000a	0.025 ± 0.001b	0.024 ± 0.000b	0.024 ± 0.000b	0.009
Fe (mgkg^{-1})	1.543 ± 0.036ab	1.681 ± 0.005a	1.444 ± 0.038bc	1.310 ± 0.083c	0.000
Cu (mgkg^{-1})	1.012 ± 0.009a	0.927± 0.034b	0.986 ± 0.010a	1.032 ± 0.012a	0.007
Zn (mgkg^{-1})	6.526 ± 0.108	5.838 ± 0.236	6.663 ± 0.131	6.457 ± 0.179	0.098
Mn (mgkg^{-1})	3.262 ± 0.054	2.918 ± 0.118	3.332 ± 0.066	3.228 ± 0.090	0.091
B (mgkg^{-1})	0.153 ± 0.003a	0.141 ± 0.010b	0.157 ± 0.004a	0.157 ± 0.007a	0.006
Ni (mgkg^{-1})	0.777 ± 0.002a	0.721 ± 0.010b	0.763 ± 0.004a	0.772 ± 0.006a	0.000

The data are given as mean ±standard deviation of triplicates. Different letters indicate difference among groups according to Duncan's test following one way ANOVA or Dunn's test following Kruskal-Wallis test. No letters mean non-significant difference.

Sole mycorrhiza application also increased the concentration of these elements in plant (Table 3). However, for Cu the combination of microorganisms resulted in higher content in the plant (32.7% higher than the control). Micronutrient elements are vital for activation of several enzymes such as those playing role in redox balance in the cells, antioxidant enzymes such as catalase, peroxidase, superoxide dismutase, etc. [42]. Therefore, in the germination phase, the application of *R. sphaeroides* cannot be suggested alone, while AMF application or the combination of this bacterium with AMF can be suggested for healthy Saffron cultivation

The Ni content in the bacteria only condition after the harvest was found to be the highest, followed by mycorrhiza, the combination, and the control condition (Table 3). The increased solubility of the heavy metal Ni by the microorganisms applied resulted in the uptake of the metal by the plant. The content of Ni in soil after the harvest was the lowest by the application of the bacteria only (Table 4). This suggests that *R. sphaeroides* might be used in the enhancement of phytoremediation of this heavy metal from the soil. It solubilizes the heavy metal and helps the plant to uptake it more by the plant. The augmentation of phytoremediation of hexavalent chromium by purple non sulfur bacterium *Rhodobacter capsulatus* was shown in our previous study [43].

The contents of macro nutrients N, P and K were not significantly different from each other in the soil after the harvest of saffron. However, the Ca and Mg content in soil decreased upon applications of *R. sphaeroides,* AMF and in combination (Table 4).

Among the micronutrient elements, there is no significant difference between the treatments in terms of Zn and Mn. However, the application of *R. sphaeroides* increased the Fe in soil, but not in plant (Table 3). But the combination of microorganisms lowered the Fe content compared to the control condition. The results suggest that the combination of mycorrhiza and bacterium both solubilize the elements and make them available for the plant. However, the contents of Cu, Zn, Mn, and Ni were all the lowest in the bacterial only treatment. This suggest that *R. sphaeroides* might use the elements and might compete with the plant for uptake. Therefore, this bacterium cannot be suggested as a microbial fertilizer for Saffron cultivation alone [44, 45].

4. Conclusion

Saffron is a highly prized spice derived from the stigmas of saffron plant (*Crocus sativus* L.). After the harvest of the flowers, the corms of the plant are kept for the next season while the leaves are considered as agricultural byproduct. This investigation focused on assessing the macro and micronutrient composition of saffron leaves following inoculation with *R. sphaeroides*, *Glomus iranicum* var. *tenuihypharum*, and their combination, particularly in a soil characterized by low organic content.

When the microbial fertilizers were applied, the morphological results revealed that the root length of saffron upon AMF spore inoculation alone was almost twice that of control. The application of bacteria alone resulted in higher fresh and dry weight of leaves. *R. sphaeroides* exhibited plant growth promoter effect saffron. The macro nutrient phosphorus (P) was observed the highest in saffron grown with the addition of bacteria and AMF combination, followed by the application of AMF alone. The macro nutrients Ca and Mg were found to be the lowest by bacterial application alone, however, the Mg content of saffron was found the highest in the plants grown upon the use of combination of bacteria and mycorrhiza. Therefore, in the germination phase, the application of *R. sphaeroides* cannot be suggested for saffron alone, while AMF application or the combination of these microorganisms can be suggested. The nutrient contents of the plant are important for the phytochemicals, too.

Article Information Form

Funding
The authors have no received any financial support for the research, authorship or publication of this study.

Authors' Contribution
MG: Design of the study, data collection, data analysis, writing, critical review of content, literature review
SY: Design of the study, data collection, data analysis, writing, critical review of content, literature review
SP: Data collection

The Declaration of Conflict of Interest/ Common Interest
No conflict of interest or common interest has been declared by the authors.

Artificial Intelligence Statement
No artificial intelligence tools were used while writing this article.

Copyright Statement

References

[1] T. ul G. Mir, A. K. Wani, J. Singh, S. Shukla, "Therapeutic application and toxicity associated with *Crocus sativus* (saffron) and its phytochemicals," Pharmacological Research - Modern Chinese Medicine, vol. 4, 2022.

[2] M. Sharma, R. Thakur, M. Sharma, "Ethnomedicinal, phytochemical and pharmacological properties of *Crocus sativus* (saffron)," The Journal of Indian Botanical Society, vol. 99, pp. 115–125, 2020.

[3] M. R. Khazdair, M. Hossein Boskabady, M. Hosseini, R. Rezaee, A. M. Tsatsakis, "The effects of *Crocus sativus* (saffron) and its constituents on nervous system: A review," Avicenna Journal of Phytomedicine, vol. 5, pp. 376–391, 2015.

[4] M. Butnariu, C. Quispe, J. Herrera-Bravo, J. Sharifi-Rad, L. Singh, N. M. Aborehab, A. Bouyahya, A. Venditti, S. Sen, K. Acharya, M. Bashiry, S. M. Ezzat, W. N. Setzer, M. Martorell, K. S. Mileski, I. C. Bagiu, A. O. Docea, D. Calina, W. C. Cho, "The Pharmacological Activities of Crocus sativus L.: A Review Based on the Mechanisms and Therapeutic Opportunities of its Phytoconstituents," Oxidative Medicine and Cellular Longevity, vol. 2022, 2022.

[5] H. Asil, "Effects of Chelated Iron (Eddha-Fe) Treatments on Corm And Stigma Quality in Saffron (Crocus Sativus L.)," Bangladesh Journal of Botany, vol. 52, pp. 97–103, 2023.

[6] A. Ozel, K. Erden, A. Özel, T. Demirbilek, "Determination of Optimum Corm Size for Saffron (Crocus sativus L.) and Corm Yield Under the Harran Plain Conditions," vol. 12, 2017.

[7] S. M. Jadouali, H. Atifi, Z. Bouzoubaa, K. Majourhat, S. Gharby, F. Achemchem, A. Elmoslih, A. Laknifli, R. Mamouni, "Chemical characterization, antioxidant

and antibacterial activity of Moroccan Crocus sativus L petals and leaves," Journal of Materials and Environmental Sciences, vol. 9, pp. 113–118, 2018.

[8] R. Srivastava, H. Ahmed, R. Dixit, Dharamveer, S. Saraf, "Crocus sativus L.: A comprehensive review," Pharmacognosy Reviews, vol. 4, pp. 200–208, 2010.

[9] UN Comtrade, Leading saffron spice exporters worldwide in 2022 (in million U.S. dollars), 2023.

[10] K. M. A. Rahman, D. Zhang, "Effects of fertilizer broadcasting on the excessive use of ınorganic fertilizers and environmental sustainability," Sustainability 2018, vol. 10, Page 759, vol. 10, p. 759, 2018.

[11] Z. A. Siddiqui, J. Pichtel, "Mycorrhizae: An overview," in: Mycorrhizae: Sustainable Agriculture and Forestry, Springer Netherlands, pp. 1–35, 2008.

[12] A. L. Alarcón, M. J. Gómez-Bellot, A. J. Bernabe, G. Calvo, F. Fernández Martín, "Changes in root architecture and productivity of melon (Cucumis melo L. cv. Hispano Nunhems) promoted by Glomus iranicum var. tenuihypharum," Journal of Horticultural Science and Biotechnology, vol. 95, pp. 364–373, 2020.

[13] G. Roccuzzo, F. Stagno, C. Frassineti, M. L. Maltoni, A. Assirelli, P. Sbrighi, G. Baruzzi, "Effects of arbuscular mycorrhizae Glomus iranicum var. tenuihypharum on strawberry fruit yield and quality," Acta Horticulturae, vol. 1309, pp. 613–620, 2021.

[14] F. Fernández, J. Juárez, A. J. Bernabe, F. J. García, J. M. Gómez, "Activity of the arbuscular mycorrhizal fungus, Glomus iranicum var. tenuihypharum var. nova, and its effect on citrus development in southeastern Spain," Acta Horticulturae, vol. 1230, pp. 73–84, 2019.

[15] M. Gürgan, S. Adiloğlu, "Phytoremediation and Purple Non Sulfur Bacteria, in: J.C. Flores (Ed.), The Future of Phytoremediation," Nova Science Publishers, New York, pp. 221–244, 2021.

[16] J. Sakpirom, D. Kantachote, T. Nunkaew, E. Khan, "Characterizations of purple non-sulfur bacteria isolated from paddy fields, and identification of strains with potential for plant growth-promotion, greenhouse gas mitigation and heavy metal bioremediation," Research in Microbiology, vol. 168, pp. 266–275, 2017.

[17] W.-T. Wong, C. Tseng, S.-H. Hsu, H.-S. Lur, C.-W. Mo, C.-N. Huang, S.-C. Hsu, K.-T. Lee, C.-T. Liu, "Promoting Effects of a Single Rhodopseudomonas palustris Inoculant on Plant Growth by Brassica rapa chinensis under Low Fertilizer Input," Microbes and Environments, vol. 29, pp. 303–313, 2014.

[18] T. Nunkaew, D. Kantachote, T. Nitoda, H. Kanzaki, "Selection of salt tolerant purple nonsulfur bacteria producing 5-aminolevulinic acid (ALA) and reducing methane emissions from microbial rice straw degradation," Applied Soil Ecology, vol. 86, pp. 113–120, 2015.

[19] T. Kantha, C. Chaiyasut, D. Kantachote, S. Sukrong, A. Muangprom, "Selection of photosynthetic bacteria producing 5-aminolevulinic acid from soil of organic saline paddy fields from the Northeast region of Thailand," African Journal of Microbiology Research, vol. 4, pp. 1848–1855, 2010.

[20] S. Kırıcı, B. Sevindik, Y. Yalçın Mendi, "Production of saffron in Turkey," Acta Horticulturae, pp. 403–410, 2020.

[21] F. Daldal, S. Cheng, J. Applebaum, E. Davidson, R. C. Princet, Cytochrome c2 is not essential for photosynthetic growth of Rhodopseudomonas capsulata, 1986.

[22] S. Adiloglu, F. Eryilmaz Acikgoz, F. Irmak Yilmaz, Y. Solmaz, A. Adiloglu, "The Effect of Increasing Mycorrhiza Applications on Nutrition of Pak Choi (Brassica rapa L. subsp. chinensis L.) Plant," International Journal of Secondary Metabolite, vol. 5, pp. 27–33, 2018.

[23] M. Jackson, Soil Chemical Analysis, Prentice-Hall of India Pvt. Ltd, New Delhi, 1967.

[24] M. T. Sağlam, Chemical analysis methods of soil and water, Namık Kemal University Publications, 2012.

[25] G. J. Bouyoucos, "A Recalibration of the Hydrometer Method for Making Mechanical Analysis of Soils," Agronomy Journal, vol. 43, pp. 434–438, 1951.

[26] B. Kacar, Chemical analysis of Plant and Soil-III. Soil Analysis, A. U. Agriculture Facultu Education, Research and Development Society Publishing House, Ankara, 1995.

[27] W. L. Lindsay, W. A. Norvell, "Development of a DTPA Soil Test for Zinc, Iron, Manganese, and Copper1," Soil Science Society of America Journal, vol. 42, pp. 421–428, 1978.

[28] B. Wolf, "The determination of boron in soil extracts, plant materials, composts, manures, water and nutrient solutions," Soil Science and Plant Analysis, vol. 2, pp. 363–374, 1971.

[29] Q. S. Wu, C. Y. Liu, D. J. Zhang, Y. N. Zou, X. H. He, Q. H. Wu, "Mycorrhiza alters the profile of root hairs in trifoliate orange," Mycorrhiza, vol. 26, pp. 237–247, 2016.

[30] M. Sheng, M. Tang, H. Chen, B. Yang, F. Zhang, Y. Huang, "Influence of arbuscular mycorrhizae on the root system of maize plants under salt stress," Canadian Journal of Microbiology, vol. 55, pp. 879–886, 2009.

[31] R. Hestrin, E. C. Hammer, C. W. Mueller, J. Lehmann, "Synergies between mycorrhizal fungi and soil microbial communities increase plant nitrogen acquisition," Communications Biology 2019 2:1, vol. 2, pp. 1–9, 2019.

[32] S.-M. Kang, R. Radhakrishnan, Y.-H. You, A. L. Khan, J.-M. Park, S.-M. Lee, I.-J. Lee, A. Latif Khan, "Cucumber performance is improved by inoculation with plant growth-promoting microorganisms," Acta Agriculturae Scandinavica, Section B, vol. 65, pp. 34–44, 2014.

[33] S. M. Kang, M. Imran, S. Shaffique, E. H. Kwon, Y. S. Park, I. J. Lee, "Growth and Photosynthetic Characteristics of Sesame Seedlings with Gibberellin-Producing Rhodobacter sphaeroides SIR03 and Biochar," International Journal of Plant Biology 2022, vol. 13, pp. 257-269, 2022.

[34] S. K. Lee, H. S. Lur, C. Te Liu, "From lab to farm: Elucidating the beneficial roles of photosynthetic bacteria in sustainable agriculture," Microorganisms, vol. 9, p. 2453, 2021.

[35] M. G. A. Van Der Heijden, R. D. Bardgett, N. M. Van Straalen, "The unseen majority: soil microbes as drivers of plant diversity and productivity in terrestrial ecosystems," Ecology Letters, vol. 11, pp. 296–310, 2008.

[36] Y. Wang, S. Peng, Q. Hua, C. Qiu, P. Wu, X. Liu, X. Lin, "The Long-Term Effects of Using Phosphate-Solubilizing Bacteria and Photosynthetic Bacteria as Biofertilizers on Peanut Yield and Soil Bacteria Community," Frontiers in Microbiology, vol. 12, p. 1871, 2021.

[37] T. N. Huu, T. T. N. Giau, P. N. Ngan, T. T. B. Van, N. Q. Khuong, "Potential of Phosphorus Solubilizing Purple Nonsulfur Bacteria Isolated from Acid Sulfate Soil in Improving Soil Property, Nutrient Uptake, and Yield of Pineapple (Ananas comosus L. Merrill) under Acidic Stress," Applied

and Environmental Soil Science, vol. 2022, 2022.

[38] M. S. Khan, E. Ahmad, A. Zaidi, M. Oves, "Functional aspect of phosphate-solubilizing bacteria: Importance in crop production," in: Bacteria in Agrobiology: Crop Productivity, Springer-Verlag Berlin Heidelberg, pp. 237–263, 2013.

[39] Q. Saeed, W. Xiukang, F. U. Haider, J. Kučerik, M. Z. Mumtaz, J. Holatko, M. Naseem, A. Kintl, M. Ejaz, M. Naveed, M. Brtnicky, A. Mustafa, "Rhizosphere bacteria in plant growth promotion, biocontrol, and bioremediation of contaminated sites: A comprehensive review of effects and mechanisms," International Journal of Molecular Sciences, vol. 22, 2021.

[40] M. Hawkesford, W. Horst, T. Kichey, H. Lambers, J. Schjoerring, I. S. Møller, P. White, "Functions of Macronutrients", in: Marschner's Mineral Nutrition of Higher Plants: Third Edition, Elsevier Ltd, pp. 135–189, 2011.

[41] O. S. Olanrewaju, B. R. Glick, O. O. Babalola, "Mechanisms of action of plant growth promoting bacteria," World Journal of Microbiology & Biotechnology, vol. 33, p. 197, 2017.

[42] M. Broadley, P. Brown, I. Cakmak, Z. Rengel, F. Zhao, "Function of nutrients: Micronutrients", in: Marschner's Mineral Nutrition of Higher Plants: Third Edition, Elsevier Inc., pp. 191–248, 2011.

[43] S. Adiloğlu, F. E. Açikgöz, M. Gürgan, "Use of phytoremediation for pollution removal of hexavalent chromium-contaminated acid agricultural soils," Global Nest Journal, vol. 23, pp. 400–406, 2021.

[44] W. Peng, X. Li, J. Song, W. Jiang, Y. Liu, W. Fan, "Bioremediation of cadmium- and zinc-contaminated soil using Rhodobacter sphaeroides," Chemosphere, vol. 197, pp. 33–41, 2018.

[45] H.-J. Bai, Z.-M. Zhang, G.-E. Yang, B.-Z. Li, "Bioremediation of cadmium by growing Rhodobacter sphaeroides: Kinetic characteristic and mechanism studies", Bioresource Technology, vol. 99, pp. 7716–7722, 2008.

Effect of Nickel on CO Conversion Over Cordierite-Supported Bi-Metallic Pd-Ni Catalysts

Ugur Caglayan [iD]

Cukurova University, Central Research Laboratory, Adana, Türkiye, ugurcalyan@hotmail.com, ror.org/05wxkj555
*Corresponding Author

ARTICLE INFO	ABSTRACT
	This study focused on the preparation and characterization of Pd-Ni bimetallic catalysts supported on cerium-coated cordierite for carbon monoxide oxidation in a batch system. Using techniques such as XRD, FTIR, SEM/EDS, and BET, we confirmed successful metal loading and strong interactions between the metals and the support. The BET results showed that catalysts with balanced Pd and Ni ratios, especially Ni50, had larger surface areas, likely due to synergistic effects. Catalytic tests carried out at 300 °C demonstrated that these bimetallic catalysts performed nearly as well as the pure Pd catalyst in converting CO, while also benefiting from the inherent activity of the cerium-coated support. Overall, this study suggests that combining Pd with Ni can reduce the amount of precious metal needed without sacrificing efficiency, pointing to a more cost-effective solution for emission control applications.

1. Introduction

Nowadays, air pollution caused by motor vehicles has become a serious environmental problem due to the release of toxic gases such as carbon monoxide (CO), hydrocarbons (HC) and nitrogen oxides (NO_x) into the atmosphere. Catalytic converters are widely used to convert these harmful gases into less harmful compounds before they are released into the atmosphere [1]. Catalytic converter technology plays a critical role in converting exhaust gases into harmless compounds. The success of this conversion depends largely on the type and nature of the catalyst used. The most commonly preferred catalysts in conventional converters were precious metals such as platinum (Pt), palladium (Pd) and rhodium (Rh) [2]. Although precious metals such as palladium (Pd) exhibit high catalytic activity in traditional catalytic converters, alternative systems need to be developed due to their high costs and limited availability [2].

In this context, bimetallic catalysts, especially the use of Pd together with the transition metal were promising in terms of both economics and catalytic performance [3, 4]. The metal that can potentially increase Pd activity was nickel (Ni). Recent studies on three-way catalyst (TWC) systems have revealed the role of transition metals, especially nickel, in enhancing catalytic activity. The strong interactions formed by nickel with ceria–zirconia-based oxide structures improve the redox properties at low temperatures, allowing lower light-off temperatures to be achieved during the cold start-up phase. In addition, the effect of nickel on catalytic behavior appears to be largely dependent on its interaction with the support material. Therefore, nickel is considered as an important supporting element in Pd-based systems [5, 6]. In bimetallic systems, the temperature at which the system is studied plays a critical role in determining the extent of metal-support and metal-metal interactions. For instance, one study demonstrated that the interaction between nickel and an alumina support is significantly enhanced at elevated

temperatures [7]. The synergistic interaction between palladium (Pd) and nickel (Ni) in bimetallic catalysts has been widely associated with enhanced catalytic activity, particularly when compared to their monometallic counterparts [8]. This enhancement becomes especially pronounced when the total metal loading exceeds 7 wt%, a condition under which direct metal–metal interaction has been reported [9].

The choice of support material for metal loading has a significant effect on catalyst performance as well. Cordierite stands out as an ideal support material for automotive applications thanks to its low thermal expansion coefficient and high temperature resistance [10, 11]. In this direction, cordierite was widely used as the preferred ceramic support material, especially for automotive applications. Thanks to its high mechanical stability and thermal resistance, the active phases coated on cordierite show long-term stability. The combined use of Pd and Ni on cordierite support material can offer significant advantages in reactions such as oxidation of CO and hydrocarbons due to their synergistic interactions. Therefore, understanding the nature of the Pd-Ni interaction and determining the key factors affecting it is important for the development of more effective Pd-Ni based catalytic systems.

It was seen that the studies examining Pd-Ni bimetallic systems on cordierite were limited in the literature. In this study, cordierite supported Pd-Ni bimetallic catalysts were prepared at different ratios and their effects on carbon monoxide conversion were systematically investigated in batch reactor. The study aims to evaluate the effect of Pd-Ni ratios on catalytic activity and to contribute to the lack of knowledge in this area.

2. Materials Methods

2.1. Catalyst preparation

A commercial cordierite honeycomb cordierite ($MgO–Al_2O_3–SiO_2$), measuring 20 mm × 25 mm × 25 mm with a cell density of 200 cpsi, was used as the catalyst support. Prior to metal deposition, the support was activated in 1 M HCl at 90 °C for

8 h. Metal catalysts were prepared via the impregnation method after cerium coating. The details on cerium coating were given elsewhere [12]. Metal salts ($PdCl_2$ and $NiSO_4.6H_2O$) corresponding to a total metal loading of 1 wt.% were dissolved in a mixture of 0.8 mL 0.5 M HNO_3 and 50 mL deionized water to enhance solubility and ensure uniform distribution. The cordierite supports were then introduced into this solution, and the mixture was stirred for 1 h at room temperature.

Catalysts with varying Pd:Ni ratios (100:75:50:25:0) were synthesized and labeled as Ni0, Ni25, Ni50, Ni75, and Ni100, respectively. Reduction of the metal ions was carried out by the dropwise addition of 10 mL of 0.20 M $NaBH_4$. Following reduction, the solvent was evaporated under heating and continuous stirring. The resulting materials were dried at 120 °C for 4 h and calcined at 500 °C for 16 h. Finally, thermal reduction was performed at 350 °C under a argon-hydrogen (95:5) atmosphere in a tubular furnace to ensure complete metal reduction on the support surface.

2.2. Catalyst characterization

The catalysts were subjected to X-ray diffraction examination using a PANalytical Powder Diffractometer operating at 45 KV and equipped with a Cu kα source (1 = 1.54 A). We obtained the scans from $2\theta = 10–80°$. Pd and Ni particles were identified on the carbon support using the scanning electron microscopy with energy dispersive X-ray spectroscopy (SEM/EDX) technique. A PerkinElmer Optima 7000 DV was used for inductively coupled plasma (ICP) analysis in order to quantify Pd and Ni particles on the support. FTIR analyses were carried out to determine the surface functional groups and support-metal interactions of the catalysts. Spectra were recorded in the $4000–400 cm^{-1}$ range in ATR (Attenuated Total Reflectance) mode using a Jasco FTIR spectrometer. The specific surface area of the samples was determined using the Brunauer–Emmett–Teller (BET) method with nitrogen adsorption at 77 K, and the BET surface area was calculated using a Micromeritics TriStar Plus II instrument.

2.3. Catalyst performance

The carbon monoxide conversion experiments were carried out in a batch reactor (Uniterm 100 mL). The 2.5 g catalyst was placed in the reactor and sealed, after that purged the air with Argon. The reactor was pressurized with CO at 1.0 bar. The temperature used for conversion was 300 °C at 250 rpm stirred for 30 min. The details on experiments were given elsewhere [12]. A thermal conductivity detector (TCD)-equipped online gas chromatograph (Agilent GC/TCD 7842) was used to analyze the compositions of the output gases. The Supelco 60/80 Carboxen 1000 columns were used in the instrument. For the GC analysis, the following temperature program was utilized: holding at 35 °C for 5 minutes, heating at a rate of 20 °C per minute to 225 °C, and then holding at this temperature for 10 minutes.

3. Results and Discussion

3.1. Evaluation of catalyst

Cordierite ($Mg_2Al_4Si_5O_{18}$) is a well-defined crystalline material used as a ceramic and catalytic carrier. When cerium (usually in the form of CeO_2) was loaded onto it, some differences in the XRD (X-ray diffraction) pattern can be observed (Fig 1a). The XRD peak intensity of the main phase was decreased by coating the cordierite surface following Ce loading.

XRD analyses were performed to determine the metallic phases and possible alloy formations in the catalysts (Fig 1b). Although the main phase diffraction peaks of cordierite slightly decreased upon cerium loading, no significant changes were observed in the XRD patterns of the resulting catalysts due to the low metal loading (~1%) on the surface. The increase in the intensity of cordierite diffraction peaks with higher Pd loading may be attributed to enhanced X-ray reflectivity due to the presence of Pd species on the surface, improved crystallinity of the cordierite phase induced by Pd deposition, or changes in surface morphology facilitating better diffraction signal collection [13, 14].
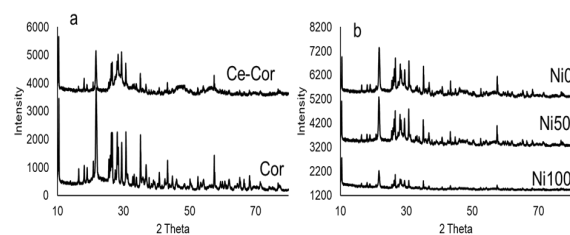
Figure 1. XRD spectras of cordierite (a) and catalysts (b)

Ni and Pd were loaded onto a cerium-coated cordierite support at different ratios, and structural analyses of the resulting catalysts were performed using Fourier Transform Infrared Spectroscopy (FTIR). FTIR measurements were used to determine the interactions between the support material and the metal species and to determine the functional groups on the surface. In the FTIR spectra shown in Figure 2a, the characteristic bands observed particularly in the 700–500 cm^{-1} range correspond to metal–oxygen (M–O) vibrations. The prominent peak observed around 670 cm^{-1} indicates Ce–O bonds and demonstrates the successful application of the cerium oxide coating [15]. Furthermore, the weak bands around 460–480 cm^{-1} can be attributed to the Si–O–Si and Al–O–Si vibration modes in the cordierite support structure.

Small shifts and intensity differences were observed in this region depending on the Ni and Pd loadings [16-18]. This indicates that the metal species interacted with the CeO_2 matrix and caused structural changes on the surface. In CeO_2 supported Ni and Pd based catalysts, the shifts and intensity differences observed in the range of 400–800 cm^{-1} showed that metal species interact with the CEO_2 matrix and cause structural changes on the surface. In our study, cerium nitrate was used as a cerium source. A nitrate N-O stretching centered at 1350 cm^{-1} [19-21]. The absence of bands belonging to residues such as nitrate (NO_3^-) in the spectra indicates that the prepared catalysts had clean surfaces.
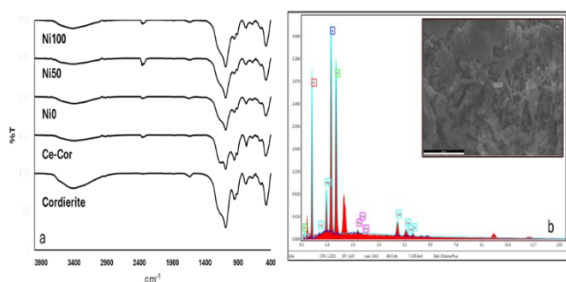
Figure 2. FTIR spectra of samples (a), SEM-EDS of Ni0 catalyst

BET surface area measurements revealed that the metal composition loaded onto the support material has a significant effect on the surface properties of the catalyst. The Ni50 sample had the largest surface area, measuring 13.3754 m²/g, when various Ni-Pd ratios were deposited onto a cerium-coated cordierite support. The sample with only Pd (Ni0) had a surface area of 6.3879 m²/g, whereas the sample with only Ni (Ni100) had the lowest surface area, at 4.2271 m²/g. This suggested that the combined use of Ni and Pd created a synergistic effect, creating a more open and porous structure on the support surface. Similarly, it has been reported in the literature that bimetallic catalysts can provide higher surface areas and more active centers compared to monometallic catalysts [22, 23]. The Ni-Pd combination, in particular, is known to improve catalytic properties through both structural and electronic interactions [24]. The decrease in surface area observed with increasing Ni content can be explained by nickel particles partially blocking the pores on the support surface or agglomeration, reducing the surface area. Indeed, it has been reported in the literature that Ni can form larger particles on the support surface at higher temperatures, limiting the surface area [25].

3.2. Catalyst activity

The catalytic activity of the synthesized catalyst was evaluated through the oxidation of carbon monoxide. Cordierite-supported bimetallic PdNi catalysts were developed in the present study. The Ni metal was taken into consideration when naming the catalysts. Ni100 was the name of the catalyst that had no Pd metal, while Ni0 was the name of the catalyst that contained all Pd. As indicated in Fig 3, the presence of noble metals strongly enhanced carbon monoxide conversion.

The cordierite support material used in this study was coated with cerium (Ce) before metal loading in the catalyst preparation (Ce-Cor). A very high CO conversion rate of 87.88% was obtained in CO oxidation experiments performed without any metal (Pd or Ni) loading on the cerium-coated cordierite. This result clearly showed that the support material itself has significant catalytic activity. This high activity was mainly due to the strong oxygen storage and release capacity (OSC) of cerium based on the $Ce^{4+} \rightleftharpoons Ce^{3+}$ redox couple. The CeO_2 phase facilitated the conversion of molecular oxygen into the active form by creating oxygen vacancies on its surface, thus supporting the oxidative transformation of CO [26, 27].

Thus, active oxygen species were continuously provided in the reaction medium, enabling CO molecules to effectively react with oxygen on the surface. The redox capability of the CeO_2 support created the oxidative environment even though, as mentioned in the experimental section, no external oxidant other than CO was added during the reaction. The CeO_2 facilitates oxygen transport to the active metal sites by acting as an oxygen reservoir through its Ce^{4+}/Ce^{3+} redox cycle [28]. Oxidation processes were helped by stabilizing chemical intermediates and providing lattice oxygen. The interaction between CeO_2 and Pd–Ni particles might be an essential point for oxygen overflow, improving catalytic activity. However, despite the high performance of the cerium-coated cordierite support, the presence of transition metals such as Pd and Ni is critical, especially in terms of increasing the reaction rate, lowering the activation energy and providing activity at lower temperatures.

The catalyst with only Pd (Ni0) exhibited the maximum activity with a CO conversion of 99.88%, According to this result, Pd had strong catalytic activity in the CO oxidation reaction, and cordierite-supported systems may successfully sustain this activity. The catalyst Ni25 showed a performance very close to the pure Pd catalyst with a conversion rate of 99.80%. This implied that adding small levels of Ni did not significantly affect the catalytic activity of Pd and, in certain cases, may even have a synergistic effect [29, 30]. It was possible that Ni electron-donating ability enhanced the

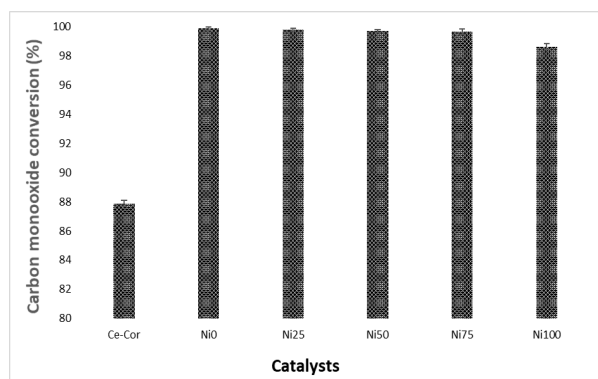reaction kinetics by balancing the CO adsorption and desorption on Pd.

Figure 3. The percentages carbonmonoxide conversion of catalysts

The catalyst containing 50% Ni (Ni50) again exhibited a very high performance with a conversion rate of 99.71%, but a small decrease in catalytic efficiency was observed with the decrease of the Pd content. Although this conversion indicated that Pd and Ni continue to work together, the Pd content shouldn't be lowered below the essential range. According to Liu et al. investigation on the catalytic performance of Pd–Ni nanoalloys in CO oxidation, the composition of 50% Pd–50% Ni exhibited the maximum activity. The strong relationship between this synergistic impact and the alloy phase state, chemical composition, and atomic structure was underlined [31]. There were examples in the literature where Pd–Ni alloys or doping alter energy barriers, creating a balance between concentration and activity-selectivity. Here, it was shown that doping Pd into Ni containing CeO_2 supported systems not only resulted in the formation of a Pd–Ni alloy structure, but also reduced energy barriers for dehydrogenation reactions with the assistance of oxygen species. This provides an example of how electron interactions between Pd–Ni can regulate catalytic activity [32]. Pd-Ni alloys can also exhibit concentration-selective behavior; selectivity and C-C bond breakage are affected by changes in Pd/Ni ratio and concentration.

In the case of Ni75, the conversion rate of catalyst was 99.67%. Despite achieving a high conversion, catalytic performance noticeably decreased as the Pd content decreased. This indicated that in order for Pd to maintain its role as an active center, it must be present at a minimum concentration. The lowest carbon monoxide conversion was shown by Ni100 catalyst (98.64%). This result clearly showed that Ni alone can be active in CO oxidation, but it did not have as high an activity as Pd. The low activity of Ni can be explained by the fact that CO molecules cannot be adsorbed sufficiently effectively on the surface or that oxygen activation was limited. Additionally, the work by Requies et al. shown that the activity of CO oxidation was enhanced by the addition of noble metals [33].

Pd was often necessary for catalytic activity, and alloying it with Ni in specific ratios can be regarded as a cost-cutting method without lowering performance much. These metals can have synergistic effects, as seen by the high conversion rates seen in Pd-Ni bimetallic systems. Furthermore, it was determined that, in terms of cost/performance, Ni25 and Ni50 ratios could be more appropriate for industrial applications, even though the reduction of Pd content results in minor performance losses.

4. Conclusion

The efficiency of the system design solution, which combined catalyst and engine technology, was realized decades after converters were invented. In this study, Pd-Ni bimetallic catalysts supported on cerium-coated cordierite were successfully prepared and characterized through a range of techniques including XRD, FTIR, SEM/EDS, and BET analysis. The characterization results confirmed that both metal dispersion and metal–support interactions were effectively achieved. BET measurements, in particular, showed that bimetallic compositions such as Ni25 and Ni50 provided increased surface areas, suggesting a synergistic structural effect.

Catalytic tests further demonstrated that these compositions maintained high CO conversion rates, nearly matching that of the pure Pd catalyst. These findings highlight the potential of Pd-Ni systems to reduce noble metal usage without compromising performance, offering a promising route toward more cost-effective and efficient catalytic materials for emission control. The significance of cerium oxide coatings in improving oxygen storage and transfer was

highlighted in this work, which contributed to the growing body of research exploring noble-metal dilution approaches through bimetallic design. Future studies should concentrate on thermal aging effects, long-term stability testing under actual exhaust settings, and mechanical insights using in situ or operating spectroscopic methods. It would also be crucial for developing up the catalyst composition and include it into monolithic converter systems in order to assess its economic potential. High catalytic efficiency with significantly reduced Pd loading has important economic and environmental advantages from an industrial perspective, especially for use in stationary pollution control systems and automotive exhaust treatment.

Article Information Form

The Declaration of Conflict of Interest/ Common Interest
No conflict of interest or common interest has been declared by authors.

Artificial Intelligence Statement
No artificial intelligence tools were used while writing this article.

Copyright Statement
The author owns the copyright of their work published in the journal and their work is published under the CC BY-NC 4.0 license.

References

[1] E. S. J. Lox, B. H. Engler, in: G. Ertl, H. Knözinger, J. Weitkamp (Eds.), Environmental Catalysis, Wiley-VCH, p. 1, 1999.

[2] A. Martínez-Arias, J. C. Conesa, M. Fernández-García, J. A. Anderson, in: J. A. Anderson, M. Fernández-García (Eds.), Supported Metals in Catalysis, Imperial College Press, p. 283, 2005.

[3] J. F. Trillat, J. Massadier, B. Morawek, H. Praliaud, A. J. Renouprez, "Reduction of NO by CO on manganese promoted palladium catalysts," Studies in Surface Science and Catalysis, vol. 116, p. 103, 1998.

[4] A. B. Hungría, A. Iglesias-Juez, A. Martínez-Arias, M. Fernández-García, J. A. Anderson, J. C. Conesa, J. Soria, "The effect of Ni in Pd–Ni/(Ce,Zr)O$_x$/Al$_2$O$_3$ catalysts used for stoichiometric CO and NO elimination. Part 1: Nanoscopic characterization of the catalysts," Journal of Catalysis, vol. 235, pp. 251–432, 2005.

[5] V. R. Mastelaro, V. Briois, D. P. F. de Souza, C. L. Silva, "Structural studies of a ZrO$_2$–CeO$_2$ doped system," Journal of the European Ceramic Society, vol. 23, pp. 273–282, 2003.

[6] A. B. Hungría, A. Iglesias-Juez, A. Martínez-Arias, M. Fernández-García, J. A. Anderson, J. C. Conesa, J. Soria, "The effect of Ni in Pd–Ni/(Ce,Zr)O$_x$/Al$_2$O$_3$ catalysts used for stoichiometric CO and NO elimination. Part 2: Catalytic activity and in situ spectroscopic studies," Journal of Catalysis, vol. 235, p. 262, 2005.

[7] A. Ivanova, E. Slavinskaya, R. Gulyaev, V. Zaikovskii, O. Stonkus, I. Danilova, L. Plyasova, I. Polukhina, A. Boronin, "Metal–support interactions in Pt/Al$_2$O$_3$ and Pd/Al$_2$O$_3$ catalysts for CO oxidation," Applied Catalysis B: Environmental, vol. 97, no. 1-2, pp. 57–71, 2010.

[8] M. Mihet, M. Lazar, "Effect of Pd and Rh promotion on Ni/Al$_2$O$_3$ for NO reduction by hydrogen for stationary applications," Chemical Engineering Journal, vol. 251, pp. 310–318, 2014.

[9] F. B. Noronha, M. C. Durão, M. S. Batista, L. G. Appel, "The role of Ni on the performance of automotive catalysts: Evaluating the ethanol oxidation reaction," Catalysis Today, vol. 85, pp. 13–21, 2003.

[10] O. A. Al-Harbi, C. Özgür, M. M. Khan, "Fabrication and characterization of single phase cordierite honeycomb monolith with porous wall from natural raw materials as catalyst support," Ceramics International, vol. 41, no. 3, pp. 3526–3532, 2015.

[11] A. V. Boix, J. M. Zamaro, E. A. Lombardo, E.E. Miró, "The beneficial effect of silica on the activity and thermal stability of PtCoFerrierite-washcoated cordierite monoliths for the SCR of NOx with CH4," Applied Catalysis B: Environmental, vol. 46, no. 1, pp. 121–132, 2003.

[12] U. Caglayan, G. Avsar, "Enhancing catalytic converter performance: effects of noble metals and rare earth washcoating on CO and NOx conversion," Research in Chemistry, pp. 1–17, 2024.

[13] Y. Li, Q. Liao, W. Ling, F. Ye, F. Liu, X. Zhang, J. He, G. Cheng, "Pd/δ-MnO$_2$ nanoflower arrays cordierite monolithic catalyst toward toluene and o-xylene combustion," Frontiers in Chemistry, vol. 10, p. 978428, 2022.

[14] H. Rönkkö, J. Keskinen, J. Keskinen, J. Jokiniemi, "Investigation of CO deactivation of passive NOx adsorption on la promoted Pd/BEA," Emission Control Science and Technology, 2021.

[15] S. R. De Miguel, M. E. Rivas, "Surface characterization of cordierite monoliths washcoated with Pt/Al$_2$O$_3$ catalysts," Applied Surface Science, vol. 172, no. 1–2, pp. 78–85, 2001.

[16] H. Chen, L. Luo, Z. Zhang, H. Zhang, X. Wang, "Ni/CeO$_2$ nanocomposite catalysts for CO methanation: Influence of Ni loading and reaction temperature," RSC Advances, vol. 6, no. 45, pp. 41275–41283, 2016.

[17] S. Ghosh, S. Dash, C. R. Raj, "In situ FTIR and electrochemical studies on methanol oxidation over Pd supported on ceria," Topics in Catalysis, vol. 62, no. 17–20, pp. 1291–1301, 2019.

[18] S. M. Abbas, S. Anwer, "Structural, optical and catalytic properties of CeO$_2$ nanoparticles doped with Fe and Ni ions," Journal of Materials Science: Materials in Electronics, vol. 30, pp. 11172–11184, 2019.

[19] E. Pérez-Gallent, M. C. Figueiredo, I. Katsounaros, M. T. Koper, "Electrocatalytic reduction of Nitrate on Copper single crystals in acidic and alkaline solutions," Electrochimica Acta, vol. 227, pp. 77-84, 2017.

[20] J. Baltrusaitis, J. Schuttlefield, J. H. Jensen, V. H. Grassian, "FTIR spectroscopy combined with quantum chemical calculations to investigate adsorbed nitrate on aluminium oxide surfaces in the presence and absence of co-adsorbed water," Physical Chemistry Chemical Physics, vol. 9, no. 36, pp. 4970-4980, 2007.

[21] L. V. Volod'ko, L. T. Huoah, "The vibrational spectra of aqueous nitrate solutions," Journal of Applied Spectroscopy, vol. 9, no. 4, pp. 1100-1104, 1968.

[22] A. Wang, X. Y. Liu, C. Y. Mou, T. Zhang, "Understanding the synergistic effects of gold bimetallic catalysts," Journal of catalysis, vol. 308, pp.258-271, 2013.

[23] R. J. Zhang, W. U. Yu, N. I. E, Hong, "Effect of support on the performance of Ni-based catalyst in methane dry reforming," Journal of Fuel Chemistry and Technology, vol. 43, no. 11, pp. 1359-1365, 2015.

[24] F. Liao, T. W. B. Lo, S. C. E. Tsang, "Recent Developments in Palladium-Based Bimetallic Catalysts," ChemCatChem, vol. 7, no. 14, pp. 1998-2014, 2015.

[25] H. Wan, X. Li, S. Ji, B. Huang, K. Wang, C. Li, "Effect of Ni loading and CexZri-xO2 promoter on Ni-based SBA-15 catalysts for steam reforming of methane," Journal of Natural Gas Chemistry, vol. 16, no. 2, pp. 139-147, 2007.

[26] A. Martínez-Arias, M. Fernández-García, A. Iglesias-Juez, A. B. Hungría, J. A. Anderson, J. C. Conesa, J. Soria, "New Pd/Ce$_x$Zr$_{1-x}$O$_2$/Al$_2$O$_3$ three-way catalysts

prepared by microemulsion: Part 2. In situ analysis of CO oxidation and NO reduction under stoichiometric CO+NO+O$_2$," Applied Catalysis B: Environmental, vol. 31, no. 1, pp. 51–60, 2001.

[27] M. Fernández-García, A. Martínez-Arias, L. N. Salamanca, J. M. Coronado, J. A. Anderson, J. C. Conesa, J. Soria, "Influence of ceria on Pd activity for the CO+O2 reaction," Journal of Catalysis, vol. 187, no. 2, pp. 474–485, 1999.

[28] J. Lee, T. H. Lim, E. Lee, D. H. Kim, "Promoting the methane oxidation on Pd/CeO$_2$ catalyst by increasing the surface oxygen mobility via defect engineering," ChemCatChem, vol 13, no. 16, pp. 3706-3712, 2021.

[29] W. W. Lonergan, T. Wang, D. G. Vlachos, J. G. Chen, "Effect of oxide support surface area on hydrogenation activity: Pt/Ni bimetallic catalysts supported on low and high surface area Al$_2$O$_3$ and ZrO$_2$," Applied Catalysis A: General, vol. 408, pp. 87–95, 2011.

[30] L. Liu, L. Yu, X. Zhou, C. Xin, S. Sun, Z. Liu, X. Tai, "Comparative study of Pd–Ni bimetallic catalysts supported on UiO-66 and UiO-66-NH$_2$ in selective 1,3-butadiene hydrogenation," Nanomaterials, vol. 12, no. 9, p. 1484, 2022.

[31] S. Shan, V. Petkov, L. Yang, J. Luo, P. Joseph, D. Mayzel, C. J. Zhong, "Atomic-structural synergy for catalytic CO oxidation over palladium–nickel nanoalloys," Journal of the American Chemical Society, vol. 136, no. 19, pp. 7140–7151, 2014.

[32] X. Li, Z. Yang, L. Zhang, Z. He, R. Fang, Z. Wang, Z., Y. Yang, J. Ran, "Effect of Pd doping in (Fe/Ni)/CeO$_2$ catalyst for the reaction path in CO$_2$ oxidative ethane dehydrogenation/reforming," Energy, vol. 234, pp. 121261, 2021.

[33] J. Requies, M. C. Alvarez-Galvan, V. L. Barrio, P. L. Arias, J. F. Cambra, M. B. Güemez, A. Manrique, V. A. de la Peña, J. L. G. Fierro, "Palladium–manganese catalysts supported on monolith systems for methane combustion," Applied Catalysis B: Environmental, vol. 79, pp. 122–131, 2008.

The Effects of Pre-evaporation Time on the Structure and Performance of Na-Lignosulfonate/PVA Composite Films

Emir Erişir [ID]

Sakarya University of Applied Sciences, Pamukova Vocational School, Department of Material and Material Prcessing Technologies, Sakarya, Türkiye, emirerisir@subu.edu.tr, ror.org/01shwhq58
*Corresponding Author

ARTICLE INFO

ABSTRACT

Lignin, an abundant renewable biopolymer in nature, contains specific structural limitations affecting its application strategies. So, a favoured strategy is to use it into the manufacturing of composite materials with other natural or synthetic polymers. This study examines the impact of controlled accelerated solvent removal (pre-evaporation), a subject that is still not thoroughly explored, on the structural, morphological, and thermal characteristics of Na-lignosulfonate (LS) and polyvinyl alcohol (PVA) composite films. Aqueous solutions containing LS, PVA, glycerol and urea were formulated for the casting of composite films. A pre-evaporation at 85-90 °C for 0 to 240 min was employed to solution enhancing its concentration prior to being poured into moulds. The ^{13}C-NMR and FTIR used for structural characterisation validated the specific aromatic and aliphatic structure of LS. FTIR analysis identified interactions between LS and PVA in the films, indicating changes in the ether bond peaks (~1039 cm^{-1}). TGA demonstrated that LS enhanced the thermal stability of the composites and facilitated carbonisation above 450°C. Examination by SEM of the composite films indicated that the pre-evaporation duration significantly affected the morphology. A 5–14% decrease in film thickness and an increase in pore size and number, particularly on the exposed surface, were observed, but the change did not occur uniformly. LS/PVA films were effectively produced without internal stress during pre-evaporation durations of up to 150 min. At times exceeding 150 min, excessive solvent loss and increased solution viscosity resulted in significant morphological defects such as internal stresses, large pores, and structural integrity failure, leading film casting impossible at 240 min. The study determined that the 150 min pre-evaporation procedure is an essential limit for the production of composite films from these polymers. The results obtained are crucial for improving the processing parameters of lignin-based composites intended for packaging or carbon precursor applications.

1. Introduction

A considerable portion of biopolymer research focuses on biomass components, including cellulose, hemicellulose, and lignin, which are some of the most abundant polymers in nature. Lignin, a natural aromatic polymer, is a crucial structural component, providing rigidity and strength to plant cell walls, and serves as a renewable feedstock. It is found heterogeneously distributed in the middle lamella within the cell wall and between cells. However, lignin is found in the middle lamella or cell walls in a complex mixture with other plant polymers, which complicates its pure extraction and direct utilization.

The diversity of plant sources from which lignin is obtained, and delignification methods enable the production of different types of lignin suitable for various application areas. In addition to traditional lignin types such as kraft lignin and lignosulfonates, new-generation lignin variants obtained through methods such as steam

explosion, organosolv, deep eutectic solvents, or dilute acid treatments are also available [1].

The fact that the pulping (or delignification) method directly affects the physical and chemical properties of lignin significantly expands and diversifies the application areas of this valuable biopolymer. Historically, lignin was considered a waste product, especially for the paper industry, and until recently, it was generally disposed of by burning for energy production.

In recent years, research into the use of this valuable biopolymer and its composites as carbon precursors for graphene production has attracted considerable attention [2-9]. However, the limited film-forming capabilities of lignin and its derivatives limit their direct application. Therefore, the evaluation in combination with other polymers is essential for applications such as film production.

Due to its water solubility, biodegradability potential, and compatibility with natural polymers [10, 11], polyvinyl alcohol (PVA) is a widely used polymer such as lacquers, adhesives, surface coating materials, films, and plastic materials [12]. While lignin/PVA composite films have been successfully produced, the studies investigating the effects of process parameters on film properties during film production are relatively limited in the literature.

In this study, the effects of increasing the lignin/PVA solutions concentration before the film casting process on film properties were investigated. It was anticipated that film characteristics would rise to a specific threshold with increasing concentration, subsequently declining thereafter. To this end, a controlled accelerated solvent removal process was applied to increase the concentration of solutions prepared at a specific initial concentration. The solutions obtained at different concentrations were cast into molds of the same volume and size to produce films, and the structural, thermal and morphological properties of these films were thoroughly investigated.

2. General Methods

2.1. Materials

Sodium lignosulfonate (LS, Pars Kimya, M_w: 500-2000 g/mol), polyvinyl alcohol (PVA, Merck, ≥98% hydrolzed, M_w: 60000 g/mol), glycerol (Balmumcu Kimya, USP grade, M_w: 92.09 g/mol), and urea (Merck, M_w: 60.06 g/mol, purity ≥99%) were used for film production without any purification procedure. Deionized water (DI) was utilized throughout all production and characterization phases.

2.2. Production of lignin-PVA films

Approximately 2.00 g of PVA was dissolved in 20 ml of DI water. The dissolution was conducted in an oil bath at 85-90°C, with magnetic stirring maintained at a constant speed of 500 rpm. In another container, approximately 2.00 g of LS, 0.20 g of urea, and 4.00 ml of a 25 wt% glycerol solution were dissolved in 20 ml of DI water using a stirring rod. The solution was thereafter allowed to heat at 85-90°C. After 15 min, the LS solution (20 ml) was incorporated into the PVA solution (20 ml). The container was covered and the LS-PVA mixture was continued to be stirred at 85–90°C and 500 rpm for 60 min. At the end of the 60 min mixing period, the cover of the reaction container was removed to facilitate the preliminary evaporation of the solvent. The preliminary evaporation of water occurred for 0, 30, 60, 90, 105, 120, 135, 150, 180 or 240 min.

The prepared LS-PVA mixture was poured into two silicon casting molds with an inner diameter of 10 cm and allowed to cure at 28°C for approximately 12-16 hours in a climate-controlled setting. Upon completion of the drying period, the films were removed from the molds and preserved in zip-sealed bags.

2.3. Characterization methods

2.3.1. Wet chemistry analysis

The lignin and ash contents of sodium lignosulfonate were determined according to TAPPI standards (T222 om-11 and T211 om-02, respectively).

2.3.2. NMR analysis

NMR studies were performed to evaluate the structure of LS. Samples were dissolved to make 20 g/L solutions in DMSO-d$_6$ for analysis on a Bruker Ascend high-resolution digital 500 MHz nuclear magnetic resonance (NMR) spectrometer.

2.3.3. Thermogravimetric (TGA) analysis

A Mettler Toledo TGA 2 model thermogravimetric analyser was used for thermal analysis. Approximately 8.00 mg of sample was accurately weighed for each test. The tests were conducted under a nitrogen atmosphere at a heating rate of 10°C/min within a temperature range of 30°C to 900°C.

2.3.4. Fourier transform infrared spectroscopy

A Bruker Optik GMBH Tensor 37 instrument was used for the measurements. Operating range was from 4000 to 400 cm^{-1} and the spectral resolution was set to 2 cm^{-1}.

2.3.5. Scanning Electron Microscopy (SEM)

Images from a scanning electron microscope (SEM) were obtained to analyze the morphological properties of the films. The images were captured from both surfaces of the films: the open (exposed) surface where evaporation occurred unimpeded and the closed surface in contact with the mold. Prior to starting the imaging process, the films were cut into small pieces for the morphological imaging. The samples were subsequently coated with gold-palladium before measurement. Imaging was conducted utilizing a Thermo Scientific Axia device at magnification levels of 100x, 1000x, 2500x, and 5000x. All tests were performed under vacuum conditions at an acceleration voltage of 15 kV.

3. Results and Discussion

3.1. Characterization of neat lignosulfonate

The structural characteristics of LS obtained commercially from a local provider were determined using wet chemical and instrumental analysis methods. The lignin content of LS was determined to be 93.92%, while the ash content was found to be 5.86%. The spectrum obtained from the ^{13}C-NMR analysis is presented in Figure 1.

The aliphatic carboxyl groups in LS were observed at 172.54 ppm [13-15]. The absence of distinct signals in the 90–102 ppm range indicates that the sample contains a low amount of residual wooden carbohydrates [15]. In the 161.43–112.33 ppm range, aromatic moieties of lignin were detected in accordance with previous studies [14, 16-18]. In this region, strong signals indicating p-coumaric ester for C-4 were identified around 159 ppm [15], while similarly strong signals for aromatic C–H of C5 were present between 114.63 and 116.93 ppm [18].
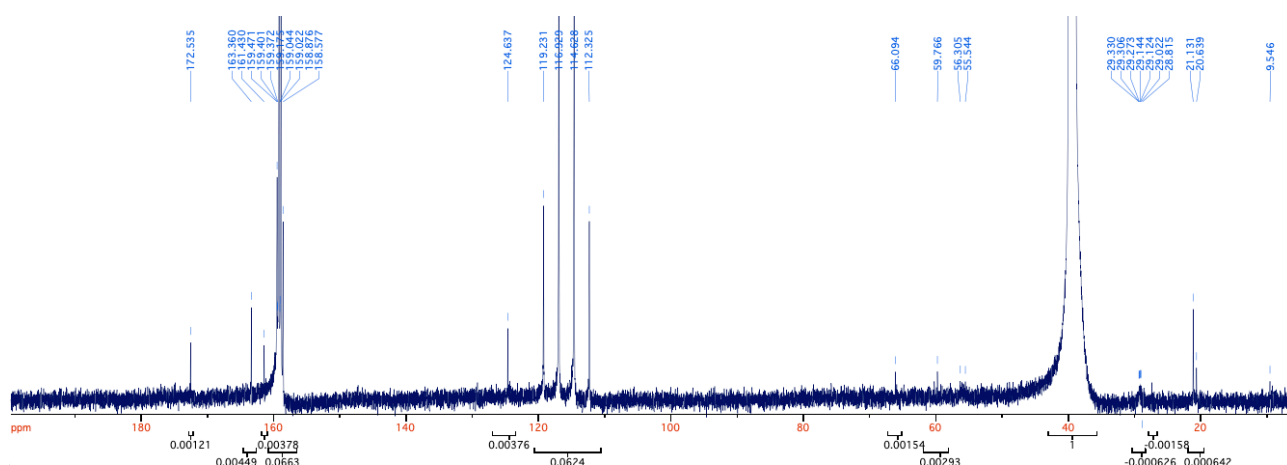

Figure 1. ^{13}C-NMR spectrum of neat Na-lignosulfonate

Relatively weaker signals observed at 112.33 and 119.23 ppm indicate aromatic C–H bonds in C2 and C6, respectively [18]. Aliphatic oxygen-containing groups are present in the 60–90 ppm region [19]. The signals indicating the carbon in the methoxy group were detected at 56.31 ppm [13-14, 18]. The strong signal in the 40 ppm region is attributed to DMSO-d6, which was used to dissolve the sample.

The FTIR patterns of neat LS in Figure 2 reveal that peaks associated with C=C stretching vibrations from the aromatic ring structure of the lignin, detected at 1440–1594 cm^{-1} [18, 20-22].
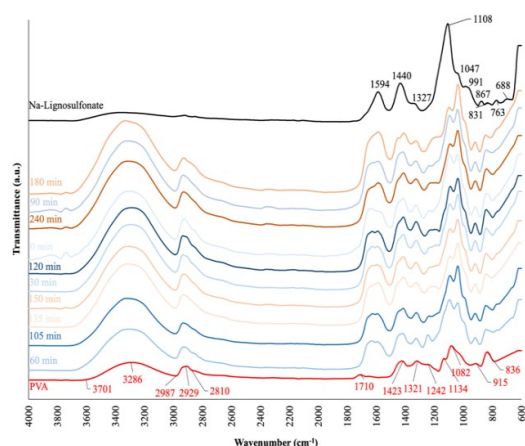

Figure 2. The FTIR spectrum of neat PVA and LS with their films

Very weak absorptions indicating methylene and methyl groups of side chains and aromatic methoxy groups were observed in the 2800–3000 cm^{-1} range, and hydroxyl groups were indicated in the 3000–3600 cm^{-1} range [23]. A shoulder at 1047 cm^{-1} indicates S=O stretching and sulfonate group (SO$_3$) absorption vibrations [18, 20-21].

The vibrations observed in the 900–750 cm^{-1} region are attributed to bending vibrations from aromatic component C-H bonds, and the vibrations observed in the 1280–1030 cm^{-1} region are attributed to stretching vibrations from C-O bonds of various alcohols, phenols, esters, and ethers [24]. The vibration observed around 688 cm^{-1} is thought to originate from the out-of-plane bending of C–H bonds [18].

3.2. Characterization of lignosulfonate-PVA films

3.2.1. FTIR analysis

The FTIR pattern of neat PVA presented in Figure 2 exhibits some characteristic bands. The PVA skeletal band was observed at 836 cm^{-1} [25]. In the 3000-3600 cm^{-1} region, stretching vibrations indicating O–H from intermolecular and intramolecular hydrogen bonds can be clearly observed compared to the LS pattern [26]. However, the magnitude of this peak is small rather than that of LS-PVA films, as explained later. Furthermore, the bending vibration of OH groups can be seen in the 1423-1242 cm^{-1} band range [27].

In the same figure, the stretching vibration of C–H from alkyl groups was detected in the 2810–2927 cm^{-1} band range [28, 29] while C-O stretching vibrations were observed around 1134 cm^{-1} [27, 29]. Additionally, the vibrational band in this region is attributed to the crystallinity of PVA [26]. Weak shoulders observed in the 1000–1200 cm^{-1} band range were detected at 1082 cm^{-1} in this study and are attributed to ether bonds [30]. The vibrations observed in the form of shoulders at 1710 cm^{-1} are attributed to stretching vibrations originating from C=O [29].

Upon comparing the FTIR spectra of LS-PVA films, it was observed that the peak intensity corresponding to OH groups, which are indicative of neat LS and PVA, increased in the 3000–3600 cm^{-1} range. In contrast, according to Su & Fang [27], the vibration peaks in the relevant region decreased compared to neat polymers. A possible explanation for this is that water evaporation without a thermal process was carried out during film formation, resulting in a large amount of remaining water in the film.

The peak observed at 1030 cm^{-1} has been identified by previous researchers as indicating an ether bond (C-O-C), and it has been determined that the magnitude of this peak is related to the extent of the aldol reaction between lignin and PVA [31]. In the present study, the relevant peak was observed at 1039 cm^{-1}, but it is slightly affected by the peak at 1108 cm^{-1}, which belongs to the stretching vibrations of the C-O functional groups of LS. However, the same peak was observed with a shift to 1097 cm^{-1}, and its intensity decreased. Additionally, the sulfur-containing compounds present in LS also vibrate in a region very close to this point. As a result of these interactions, both a slight change in peak intensity and a slight shift in the expected wavenumber have occurred. However, despite all

this, it is clear that there is an interaction between LS and PVA.

3.2.2. TGA and DTG analysis

The effects of different pre-evaporation times (0–240 min) on the thermal behaviour of LS/PVA films derived from solutions were investigated using TGA and DTG curves presented in Figures 3 and 4.

In the initial analysis of the TGA curves (Figure 3), common trends were identified. A multi-step and gradual thermal degradation was observed in both neat PVA and all LS/PVA films between 30°C and 900°C. A distinct mass loss starting at 30°C and ending around 120°C was also observed in all samples, which is generally associated with the removal of free and bound water from the polymers [32, 33]. DTG curves (Figure 4) also show peaks of varying sizes in this region. Notably, neat PVA demonstrates the lowest mass loss compared to other samples in this specific region, which is consistent with the FTIR patterns presented in Figure 2.

The mass loss of neat PVA accelerated around 300°C, reached 50% at about 350°C and 90% around 430°C. The complete decomposition of PVA mass observed at approximately 494°C. All these stages were reported in previous studies describing the degradation and dehydrogenation of the PVA main chain [33]. In films containing lignosulfonate, it was observed that at least 30% of the mass was retained at the temperature at which PVA was completely degraded.

The degradation of LS/PVA composite films follows a three-stage process (Figures 3 and 4). The initial region, beginning around 180°C and extending to approximately 250°C, indicates certain reactions resembling, yet occurring at lower temperatures compared to, the degradation process of neat PVA. The DTG curves (Figure 4) distinctly exhibit peaks associated with these modifications. It is hypothesized that the main degradation mechanism of PVA is affected and occurs at lower temperatures due to the degradation of low molecular weight and unstable lignosulfonate components and side chains attached to the aromatic ring of lignin in this region [34].

The more stable aromatic structure and higher molecular weight components of lignosulfonate degrade at higher temperatures compared to the lower molecular weight lignin chains. Given that neat PVA is expected to completely degrade above 450°C, the significant amount of residual mass detected above this temperature in LS/PVA films is explained by their char formation tendency [34].
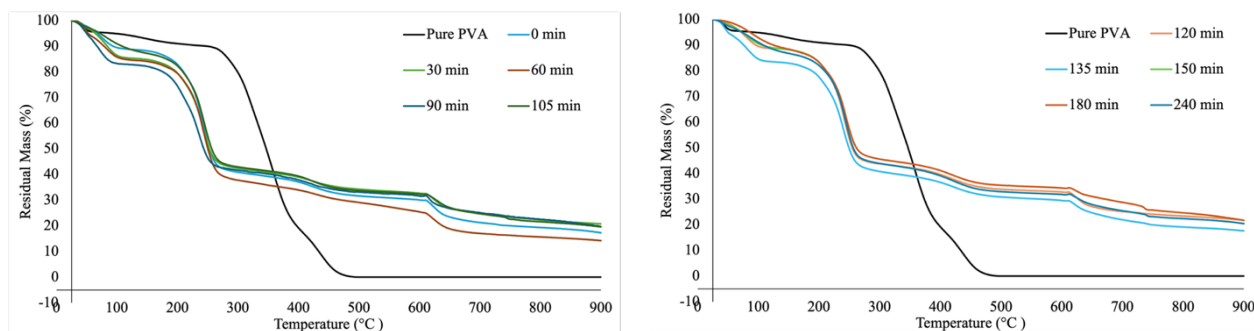

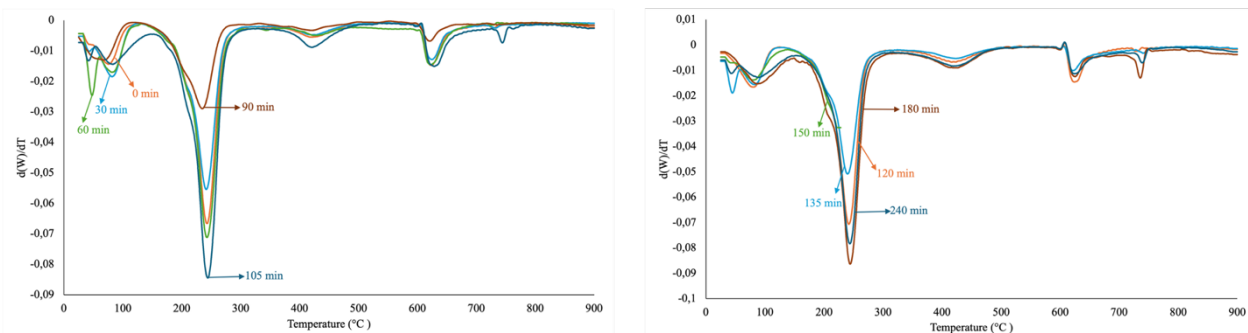**Figure 3.** Thermal decomposition graphs of neat PVA and LS/PVA films

Figure 4. DTG curves for LS/PVA films

The thermal decomposition results suggest that the stepwise degradation observed in LS/PVA films holds promise for graphene production without the need for a substrate. Extensive research on this topic is planned for subsequent studies.

3.2.3. SEM analysis

The morphological structures of the films were examined using SEM with the previously described method and the film images were presented in Figures 5 and 6. This enabled a topographical comparison between the open (top) surfaces (contact with atmosphere) and the closed (bottom or mold-contacting) surfaces (contact with the filming mold) of films.

Increasing the pre-evaporation time during film formation caused significant structural changes in the morphology and surfaces of films. The most critical effect observed was the evolution of porosity. As the pre-evaporation time extended from 150 to 240 min, the increased solvent removal led to a higher viscosity of the lignin-PVA solution. This led to disorders in the film matrix and the larger pores.

It was found that the film-forming ability of the samples cast from solutions applied above 150 min of pre-vaporization is significantly reduced. The situation can be clearly recognized from the macroscopic images of the films depicted in Figures 7. This phenomenon can be attributed to the increase in viscosity of solution resulting from the evaporation of more than half of the solvent, leading to the formation of a thicker, gel-like matrix. The gelation prevents the solution from spreading uniformly in the mold, inhibiting the formation of a continuous, smooth film layer. Changing the evaporation rate is known to raise the internal tension during high film development [35]. Conversely, the research by Feng et al. [36] revealed that films produced from higher concentration solutions had superior surface morphology.

Extended pre-vaporization reduced the drying time, but it probably increased internal stresses, leading to the deterioration of film morphology. Excessive solvent loss makes it difficult for polymer chains to rearrange and form a stable network structure, leading to microstructural defects, which in turn reduce the integrity and morphological quality of the films.

SEM images of the films with higher magnifications such as 2500 and 5000x revealed a network structure morphology as a network structure up to 150 min. However, this network structure appears to be layered, especially for some films. A noticeable colour difference can be observed between the closed and open surfaces of the films. The bottom surfaces that encounter the mold surface of the films take on a distinct light color, while the upper surfaces are darker in tone (Figure 7).

The chemical incompatibility between lignosulfonate and PVA can be seen in film morphology as polymer aggregates and microphase separation [37]. It was shown that at elevated lignin concentrations, additional lignin does not interact uniformly with the PVA matrix, functioning just as a filler [38]. This results in a heterogeneous morphology that decreases the film's structural integrity and adversely affects its mechanical properties. This kind of behaviour is quite similar to the idea of microphase separation, which describes how two parts of a film might generate separate phases at the molecular level

4. Conclusion

This study investigated the effects of pre-evaporation time on the properties of Na-lignosulfonate (LS)/PVA composite films, identifying a critical processing threshold for successful film fabrication.

Structural characterization analyses revealed the high purity of the lignin used in the study and the details of its aromatic structure. FTIR spectroscopy indicated the characteristic vibrations of both neat LS and PVA. The presence of an ether bond vibrations around 1039 cm^{-1}, indicating aldol reactions between LS and PVA, demonstrates the successful production of composite films. However, in the films, the peaks located at 3000-3600 cm^{-1} were larger than those of both polymers, suggesting that the drying conditions chosen for film production were insufficient for solvent removal.
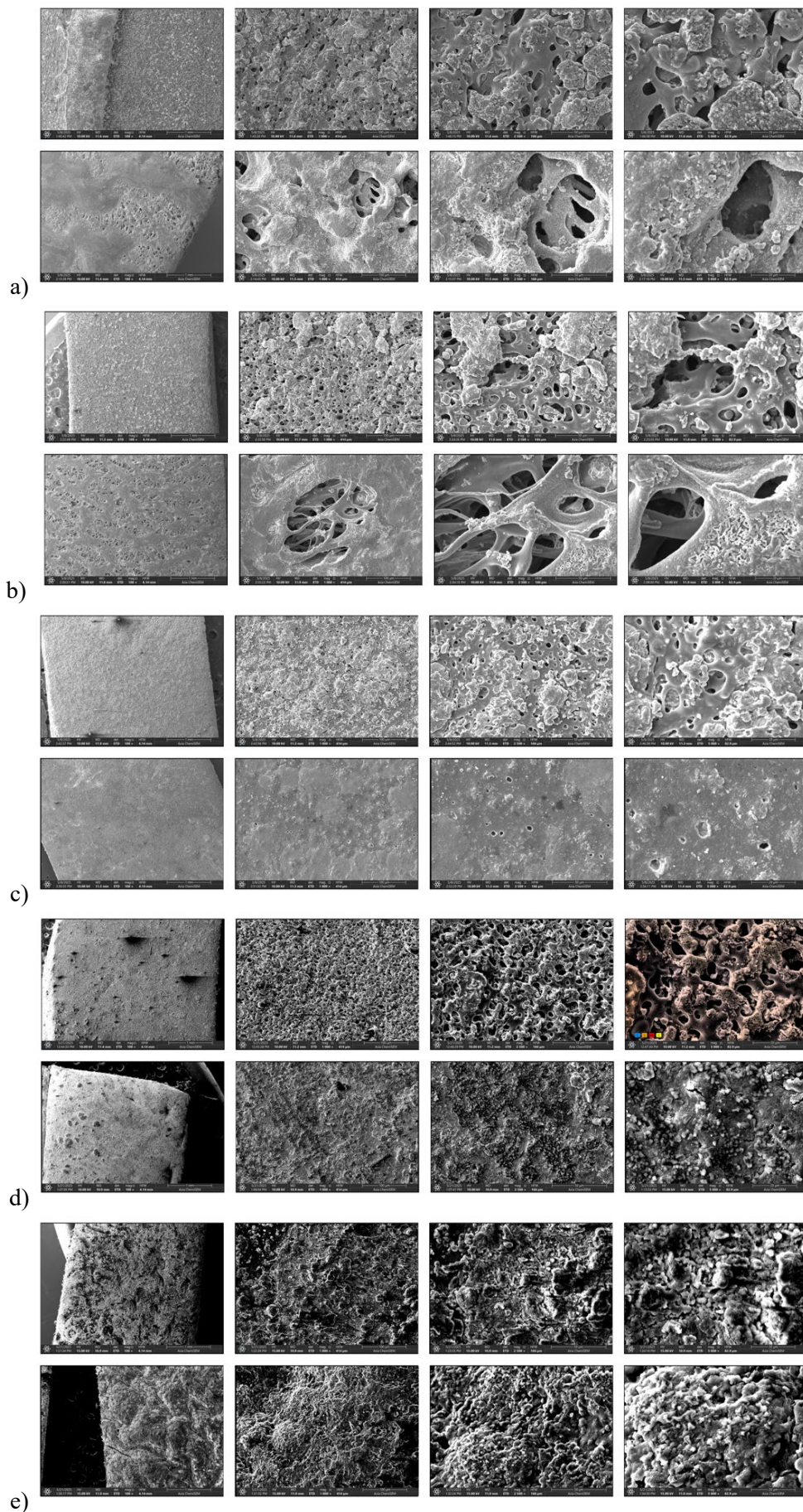
Figure 5. SEM images of lignin-PVA films' surfaces recorded at magnifications of 100, 1000, 2500, and 5000x (a: 0 min., b: 30 min., c: 60 min., d: 90 min., e: 105 min.)
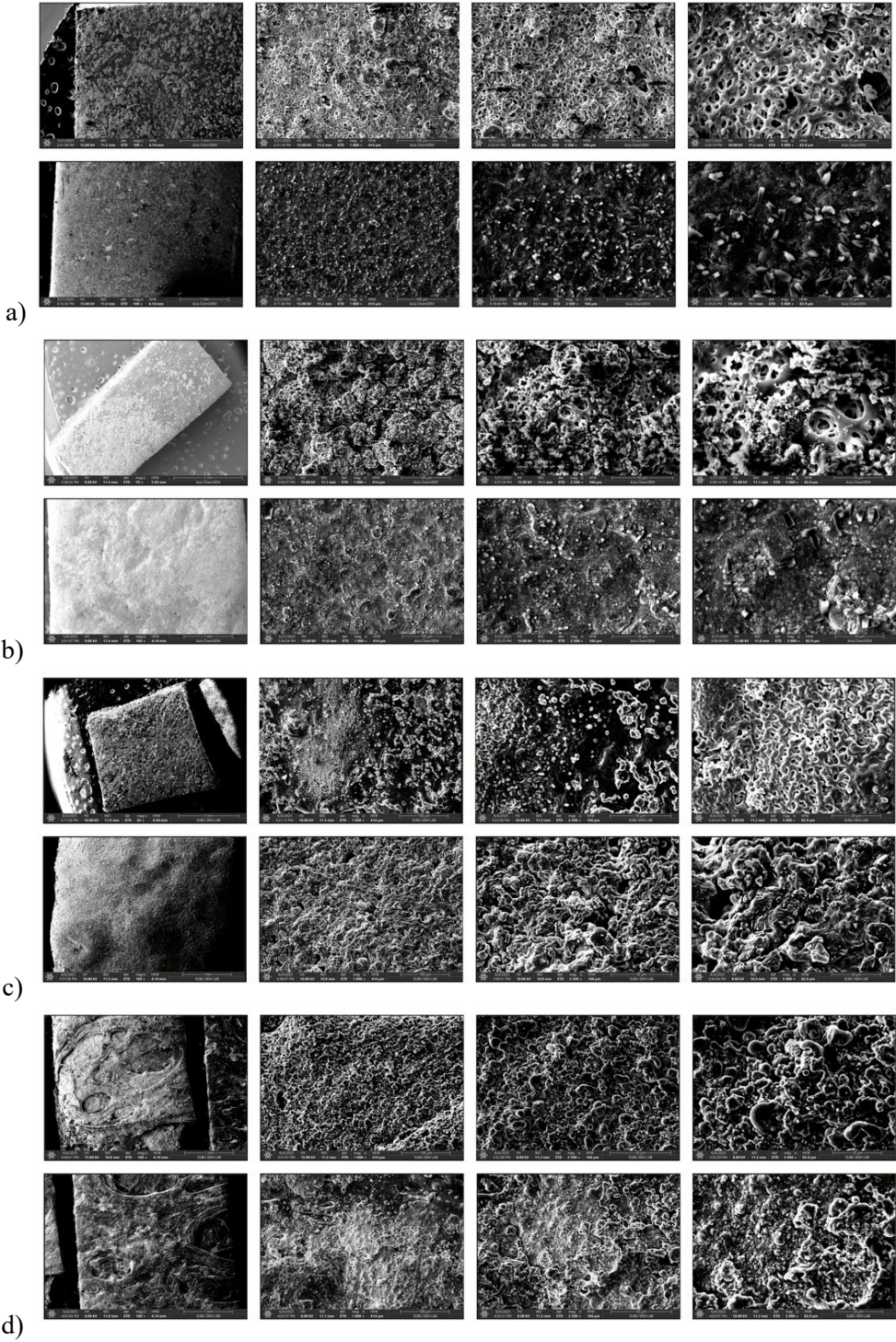
Figure 6. SEM images of lignin-PVA films' surfaces recorded at magnifications of 100, 1000, 2500, and 5000x (a: 120 min., b: 135 min., c: 150 min., and d: 240 min.)
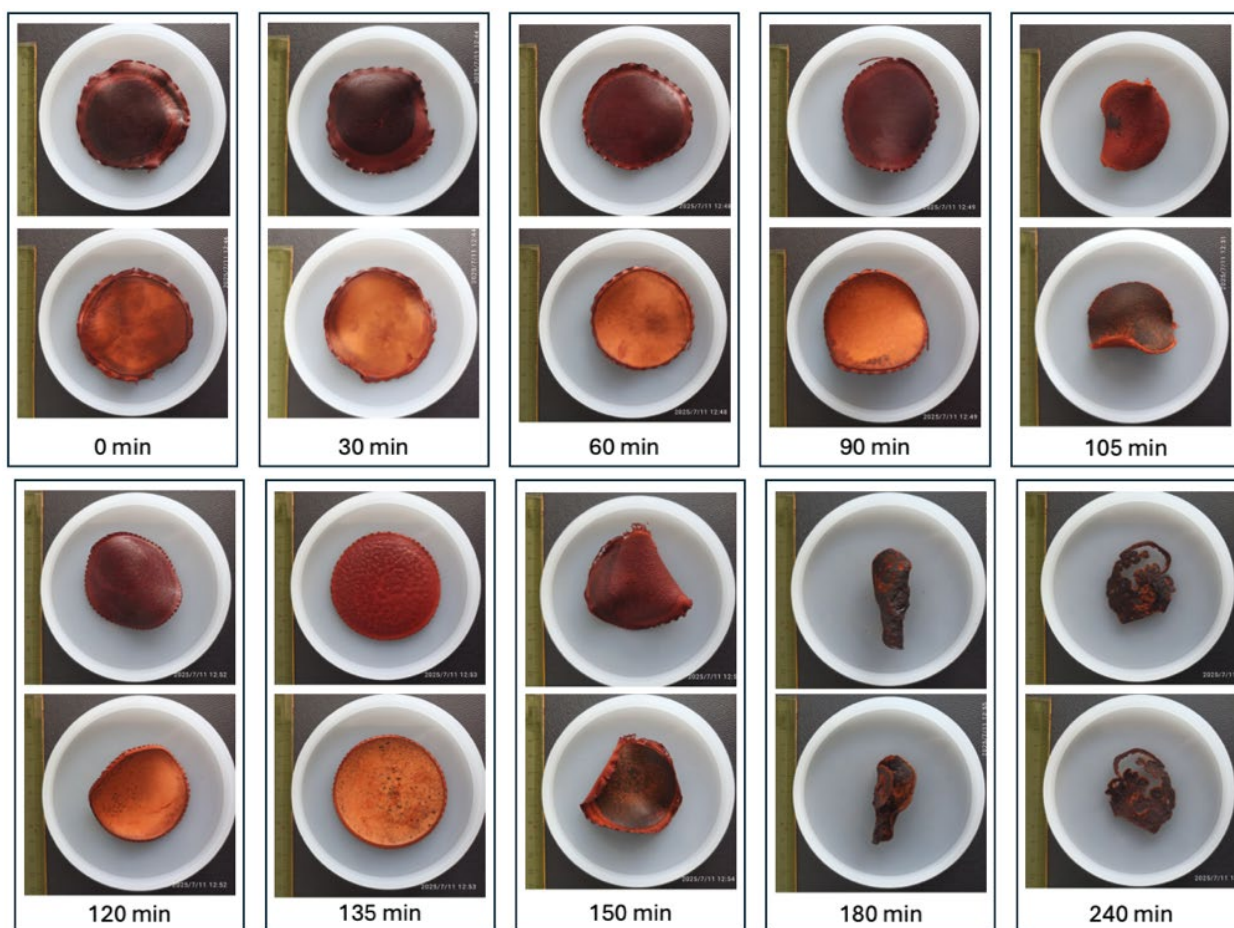
Figure 7. Macroscopic images of lignin-PVA films

A thermal treatment step at a higher temperature is needed to reduce the water content in the films. The remaining water content in the films was confirmed by thermogravimetric analysis. The most significant conclusion is the influence of pre-evaporation time on film morphology. A distinct point was found at 150 min. The pre-evaporation process created films with a continuous network structure. The process successfully increased the solution concentration without causing catastrophic consequences. Prolonged pre-evaporation led to the removal of excessive amounts of solvent, creating a highly viscous, gel-like solution. It resulted in a solution that was not spread evenly across the mold, creating a lot of internal stress in the film.

Thermogravimetric investigations demonstrated that the addition of LS enhanced the thermal stability of neat PVA and promoted carbonisation in the composites at elevated temperatures (>450°C). This, along with the mentioned enhancements in film structure, increases the possible uses of these composites for applications requiring heat resistance or as precursors to carbon-based materials like graphene.

Consequently, the pre-evaporation process must be carried out with considerable precision. It saves time by removing excess solvent from the casting solution, but the time must be carefully optimized within a narrow range (≤150 min under these specific conditions) to avoid morphological defects. Future research should focus on removing residual solvent from the films and exploring opportunities for improvement in interfacial adhesion and microphase separation.

Article Information Form

Kocaeli University for providing access to their laboratory facilities.

References

[1] H. Chung, N. R. Washburn, "Extraction and types of lignin," in Lignin in Polymer Composites, O. Faruk and M. Sain, Eds. Oxford, UK: Elsevier Inc., pp. 13-25, 2016.

[2] Y. Lei, A. H. Alshareef, W. Zhao, S. Inal, "Laser-scribed graphene electrodes derived from lignin for biochemical sensing," ACS Applied Nano Materials, vol. 3, no. 2, pp. 1166-1174, 2020.

[3] Y. Lei, W. Zhao, Y. Zhu, U. Buttner, X. Dong, H. N. Alshareef, "Three-dimensional Ti_3C_2T x MXene-Prussian blue hybrid microsupercapacitors by water lift-off lithography," ACS Nano, vol. 16, no. 2, pp. 1974-1985, 2022.

[4] C. Lee, S. Jeong, Y. Kwon, J. Lee, S. Cho, B. Shin, "Fabrication of laser-induced graphene-based multifunctional sensing platform for sweat ion and human motion monitoring," Sensors and Actuators A: Physical, vol. 334, p. 113320, 2021.

[5] Y. Lin, Q. Zhang, Y. Deng, Q. Wu, X. P. Ye, S. Wang, G. Fang, "Fabricating graphene and nanodiamonds from lignin by femtosecond laser irradiation," ACS Omega, vol. 6, no. 49, pp. 33995-34002, 2021.

[6] F. Mahmood, C. Zhang, Y. Xie, D. Stalla, J. Lin, C. Wan, "Transforming lignin into porous graphene via direct laser writing for solid-state supercapacitors," RSC Advances, vol. 9, pp. 22713-22720, 2019.

[7] L. Meng, S. Chirtes, X. Liu, M. Eriksson, W. C. Mak, "A green route for lignin-derived graphene electrodes: A disposable platform for electrochemical biosensors," Biosensors and Bioelectronics, vol. 218, p. 114742, 2022.

[8] K. Sinha, L. Meng, Q. Xu, X. Wang, "Laser induction of graphene onto lignin-upgraded flexible polymer matrix," Materials Letters, vol. 286, p. 129268, 2021.

[9] A. Wen, C. Wang, J. Nong, C. Hu, "Rapid construction of robust and hydrophilic lignin-derived laser-induced graphene electrodes using PVA-free dopants," Carbon, vol. 232, p. 119767, 2025.

[10] J. Du, J. Guo, Q. Zhu, J. Guo, J. Gu, Y. Wu, L. Ren, S. Yang, J. Jiang, "Enhancement of polyvinyl alcohol-based films by chemically modified lignocellulosic nanofibers derived from bamboo shoot shells," Polymers, vol. 17, no. 11, p. 1571, 2025.

[11] S. G. Jin, "Production and application of biomaterials based on polyvinyl alcohol (PVA) as wound dressing," Chemistry–An Asian Journal, vol. 17, no. 21, p. e202200595, 2022.

[12] R. Nagarkar, J. Patel, "Polyvinyl alcohol: A comprehensive study," Acta Scientific Pharmaceutical Sciences, vol. 3, no. 4, pp. 34-44, 2019.

[13] R. El Hage, N. Brosse, L. Chrusciel, C. Sanchez, P. Sannigrahi, A. Ragauskas, "Characterization of milled wood lignin and ethanol organosolv lignin from miscanthus," Polymer Degradation and Stability, vol. 94, no. 10, pp. 1632-1638, 2009.

[14] I. Korbag, S. Mohamed Saleh, "Studies on the formation of intermolecular interactions and structural characterization of polyvinyl alcohol/lignin film," International Journal of Environmental Studies, vol. 73, no. 2, pp. 226-235, 2016.

[15] L. Yang, D. Wang, D. Zhou, Y. Zhang, T. Yang, "Isolation and further structural characterization of lignins from the valonea of Quercus variabilis," International Journal of Biological Macromolecules, vol. 97, pp. 164-172, 2017.

[16] Z. Xia, L. G. Akim, D. S. Argyropoulos, "Quantitative ^{13}C NMR analysis of lignins with internal standards," Journal of Agricultural and Food Chemistry, vol. 49, no. 8, pp. 3573-3578, 2001.

[17] P. Phansamarng, A. Bacchus, F. H. Pour, C. Kongvarhodom, P. Fatehi, "Cationic lignin incorporated polyvinyl alcohol films for packaging applications," Industrial Crops and Products, vol. 221, p. 119217, 2024.

[18] S. M. Nasef, A. Sayed, G. A. Mahmoud, "Comparative study of lignin and sodium lignosulfonate extracted from irradiated and non-irradiated sawdust wastes," Radiation Physics and Chemistry, vol. 214, p. 111302, 2024.

[19] O. Y. Abdelaziz, S. Meier, J. Prothmann, C. Turner, A. Riisager, C. P. Hulteberg, "Oxidative depolymerisation of lignosulphonate lignin into low-molecular-weight products with Cu–Mn/δ-Al$_2$O$_3$," Topics in Catalysis, vol. 62, pp. 639-648, 2019.

[20] N. S. Abdelrahman, E. Galiwango, A. H. Al-Marzouqi, E. Mahmoud, "Sodium lignosulfonate: A renewable corrosion inhibitor extracted from lignocellulosic waste," Biomass Conversion and Biorefinery, vol. 14, no. 6, pp. 7531-7541, 2024.

[21] J. Ou, J. Zhao, "Modification of sodium lignosulfonate and evaluation of its potential use as detergent builders," Journal of Wood Chemistry and Technology, vol. 37, no. 2, pp. 99-109, 2017.

[22] E. S. Wibowo, B. D. Park, "Chemical and thermal characteristics of ion-exchanged lignosulfonate," Molecules, vol. 28, no. 6, p. 2755, 2023.

[23] X. Li, Y. Liu, X. Ren, "Transparent and ultra-tough PVA/alkaline lignin films with UV shielding and antibacterial functions," International Journal of Biological Macromolecules, vol. 216, pp. 86-94, 2022.

[24] E. Apaydın Varol, Ü. Mutlu, "TGA-FTIR analysis of biomass samples based on the thermal decomposition behavior of hemicellulose, cellulose, and lignin," Energies, vol. 16, no. 9, p. 3674, 2023.

[25] H. E. Mahmud, A. Kassim, Z. Zainal, W. M. M. Yunus, "Fourier transform infrared study of polypyrrole–poly (vinyl alcohol) conducting polymer composite films: evidence of film formation and characterization," Journal of Applied Polymer Science, vol. 100, no. 5, pp. 4107-4113, 2006.

[26] H. S. Mansur, R. L. Oréfice, A. A. Mansur, "Characterization of poly (vinyl alcohol)/poly (ethylene glycol) hydrogels and PVA-derived hybrids by small-angle X-ray scattering and FTIR spectroscopy," Polymer, vol. 45, no. 21, pp. 7193-7202, 2004.

[27] L. Su, G. Fang, "Characterization of cross-linked alkaline lignin/poly (vinyl alcohol) film with a formaldehyde cross-linker," BioResources, vol. 9, no. 3, pp. 4477-4488, 2014.

[28] P. B. Bhargav, V. M. Mohan, A. K. Sharma, V. N. Rao, "Structural, electrical and optical characterization of pure and doped poly (vinyl alcohol)(PVA) polymer

electrolyte films," International Journal of Polymeric Materials and Polymeric Biomaterials, vol. 56, no. 6, pp. 579-591, 2007.

[29] H. S. Mansur, C. M. Sadahira, A. N. Souza, A. A. Mansur, "FTIR spectroscopy characterization of poly (vinyl alcohol) hydrogel with different hydrolysis degree and chemically crosslinked with glutaraldehyde," Materials Science and Engineering: C, vol. 28, no. 4, pp. 539-548, 2008.

[30] S. Akhter, K. Allan, D. Buchanan, J. A. Cook, A. Campion, J. M. White, "XPS and IR study of X-ray induced degradation of PVA polymer film," Applied Surface Science, vol. 35, no. 2, pp. 241-258, 1988.

[31] L. Su, Z. Xing, D. Wang, G. Xu, S. Ren, G. Fang, "Mechanical properties research and structural characterization of alkali lignin/poly (vinyl alcohol) reaction films," BioResources, vol. 8, no. 3, pp. 3532-3543, 2013.

[32] M. E. El Moustaqim, A. El Kaihal, M. El Marouani, S. Menlayakhaf, M. Taibi, S. Sebbahi, S. El Hajjaji, F. Kifani-Sahban, "Thermal and thermomechanical analyses of lignin," Sustainable Chemistry and Pharmacy, vol. 9, pp. 63-68, 2018.

[33] M. T. Taghizadeh, N. Yeganeh, M. Rezaei, "The investigation of thermal decomposition pathway and products of poly (vinyl alcohol) by TG-FTIR," Journal of Applied Polymer Science, vol. 132, no. 25, p. 42117, 2015.

[34] Y. W. Chua, H. Wu, Y. Yu, "Interactions between low-and high-molecular-weight portions of lignin during fast pyrolysis at low temperatures," Energy & Fuels, vol. 33, no. 11, pp. 11173-11180, 2019.

[35] J. Li, M. H. P. de Heer Kloots, G. van Ewijk, D. J. van Dijken, W. M. de Vos, J. van der Gucht, "Evaporation-induced polyelectrolyte complexation: The role of base volatility and cosolvents," Langmuir, vol. 40, no. 5, pp. 2531-2542, 2024.

[36] S. Feng, D. Ma, Y. Qiu, L. Duan, "Deep insights into the viscosity of small molecular solutions for organic light-emitting diodes," RSC Advances, vol. 8, no. 8, pp. 4153-4161, 2018.

[37] G. Xu, S. Ren, D. Wang, L. Su, G. Fang, "Fabrication and properties of alkaline lignin/poly (vinyl alcohol) blend membranes," BioResources, vol. 8, no. 2, pp. 2510-2520, 2013.

[38] S. Kubo, J. F. Kadla, "The formation of strong intermolecular interactions in immiscible blends of poly(vinyl alcohol) (PVA) and lignin," Biomacromolecules, vol. 4, no. 3, pp. 561-567, 2003.

Flow Patterns Around a Sphere in Terms of Wall Proximity

Ilker Goktepeli[1*] (iD), Murat Ispir[1] (iD), Muharrem Hilmi Aksoy[1] (iD)

[1] Konya Technical University, Faculty of Engineering and Natural Sciences, Department of Mechanical Engineering, Konya, Türkiye, igoktepeli@ktun.edu.tr, mispir@ktun.edu.tr, mhaksoy@ktun.edu.tr, ror.org/02s82rs08
* Corresponding Author

ARTICLE INFO

ABSTRACT

Flow over a sphere exhibits three-dimensional phenomena even at lower values of Reynolds number (Re). Nonetheless, three-dimensional flow structures may also be affected by boundary layers on the rough walls. For this reason, the effects of wall proximity are very significant for the present case. Regarding these issues, flow characteristics of a sphere have been examined for several gap ratios from $G^* = 0.01$ to $G^* = 2$ at Re = 250. The influence of jet flow between the sphere and the wall has increased by decreasing the gap ratio. Although symmetrical flow patterns have been observed for $G^* = 1$ and $G^* = 2$, this situation is not valid for $G^* \leq 0.5$ in the present study. It is clearly observed in the wake regions for $G^* \leq 0.25$ and the positive cross-stream velocity components become more dominant, especially for $G^* = 0.1$ and $G^* = 0.25$, respectively. The positive spanwise vorticity component becomes more dominant; however, the negative one is more dominant for $G^* \leq 0.1$ in terms of gap ratios. For the case of $G^* \leq 0.05$, the drag coefficients are less than $C_D = 0.47$ and these values are so close to each other. For $G^* = 0.1$, it is around $C_D = 0.5$ for the present problem. By increasing the gap ratios, drag coefficient values also indicated an increasing trend. Moreover, $C_D = 0.579$ has been attained for the case of $G^* = 0.25$ and it is approximately $C_D = 0.68$ for $G^* = 0.5$ as observed. On the other hand, the values of $G^* = 1$ and $G^* = 2$ approached the values of the uniform flow conditions and the effect of the wall proximity by the boundary layer of the bottom surface disappeared.

1. Introduction

Flow characteristics around bluff bodies are important for discussions about aerodynamics. Viscous fluid flow over a sphere could be evaluated as a simplified problem in terms of a prevailing family of immersed bluff bodies owing to its widespread applications [1]. Furthermore, flowing past a sphere indicates three-dimensional phenomena even for lower Reynolds number values [2]. The vortex behavior with instability could show the nature of the resulting flow and large scale shed vortices around these bodies are related to the shear layers separation from the spherical surfaces [3]. Therefore, investigation of flow past a sphere is linked to various engineering applications and the particle transport is considered due to its

modelling as a sphere [4]. The flow interference is seen by the vortex shedding and pressure field in the wake region [5].

Regarding previous issues, various studies on the flow around a sphere are significant due to their consideration in engineering cases and this problem has been examined for the effects of several flow parameters. Sweeney and Finlay [6] observed the drag and lift forces of a sphere attached to a wall for boundary layer effect. Tsutsui [7] considered the turbulent boundary layer influence on flow around a sphere Re = 83000. Different height values have been evaluated for the problem. Martinez et al. [8] considered forces of a sphere and a cylinder close to a wall in a boundary layer. Mongruel et al. [9] presented a study on the sphere approach to a

wall. Liu and Prosperetti [10] considered the influence of walls on a rotating sphere. Yahiaoui and Feuillebois [11] scrutinized the lift effect on a sphere moving close to a wall in terms of parabolic flow. Dey et al. [12] studied the turbulent wake flows of a sphere on a rough wall. Rodriguez et al. [13] numerically investigated the flow around a sphere. Homann et al. [14] scrutinized the effects of drag and lift fluctuations for a sphere and its boundary layer. Hajimirzaie et al. [15] presented a study for flow around a surface-mounted spherical body in a boundary layer. Chastel and Mongruel [16] observed the flow between a sphere and a textured wall. Zhao et al. [17] examined the vortex structures of a sphere by considering the boundary layer effect at Re = 4170. Experimental study has been presented by van Hout et al. [18] for the sphere wake immersed in a boundary layer. Tee et al. [19] studied the motion of spheres in a turbulent boundary layer. Numerical simulations have been carried out by Yin and Ong [20] for the wake flow of a sphere in a pipe at lower Reynolds number values. Chandel and Das [21] examined the effects of wall proximity on the wake regions of a rotating and translating spheres. Chizfahm et al. [22] numerically studied the flow-induced vibrations of a sphere in terms of free surface proximity. Feng et al. [23] determined the effects of the wall on the flow dynamics for a sphere in motion. Shang et al. [24] simulated the flow characteristics around a sphere on a flat plate for boundary layer. Shepard et al. [25] considered the flow structure for the junction of cylinder-sphere. Li et al. [26] investigated the flow interaction between a sphere and turbulent boundary layer. Kumar et al. [27] examined the wall influence on the sphere wake for the transverse rotation. Considering the previous studies, flow charactistics of a sphere have been examined for different gap ratios.

The purpose of this study is to investigate the impact of gap ratios on the flow dynamics surrounding a sphere at a Reynolds number of 250. As previously highlighted, the flow around a sphere demonstrates three-dimensional characteristics even at lower Reynolds number values. However, the three-dimensional flow patterns could also be influenced by the boundary layers on rough surfaces. It is widely recognized that there are few studies available in open literature regarding the effects of wall proximity. Nevertheless, it is essential to take into account the boundary layer effects for spherical objects in engineering applications.

2. Numerical Method

In the present study, as presented in Figure 1, three-dimensional flow volume has been established for flow around a sphere having a diameter of D = 12.5 mm close to the wall in terms of the different gap ratios ranging for $0.01 \leq G^* = G/D \leq 2$. The dimensions for the flow volume are $-20 \leq x^* = x/D \leq 40$, $-20 \leq y^* = y/D \leq 20$ and $-20 \leq z^* = z/D \leq 20$. The sphere is at $x^* = y^* = z^* = 0$. Aerodynamic flow characteristics have been considered for Re = $U_\infty D \nu^{-1}$ = 250 by the kinematic viscosity for air. Uniform velocity has been used at the inlet. For the outlet of the three-dimensional flow volume, pressure outlet has been considered. As implemented for the spherical surfaces, wall boundary condition has been applied for both top and bottom walls.
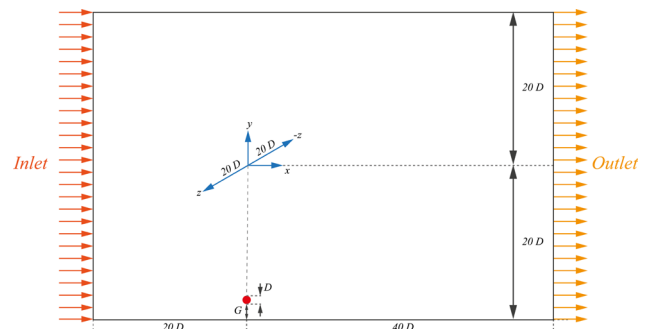
Figure 1. Schematic of the present study

In the current study, ANSYS-Fluent 2021 R1 has been utilized for numerical simulations. The continuity equation has been indicated by Eq. (1). The momentum equations have been presented in Eqs. (2-4).

These equations are valid for three-dimensional, incompressible flow and steady flow conditions. Furthermore, body forces are negligible. These equations have also been given similarly by Mahir [5]. These equations for three-dimensonal case have been derived from two-dimensional ones [28, 29].

$$\frac{\partial u}{\partial x} + \frac{\partial v}{\partial y} + \frac{\partial w}{\partial z} = 0 \qquad (1)$$

$$u\frac{\partial u}{\partial x} + v\frac{\partial u}{\partial y} + w\frac{\partial u}{\partial z} = -\frac{1}{\rho}\frac{\partial P}{\partial x} + \nu\left(\frac{\partial^2 u}{\partial x^2} + \frac{\partial^2 u}{\partial y^2} + \frac{\partial^2 u}{\partial z^2}\right) \qquad (2)$$

$$u\frac{\partial v}{\partial x} + v\frac{\partial v}{\partial y} + w\frac{\partial v}{\partial z} = -\frac{1}{\rho}\frac{\partial P}{\partial y} + \nu\left(\frac{\partial^2 v}{\partial x^2} + \frac{\partial^2 v}{\partial y^2} + \frac{\partial^2 v}{\partial z^2}\right) \qquad (3)$$

$$u\frac{\partial w}{\partial x} + v\frac{\partial w}{\partial y} + w\frac{\partial w}{\partial z} = -\frac{1}{\rho}\frac{\partial P}{\partial z} + \nu\left(\frac{\partial^2 w}{\partial x^2} + \frac{\partial^2 w}{\partial y^2} + \frac{\partial^2 w}{\partial z^2}\right) \qquad (4)$$

Velocity components have been used in these equations. The variations of the velocity components in respect to three-dimensional coordinates have been taken into account. Pressure, density and kinematic viscosity terms have been included in the equations. For pressure-velocity coupling, the coupled scheme has been used. Gradient, pressure and momentum have been considered for spatial discretization. The convergence has been attained by 10^{-6} for these equations.

The grid structure has been shown for a sample case of $G^* = 0.01$ in Figure 2. For the grid structures, element size has been defined. Inflation has been applied by smooth transition with the growth rate of 1.2 for maximum five layers. For several element sizes, the number of grid elements has been changed.
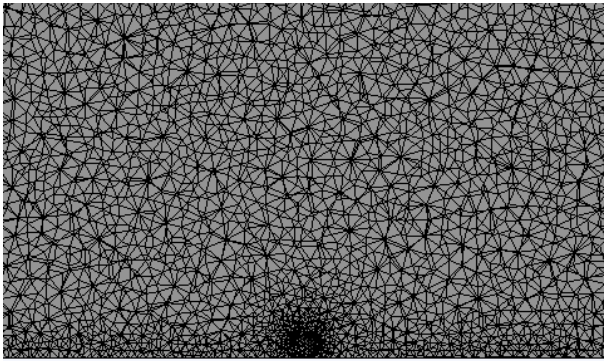
Figure 2. The grid structure

All grid structures have been compared by the drag coefficient of a sphere at Re = 250 for uniform flow conditions. The grid numbers of 1.6×10^6, 2.9×10^6 and 5.3×10^6 have been tested. The following results have been listed in Table 1. The drag coefficients are $C_D = 0.733$ for 1.6×10^6 grid elements, $C_D = 0.734$ for 2.9×10^6 grid elements and $C_D = 0.727$ for 5.3×10^6 grid elements.

Table 1. Drag coefficients with respect to the grid numbers

Grid numbers	C_D
1.6×10^6	0.733
2.9×10^6	0.734
5.3×10^6	0.727

The grid element number of 2.9×10^6 has been chosen for the numerical simulations since the value is in good agreement in the previous results as $C_D = 0.7$ [1], $C_D = 0.702$ [2], $C_D = 0.7$ [3] and $C_D = 0.702$ [4] at Re = 250.

3. Results and Discussion

The present case has been examined by considering the effects of gap ratios on flow patterns around a sphere at Re = 250. In terms of gap ratios, the range of $0.01 \leq G^* \leq 2$ has been taken into account. The numerical results of pressure distributions, streamwise velocity components, cross-stream velocity components, velocity magnitude values, spanwise vorticity components, vorticity magnitude values and drag coefficient values have been presented with respect to the change of gap ratios. The non-dimensional legends have been given for each situation.

Pressure distributions of $P^* = P \rho^{-1} (U_\infty)^{-2}$ have been presented from $P^* = -0.3$ to $P^* = 0.55$ as in Figure 3. The highest value has been attained at the upstream of the sphere. This situation is due to the flow stagnation. It is more obvious for the cases of $G^* = 1$ and $G^* = 2$. On the other hand, the values tend to decrease because of decrement in the gap ratios. Moreover, the effective regions indicated shrinkage as the sphere came closer to the bottom wall. Because jet flow effect between the sphere and the wall increased by decreasing the gap ratio. Another influence is the increasing effect of the boundary layer of the bottom wall. Furthermore, flow separations from the upper and the lower surfaces of the sphere have been affected. This observation has been clearly obtained by the minimum pressure zones. The minimum pressure values have been attained in the regions where flow acceleration is seen. The increment of velocity values triggered the pressure drops. It is attributed to the flow separation from the upper and the lower surfaces of the sphere. On the contrary, the decreasing gap ratios caused the disappearance of the lower
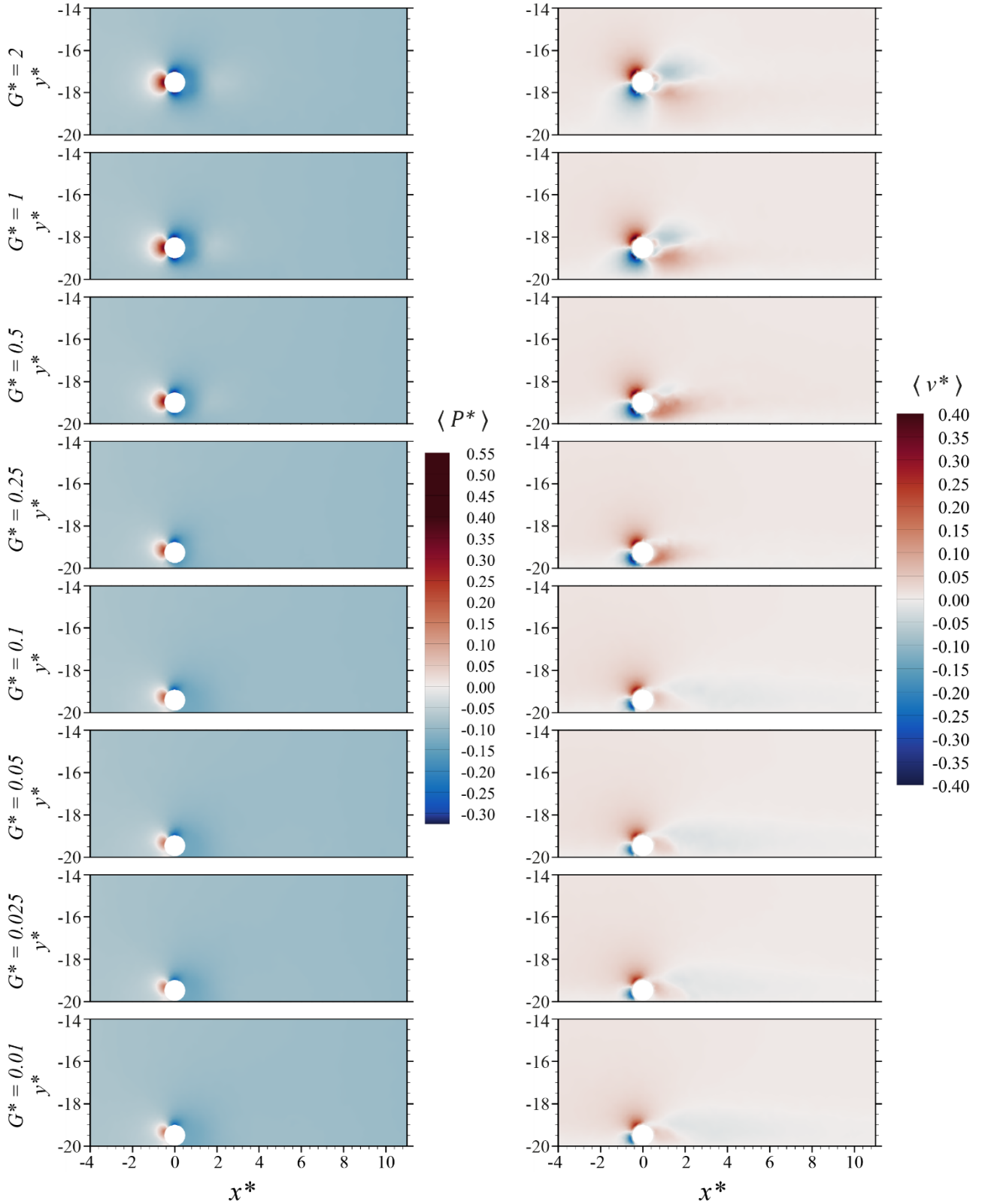
Figure 3. Pressure distributions and cross-stream velocity components with respect to the gap ratios

zones with minimum pressure values. Moreover, the values of the upper regions tended to decrease because of the same reason.

Cross-stream velocity components have been obtained as $v^* = v\,(U_\infty)^{-1}$ for the values ranging

from $v^* = -0.4$ to $v^* = 0.4$ as in Figure 3. The peak value has been attained in the upper region of the upstream. On the other hand, the lowest value has been obtained in the lower region of the upstream. Damping of these clusters is valid for the symmetrical axis. For $G^* = 2$, two positive
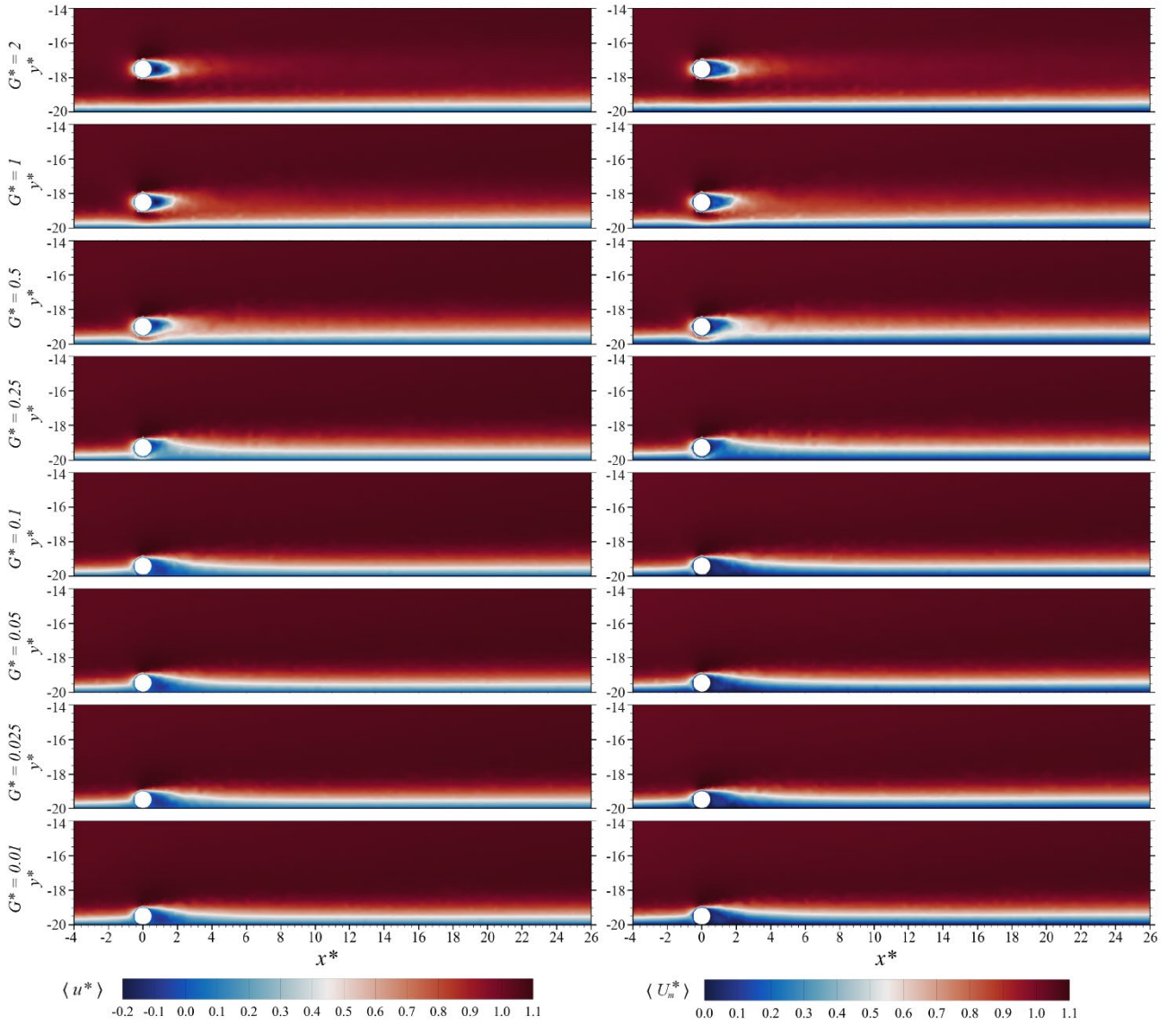
Figure 4. Streamwise velocity components and velocity magnitude values with respect to the gap ratios

and two negative clusters have been observed in the wake region. For these clusters, the positive one and the negative one are smaller and closer to the sphere. Similar situations have also been seen in the case of $G^* = 1$. However, this effect has been diminished by the interaction of the wake flow and the boundary layer of the bottom wall. It is clearly observed in the wake regions for the case of $G^* \leq 0.25$ and the positive one becomes more dominant especially for the cases of $G^* = 0.1$ and $G^* = 0.25$ as in the graphics. On the contrary, for $G^* \leq 0.05$, the negative one has been attained as more dominant because of flow separation and jet flow diminishing the positive one.

Streamwise velocity components have been presented as $u^* = u\,(U_\infty)^{-1}$ and given in the range from $u^* = -0.2$ to $u^* = 1.1$ as in Figure 4. The

maximum value has been obtained in the regions where no effect of sphere is valid. On the other hand, the minimum value has been attained in the wake regions of the sphere for $0.5 \leq G^* \leq 2$. However, for $G^* \leq 0.25$, it has been observed by the interaction between the wake flow and the boundary layer of the rough wall. What is more, the size change in the region has been obviously seen because of decrement in the gap ratios. The wake length is nearly 2D for $G^* = 2$ and it is around 1.95D for $G^* = 1$. For $G^* = 0.5$, it is approximately 1.9D due to the beginning of the wall effect. Moreover, symmetrical flow patterns have been observed for $G^* = 1$ and $G^* = 2$. This situation is not valid in the case of $G^* = 0.5$ as in the figure. For this reason, the wake regions have been combined by the boundary layer of the bottom wall. This effect has been clearly observed up to even $x^* = 12.5$ for $G^* \leq 0.25$ as
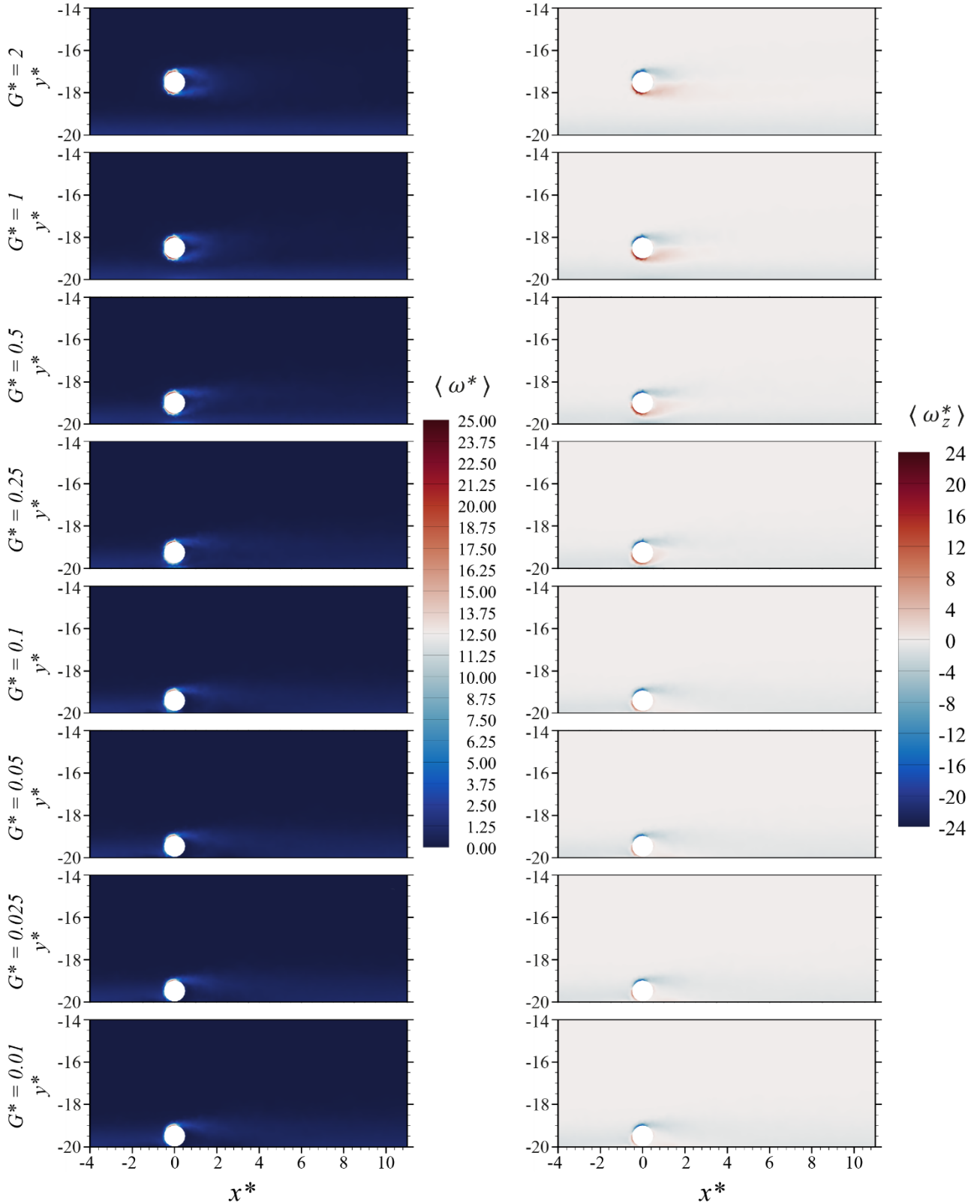
Figure 5. Vorticity magnitude values and spanwise vorticity components with respect to the gap ratios

presented in the contour graphics. On the other hand, these regions have shown shrinkage.

Velocity magnitude values have been attained as $U_m^* = U_m (U_\infty)^{-1}$ from $U_m^* = 0$ to $U_m^* = 1.1$ as in Figure 4. In the zones with no sphere effect,

the peak value has been attained. In the wake regions of the sphere for $0.5 \leq G^* \leq 2$, the minimum value has been obtained. Nonetheless, it has been seen because of the interaction of the wake flow and the boundary layer of the wall for $G^* \leq 0.25$. The size change in the region has also

been seen by the decreasing gap ratios. Even though symmetrical flow structures are valid for G* = 1 and G* = 2, it is not observable for G* = 0.5 as in the figure. For this reason, flow patterns have been considerably observed for G* = 0.25 because of the influence triggered by the boundary layer. Based on this deduction, it caused the combination of the wake regions and the boundary layer of the bottom wall. On the contrary, these zones have indicated shrinkage via the decrement of the gap ratios.

Vorticity magnitude values have been presented as ω* = ω D (U∞)^{-1} in the range from ω* = 0 to ω* = 25 as in Figure 5. The peak value has been obtained by both upper and lower regions of the sphere upstream. On the contrary, the lowest value has been seen in the regions with no vortices. The damping is valid for these zones on the symmetrical axis. Nonetheless, its effect has been diminished by the interaction of the wake flow and the boundary layer of the bottom surface. It is obviously seen for G* = 0.25 as given in the figures. The maximum value one becomes more dominant only in the upper zone of the sphere upstream for the same case. What is more, flow separation and jet flow affected the patterns for the contour graphics. Another influence is the value decrement and the shrinkage for these clusters and it is due to the gap ratio decrement between the sphere and the wall.

Spanwise vorticity components have been given as ω_z* = ω_z D (U∞)^{-1} ranging from ω_z* = -24 to ω_z* = 24 as in Figure 5. The highest value has been seen in the lower region of the sphere. On the other hand, the minimum value has been observed in the upper region of the body. The damping of positive and negative ones is valid on the symmetrical axis. Nevertheless, this influence has disappeared by the interaction of the wake flow and the wall boundary layer. It is clearly observed for G* = 0.25 and G* = 0.5 as given in the figures. The positive one becomes more dominant as in the contour graphics of the present study. On the other hand, the negative one is more dominant for G* ≤ 0.1 because of flow separation and jet flow diminishing the positive one. With respect to the observations, nnother effect is the changes for both value and

cluster size. The decreasing gap ratios is the reason for these situations.

In Figure 6, the effects of the gap ratios on the drag coefficient values have been presented. For G* ≤ 0.05, the drag coefficients are less than C_D = 0.47 and these values are so close to each other as given in the chart. For G* = 0.1, it is around C_D = 0.5 for the present problem. For increasing gap ratios, drag coefficient values also increased. Moreover, C_D = 0.579 has been attained for the case of G* = 0.25 and it is approximately C_D = 0.68 for G* = 0.5 in terms of drag coefficient values. On the other hand, the values of G* = 1 and G* = 2 approached the values of the uniform flow conditions and the effect of the wall proximity by the boundary layer of the bottom surface disappeared.
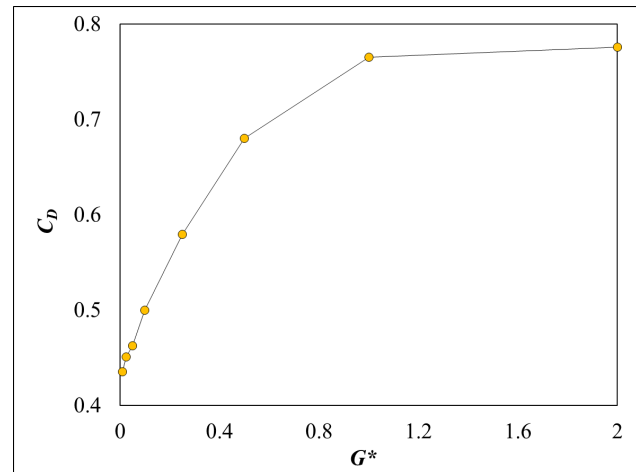
Figure 6. Drag coefficients with respect to the gap ratios

The drag reduction near the wall could be explained by decomposing it into pressure drag and viscous drag contributions. Drag due to pressure dominates, however, viscous effects are still inevasible for the current Reynolds number. When a sphere is close to a wall, the wake symmetry has been broken. The situation led to the wake shrinkage. It is linked to the drag reduction [30]. Moreover, pressure difference between the upstream and the downstream has been reduced. Decrement of drag due to pressure has been seen and it indicated lower drag coefficient near the wall. The drag owing to viscous effects may increase slightly owing to the wall-induced shear; however, it is still lower than drag reduction due to pressure. For lower gap ratios, the jet effect lost its ability to penetrate and deflect the flow mechanism, owing to the

attenuation triggered by the significant influence of the near-wall boundary layer and the proximity to the wall. It also included the combination of reduced jet momentum relative to boundary layer shear, suppression of vortex formation and viscous effects near the wall.

4. Conclusions

Aerodynamic flow characteristics of a sphere have been examined for different gap ratios from $G^* = 0.01$ to $G^* = 2$ in the present study. Numerical results for pressure distributions, streamwise and cross-stream velocity components, velocity magnitude values, spanwise vorticity components, vorticity magnitude values and drag coefficients have been presented at Reynolds number of $Re = 250$. Gap ratios affected flow structures around the sphere. A maximum static pressure occurs at the upstream stagnation point. The effect of the jet flow has increased by decreasing the gap ratio. Another influence is the increasing effect of the boundary layer on the bottom wall. Although symmetrical flow patterns have been observed for $G^* = 1$ and $G^* = 2$ by the streamwise velocity values, this situation is not valid by the case of $G^* = 0.5$ in this study. It is clearly observed in the wake regions for $G^* \leq 0.25$ and the positive cross-stream component value becomes more dominant especially for the cases of $G^* = 0.1$ and $G^* = 0.25$ in the current study. On the contrary, for $G^* \leq 0.05$, the negative one has been attained as more dominant because of flow separation and jet flow diminishing the positive one. The negative spanwise vorticity component value is more dominant for $G^* \leq 0.1$ as observed. For $G^* \leq 0.05$, the drag coefficients are less than $C_D = 0.47$ and these values are so close to each other. For $G^* = 0.1$, it is around $C_D = 0.5$ for the present study. By increasing gap ratios between the sphere and the wall, drag coefficient values also increased. What is more, $C_D = 0.579$ has been attained for $G^* = 0.25$ and it is approximately $C_D = 0.68$ for $G^* = 0.5$, respectively. On the other hand, the values of $G^* = 1$ and $G^* = 2$ approached the values which are valid for the uniform flow conditions.

Article Information Form

Authors' Contribution
IG: Conceptualization, Methodology, Software, Validation, Investigation, Resources, Writing-Original Draft, Writing-Review & Editing
MI: Software, Resources, Data Curation, Writing-Review & Editing, Visualization
MHA: Software, Writing-Review & Editing

The Declaration of Conflict of Interest
No conflict of interest or common interest has been declared by authors.

Artificial Intelligence Statement
No artificial intelligence tool has been used while writing this article.

References

[1] T. Johnson, V. Patel, "Flow past a sphere up to a Reynolds number of 300," Journal of Fluid Mechanics, vol. 378, pp. 19-70, 1999.

[2] D. Kim, "Laminar flow past a sphere rotating in the transverse direction," Journal of Mechanical Science and Technology, vol. 23, pp. 578-589, 2009.

[3] G. S. Constantinescu, K. D. Squires, "LES and DES investigations of turbulent flow over a sphere at Re= 10,000," Flow, Turbulence and Combustion, vol. 70, pp. 267-298, 2003.

[4] D. Kim, H. Choi, "Laminar flow past a sphere rotating in the streamwise direction," Journal of Fluid Mechanics, vol. 461, pp. 365-386, 2002.

[5] N. Mahir, "Three-dimensional flow around a square cylinder near a wall," Ocean Engineering, vol. 36, no. 5, pp. 357-367, 2009.

[6] L. Sweeney, W. Finlay, "Lift and drag forces on a sphere attached to a wall in a Blasius boundary layer," Journal of Aerosol Science, vol. 38, no. 1, pp. 131-135, 2007.

[7] T. Tsutsui, "Flow around a sphere in a plane turbulent boundary layer," Journal of Wind Engineering and Industrial Aerodynamics, vol. 96, no. 6-7, pp. 779-792, 2008.

[8] R. Martinez, L. Sweeney, W. Finlay, "Aerodynamic forces and moment on a sphere or cylinder attached to a wall in a Blasius boundary layer," Engineering Applications of Computational Fluid Mechanics, vol. 3, no. 3, pp. 289-295, 2009.

[9] A. Mongruel, C. Lamriben, S. Yahiaoui, F. Feuillebois, "The approach of a sphere to a wall at finite Reynolds number," Journal of Fluid Mechanics, vol. 661, pp. 229-238, 2010.

[10] Q. Liu, A. Prosperetti, "Wall effects on a rotating sphere," Journal of Fluid Mechanics, vol. 657, pp. 1-21, 2010.

[11] S. Yahiaoui, F. Feuillebois, "Lift on a sphere moving near a wall in a parabolic flow," Journal of Fluid Mechanics, vol. 662, pp. 447-474, 2010.

[12] S. Dey, S. Sarkar, S. K. Bose, S. Tait, O. Castro-Orgaz, "Wall-wake flows downstream of a sphere placed on a plane rough wall," Journal of Hydraulic Engineering, vol. 137, no. 10, pp. 1173-1189, 2011.

[13] I. Rodriguez, R. Borell, O. Lehmkuhl, C. D. P. Segarra, A. Oliva, "Direct numerical simulation of the flow over a sphere at Re= 3700," Journal of Fluid Mechanics, vol. 679, pp. 263-287, 2011.

[14] H. Homann, J. Bec, R. Grauer, "Effect of turbulent fluctuations on the drag and lift forces on a towed sphere and its boundary layer," Journal of Fluid Mechanics, vol. 721, pp. 155-179, 2013.

[15] S. M. Hajimirzaie, A. G. Tsakiris, J. H. Buchholz, A. N. Papanicolaou, "Flow characteristics around a wall-mounted spherical obstacle in a thin boundary layer," Experiments in Fluids, vol. 55, pp. 1-14, 2014.

[16] T. Chastel, A. Mongruel, "Squeeze flow between a sphere and a textured wall," Physics of Fluids, vol. 28, no. 2, p. 023301, 2016.

[17] H. Zhao, X. Liu, D. Li, A. Wei, K. Luo, J. Fan, "Vortex dynamics of a sphere wake in proximity to a wall," International Journal of Multiphase Flow, vol. 79, pp. 88-106, 2016.

[18] R. van Hout, J. Eisma, G. E. Elsinga, J. Westerweel, "Experimental study of the flow in the wake of a stationary sphere immersed in a turbulent boundary layer," Physical Review Fluids, vol. 3, no. 2, p. 024601, 2018.

[19] Y. H. Tee, D. C. Barros, E. K. Longmire, "Motion of finite-size spheres released in a turbulent boundary layer," International Journal of Multiphase Flow, vol. 133, p. 103462, 2020.

[20] G. Yin, M. C. Ong, "On the wake flow behind a sphere in a pipe flow at low Reynolds numbers," Physics of Fluids, vol. 32, no. 10, p. 103605, 2020.

[21] A. Chandel, S. Das, "Effect of wall proximity on the wake of a rotating and translating sphere," Acta Mechanica, vol. 232, pp. 4833-4846, 2021.

[22] A. Chizfahm, V. Joshi, R. Jaiman, "Transverse flow-induced vibrations of a sphere in the proximity of a free surface: A numerical study," Journal of Fluids and Structures, vol. 101, p. 103224, 2021.

[23] Z. G. Feng, J. Gatewood, E. E. Michaelides, "Wall effects on the flow dynamics of a rigid sphere in motion," Journal of Fluids Engineering, vol. 143, no. 8, p. 081106, 2021.

[24] W. Shang, H. Zhao, D. Li, K. Luo, J. Fan, "Direct numerical simulation of the flow around a sphere immersed in a flat-plate turbulent boundary layer," Physics of Fluids, vol. 33, no. 11, p. 115106, 2021.

[25] T. G. Shepard, D. Law, R. K. Menon, K. Ordahl, A. Gutenberg, "Interference drag and flow structure around cylinder-sphere junction," Ocean Engineering, vol. 234, p. 109276, 2021.

[26] D. Li, K. Luo, H. Zhao, W. Shang, J. Fan, "Interaction between a stationary sphere and turbulent flow in a boundary layer," Physics of Fluids, vol. 34, no. 8, p. 085138, 2022.

[27] A. Kumar, S. Das, S. Tiwari, "Wall effect on the wake characteristics of a transversely rotating sphere," Physics of Fluids, vol. 36, no. 1, p. 013611, 2024.

[28] N. Mahir, Z. Altac, "Numerical investigation of convective heat transfer in unsteady flow past two cylinders in tandem arrangements," International Journal of Heat and Fluid Flow, vol. 29, no. 5, pp. 1309-1318, 2008.

[29] I. Goktepeli, "Examination of wake characteristics for tandem circular cylinders via Computational Fluid Dynamics," Journal of Advanced Research in Natural and Applied Sciences, vol. 11, no. 1, pp. 1-11, 2025.

[30] I. Goktepeli, M. Ispir, M H. Aksoy, "Experimental flow control around circular cylinders with porous media coatings," Acta Mechanica, pp. 1-17, 2025.

Lead-Free Alternatives for Radiation Shielding in Medical Environments: A Comprehensive Review

Khalid Hani Abushahla[1*] (ID), Halil Arslan[2] (ID)

[1] Biomedical Technologies Application and Research Center (Biyotam), Sakarya University of Applied Sciences, Sakarya, Türkiye, 22500305002@subu.edu.tr, ror.org/01shwhq58
[2] Electrical and Electronics Engineering Department, Sakarya University of Applied Sciences, Sakarya, Türkiye, harslan@subu.edu.tr, ror.org/01shwhq58
*Corresponding Author

ARTICLE INFO	ABSTRACT
  	In radiography, effective radiation shielding plays a vital role in safeguarding patients, medical staff, and the public, as well as in preserving the integrity of surrounding materials. Traditionally, lead has been the primary shielding material due to its high atomic number and density, which provide efficient attenuation of radiation. However, lead presents several challenges, including significant weight, toxicity, long-term health risks, and serious environmental concerns. Lead waste is classified as hazardous due to its non-biodegradable nature, its potential for contaminating soil and water, and the difficulties associated with safe disposal and recycling processes. These issues have driven the search for safer and more sustainable alternatives. Recent advancements have led to the development of lead-free shielding materials designed to replace conventional lead-based shields. Among these, lead-free multilayered polymer composites have emerged as promising substitutes, often enhanced with elements such as bismuth, tungsten, barium, tin, cadmium, gadolinium, antimony, and molybdenum to improve their radiation protection capabilities. This study examines the potential of these alternatives to address the limitations of traditional lead shielding, with a particular focus on their development and application in medical settings. By reducing toxicity, lowering weight, and improving recyclability, these materials offer a more environmentally friendly and health-conscious approach to radiation protection.

1. Introduction

1.1. Types and biological effects of ionizing and non-ionizing radiation

Radiation is the process through which energy travels or propagates in the form of waves or particles through space or through some other medium [1]. Radiation is classified into ionizing radiation (IR) and non-ionizing radiation (NIR). IR, such as high-energy photons, neutrons, protons, and alpha particles, has sufficient energy to liberate tightly bound electrons from atoms, creating charged particles (ions). This ionization process can damage biological tissues and lead to severe health effects, including acute radiation syndrome, organ damage, and an increased risk of cancers such as leukemia. In contrast, NIR (e.g., visible light, infrared, and radio waves) has lower energy and cannot ionize atoms or molecules [2-4].

Among ionizing radiation are alpha particles, consisting of two protons and two neutrons (helium nuclei), making them relatively heavy and positively charged. Due to their high mass and charge, alpha particles have low penetration power and can be stopped by a sheet of paper or the outer layer of human skin [5, 6].

Other types of ionizing radiation are beta particles, which are high-speed electrons or

positrons with moderate penetration power. They are more penetrating than alpha particles but can be stopped by materials such as plastic, glass, or a few millimeters of aluminum [7].

Moreover, X-rays and gamma rays are electromagnetic radiation with very high energy and penetration power [8]. In recent years, their use in medicine has expanded with the development of new technologies and applications in diagnostics, especially in imaging and in some therapy protocols [9-11].

Radiation is a crucial component in modern medicine, encompassing electromagnetic waves and particulate radiation. Advanced imaging techniques have improved diagnostic and therapeutic procedures. X-ray systems create images of internal structures, while CT provides detailed cross-sectional views. Positron emission tomography (PET) evaluates physiological and metabolic processes. Other radiation-based methods include radionuclide imaging for organ function assessment, laser technology for precise surgical interventions, and ultraviolet radiation for therapeutic purposes. Radiation processing is also used in industrial contexts for material properties enhancement and sterilization [12].

1.2. Applications of radiation in medicine and industry

Radiation is widely applied in medicine and industry, but its use requires careful control due to potential health hazards. It is essential in medical imaging, cancer therapy, industrial inspection, material processing, and research. Radiation injury severity can be affected by a wide range of confounding factors, including age, gender, prior medical conditions, radiation types, duration, and dose rates. Radiation types, radiation dosages, and radiation dose rates are positively linked with the death rate [13].

1.3. Radiation hazards and protective measures

Although radiation has many uses in industry and medicine, there are serious hazards associated with it, particularly when exposure is extended. Ionizing radiation penetrates biological tissues, damages DNA, produces free radicals, and interferes with cellular processes. This may result in health problems such as an elevated risk of cancer due to genetic mutations, severe burns from radiation, and possible genetic harm from the ionizing effects of X-rays and gamma rays. Acute Radiation Syndrome, which is marked by nausea, vomiting, and death, can also be brought on by high exposure. The most serious long-term health dangers in the medical field are from the ionizing effects of X-rays and gamma rays, even while other forms of radiation cause sunburn and heating of tissues [14].

To reduce the risks of radiation exposure, various protective measures are implemented. In medical imaging, especially in radiation-based procedures, three fundamental principles—time, distance, and shielding—are crucial for minimizing exposure. Decreasing exposure time and increasing distance are both effective strategies, as radiation exposure is inversely proportional to the square of the distance from the source [15, 16]. Shielding plays a crucial role in protecting healthcare professionals. Shielding devices such as lead aprons, glasses, and thyroid protectors are designed to absorb and block radiation, thus significantly reducing exposure [17].

Despite their cost and potential discomfort, these devices are vital for ensuring safety. Shielding is universally important across all forms of medical imaging, as it provides an additional layer of protection beyond merely managing exposure time and distance. By effectively utilizing shielding, healthcare professionals can substantially decrease their radiation dose, making it a critical component of radiation safety practices [18].

1.4. ALARA principle and shielding material selection

The ALARA principle was generally introduced by the ICRP in 1977 under the general term of "As Low as Reasonably Achievable" [19], and then introduced in endourology by Greene et al. in 2011 [20]. In medical imaging, the ALARA principle is crucial for minimizing radiation exposure while maintaining the required diagnostic quality. Based on this idea, the lowest possible effective radiation dose is used during

radiological procedures [21]. For radiation shielding materials to be both practical and effective, a number of important criteria must be balanced.

Due to their increased likelihood of interacting with radiation and resulting in increased energy transfer, high atomic number (high-Z) materials with high-density materials such as bismuth (Bi), lead (Pb), and barium (Ba) are favored [22]. However, if employed in greater thicknesses, materials with lower atomic numbers and densities can also offer efficient shielding, producing comparable protective effects to those of high-Z materials. Aside from the type and intensity of radiation, other important factors to consider are the handling, weight, and cost of the materials. In addition to efficiently attenuating or absorbing radiation, effective shielding materials should also be affordable and manageable in real-world applications. Traditional materials are effective, but they frequently have drawbacks like high cost, heaviness, and toxicity. This situation has led to continuous research to create better substitutes [23].

1.5. Role and limitations of lead

Lead (Pb) is widely recognized as the most toxic heavy metal in radiation shielding contexts, and, along with mercury (Hg), arsenic (As), cadmium (Cd), and chromium (Cr), it ranks among the top priority metals of public health concern due to their ability to cause systemic toxicity, multi-organ damage, and carcinogenic effects even at low exposure levels [24, 25]. Due to its high atomic number (Z) and favorable interaction cross-section, which make it extremely effective at blocking photon radiation, lead has long been utilized as a radiation shield [26]. Lead can be found in various forms, including lead bricks, leaded glass, leaded plastics, and lead shot, to suit different applications [27]. Its density and compactness improve its shielding ability, which makes it very suitable for space-limited applications, like nuclear medicine and medical radiology [28, 29]. For example, clinical personnel also use lead-based protective materials when performing radiological imaging, like X-ray image-guided interventional radiology procedures.

Furthermore, from an economic standpoint, there is no commercial product with a similarly excellent shielding capacity and workability as lead [30]. However, lead has significant drawbacks, including its toxicity and high cost, which restrict its use in many applications. Lead-based materials pose serious health risks due to their toxicity and the potential formation of harmful particles on surfaces, which contributes to lead's decreased desirability despite its effective shielding properties [31].

1.6. Lead-free alternatives

Furthermore, lead aprons, which are frequently used in medical settings, are traditionally very heavy and can be uncomfortable and problematic for the back when worn for extended periods [32]. These issues highlight the need for safer, non-toxic, and more sustainable alternatives for radiation shielding, as lead has poor strength and hardness also limit its durability [29]. Due to the disadvantages of lead, scientists are investigating alternative materials for radiation shielding. Various lead-free materials have been explored and categorized into glasses, ceramics, pure metals, polymers, concrete, and various composites. Among these materials, the literature often highlights metals and metals under different compositions and variations as key elements, with the most common ones being Bismuth [33-36], Tungsten [37, 38], Barium [39], Tin [40], Molybdenum [41], Cadmium [42], Gadolinium [43] and Antimony [44].

These substitutes for lead are meant to limit the negative impacts on patients, medical personnel, and the environment while encouraging safer and more environmentally friendly procedures. This review examines radiation-shielding materials, which contain Bismuth, Tungsten, Barium, Tin, Molybdenum, Cadmium, Gadolinium, and Antimony. Each of these materials has the potential to replace lead in radiation shielding, with an emphasis on their characteristics, efficacy, and possible uses in healthcare environments. In other words, alternatives are discussed in this review, going over their makeup, radiation-attenuation properties, and potential applications in medical radiation protection. Research is still ongoing to optimize

these materials for particular uses, weighing the advantages against any potential disadvantages.

2. Lead-Free Alternative Materials

2.1. Material selection criteria

The essential characteristics of some materials that improve the radiation-shielding efficacy are listed in Table 1, together with those of lead. Lead is widely used as a reference material due to its established shielding properties. The other materials are typically incorporated as additives in various chemical compositions, some of which are discussed in detail in the following sections (see Table 1).

2.2. Physical properties of elements

Basic properties, including atomic number, weight, density, and melting point, of the elements of interest and lead are given in Table 1. Bismuth (Bi), a non-toxic, high-density heavy metal, is increasingly valued for its strong radiation absorption properties, making it a promising lead-free alternative for shielding applications. Its oxide form, Bi_2O_3, offers

enhanced durability and efficiency in blocking radiation, competing with lead-based materials while addressing health and environmental concerns. Tungsten (W) also stands out as an effective shielding material due to its high atomic number and density, offering good protection against radiation. Its thermal stability and resistance to environmental degradation make it ideal for high-temperature applications, even though there are still issues with its processing.

Barium (Ba), particularly in oxide form (BaO), enhances gamma radiation attenuation in glass systems and other composites, contributing to the development of sustainable, lead-free shielding solutions.

Other metals, such as tin (Sn), cadmium (Cd), gadolinium (Gd), antimony (Sb), and molybdenum (Mo), also offer valuable contributions to radiation shielding technologies. Their unique properties, including high atomic numbers and densities, help improve material performance across diverse applications. These metals pave the way for advanced, eco-friendly shielding materials that meet the growing need for non-toxic, safer alternatives.

Table 1. Basic properties of lead and its radiation-shielding alternatives

Element	Latin Names	Symbol	Atomic Number	Atomic Weight	Density (g/cm³)	Melting Point (°C)
Lead	Plumbum	Pb	82	207.2	11.3	327.5
Bismuth	Bismuthum	Bi	83	209	9.78	271.3
Tungsten	Wolframium	W	74	183.9	19.3	3410
Barium	Barium	Ba	56	137.3	3.62	727
Tin	Stannum	Sn	50	118.7	7.31	231.9
Cadmium	Cadmium	Cd	48	112.41	8.65	321
Gadolinium	Gadolinium	Gd	64	157.25	7.9	1312
Antimony	Stibium	Sb	51	121.76	6.68	630.6
Molybdenum	Molybdaenum	Mo	42	95.95	10.28	2623

3. Detailed Material Analysis

3.1. Bismuth (Bi)

Bismuth (Bi) is a non-toxic, inexpensive heavy metal with distinctive properties, including high specific gravity, photoluminescence, photoelectric and photovoltaic effects, strong oxidation ability, and water insolubility. It also has a white crystalline structure, high electrical

resistance, and strong diamagnetic properties. The surface of Bi crystals typically displays iridescent rainbow colors due to interference effects from the oxide layer [45, 46].

Bismuth is known as the wonder metal due to its diverse oxidation states and strong tendency to form bismuth clusters as a result of the electrons' easy involvement in chemical combinations in the p orbital [47].

Bismuth, a metallic element with an atomic number of 83 and a mass number of 208.980, exhibits strong absorption characteristics for ionizing radiation due to its high atomic number. With a density of 9.78 g/cm³, melting point approximately 271.5°C, bismuth atoms contribute to increasing the material's overall density. The high concentration of electrons in bismuth enhances interactions between incident photons and the material's electrons, leading to a significant reduction in radiation intensity. This combination of high atomic number and density makes bismuth an excellent candidate for radiation protection and shielding, positioning it as a promising material for developing advanced shielding solutions in various applications. Bismuth metal (99.5%) costs about $250/kg [48, 49].

Bismuth oxide is a highly effective lead alternative for radiation shielding. Its non-toxic nature, high atomic number, and 8.9 g/cm³ density. Its higher melting point compared to lead ensures better durability. As the bismuth oxide content increases, shielding parameters such as the half-value layer and tenth-value layer improve, enhancing its efficiency in blocking radiation. While lead is inexpensive and readily available due to its abundant supply and established mining processes, bismuth requires a larger initial investment. However, the long-term savings with bismuth come from reduced health and environmental protection needs [50-54].

Karimi et al. highlighted the growing demand for lead-free radiation shielding materials due to health concerns surrounding lead poisoning and leakage [55]. They compared various glass shields, including a commercial lead-based shield, four previously studied shields, and three new lead-free variants, by evaluating their shielding performance according to international standards (IEC 61331). The materials were analyzed for air kerma ratios, lead equivalent values, and shielding properties using Monte Carlo N-Particle eXtended (MCNPX) simulations [56].

Mass attenuation coefficients and effective atomic numbers (Zeff) were obtained from the XCOM database [57], covering the diagnostic X-ray energy range (40–120 keV). The study introduced three novel glasses—borate-based (Ir1), phosphate-based (Ir2), and silicate-based (Ir3). The Ir3 glass, composed of 0.05 Al_2O_3, 0.3 SiO_3, 0.1 BaO, and 0.55 Bi_2O_3 with a density of 5.4 g/cm³, along with the borosilicate-barium-based Tu glass, exhibited superior shielding properties, rivaling those of lead-based glass. These findings indicate that Ir3 and Tu glasses are promising alternatives as lead-free transparent shields for use in diagnostic X-ray energy ranges [55].

Yu et al. addressed the need for lightweight, lead-free X-ray shielding materials due to the toxicity and heaviness of conventional lead-based shields [58]. They synthesized bismuth titanate (BTO) particles and incorporated them into an epoxy resin (ER) matrix at varying loadings (0–65 wt%). The surface roughness and hardness of the BTO-ER composites were analyzed to assess their X-ray attenuation. Results showed that a 2 mm thick 65BTO-ER composite (0.65 $Bi_4Ti_3O_{12}$ + 0.35 CHO) achieved X-ray attenuation efficiencies of 97% at 80 kVp and 95% at 100 kVp, equivalent to 0.35 mm of lead but with half the weight. This demonstrates the potential of BTO-based composites as non-toxic, environmentally friendly alternatives to conventional lead shielding in diagnostic X-ray protection [58].

Khazaalah et al. focused on improving the efficiency of lead-free glass as a radiation shield while addressing the issues of dark brown bismuth glass and reducing waste glass accumulation in landfills by incorporating soda-lime-silica (SLS) glass waste [59].

Using the melt-quenching method, WBiBZn-SLS glass was fabricated at 1200 °C with varying concentrations of WO_3 (0–0.05 mol). The waste glass, composed of 74.1% SiO_2, provided the SiO_2 content. Radiation attenuation parameters were measured using narrow-beam geometry and X-ray fluorescence (XRF). Results indicated that increasing WO_3 concentration reduced the half-value layer and increased the linear attenuation coefficient (μ). WBiBZn-SLS glass, composed of WO_3 (0.05%), Bi_2O_3 (19%), ZnO (28.5%), and other components, proved to be a non-toxic, transparent, and effective radiation shielding material [59].

Li et al. tackled the challenge of designing flexible, lightweight radiation shielding materials for complex structures by developing for designing and assessing the safety of nuclear systems to predict γ-ray shielding performance [60, 61]. The study tested Pb- and Ta-doped Bi/PU coated fabric composites for shielding properties, mechanical performance, and wear resistance. The results showed that Ta doping enhanced γ-ray shielding, surpassing non-doped composites. However, Ta doping reduced wear resistance and tensile strength. The Bi/Ta/PU composite (50% Bi + 5% Ta + 45% $C_5H_6N_2O_2$) provides efficient, eco-friendly radiation protection, suitable for personal protective gear and collective shielding equipment, offering excellent γ-ray shielding while remaining lightweight and flexible [60].

Uosif et al. explored the need for effective, lead-free protective cover glass for solar cells in superstrate arrangements, where lightweight, radiation resistance, optical clarity, and structural integrity are essential [62]. Solar panels used in spacecraft suffer from reduced energy output due to UV and radiation damage to the cover glass. To address this, lead-free phosphate glasses with varying Bi_2O_3 content [xBi_2O_3–$(40 - x)CaO$–$60P_2O_5$, x = 5–30 mol%] were fabricated using high-temperature melting.

The study measured gamma shielding across multiple photon energies (81–2614 keV) and found that increasing Bi_2O_3 content enhanced the mass attenuation coefficient, though it decreased with rising photon energy. The $60P_2O_5$–$30Bi_2O_3$–$10CaO$ glass exhibited the best overall performance, making it a promising lead-free option for radiation shielding in space-based solar cell applications [62].

Al-Hadeethi et al. investigated bismuth borate glass samples with varying compositions [$(99-x)$ $B_2O_3 + 1 Cr_2O_3 + (x) Bi_2O_3$, where x = 0–25 wt%] using the melt quenching technique [63]. The mass attenuation coefficient (MAC) of the glasses was measured using four different point sources (^{241}Am, ^{133}Ba, ^{152}Eu, ^{137}Cs). The experimental MAC values closely matched theoretical results from XCOM [57], with

deviations under 3%. The glass with 25 wt% Bi_2O_3 showed high attenuation, comparable to commercial lead borate glasses. Transmission factor (TF) values were found to be lower at lower energies and increased with photon energy. The addition of Bi_2O_3 reduced TF, enhancing shielding performance. Half-value layer (HVL) data highlighted greater photon penetration at higher energies, with HVL for BCrBi-20 glass being 0.171 cm at 0.0595 MeV and 4.334 cm at 1.408 MeV. The study also determined the fast neutron removable cross section (FNRC), showing that bismuth borate glasses, particularly the 25 wt% sample ($74 B_2O_3 + CrO_3 + 25 Bi_2O_3$), outperformed lead borate glass and concrete in radiation shielding [63].

Liu et al. explored the development of bismuth tungstate (Bi_2WO_6) nanostructures as potential alternatives to lead-based materials for radiation shielding [64].

With increasing nuclear activities and the need for low-toxicity protective materials, this study focused on fabricating Bi_2WO_6 nanosheets.
These nanosheets demonstrated gamma-ray attenuation properties comparable to lead-based materials for low-energy gamma rays. Given their lower toxicity, Bi_2WO_6 nanosheets are considered more suitable for fabricating personal protective equipment, offering promising prospects for shielding low-energy radiations and significant market potential in healthcare, nuclear facilities, aerospace, and other radiation-intensive industrial applications.[64].

Mass attenuation coefficient (MAC) values of the bismuth-based materials studied by the abovementioned groups are provided in Table 2 and Table 3 for various photon energies. These values were calculated for the composition of materials using the web database Epixs. Additionally, the MAC values are illustrated in Figure 1 as a function of energy, alongside those for lead.
As it can be seen from Table 2 ,3 and Figure 1, lead shows higher MAC values than bismuth-based materials at low photon energies (15–60 keV),

Table 2. Mass attenuation coefficients (cm^2/g) and lead equivalent for bismuth-based materials at various energies

Energy (MeV)	Karimi et al., 2020	Pb Eq.	Yu et al., 2021	Pb Eq.	Khazaalah et al., 2022	Pb Eq.	Li et al., 2023	Pb Eq.
0.015	64.9535	0.5844	57.2564	0.5151	43.0642	0.3874	65.0400	0.5851
0.02	47.5849	0.5528	42.9795	0.4993	26.2039	0.3044	48.0042	0.5577
0.03	16.7666	0.5526	15.1838	0.5004	9.0106	0.2970	16.9876	0.5599
0.04	9.7453	0.6791	7.2213	0.5032	4.2236	0.2943	8.0812	0.5631
0.05	5.4813	0.6844	4.0657	0.5076	2.3674	0.2956	4.5461	0.5676
0.06	3.4287	0.6886	2.5576	0.5137	1.4948	0.3002	2.8545	0.5733
0.08	1.6504	0.7006	1.2520	0.5315	0.7547	0.3204	1.6867	0.7160
0.1	3.0872	0.5563	2.7453	0.4947	1.2434	0.2241	3.1426	0.5663
0.15	1.1550	0.5733	1.0416	0.5171	0.5106	0.2535	1.1797	0.5856
0.2	0.5989	0.5986	0.5481	0.5478	0.2968	0.2967	0.6129	0.6127
0.3	0.2670	0.6624	0.2514	0.6237	0.1639	0.4067	0.2740	0.6799
0.4	0.1689	0.7283	0.1627	0.7013	0.1208	0.5208	0.1737	0.7487
0.5	0.1268	0.7866	0.1240	0.7696	0.1001	0.6213	0.1305	0.8095
0.6	0.1040	0.8344	0.1029	0.8255	0.0877	0.7036	0.1071	0.8592
0.8	0.0799	0.9043	0.0802	0.9071	0.0728	0.8237	0.0824	0.9320
1	0.0671	0.9486	0.0678	0.9587	0.0637	0.9000	0.0692	0.9780
1.5	0.0516	0.9925	0.0525	1.0090	0.0508	0.9760	0.0532	1.0228
2	0.0451	0.9826	0.0457	0.9950	0.0441	0.9599	0.0464	1.0096
3	0.0394	0.9341	0.0393	0.9317	0.0371	0.8788	0.0402	0.9512
4	0.0372	0.8883	0.0365	0.8723	0.0336	0.8026	0.0375	0.8964
5	0.0363	0.8521	0.0352	0.8252	0.0317	0.7423	0.0364	0.8528
6	0.0361	0.8241	0.0346	0.7887	0.0305	0.6956	0.0359	0.8190
8	0.0366	0.7845	0.0344	0.7373	0.0294	0.6299	0.0360	0.7713
10	0.0377	0.7583	0.0349	0.7032	0.0291	0.5865	0.0367	0.7397
15	0.0408	0.7214	0.0370	0.6554	0.0296	0.5245	0.0393	0.6955

Table 3. Mass attenuation coefficients (cm^2/g) and lead equivalent for bismuth-based materials at various energies

| Energy (MeV)	Uosif et al., 2023	Pb Eq.	Al-Hadeethi et al., 2022	Pb Eq.	Liu et al., 2018	Pb Eq.
0.015	37.2820	0.3354	27.3167	0.2458	106.0480	0.9541
0.02	26.6959	0.3101	20.6541	0.2399	70.9025	0.8237
0.03	9.3782	0.3091	7.3601	0.2426	24.9387	0.8219
0.04	4.4689	0.3114	3.5480	0.2472	11.7914	0.8217
0.05	2.5345	0.3165	2.0346	0.2540	6.5854	0.8223
0.06	1.6130	0.3240	1.3097	0.2631	4.0985	0.8232
0.08	0.8167	0.3467	0.6794	0.2884	3.5603	1.5114
0.1	1.6674	0.3005	1.3995	0.2522	4.6158	0.8317
0.15	0.6635	0.3293	0.5696	0.2828	1.6824	0.8352
0.2	0.3701	0.3700	0.3257	0.3255	0.8439	0.8435
0.3	0.1901	0.4717	0.1744	0.4327	0.3494	0.8668
0.4	0.1337	0.5765	0.1260	0.5431	0.2068	0.8914
0.5	0.1078	0.6686	0.1032	0.6403	0.1473	0.9141
0.6	0.0928	0.7440	0.0897	0.7198	0.1163	0.9324
0.8	0.0755	0.8542	0.0739	0.8359	0.0849	0.9604
1	0.0654	0.9240	0.0644	0.9096	0.0692	0.9778
1.5	0.0517	0.9928	0.0511	0.9815	0.0518	0.9958
2	0.0448	0.9760	0.0441	0.9610	0.0456	0.9929
3	0.0378	0.8962	0.0367	0.8692	0.0412	0.9764
4	0.0344	0.8214	0.0328	0.7833	0.0402	0.9607
5	0.0325	0.7620	0.0305	0.7149	0.0404	0.9481
6	0.0314	0.7161	0.0290	0.6619	0.0411	0.9382
8	0.0304	0.6514	0.0274	0.5869	0.0432	0.9243
10	0.0302	0.6087	0.0267	0.5375	0.0454	0.9149
15	0.0310	0.5482	0.0265	0.4681	0.0510	0.9018
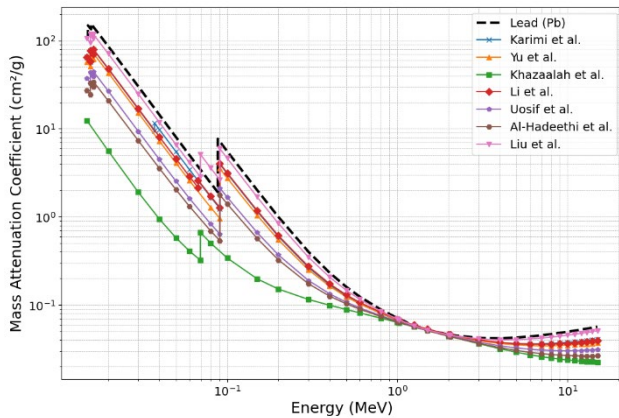
Figure 1. Mass attenuation coefficient values of various bismuth-based materials compared with lead

showing superior attenuation. For instance, at 15 keV, lead's MAC is 111.1520 cm²/g, while bismuth-based materials values range from 27.3167 cm²/g to 106.0480 cm²/g which indicates good performance although lead has the superiority. As the photon energy increases to moderate levels (100–1000 keV), bismuth's MAC values approach lead's values, as the performance of materials based on bismuth becomes comparable. For example, at 100 keV, lead's MAC is 5.5496 cm²/g, whereas bismuth-based materials values range from 1.2434 cm²/g to 4.6158 cm²/g also in the same interval when the energy is 800 keV MAC ranges between 0.0728 cm²/g (Khazaalah et al., 2022) and 0.0849 cm²/g (Liu et al., 2018) which almost equals the lead's MAC value 0.0884 cm²/g. At high energies (1000 keV and above), both materials exhibit significantly lower MAC values, with bismuth-based materials' values closely matching those of lead. At 1500 keV, lead's MAC is 0.0521 cm²/g, while bismuth's values range from 0.0511 cm²/g to 0.0532 cm²/g. Overall, while lead provides better attenuation at lower energies, bismuth-based materials offer comparable shielding effectiveness at moderate to high energies, making it a viable lead-free alternative for high-energy photon shielding applications.

3.2. Tungsten (W)

Tungsten (W), also known as wolfram, is a greyish-white to steel-grey metal characterized by extreme hardness, wear resistance, high melting point, high density, and excellent thermal and electrical conductivity; while pure tungsten is malleable and ductile, adding small amounts of carbon and oxygen enhances its hardness and brittleness [65]. Tungsten has an atomic weight of 183.9, an atomic number of 74, and a density of 19.3 g/cm³. It has a melting point of 3410°C and a boiling point of 5660°C, with a specific gravity of 19.3. Its crystalline form is gray-black and cubic, and it remains unoxidized in air at ordinary temperatures while being highly resistant to acids. Compared to lead (Pb), tungsten has a higher density with values of 19.3 g/cm³ [66, 67].

Tungsten's high melting point of 3387°C makes it a challenging material to machine or cast, but it has better shielding qualities than lead because of its high atomic number (Z). Due to its high melting point, tungsten is a high temperature material that has long been used to make light bulb filaments [68, 69]. Tungsten can be used to create radiation shielding materials with greater potential, lower costs, environmental friendliness, and improved optical properties when it is used in the development of such materials. Approximately, tungsten powder (99.999%) costs about $2900/kg [70].

Jamal AbuAlRoos et al. assessed tungsten carbide (WC), composed of 98.65% tungsten and 1.35% carbon, as a lead-free radiation shielding material for nuclear medicine [71]. The study analyzed WC using Field-Emission Scanning Electron Microscopy (FESEM) and energy dispersive X-ray (EDX), confirming its 99.9% purity and an average particle size of 40–50 μm. Discs of WC (0.1 cm, 0.5 cm, and 1.0 cm thickness) were compared to lead discs of similar thickness. Gamma spectroscopy with sources (^{123}I, [133]Ba, [152]Eu, and ^{137}Cs) across 0.160 MeV to 0.779 MeV energies measured attenuation properties. The experimental attenuation coefficients of WC and lead were compared to theoretical values from the NIST database. The results showed that gamma spectroscopy peaks exhibited a linear relationship with energy. Relative differences between measured and theoretical mass attenuation coefficients were within 0.19–5.11% for both materials. WC demonstrated lower half-value layers and mean free paths compared to lead, indicating its potential as an effective, lead-free alternative for radiation shielding in nuclear medicine [71].

Azman et al. reviewed tungsten carbide (WC), with a composition of 98.65% tungsten and 1.35% carbon, as a lead-free alternative for radiation shielding [72]. They addressed lead's drawbacks, including toxicity, weight, and opacity. Tungsten carbide's high atomic number, density, and excellent shielding properties make it a promising material. The review covers recent advancements in WC's physical properties, its application as a nanofilm for radiation shielding, and various deposition techniques for fabricating these films. It also discusses the morphological structure of WC nanofilms, as well as key challenges and future directions in this field [72].

Lee et al. proposed a dual-layered Pb-free shielding method to protect workers from external radiation exposure during the decommissioning of the Kori-1 nuclear power plant, which has been shut down since 2017 [73]. Using the Monte Carlo method, the study optimized and estimated the performance of various materials in terms of equivalent dose rate and radiation shielding effectiveness. The dual-layer Pb-free shielding outperformed conventional shields, with WC-Co showing particularly high performance in reducing external radiation during the dismantling of the steam generator (S/G). The simulation results provide valuable guidance for selecting materials and designing effective Pb-free dual-layer shields for this decommissioning process [73].

Das et al. examined metal-based polymer composites, specifically tungsten (W) – polymethyl methacrylate (PMMA), for radiation shielding [73]. They used FLUKA Monte Carlo [74] code to assess the effectiveness of W-PMMA composites in attenuating coupled neutron-gamma radiation. Results indicated that even a 20 vol% concentration of W particles significantly enhances the radiation shielding capability of PMMA. The study identified optimum heavy metal concentrations for shielding: 70 vol% W and 30 vol% Pb, with the Pb shield showing significantly higher doses. Additionally, the research explored double-layer laminates with W and PMMA in various configurations, finding that the new W-PMMA composite-based double-layer shield performed best in volumetric dose reduction, while single-layer W-PMMA composites offered the lowest specific dose [75]. Olivieri et al. developed lead-free x-ray shielding materials using Acrylonitrile-butadiene-styrene (ABS)-based composites with high tungsten and bismuth oxide content [75].

These composites, selected for their mechanical strength and ABS's availability as a recycled material, exhibited good filler dispersion within the polymer matrix while retaining their mechanical properties. The optimal formula, consisting of 70% WO_3 and 30% ABS, shows promise for lead-free x-ray shielding applications, including wearable personal protective equipment [76].

Mass attenuation coefficient (MAC) values of the tungsten-based materials studied by the abovementioned groups are provided in Table 4 for various photon energies. These values were calculated for the composition of materials using the web database Epixs. Additionally, the MAC values are illustrated in Figure 2 as a function of energy, alongside those for lead.
Considering the values given in Table 4 and plotted in Figure 2, some of the tungsten-based materials generally exhibit higher MAC values than lead at very low energies and in some low to moderate photon energies.

For example, at 15 keV, tungsten's MAC ranges from 77.2264 cm²/g (Olivieri et al., 2024) to 136.3780 cm²/g (Jamal AbuAlRoos et al., 2020 and Azman et al., 2023), compared to lead's MAC of 111.1520 cm²/g. At moderate energies (100–1000 keV), tungsten-based material's MAC values are still higher, with a 100 keV value ranging from 2.5364 cm²/g (Olivieri et al., 2024) to 4.3836 cm²/g (Jamal AbuAlRoos et al., 2020 and Azman et al., 2023), compared to lead's 5.5496 cm²/g. At high energies (1000 keV and above), tungsten's MAC converges with that of lead, with a 1000 keV value from 0.0654 cm²/g (Lee et al., 2021) to 0.0667 cm²/g (Das et al., 2023), while lead's is 0.0708 cm²/g. Overall, tungsten-based materials offer superior attenuation at lower energies and comparable performance at higher energies.

Table 4. Mass attenuation coefficients (cm²/g) and lead equivalent for tungsten-based materials at various energies

Energy (MeV)	AbuAlRoos et al., 2020	Azman et al., 2023	Pb Eq.	Lee et al., 2021	Pb Eq.	Das et al., 2023	Pb Eq.	Olivieri et al., 2024	Pb Eq.
0.015	136.3780	136.3780	1.2270	126.1490	1.1349	97.0939	0.8735	77.2264	0.6948
0.02	64.9188	64.9188	0.7541	59.9718	0.6967	46.2325	0.5371	36.7799	0.4273
0.03	22.4349	22.4349	0.7394	20.6911	0.6819	16.0079	0.5276	12.7550	0.4204
0.04	10.4978	10.4978	0.7315	9.6745	0.6741	7.5176	0.5238	6.0080	0.4187
0.05	5.8199	5.8199	0.7267	5.3634	0.6697	4.1901	0.5232	3.3637	0.4200
0.06	3.5971	3.5971	0.7225	3.3171	0.6662	2.6084	0.5239	2.1064	0.4231
0.08	7.7232	7.7232	3.2785	6.9941	2.9690	5.5312	2.3480	4.4201	1.8763
0.1	4.3836	4.3836	0.7899	3.9742	0.7161	3.1582	0.5691	2.5364	0.4570
0.15	1.5649	1.5649	0.7768	1.4258	0.7077	1.1528	0.5722	0.9426	0.4679
0.2	0.7777	0.7777	0.7773	0.7136	0.7133	0.5904	0.5902	0.4943	0.4940
0.3	0.3210	0.3210	0.7965	0.2998	0.7438	0.2613	0.6483	0.2298	0.5702
0.4	0.1911	0.1911	0.8236	0.1814	0.7819	0.1655	0.7136	0.1515	0.6531
0.5	0.1371	0.1371	0.8508	0.1319	0.8184	0.1247	0.7734	0.1173	0.7279
0.6	0.1088	0.1088	0.8723	0.1057	0.8478	0.1025	0.8219	0.0983	0.7887
0.8	0.0803	0.0803	0.9085	0.0791	0.8948	0.0792	0.8961	0.0778	0.8803
1	0.0659	0.0659	0.9314	0.0654	0.9246	0.0667	0.9431	0.0664	0.9383
1.5	0.0499	0.0499	0.9588	0.0499	0.9585	0.0516	0.9926	0.0519	0.9978
2	0.0442	0.0442	0.9630	0.0441	0.9604	0.0453	0.9867	0.0453	0.9874
3	0.0406	0.0406	0.9615	0.0401	0.9498	0.0400	0.9467	0.0393	0.9296
4	0.0402	0.0402	0.9592	0.0393	0.9389	0.0380	0.9085	0.0366	0.8749
5	0.0408	0.0408	0.9565	0.0396	0.9296	0.0374	0.8774	0.0354	0.8309
6	0.0418	0.0418	0.9540	0.0404	0.9219	0.0374	0.8530	0.0349	0.7965
8	0.0444	0.0444	0.9502	0.0425	0.9110	0.0382	0.8183	0.0349	0.7477
10	0.0471	0.0471	0.9474	0.0449	0.9034	0.0395	0.7953	0.0355	0.7154
15	0.0533	0.0533	0.9431	0.0504	0.8924	0.0431	0.7626	0.0379	0.6698
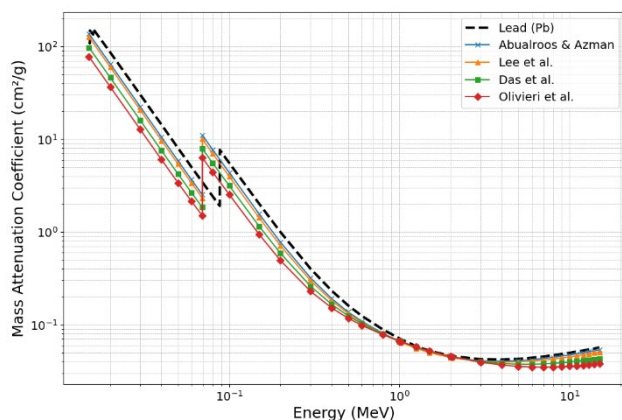
Figure 2. Mass attenuation coefficient values of various tungsten-based materials compared with lead

3.3. Barium (Ba)

Barium is the heaviest of the stable alkaline earth metals, with an atomic weight of 137.3, density of 3.62 g/cm3, and atomic number of 56. A soft metal that is silver-white and melts at 725°C is the free element. Barium volatiles, particularly halide salts, give the Bunsen flame a light green tint [77]. Barium as metal is generally non-toxic to humans and functions as a bone opacifier in the human body [78]. Barium oxide opens up new possibilities for environment friendly radiation shielding materials [79]. Due to its high atomic number and good attenuation coefficient, barium-based glasses have a very promising gamma radiation attenuation coefficient [30]. Due to its high density and atomic number, barium is a substance that is very good at absorbing ionizing radiation.

Barium oxide (BaO), for instance, can improve glass systems' capacity to guard against gamma radiation. strong atomic number, strong electrical resistance, high refraction, low coefficient of thermal expansion, low dispersion, and comparatively low melting point are only a few of barium's advantageous characteristics. Due to barium's high density and heavy-metal characteristics, adding more of it to materials enhances their shielding capabilities even further. Barium metal (99.2 + %) costs roughly $3 per gram. Sen Baykal et al. designed and synthesized a lead-free, high-density borosilicate glass sample, BSBaZn, for potential use in radiation shielding applications in medical and industrial settings [80].

The glass composition is given by $7B_2O_3$-$50SiO_2$-$38ZnO$-$5BaO$. Structural and optical analyses, including FTIR spectroscopy, revealed four fundamental regions of interest in the glass, and it showed a transmittance rate of 80% in the 350–1100 nm wavelength range. Gamma-ray attenuation properties were assessed using a high-purity Germanium (HPGe) detector and a $133Ba$ radioisotope. The study employed the MCNPX Monte Carlo code to calculate gamma-ray transmission factors (TF) [56]. The results demonstrated that BSBaZn exhibits promising structural, optical, and gamma-ray shielding characteristics. Its high transparency and density make it a strong candidate for radiation protection in medical and industrial facilities where both source and patient monitoring are crucial [80].

Moradi et al. investigated barium tantalate ($Ba_5Ta_4O_{15}$) as a lead-free alternative for x-ray shielding in interventional radiology [81]. Traditional lead-based materials, while effective, pose challenges due to their weight and toxicity. The study employed Geant4 Monte Carlo simulations to explore various barium tantalate formulations doped with rare earth elements. Results indicated that barium tantalate doped with 15% Erbium or 10% Samarium by weight offers effective x-ray shielding with over 30% weight reduction compared to lead-based materials. These findings suggest that barium tantalate could serve as a viable, lighter, and safer option for radiation shielding in medical settings [81].

Souza et al. introduced a novel, cost-effective lead-free elastomeric material for radiation shielding, designed to enhance user ergonomics while preventing exposure to harmful levels of ionizing radiation [82]. The material comprises a blend of 1 $BaSO_4$ (barium sulfate) with 0.9 Si (silicon), 1.8 C (carbon), 5.4 H (hydrogen), and 0.9 O (oxygen), combined with addition-cure liquid silicone rubber. X-ray transmission measurements were performed for various thicknesses of this material and the results were compared with Monte Carlo simulations to ensure its effectiveness. The findings confirm that this material meets the requirements for use in radiation protection garments, offering a lighter and more ergonomic alternative to conventional lead-based shields [82].

Hannachi et al. explored a new ceramic-based material for γ-radiation shielding, specifically focusing on barium tungstate ($BaWO4$) doped with holmium oxide ($Ho2O3$) in varying amounts [83]. Monte Carlo simulations were employed to assess radiation attenuation. The radiation shielding coefficients decreased with higher Ho2O3 content. Specifically, the linear attenuation coefficient decreased by 13% from 0.386 cm^{-1} to 0.338 cm^{-1} at 0.662 MeV with an increase in Ho2O3 from 0% to 75%. Concurrently, the lead equivalent thickness increased from 3.22 cm to 3.67 cm. The optimal material identified in this study for γ-radiation shielding is a composite with 75% BaWO4 and 25% Ho2O3, as it provides a balance between shielding effectiveness and material composition [83].

Mass attenuation coefficient (MAC) values of the barium-based materials studied by the abovementioned groups are provided in Table 5 for various photon energies. These values were calculated for the composition of materials using the web database Epixs. Additionally, the MAC values are illustrated in Figure 3 as a function of energy, alongside those for lead.

As it can be seen from Figure 3, barium-based materials generally show lower MAC values than lead but are comparable at higher photon energies. At 15 keV, MAC values for the materials range from 5.4464 cm²/g (Souza et al., 2023) to 89.9327 cm²/g (Hannachi et al., 2023), which are lower than that of lead (111.1520 cm²/g). At moderate energies (100–1000 keV), MAC values of the materials are significantly lower. For example, MAC values for 100 keV photon energy are ranging from 0.3535 cm²/g (Souza et al., 2023) to 2.9686 cm²/g (Hannachi et al., 2023), all are lower compared to lead's 5.5496 cm²/g value. For higher photon energies (1000 keV and above), the MAC values for barium converge with those of lead. At 1000 keV energy, lead has 0.0708 cm²/g MAC value, and materials have the values in a range between 0.0619 cm²/g (Sen Baykal et al., 2023) and 0.0970 cm²/g (Souza et al., 2023). Overall, it can be said that barium-based materials are less effective than lead at low and moderate photon energies, where attenuation is reduced. However, at higher energies their performance becomes

comparable, making them a viable, safer, and more environmentally friendly alternative in specific high-energy applications across diverse medical imaging and therapy scenarios.
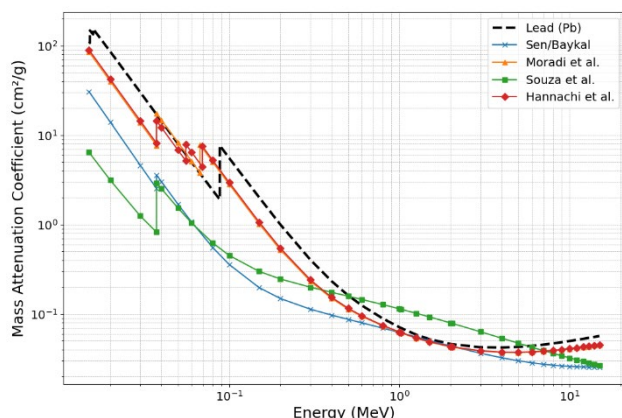

Figure 3. Mass attenuation coefficient values of various barium-based materials compared with lead

4. Other Emerging Materials

4.1. Tin (Sn)

Tin, which is not an essential metal, is a silvery, soft and pliable metal which resists corrosion and is widely used in industry and occurs in both inorganic and organic forms in nature. It has more commercially used organometallic derivatives than any other element, leading to a significant increase in global production of organotin compounds over the past decades. Due to their extensive industrial applications, substantial quantities of organotins have entered various ecosystems [84].

Tin (Sn) has an atomic weight of 118.69, an atomic number of 50, a density ranging from 5.8 to 7.3 (white tin), a melting point of 231.9°C, and a boiling point of 2602°C. Tin has three allotropic forms: white metallic, tetragonal (tin white), and white rhombic (tin brittle). When cooled below 13.2°C, it converts to gray tin or α-tin cubic [85]. Tin can be converted by chemical and biological reactions in the environment to form more toxic organotin compounds. Commercial tin has ranged in price over the last 25 years from 50¢/lb ($1.10/kg) to over $6/kg. Nowadays, a kilogram of pure tin costs roughly $260 [86].

Bjarnason et al. evaluated the absorption capability and weight of various lead-alternative radiation-shielding materials, focusing on tin, antimony, bismuth, and tungsten [87]. Factors such as toxicity, atomic number, density, K-edge absorption energy, and availability were considered. The attenuation coefficients of these elements were calculated using the XCOM software package [57], and the metals were mixed with polymers at mass ratios of 50%, 70%, 80%, and 85%. The study concluded that all new shielding materials tested are suitable for diagnostic X-ray applications. When compared to commercial lead garments, the 85% metal-polymer samples were lighter than a 0.5-mm lead garment and offered superior radiation protection. This suggests significant potential for these materials in commercial applications [87]. Bakhshandeh et al. explored the potential of a composite shield made from tin and tungsten as an alternative to traditional lead shields used in nuclear medicine [88]. Lead aprons, while effective, are criticized for their weight and toxicity. The study focused on evaluating the biological protection offered by the tin-tungsten composite compared to lead shields. Blood samples from non-radiation operatives were exposed to gamma radiation from technetium, and DNA damage was assessed. The composite shield demonstrated a density about one-tenth that of lead, at 1.23 g/cm³. Results indicated that DNA damage was lower with the lead-free shield compared to lead shields, with time being a significant factor in DNA damage, while the type of shield and distance did not show a significant effect. The study highlights the potential of tin-tungsten composites as alternative for reducing radiation-induced DNA damage, addressing the drawbacks of lead-based shielding [88].

Alım et al. investigated the potential of various alloys as replacements for lead and its derivatives in radiation shielding applications [89]. The study aimed to identify an optimal shielding material by evaluating the radiation-shielding characteristics of five different alloys: Tin-Silver, Manganin-R, Hastelloy-B, Hastelloy-X, and Dilver-P. Key photon interaction parameters were determined for these alloys across an energy range of 30 to 1333 keV using narrow-beam transmission geometry and experimental measurements with two detectors (Si(Li) and NaI(Tl)). The results were compared with theoretical calculations from Phy-X/PSD

software. Finally, while Manganin-R alloy stands out as the superior shielding material for photon energies due to its high density, melting point, tensile strength, modulus of elasticity, and specific heat, the Tin-Silver alloy excels in aspects like attenuation coefficients [89].

Table 5. Mass attenuation coefficients (cm^2/g) and lead equivalent for barium-based materials at various energies

Energy (MeV)	Sen Baykal et al., 2023	Pb Eq.	Moradi et al., 2024	Pb Eq.	Souza et al., 2023	Pb Eq.	Hannachi et al., 2023	Pb Eq.
0.015	30.7976	0.2771	85.2541	0.7670	5.4464	0.0490	89.9327	0.8091
0.02	14.0786	0.1635	40.1536	0.4665	2.6018	0.0302	42.4186	0.4928
0.03	4.6220	0.1523	13.7212	0.4522	1.0176	0.0335	14.5221	0.4786
0.04	3.0146	0.2101	14.7046	1.0247	1.7718	0.1235	12.1147	0.8442
0.05	1.6941	0.2115	8.2566	1.0309	1.0996	0.1373	6.7796	0.8465
0.06	1.0753	0.2160	5.1129	1.0269	0.7670	0.1540	6.4625	1.2980
0.08	0.5561	0.2361	5.0138	2.1284	0.4734	0.2010	5.2568	2.2315
0.1	0.3584	0.0646	2.8285	0.5097	0.3535	0.0637	2.9686	0.5349
0.15	0.1971	0.0979	1.0200	0.5063	0.2447	0.1214	1.0696	0.5310
0.2	0.1487	0.1487	0.5212	0.5210	0.2049	0.2048	0.5450	0.5447
0.3	0.1129	0.2802	0.2327	0.5772	0.1681	0.4172	0.2410	0.5980
0.4	0.0969	0.4176	0.1490	0.6423	0.1480	0.6378	0.1532	0.6604
0.5	0.0868	0.5387	0.1132	0.7022	0.1341	0.8319	0.1158	0.7183
0.6	0.0795	0.6380	0.0938	0.7520	0.1236	0.9909	0.0955	0.7662
0.8	0.0692	0.7830	0.0732	0.8282	0.1081	1.2235	0.0741	0.8388
1	0.0619	0.8753	0.0620	0.8768	0.0970	1.3712	0.0626	0.8854
1.5	0.0504	0.9678	0.0484	0.9296	0.0788	1.5147	0.0487	0.9362
2	0.0436	0.9501	0.0427	0.9303	0.0675	1.4701	0.0430	0.9367
3	0.0362	0.8568	0.0383	0.9073	0.0539	1.2764	0.0386	0.9138
4	0.0322	0.7690	0.0370	0.8843	0.0458	1.0947	0.0373	0.8910
5	0.0298	0.6995	0.0369	0.8656	0.0405	0.9499	0.0372	0.8725
6	0.0283	0.6457	0.0373	0.8507	0.0367	0.8370	0.0376	0.8576
8	0.0266	0.5700	0.0387	0.8297	0.0316	0.6773	0.0391	0.8367
10	0.0258	0.5200	0.0405	0.8154	0.0284	0.5722	0.0409	0.8226
15	0.0253	0.4483	0.0449	0.7949	0.0240	0.4247	0.0453	0.8021

4.2. Cadmium (Cd)

Cadmium (Cd) with atomic number 48 and atomic weight 112.41. It belongs to group XII of the periodic table. Its soft, silvery-white metal, with a density of 8.65 g/cm³ and melting point of 321°C. Cadmium is soft, malleable, and ductile. It is resistant to corrosion, used as a protective plate, water-insoluble, and non-flammable, although it burns in air to form cadmium oxide. Cadmium, is a non-essential transition metal that can pose health risks to humans and animals due to its lack of a physiological function [90, 91].

El-Khatib et al. investigated HDPE composites with micro-sized and nano-sized cadmium oxide (CdO) particles for gamma radiation shielding [92]. The study found that nano-CdO/HDPE composites performed better than micro-CdO/HDPE, especially at low gamma-ray energies. The best performance was achieved with a composite of 40 wt% nano-CdO and 60 wt% HDPE, which showed a decent improvement in shielding at 59.53 keV due to the higher interaction probability between gamma-rays and nano-sized particles. From this study, it can be concluded that nano-CdO exhibits strong performance as a radiation shielding material [92].

4.3. Gadolinium (Gd)

Gadolinite is a soft, silvery-white rare-earth metal named after the Finnish chemist Gadolin. With an atomic number of 64 and an atomic weight of 157.25, gadolinium has a melting point of 1313 °C, a boiling point of 3273 °C, and density approximately 7.90 g/cm³ [93]. Gadolinium oxide, also known as gadolinia, is named after gadolinite, the mineral from which it was initially derived. Gadolinium is also present in other minerals such as monazite and bastnasite, which hold significant commercial value [48, 94].

Ogul et al. used 3D printing to create poly lactic acid (PLA) samples with 10% and 20% gadolinium oxide nanoparticles to evaluate their radiation shielding potential [95]. The optimal composition of the P-PLA-Gd20 sample was C 40.0009, H 4.4757, O 38.1767, and Gd 17.3467. This sample emerged as the best material, demonstrating excellent gamma-ray attenuation comparable to lead and achieving 100% thermal neutron shielding with a 10 mm thickness. This makes it a promising alternative to traditional lead aprons for both X-ray and neutron shielding [95].

4.4. Antimony (Sb)

Antimony is a silvery white metal with atomic number 51, and atomic mass 122. Antimony name is of Greek origin, "anti" plus "monos," translating to "a metal not found alone". This is accurate as native antimony metal is rarely found, it is usually discovered as a sulfide mineral, the most important being stibnite, Sb2S3. Antimony has a fairly low melting point for a metal, 630.6°C, is very brittle and a poor conductor of heat and electricity [96-98]. Antimony is typically used in combination with other materials for radiation shielding, particularly in alloys or composites, to enhance their protective properties against X-rays and gamma radiation. It is rarely used as a standalone shielding pmaterial [99, 100].

Özkalaycı et al. aimed to fabricate and investigate the gamma photon shielding efficiency of antimony (Sb) doped polymer resin composites [101]. They used orthophthalic unsaturated polyester resin (C16O7H14) as the matrix and antimony powder as the filler. Sb particles were added to the composites in concentrations ranging from 5 to 20 wt%. Different isotopes were used to test gamma radiation shielding properties across energy levels from 59.5 to 1408.0 keV. To assess gamma-ray attenuation, the mass attenuation coefficient (MAC) was calculated, along with another key. Özkalaycı et al. found that a 20% antimony, 80% polyester resin composite provided the best gamma shielding among the tested Sb-doped polymers, showing superior attenuation performance [101].

4.5. Molybdenum (Mo)

Molybdenum, a trace element essential for microorganisms, plants, and animals, was discovered in 1778 by Karl Scheele, a Swedish scientist. It was originally thought to be lead, but its name, molybdos, comes from the Greek and means "lead-like." While molybdenum trioxide is a white powder that changes to a yellow substance when heated, molybdenum is a silver-white metal that can also be found as a black or dark-gray powder. The powdered form of molybdenite, also known as molybdenum disulfide, is gray and shiny. This metal has a melting temperature of 2610°C and a boiling point of 5560°C. Its atomic weight is 95.94 and its atomic number is 42 with density of 10.28 g/cm^3. Because it may give other materials hardness, weldability, and corrosion resistance, molybdenum is valued [102 - 105].

Al-Mugren et al. investigated HDPE composites doped with tungsten carbide, molybdenum carbide, and silicon carbide for kilovoltage radiation shielding. The produced shielding materials, composed of 85% HDPE and 15% MoC, were cut into disks, which were found to be lighter than lead (Pb). Findings suggest that HDPE composites doped with 15% MoC present the most promising configuration for low-energy X-ray shielding (30–50 keV) [106]. MACs and Pb-equivalents for tin, cadmium, gadolinium, antimony, and molybdenum are summarized in Table 6.

5. Performance Comparison and Discussion

5.1. Comparative MAC values

Mass attenuation coefficient (MAC) values of the investigated lead-free materials, namely bismuth, tungsten, barium, tin, cadmium, gadolinium, antimony and molybdenum, are presented in Tables 2–5 and Figures 1–4, with lead included as the reference material. At low photon energies in the range of 15–60 keV, where the photoelectric effect is the predominant interaction mechanism, materials with higher atomic numbers and densities demonstrate superior attenuation efficiency. Lead, with an atomic number of 82 and a density of 11.34 g/cm^3, consistently records the highest MAC

values, reaching 111.1520 cm²/g at 15 keV. Tungsten, with a slightly lower atomic number but a significantly higher density of 19.3 g/cm³, achieves comparable or in some cases higher MAC values in this low-energy range, particularly in high-purity carbide forms.

Bismuth-based materials, benefitting from an atomic number of 83 and a density close to 9.8 g/cm³, also show strong attenuation performance, with several dense bismuth oxide and glass composites approaching or exceeding 100 cm²/g at 15 keV, highlighting their effectiveness for specialized shielding, diagnostic radiology, and potential advanced therapeutic applications in modern medical environments.
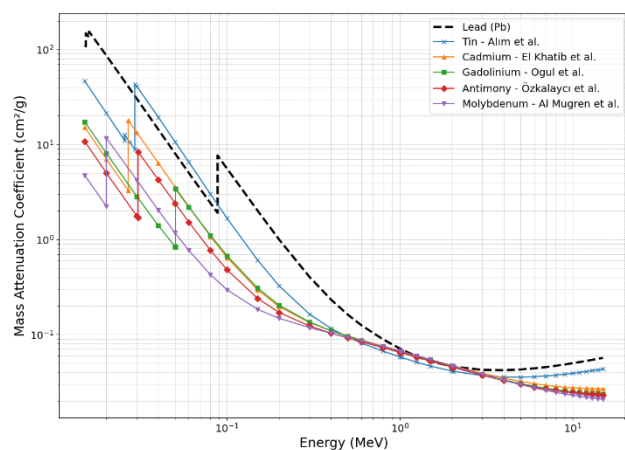

Figure 4. Mass attenuation coefficient values of various tin-, cadmium-, gadolinium-, antimony-, and molybdenum-based materials compared with lead

In contrast, barium-based materials, despite their usefulness in certain composite formulations, generally display lower MAC values unless present in high-density oxide or tungstate forms. Lower atomic number materials such as tin, cadmium, gadolinium, antimony and molybdenum exhibit noticeably reduced performance in this energy range; for instance, tin achieves 46.3733 cm²/g, gadolinium 17.2580 cm²/g and cadmium 15.1459 cm²/g, reflecting the strong dependence of photoelectric absorption probability on the cube of the atomic number. In the moderate photon energy range between 100 and 1000 keV, Compton scattering becomes the dominant interaction mechanism. In this regime, attenuation is influenced more by electron density than by atomic number alone, leading to a narrowing of the performance gap between lead and some of the high-density alternatives.

Tungsten-based composites frequently reach MAC values close to those of lead, with high-performance formulations recording up to 4.38 cm²/g at 100 keV compared to lead's 5.5496 cm²/g. Bismuth-based glasses and polymer composites also perform competitively, with values around 4.6 cm²/g at the same energy. Barium-based systems, even when optimized, generally remain below 3.0 cm²/g at 100 keV, while among the lower atomic number group, molybdenum and tin perform better than cadmium, gadolinium and antimony due to their higher densities and more favorable electron densities. These observations indicate that in the Compton scattering–dominated energy range, high-density lead-free alternatives can provide attenuation performance that is suitable for many medical and industrial applications, even if they do not exactly match lead.

At high photon energies above 1000 keV, the influence of atomic number on attenuation efficiency decreases significantly as pair production and other high-energy processes become more relevant. Under these conditions, the MAC values of all investigated materials converge. At 1000 keV, lead's MAC value of 0.0708 cm²/g is essentially identical to that of molybdenum (0.0705 cm²/g) and only slightly higher than those of tungsten, bismuth, cadmium, gadolinium and certain high-density barium composites. This convergence confirms that at high energies, a variety of lead-free materials can provide comparable shielding performance, allowing the selection of materials to be guided by other considerations such as toxicity, environmental impact, cost, ease of fabrication and mechanical properties.

In summary, lead remains the most effective shielding material at low photon energies due to the strong atomic number dependence of the photoelectric effect, while tungsten and bismuth offer the closest overall performance across the full energy spectrum. Barium is more competitive at higher energies or when incorporated into optimized composite formulations, and lower atomic number materials, although less effective at low energies, become comparable to lead in the high-energy range.

These findings highlight the importance of matching the choice of shielding material to the

photon energy range of interest, while also taking into account practical factors such as weight reduction, user comfort, cost-effectiveness and environmental sustainability in the development of next-generation radiation shielding solutions.

Table 6. Mass attenuation coefficients (cm^2/g) and lead equivalent for Tin, Cadmium, Gadolinium, Antimony and Molybdenum based materials at various energies

Energy (MeV)	Tin		Cadmium		Gadolinium		Antimony		Molybdenum	
	Alım, 2020	Pb Eq.	El-Khatib et al., 2019	Pb Eq.	Ogul et al., 2024	Pb Eq.	Özkalaycı et al., 2022	Pb Eq.	Al-mugren et al., 2024	Pb Eq.
0.015	46.3733	0.4172	15.1459	0.1363	17.2580	0.1553	10.7647	0.0968	4.4297	0.0399
0.02	21.2498	0.2469	6.9845	0.0811	8.1018	0.0941	4.9900	0.0580	2.0575	0.0239
0.03	40.7164	1.3419	13.3942	0.4414	2.8296	0.0933	1.7170	0.0566	3.9865	0.1314
0.04	19.3301	1.3470	6.3846	0.4449	1.3834	0.0964	4.2385	0.2954	1.9248	0.1341
0.05	10.6820	1.3338	3.5685	0.4456	0.8064	0.1007	2.4067	0.3005	1.1207	0.1399
0.06	6.5519	1.3159	2.2257	0.4470	2.1988	0.4416	1.5291	0.3071	0.7421	0.1490
0.08	3.0234	1.2834	1.0840	0.4602	1.1119	0.4720	0.7729	0.3281	0.4201	0.1783
0.1	1.6744	0.3017	0.6464	0.1165	0.6742	0.1215	0.4798	0.0864	0.2952	0.0532
0.15	0.6088	0.3022	0.2952	0.1465	0.3092	0.1535	0.2403	0.1193	0.1888	0.0937
0.2	0.3257	0.3255	0.1968	0.1967	0.2036	0.2035	0.1705	0.1705	0.1535	0.1535
0.3	0.1636	0.4059	0.1333	0.3308	0.1348	0.3344	0.1226	0.3042	0.1236	0.3065
0.4	0.1154	0.4974	0.1096	0.4724	0.1095	0.4718	0.1031	0.4445	0.1081	0.4660
0.5	0.0936	0.5807	0.0963	0.5977	0.0956	0.5934	0.0916	0.5685	0.0977	0.6062
0.6	0.0810	0.6497	0.0874	0.7007	0.0864	0.6930	0.0836	0.6702	0.0899	0.7213
0.8	0.0665	0.7529	0.0753	0.8517	0.0742	0.8392	0.0724	0.8191	0.0786	0.8894
1	0.0579	0.8187	0.0671	0.9477	0.0660	0.9321	0.0647	0.9138	0.0705	0.9963
1.5	0.0463	0.8906	0.0543	1.0438	0.0533	1.0240	0.0524	1.0077	0.0573	1.1011
2	0.0411	0.8946	0.0470	1.0238	0.0460	1.0012	0.0453	0.9855	0.0493	1.0726
3	0.0368	0.8722	0.0389	0.9221	0.0377	0.8931	0.0371	0.8784	0.0398	0.9426
4	0.0356	0.8493	0.0346	0.8260	0.0331	0.7915	0.0326	0.7777	0.0344	0.8205
5	0.0354	0.8311	0.0320	0.7496	0.0303	0.7105	0.0297	0.6975	0.0308	0.7233
6	0.0358	0.8164	0.0302	0.6899	0.0284	0.6475	0.0278	0.6351	0.0284	0.6477
8	0.0372	0.7966	0.0283	0.6060	0.0261	0.5585	0.0255	0.5471	0.0253	0.5409
10	0.0389	0.7834	0.0273	0.5507	0.0248	0.4998	0.0243	0.4891	0.0234	0.4706
15	0.0431	0.7625	0.0267	0.4721	0.0236	0.4172	0.0230	0.4071	0.0210	0.3714

6. Conclusion

In conclusion, this review highlights the critical need for alternatives to lead in radiation shielding, given its disadvantages, particularly in medical applications. While lead remains highly effective in attenuating radiation, its toxicity causes significant health risks to both patients and medical staff. Furthermore, environmental hazards associated with the disposal and potential contamination of lead compounds emphasize the urgency for safer, more sustainable options. The alternative materials examined in this review—Bismuth, Tungsten, Barium, Tin, Cadmium, Gadolinium, Antimony, and Molybdenum—demonstrate promising potential to address these challenges. Of these, Tungsten and Bismuth stand out because they are non-toxic, safe for the environment, and have a large amount of research and literature proving their effectiveness.

These materials not only reduce the health risks associated with lead but also align with modern sustainability goals by decreasing it's negative impacts. Although they come at a higher cost, their superior performance in radiation shielding, coupled with their safety profile, make them attractive candidates for further development. The shift toward these alternatives could greatly improve the safety standards of healthcare practices by eliminating the harmful side effects of lead, such as chronic toxicity and contamination risks. As ongoing research and technological advancements continue to enhance the performance and cost-efficiency of these materials, they hold the potential to revolutionize the future of medical radiation shielding. This transformation would not only ensure better protection for medical professionals and patients but also contribute to a significant reduction in

the environmental effects of radiation shielding practices.

Finally, these emerging alternatives may play a pivotal role in shaping a safer and more sustainable approach to radiation protection in healthcare settings. Future research should prioritize the design and experimental validation of new composite materials that combine high atomic number (high-Z) elements with lightweight polymers or ceramics, aiming to achieve effective shielding with reduced mass. Comprehensive studies covering a wide photon energy range, along with cost and lifecycle analyses, will be important to assess their practical applicability.

Moreover, exploring additive manufacturing methods, such as 3D printing, could allow for the production of patient-specific or procedure-specific shielding devices, improving both radiation protection efficiency and user comfort in clinical environments.

Article Information Form

Authors' Contribution
Conceptualization, K.H.A. and H.A.; methodology, K.H.A.; literature collection and analysis, K.H.A. and H.A.; writing—original draft preparation, K.H.A.; writing—review and editing, K.H.A. and H.A.; supervision, H.A. All authors have read and agreed to the published version of the manuscript.

The Declaration of Conflict of Interest
No conflict of interest or common interest has been declared by authors.

Artificial Intelligence Statement
No artificial intelligence tools were used while writing this article.

Copyright Statement
Author own the copyright of their work published in the journal and their work is published under the CC BY-NC 4.0 license.

References

[1]   International Agency for Research on Cancer (IARC), IARC Monographs on the Evaluation of Carcinogenic Risks to Humans, Vol. 102: Non-Ionizing Radiation, Part 2: Radiofrequency Electromagnetic Fields. Lyon: IARC, 2013.

[2]   Z. Huan, Y. Zheng, K. Wang, Z. Shen, W. Ni, J. Zua, Y. Shao, "Advancements in radiation resistance and reinforcement strategies of perovskite solar cells in space applications," J. Mater. Chem. A, vol. 12, no. 4, pp. 1910–1922, 2024.

[3]   H. Omer, "Radiobiological effects and medical applications of non-ionizing radiation," Saudi Journal of Biological Sciences, vol. 28, no. 10, pp. 5585–5592, 2021.

[4]   L. R. Dartnell, "Ionizing Radiation and Life," Astrobiology, vol. 11, no. 6, pp. 551–582, 2011.

[5]   G. Sgouros, "Alpha-particles for targeted therapy," Advanced Drug Delivery Reviews, vol. 60, no. 12, pp. 1402–1406, 2008.

[6]   B. Collum, "Radiation" in Nuclear Facilities, Elsevier, pp. 45–60, 2017.

[7]   M. Bauckneht, C. Ciccarese, R. Laudicella, C. Mosillo, F. D'Amico, A. Anghelone, A. Strusi, V. Beccia, S. Bracarda, G. Fornarini, G. Tortora, R. Iacovelli, "Theranostics revolution in prostate cancer: Basics, clinical applications, open issues and future perspectives," Cancer Treatment Reviews, vol. 124, p. 102698, 2024.

[8]   U. Akar Tarim, "Assessment of the Usability of a Composite Containing Boron Carbide for Shielding the Gamma Rays," Sakarya University Journal of Science, vol. 27, no. 1, pp. 159–167, 2023.

[9] S. Procz, C. Avila, J. Fey, G. Roque, M. Schuetz, E. Hamann, "X-ray and gamma imaging with Medipix and Timepix detectors in medical research," Radiation Measurements, vol. 127, p. 106104, 2019.

[10] International Agency for Research on Cancer (IARC), Ed., A Review of Human Carcinogens (IARC Monographs on the Evaluation of Carcinogenic Risks to Humans, Vol. 100). Lyon: IARC, 2012.

[11] E. Mansouri, A. Mesbahi, R. Malekzadeh, A. Mansouri, "Shielding characteristics of nanocomposites for protection against X- and gamma rays in medical applications: effect of particle size, photon energy and nano-particle concentration," Radiat Environ Biophys, vol. 59, no. 4, pp. 583–600, 2020.

[12] H. Kudo, Ed., Radiation Applications (An Advanced Course in Nuclear Engineering, Vol. 7). Singapore: Springer, 2018.

[13] J. G. Kiang, A. O. Olabisi, "Radiation: A poly-traumatic hit leading to multi-organ injury," Cell Biosci, vol. 9, no. 1, p. 25, 2019.

[14] B. Barrett, M. Stiles, J. Patterson, "Radiation risks: Critical analysis and commentary," Preventive Medicine, vol. 54, no. 3–4, pp. 280–282, 2012.

[15] D. İckecan, T. Nuredin, D. Erbahar, H. Gülbiçim, "Comparing the Shielding Features of Graphene and Impregnated Activated Carbon with Selected Traditional Shielding Materials for Gamma-Rays," Sakarya University Journal of Science, vol. 27, no. 3, pp. 580–589, 2023.

[16] N. Voudoukis, S. Oikonomidis, "Inverse square law for light and radiation: A unifying educational approach," EJERS, vol. 2, no. 11, p. 23, 2017.

[17] A. H. Patel, V. Patel, Y. Tang, S. Shah, G. Tang, M. J. Kern, "Implementing a 'Lead [Apron]-Free' Cardiac Catheterization:

Current Status," Curr Cardiol Rep, vol. 26, no. 9, pp. 1021–1029, 2024.

[18] J. H. Kim, "Three principles for radiation safety: Time, distance, and shielding," Korean J Pain, vol. 31, no. 3, pp. 145–146, 2018.

[19] International Commission on Radiological Protection (ICRP), Recommendations of the International Commission on Radiological Protection: Adopted 1977 (Annals of the ICRP). 1977. [Online]. Available: https://books.google.com.tr/books?id=0gcaAQAAMAAJ.

[20] V. De Coninck, X. Mortiers, L. Hendrickx, S. De Wachter, O. Traxer, E. X. Keller, "Radiation exposure of patients during endourological procedures," World J Urol, vol. 42, no. 1, p. 266, 2024.

[21] D. J. Greene, C. F. Tenggadjaja, R. J. Bowman, G. Agarwal, K. Y. Ebrahimi, D. D. Baldwin, "Comparison of a Reduced Radiation Fluoroscopy Protocol to Conventional Fluoroscopy During Uncomplicated Ureteroscopy," Urology, vol. 78, no. 2, pp. 286–290, 2011.

[22] P. Limkitjaroenporn, W. Cheewasukhanont, S. Kothan, J. Kaewkhao, "Development of New High Transparency Pb-Free Radiation Shielding Glass," Integrated Ferroelectrics, vol. 214, no. 1, pp. 181–204, 2021.

[23] C. V. More, Z. Alsayed, M. S. Badawi, A. A. Thabet, P. P. Pawar, "Polymeric composite materials for radiation shielding: A review," Environ Chem Lett, vol. 19, no. 3, pp. 2057–2090, 2021.

[24] M. Balali-Mood, K. Naseri, Z. Tahergorabi, M. R. Khazdair, M. Sadeghi, "Toxic mechanisms of five heavy metals: Mercury, lead, chromium, cadmium, and arsenic," Front. Pharmacol., vol. 12, 2021.

[25] P. B. Tchounwou, C. G. Yedjou, A. K. Patlolla, D. J. Sutton, "Heavy metals toxicity and the environment," EXS, vol. 101, pp. 133–164, 2012.

[26] I. Erkoyuncu, F. Akman, H. Ogul, M. R. Kaçal, H. Polat, I. Demirkol, K. Dilsiz, B. Ertuğral, "A detailed investigation of gamma and neutron shielding capabilities of ternary composites doped with polyacrylonitrile and gadolinium (III) sulfate," Applied Radiation and Isotopes, vol. 196, p. 110789, 2023.

[27] Canada Metal (Pacific) Ltd. 2016. A guide to the use of lead for radiation shielding [Online]. Available: https://www.canadametal.com/radiation-protection/.

[28] M. Donya, M. Radford, A. ElGuindy, D. Firmin, M. H. Yacoub, "Radiation in medicine: Origins, risks and aspirations," Global Cardiology Science and Practice, vol. 2014, no. 4, p. 57, 2014.

[29] N. J. AbuAlRoos, N. A. Baharul Amin, R. Zainon, "Conventional and new lead-free radiation shielding materials for radiation protection in nuclear medicine: A review," Radiation Physics and Chemistry, vol. 165, p. 108439, 2019.

[30] A. A. Oglat, S. M. Shalbi, "An Alternative Radiation Shielding Material Based on Barium-Sulphate (BaSO4)-Modified Fly Ash Geopolymers," Gels, vol. 8, no. 4, p. 227, 2022.

[31] M. Almurayshid, Y. Alssalim, F. Aksouh, R. Almsalam, M. ALQahtani, M. I. Sayyed, F. Almasoud, "Development of New Lead-Free Composite Materials as Potential Radiation Shields," Materials, vol. 14, no. 17, p. 4957, 2021.

[32] S. Muir, R. McLeod, R. Dove, "Light-weight lead aprons—light on weight, protection or labelling accuracy?" Australas. Phys. Eng. Sci. Med., vol. 28, no. 2, pp. 128–130, 2005.

[33] X.-L. Ni, J.-L. Li, J.-H. Lv, Z.-J. Liao, C. Yang, J. Zeng, Y.-J. Li, Y.-T. Li, Y.-L. Zhou, Q.-P. Zhang, "Intensely bonded high filling bismuth oxide with chloroprene rubber to achieve lead-free flexible materials for γ-rays shielding," Radiation Effects and Defects in Solids, pp. 1–13, 2024.

[34] E. Kusiak, M. Zaborski, W. Baryń, "Lead-free elastomers composites as X-ray radiation-absorbing materials," Przemysl Chemiczny, vol. 90, no. 5, pp. 874–877, 2011.

[35] P. Lim-aroon, E. Wimolmala, N. Sombatsompop, K. Saenboonruang, "Manufacturing process and properties of lead-free natural rubber sponge for use in X-ray and gamma ray shielding applications," IOP Conf. Ser.: Mater. Sci. Eng., vol. 526, no. 1, p. 012015, 2019.

[36] S. M. J. Mortazavi, A. Zahiri, D. Shahbazi-Gahrouei, S. Sina, M. Haghani, "Designing a shield with lead-free polymer base with high radiation protection for X-ray photons in the range of diagnostic radiology using monte carlo simulation code MCNP5," Journal of Isfahan Medical School, vol. 34, no. 385, pp. 637–641, 2016.

[37] K. Yue, W. Luo, X. Dong, C. Wang, G. Wu, M. Jiang, Y. Zha, "A new lead-free radiation shielding material for radiotherapy," Radiation Protection Dosimetry, vol. 133, no. 4, pp. 256–260, 2009.

[38] V. P. Singh, N. M. Badiger, "An investigation on gamma and neutron shielding efficiency of lead-free compounds and alloys," Indian Journal of Pure and Applied Physics, vol. 54, no. 7, pp. 443–448, 2016.

[39] O. Bawazeer, A. Fallatah, M. Alasmary, Y. Bokhary, A. Almerabi, S. Khan, N. Abuhadi, A. Alalawi, N. Asiri, S. Bawazir, S. Al-Qahtani, M. Algethami, M. Badawy, "Investigation of barium sulphate shielding during panoramic radiography," Egypt J

Radiol Nucl Med, vol. 54, no. 1, p. 203, 2023.

[40] M. Ghasemi-Nejad, L. Gholamzadeh, R. Adeli, S. P. Shirmardi, "The effect of modified Tin oxide on X-ray attenuation: An experimental and theoretical study," Nuclear Instruments and Methods in Physics Research Section B: Beam Interactions with Materials and Atoms, vol. 549, p. 165277, 2024.

[41] M. Ghasemi-Nejad, L. Gholamzadeh, R. Adeli, S. P. Shirmardi, "A comprehensive study of the antibacterial and shielding properties of micro and nano-EPVC lead-free shields," Phys. Scr., vol. 97, no. 5, 2022.

[42] C. R. Blackwell, K. D. Amundson, "Cadmium free lead alloy for reusable radiotherapy shielding," Medical Dosimetry, vol. 15, no. 3, pp. 127–129, 1990.

[43] D.-E. Kwon, D.-H. Han, K.-H. Jung, S.-J. Lee, J.-O. Kim, C.-H. Baek, "Performance and feasibility evaluation for radiation shielding of metal oxides: Monte Carlo simulation," J. Korean Phys. Soc., vol. 82, no. 8, pp. 813–817, 2023.

[44] H. Schlattl, M. Zankl, H. Eder, C. Hoeschen, "Shielding properties of lead-free protective clothing and their impact on radiation doses," Medical Physics, vol. 34, no. 11, pp. 4270–4280, 2007.

[45] M.-A. Shahbazi, L. Faghfouri, M. P. A. Ferreira, P. Figueiredo, H. Maleki, F. Sefat, J. Hirvonen, H. A. Santos, "The versatile biomedical applications of bismuth-based nanoparticles and composites: therapeutic, diagnostic, biosensing, and regenerative properties," Chem. Soc. Rev., vol. 49, no. 4, pp. 1253–1321, 2020.

[46] Y. Xin, Z. Wang, C. Yao, H. Shen, Y. Miao, "Bismuth, a Previously Less-studied Element, Is Bursting into New Hotspots," ChemistrySelect, vol. 7, no. 21, p. e202201220, 2022.

[47] H.-T. Sun, J. Zhou, J. Qiu, "Recent advances in bismuth activated photonic materials," Progress in Materials Science, vol. 64, pp. 1–72, 2014.

[48] W. M. Haynes, D. R. Lide, T. J. Bruno, CRC Handbook of Chemistry and Physics, 2016–2017, 97th ed. Boca Raton, FL: CRC Press, 2016.

[49] F. Bakri, P. L. Gareso, D. Tahir, "Advancing radiation shielding: A review the role of Bismuth in X-ray protection," Radiation Physics and Chemistry, vol. 217, p. 111510, 2024.

[50] G. Toshinsky, V. Petrochenko, "Modular Lead-Bismuth Fast Reactors in Nuclear Power," Sustainability, vol. 4, no. 9, pp. 2293–2316, 2012.

[51] N. J. Abualroos, K. A. Yaacob, R. Zainon, "Radiation attenuation effectiveness of polymer-based radiation shielding materials for gamma radiation," Radiation Physics and Chemistry, vol. 212, p. 111070, 2023.

[52] R. U. Ayres, L. W. Ayres, I. Råde, "Lead, Zinc and Other Byproduct Metals," in The Life Cycle of Copper, Its Co-Products and Byproducts, R. U. Ayres, L. W. Ayres, and I. Råde, Eds., Dordrecht: Springer Netherlands, 2003, pp. 101–147.

[53] T. Ibn-Mohammed, I. M. Reaney, S. C. L. Koh, A. Acquaye, D. C. Sinclair, C. A. Randall, F. H. Abubakar, L. Smith, G. Schileo, L. Ozawa-Meida., "Life cycle assessment and environmental profile evaluation of lead-free piezoelectrics in comparison with lead zirconate titanate," Journal of the European Ceramic Society, vol. 38, no. 15, pp. 4922–4938, 2018.

[54] A. T. Odularu, "Bismuth as Smart Material and Its Application in the Ninth Principle of Sustainable Chemistry," Journal of Chemistry, vol. 2020, pp. 1–15, 2020.

[55] M. Karimi, K. Ghazikhanlou-sani, A. R. Mehdizadeh, H. Mostaghimi, "Lead-free transparent shields for diagnostic X-rays: Monte Carlo simulation and measurements," Radiol Phys Technol, vol. 13, no. 3, pp. 276–287, 2020.

[56] L. S. Waters, G. W. McKinney, J. W. Durkee, M. L. Fensin, J. S. Hendricks, M. R. James, R. C. Johns, D. B. Pelowitz., "The MCNPX Monte Carlo Radiation Transport Code," in AIP Conf. Proc., Batavia, IL, USA, 2007, pp. 81–90.

[57] S. M. Seltzer. (1987). XCOM: Photon Cross Sections Database (NIST Standard Reference Database 8) [Online]. Available: https://www.nist.gov/pml/xcom-photon-cross-sections-database .

[58] L. Yu, P. L. Yap, A. Santos, D. Tran, D. Losic, "Lightweight Bismuth Titanate (Bi 4 Ti 3 O 12) Nanoparticle-Epoxy Composite for Advanced Lead-Free X-ray Radiation Shielding," ACS Appl. Nano Mater., vol. 4, no. 7, pp. 7471–7478, 2021.

[59] T. H. Khazaalah, I. S. Mustafa, H. Al-Ghamdi, A. A. Rahman, M. I. Sayyed, A. H. Almuqrin, M. H. M. Zaid, R. Hisam, M. F. I. A. Malik, N. S. Ezra, H. M. Shariff, "The Effect of WO3-Doped Soda Lime Silica SLS Waste Glass to Develop Lead-Free Glass as a Shielding Material against Radiation," Sustainability, vol. 14, no. 4, p. 2413, 2022.

[60] W. Li, S. Chen, M. Peng, X. Zhou, X. Zhao, "Radiation shielding design and development of Bi/Ta/PU lead-free flexible textile composites," J. Ind. Textiles, vol. 53, 2023.

[61] S. Jing, H. Liqin, L. Pengcheng, H. Tao, H. Lijuan, C. Mengyun, Z. Huaqing, Y. Shengpeng, S. Guangyao, D. Tongqiang, Y. Qi, W. Bin, C. Chaobin, F. Ling, Y. Qianfeng, W. Yican, FDS Team, "Monte Carlo Simulation Software SuperMC 2.3 for Fusion and Fission Applications," in Proc. Reactor Physics Asia 2015 (RPHA15), Jeju, Korea, 2015.

[62] M. A. M. Uosif, S. A. M. Issa, A. Ene, A. M. A. Mostafa, A. Atta, E. F. El Agammy, H. M. H. Zakaly, "Lead-free ternary glass for radiation protection: Composition and performance evaluation for solar cell coverage," Materials, vol. 16, no. 8, p. 3036, 2023.

[63] Y. Al-Hadeethi, M. I. Sayyed, A. Z. Barasheed, M. Ahmed, M. Elsafi, "Fabrication of lead-free borate glasses modified by bismuth oxide for gamma ray protection applications," Materials, vol. 15, no. 3, p. 789, 2022.

[64] J.-H. Liu, Q.-P. Zhang, N. Sun, Y. Zhao, R. Shi, Y.-L. Zhou, J. Zheng, "Elevated gamma-rays shielding property in lead-free bismuth tungstate by nanofabricating structures," Journal of Physics and Chemistry of Solids, vol. 112, pp. 185–189, 2018.

[65] S. K. Das, C. H. R. V. S. Nagesh, T. Sreenivas, T. Kundu, S. I. Angadi, "A treatise on occurrence, beneficiation and plant practices of tungsten-bearing ores," Powder Technology, vol. 429, p. 118938, 2023.

[66] P. E. Leffler, G. Kazantzis, "Tungsten," in Handbook on the Toxicology of Metals, G. F. Nordberg, B. A. Fowler, and M. Nordberg, Eds. Amsterdam: Elsevier, 2015, pp. 1297–1306.

[67] W. Cheewasukhanont, P. Limkitjaroenporn, M. I. Sayyed, S. Kothan, H. J. Kim, J. Kaewkhao, "High density of tungsten gadolinium borate glasses for radiation shielding material: Effect of WO3 concentration," Radiation Physics and Chemistry, vol. 192, p. 109926, 2022.

[68] S. Kobayashi, N. Hosoda, R. Takashima, "Tungsten alloys as radiation protection materials," Nuclear Instruments and Methods in Physics Research Section A: Accelerators, Spectrometers, Detectors and Associated Equipment, vol. 390, no. 3, pp. 426–430, 1997.

[69] J. Webb, S. Gollapudi, I. Charit, "An overview of creep in tungsten and its alloys," International Journal of Refractory Metals and Hard Materials, vol. 82, pp. 69–80, 2019.

[70] Y. Taki, K. Shinozaki, T. Honma, V. Dimitrov, T. Komatsu, "Electronic polarizability and interaction parameter of gadolinium tungsten borate glasses with high WO3 content," Journal of Solid State Chemistry, vol. 220, pp. 191–197, 2014.

[71] N. Jamal AbuAlRoos, M. N. Azman, N. A. Baharul Amin, R. Zainon, "Tungsten-based material as promising new lead-free gamma radiation shielding material in nuclear medicine," Physica Medica, vol. 78, pp. 48–57, 2020.

[72] M. N. Azman, N. J. Abualroos, K. A. Yaacob, R. Zainon, "Feasibility of nanomaterial tungsten carbide as lead-free nanomaterial-based radiation shielding," Radiation Physics and Chemistry, vol. 202, p. 110492, 2023.

[73] T. Lee, C. Yoon, S. Jo, N. Kim, "Performance estimation of lead-free dual-layered shielding in dismantling of steam generator: A Monte-Carlo simulation study," Applied Radiation and Isotopes, vol. 176, p. 109879, 2021.

[74] G. Battistoni, J. Bauer, T. T. Boehlen, F. Cerutti, M. P. W. Chin, R. Dos Santos Augusto, A. Ferrari, P. G. Ortega, W. Kozłowska, G. Magro, A. Mairani, K. Parodi, P. R. Sala, P. Schoofs, T. Tessonnier, V. Vlachoudis, "The FLUKA Code: An Accurate Simulation Tool for Particle Therapy," Front Oncol, vol. 6, p. 116, 2016.

[75] A. Das, A. Ray, T. Singh, "Tungsten-based polymer composite, a new lead-free material for efficient shielding of coupled neutron-gamma radiation fields: A FLUKA simulation study," Phys. Scr., vol. 98, no. 11, p. 115302, 2023.

[76] F. Olivieri, R. Avolio, G. Gentile, A. Mazzone, R. Rizzi, M. Nacucchi, R. Castaldo, M. E. Errico, C. Giannini, L. Ambrosio, M. Lavorgna, "High filler content acrylonitrile-butadiene-styrene composites containing tungsten and bismuth oxides for effective lead-free x-ray radiation shielding," Polymer Composites, vol. 45, no. 3, pp. 2101–2113, 2024.

[77] A. Oskarsson, "Chapter 4 – Barium," in Handbook on the Toxicology of Metals (Fifth Edition), G. F. Nordberg and M. Costa, Eds. Amsterdam: Academic Press, pp. 91–100, 2022.

[78] G. Kaur, S. G. Waldrop, V. Kumar, O. P. Pandey, N. Sriranganathan, "An Introduction and History of the Bioactive Glasses," in Biocompatible Glasses, J. Marchi, Ed., Advanced Structured Materials, vol. 53. Cham: Springer International Publishing, pp. 19–47, 2016.

[79] J. Singh, V. Kumar, Y. K. Vermani, M. S. Al-Buriahi, J. S. Alzahrani, T. Singh, "Fabrication and characterization of barium based bioactive glasses in terms of physical, structural, mechanical and radiation shielding properties," Ceramics International, vol. 47, no. 15, pp. 21730–21743, 2021.

[80] D. S. Baykal, G. Kilic, E. Ilik, E. Kavaz, G. ALMisned, R. B. Cakirli, H. O. Tekin, "Designing a Lead-free and high-density glass for radiation facilities: Synthesis, physical, optical, structural, and experimental gamma-ray transmission properties of newly designed barium-borosilicate glass sample," Journal of Alloys and Compounds, vol. 965, p. 171392, 2023.

[81] F. Moradi, M. Jalili, K. R. E. Saraee, M. R. Abdi, H. A. A. Rashid, "Radiation shielding assessment for interventional radiology personnel: Geant4 dosimetry of lead-free compositions," Biomed. Phys. Eng. Express, vol. 10, no. 2, p. 025029, 2024.

[82] E. G. Souza, K. Kruger, C. D. Nascimento, C. Aguzzoli, G. Hoff, A. C. B. K. Moraes, R. G. Lund, P. S. Nascente, C. E. Cuevas-Suárez, E. Piva, N. L. V. Carreno, "Development of lead-free radiation shielding material utilizing barium sulfate and magnesium oxide as fillers in addition cure liquid silicone rubber," Polymers, vol. 15, no. 22, p. 4382, 2023.

[83] E. Hannachi, Y. Slimani, M. I. Sayyed, K. G. Mahmoud, "Scheelite-type BaWO4 doped with Ho2O3 oxide as a promising lead-free shield for gamma rays: Structural, optical properties, and radiation attenuation efficiency," Materials Science in Semiconductor Processing, vol. 167, p. 107802, 2023.

[84] M. Hoch, "Organotin compounds in the environment—an overview," Applied Geochemistry, vol. 16, pp. 719–743, 2001.

[85] B. Cornelius, S. Treivish, Y. Rosenthal, M. Pecht, "The phenomenon of tin pest: A review," Microelectronics Reliability, vol. 79, pp. 175–192, 2017.

[86] G. Nordberg, Handbook on the toxicology of metals, 3rd ed. Amsterdam Boston: Academic Press, 2007.

[87] T. A. Bjarnason, "Letter to the editor: The absorption properties of lead-free garments for use in radiation protection," Radiation Protection Dosimetry, vol. 179, no. 3, pp. 253–253, 2018.

[88] M. Bakhshandeh, M. B. Ziarani, M. B. Farsani, E. Bakhshandeh, N. Shakeri, "Review and performance comparison of lead-free shields and lead shields, in terms of biological effects in nuclear medicine by the comet method," Koomesh, vol. 20, no. 4, pp. 792–799, 2018.

[89] B. Alım, "A comprehensive study on radiation shielding characteristics of Tin-Silver, Manganin-R, Hastelloy-B, Hastelloy-X and Dilver-P alloys," Appl. Phys. A, vol. 126, no. 4, p. 262, 2020.

[90] K. A. Isimekhai, "Environmental risk assessment for an informal E-Waste recycling site in Lagos State, Nigeria," Middlesex University, London, 2016.

[91] G. Genchi, M. S. Sinicropi, G. Lauria, A. Carocci, A. Catalano, "The Effects of Cadmium Toxicity," IJERPH, vol. 17, no. 11, p. 3782, 2020.

[92] A. M. el-Khatib, M. I. Abbas, M. Abd elzaher, M. S. Badawi, M. T. Alabsy, G. A. Alharshan, D. A. Aloraini "Gamma Attenuation Coefficients of Nano Cadmium Oxide/High density Polyethylene Composites," Sci Rep, vol. 9, no. 1, p. 16012, 2019.

[93] L. Obied, "Infrared Spectroscopy of Gadolinium," Brock University, 2013. [Online]. Available: http://hdl.handle.net/10464/4275

[94] L. Blomqvist, G. F. Nordberg, V. M. Nurchi, J. O. Aaseth, "Gadolinium in Medical Imaging—Usefulness, Toxic Reactions and Possible Countermeasures—A Review," Biomolecules, vol. 12, no. 6, p. 742, 2022.

[95] H. Ogul, B. Gultekin, H. Yildiz, H. Us, F. Bulut, "Novel 3D-Printed lead-free radiation protection apron in the medical X-ray and thermal neutron energy range," Radiation Physics and Chemistry, vol. 219, p. 111686, 2024.

[96] S. Sundar, J. Chakravarty, "Antimony Toxicity," IJERPH, vol. 7, no. 12, pp. 4267–4277, 2010.

[97] R. S. Multani, T. Feldmann, G. P. Demopoulos, "Antimony in the metallurgical industry: A review of its chemistry and environmental stabilization options," Hydrometallurgy, vol. 164, pp. 141–153, 2016.

[98] C. Reimann, J. Matschullat, M. Birke, R. Salminen, "Antimony in the environment: Lessons from geochemical mapping,"

Applied Geochemistry, vol. 25, no. 2, pp. 175–198, 2010.

[99] C. Zeng, Q. Kang, Z. Duan, B. Qin, X. Feng, H. Lu, Y. Lin, "Development of polymer composites in radiation shielding applications: A review," J Inorg Organomet Polym, vol. 33, no. 8, pp. 2191–2239, 2023, https://doi.org/10.1007/s10904-023-02725-6

[100] S. Wu, J. Bao, Y. Gao, W. Hu, Z. Lu, "Review on flexible radiation-protective clothing materials," J Mater Sci, vol. 59, no. 19, pp. 8109–8133, 2024.

[101] F. Özkalaycı, M. R. Kaçal, H. Polat, O. Agar, N. Almousa, F. Akman, "Lead-free Sb-based polymer composite for γ-ray shielding purposes," Radiochimica Acta, vol. 110, no. 5, pp. 393–402, 2022.

[102] J. A. Novotny, C. A. Peterson, "Molybdenum," Advances in Nutrition, vol. 9, no. 3, pp. 272–273, 2018.

[103] D. G. Barceloux, D. Barceloux, "Molybdenum," Journal of Toxicology: Clinical Toxicology, vol. 37, no. 2, pp. 231–237, 1999.

[104] J. M. Khurana, S. Chauhan, A. Agrawal, "Molybdenum in organic synthesis: A review," Organic Preparations and Procedures International, vol. 36, no. 3, pp. 201–276, 2004.

[105] J. A. Novotny, "Molybdenum nutriture in humans," J Evid Based Complementary Altern Med, vol. 16, no. 3, pp. 164–168, 2011.

[106] K. S. Al-mugren, L. Almalki, R. Alshehri, S. Alamri, M. Almurayshid, M. Alsuhybani, R. Alharbi, M. U. Khandaker, "Development of lead-free metal carbides and ceramic decorated HDPE composites for low energy X-ray shielding applications," Radiation Physics and Chemistry, vol. 220, p. 111688, 2024.